

Old Dominion University

ODU Digital Commons

Civil & Environmental Engineering Theses & Dissertations

Civil & Environmental Engineering

Spring 1998

Fiber-Reinforced Plastic Composite Beam Stability and Load and Resistance Factor Design Approach

Mojtaba B. Sirjani
Old Dominion University

Follow this and additional works at: https://digitalcommons.odu.edu/cee_etds



Part of the [Civil Engineering Commons](#)

Recommended Citation

Sirjani, Mojtaba B.. "Fiber-Reinforced Plastic Composite Beam Stability and Load and Resistance Factor Design Approach" (1998). Doctor of Philosophy (PhD), Dissertation, Civil & Environmental Engineering, Old Dominion University, DOI: 10.25777/1qy8-1t34
https://digitalcommons.odu.edu/cee_etds/98

This Dissertation is brought to you for free and open access by the Civil & Environmental Engineering at ODU Digital Commons. It has been accepted for inclusion in Civil & Environmental Engineering Theses & Dissertations by an authorized administrator of ODU Digital Commons. For more information, please contact digitalcommons@odu.edu.

**FIBER REINFORCED PLASTIC COMPOSITE BEAM STABILITY AND
LOAD AND RESISTANCE FACTOR DESIGN APPROACH**

By

MOJTABA B. SIRJANI
B. S. May 1984, Old Dominion University
M.S. May 1989, North Carolina A&T State University

A Dissertation Submitted to the Faculty of
Old Dominion University in Partial Fulfillment of the
Requirements for the Degree of

DOCTOR OF PHILOSOPHY

CIVIL ENGINEERING

**OLD DOMINION UNIVERSITY
MAY 1998**

Approved by:

Dr. Zia Razzaq, Chairman

Dr. Isao Ishibashi

Dr. Gene J.-W. Hou

ABSTRACT

FIBER REINFORCED PLASTIC COMPOSITE BEAM STABILITY AND LOAD AND RESISTANCE FACTOR DESIGN APPROACH

Mojtaba B. Sirjani
Old Dominion University, 1998
Advisor: Dr. Zia Razzaq

Fiber Reinforced Plastic (FRP) structural members are rapidly gaining impetus in civil engineering applications. Also, thin-walled open beams with I-shaped, channel, and other types of sections are of practical importance to both structural analysts and designers. This dissertation presents the outcome of a detailed experimental and theoretical investigation of the strength and stability of FRP composite beams. Three- and four-point loading tests are conducted on FRP I- and channel section beams. The behavior of these beams is studied under gradually increasing static loads up to the maximum load-carrying capacity corresponding to either material cracking or flexural-torsional instability. First, the theoretical analysis is formulated using an equilibrium approach based on a system of flexural and torsional differential equations. Next, a central finite-difference scheme is developed and programmed to solve the coupled system of the differential equations of equilibrium. In addition, a buckling load formula is developed for the case of four-point loading based on an energy approach, including the load height effect. The theoretical analysis based on the equilibrium approach is found to be in good agreement with the experimental results. The buckling load formula is also found to be in excellent agreement with the experimental buckling loads. Lastly, a Load & Resistance Factor Design (LRFD)

approach is presented and its use demonstrated by means of practical analysis and design examples.

TABLE OF CONTENTS

	<u>Page</u>
ABSTRACT	i
ACKNOWLEDGEMENT	iii
NOMENCLATURE	iv
LIST OF TABLES	vii
LIST OF FIGURES	xi
I. INTRODUCTION	1
1.1 Background	1
1.2 Literature Review	1
1.3 Problem Definition	5
1.4 Objective and Scope	6
1.5 Assumptions and Conditions	7
II. EXPERIMENTAL INVESTIGATION	8
2.1 Stability and Flexural-Torsional Tests	8
2.2 Mechanical Properties of Materials	9
2.3 Apparatus and Test Procedure	11
2.4 Test Results and Discussion	13
2.4.1 Minor Axis Flexure	13
2.4.2 Stability of I-Section Beam	13
2.4.2.1 Three-Point Loading Through Shear Center	14
2.4.2.2 Four-Point Loading Through Shear Center	15

	<u>Page</u>
2.4.3 Stability of Channel Section Beams	15
2.4.3.1 Three-Point Loading Through Shear Center	15
2.4.3.2 Four-Point Loading Through Shear Center	16
2.4.3.3 Four-Point Loading Away From Shear Center	17
III. THEORETICAL ANALYSES	18
3.1 Prologue	18
3.2 Cross-Sectional Equilibrium Equations	19
3.2.1 Governing Differential Equations For Three-Point Loading	21
3.2.2 Governing Differential Equations For Four-Point Loading	23
3.3 BOUNDARY AND OTHER CONDITIONS	23
3.4 Finite-Difference Formulation	24
3.5 Moment-Curvature and Load-Deflection Curves	
Including Material Cracking	26
3.6 Bucking Load Formula for Four-Point Loading with Energy Approach ...	28
3.7 BEAM STABILITY	30
3.7.1 I-Section Beams	30
3.7.1.1 Three-Point Loading	30
3.7.1.2 Four-Point Loading	30
3.7.2 Channel Section Beams	30
3.7.2.1 Three-Point Loading	30
3.7.2.2 Four-Point Loading	31
3.7.3 Flexural-Torsional Behavior of Channel Beam	31

IV	LOAD AND RESISTANCE FACTOR DESIGN APPROACH	
	FOR FRP BEAM STABILITY	32
4.1	LRFD Philosophy For FRP Composite e Beams	33
4.2	Maximum Bending Moment versus Beam Length Relations	34
4.3	LRFD Approach For FRP Composite Beams	36
4.4	LRFD Analysis Example	37
4.5	LRFD Design Example	39
V.	COMPARISON OF RESULTS AND CONCLUSIONS	42
5.1	Comparison of Theory and Experiments	42
5.2	Load Height Effect	41
5.3	Conclusions	41
5.4	Future Research	42
	REFERENCES	43
	TABLES	44
	FIGURES	98
	APPENDIX: FINITE-DIFFERENCE PROGRAM FOR SOLVING SYSTEM OF FRP BEAM DIFFERENTIAL EQUATIONS	198
	VITA	223

ACKNOWLEDGEMENT

The author wishes to express his sincerest thanks to his advisor Dr. Zia Razzaq, Professor of Civil Engineering, for his continuous guidance, help, cooperation, and moral support throughout the course of this research. The participation of Dr. Ram Prabhakaran, Professor of Mechanical Engineering, in the initial phases of the experimental work is sincerely acknowledged. Special thanks are due to Dr. Isao Ishibashi, Professor of Civil Engineering, and Dr. Gene Hou, Professors of Mechanical Engineering for their helpful input. Also, the assistance provided by Jerry Robertson, Manager of Engineering Workshop at ODU, in the fabrication of test fixtures is sincerely appreciated.

The author wishes to express his gratitude to his parents Mohammed Sadgh Sirjani and Nossrat Sirjani, from Iran, for providing the encouragement to pursue higher education.

NOMENCLATURE

A	Area
B	Section width
D	Section depth
E	Young's modulus
E_T	Tensile Young's modulus
E_C	compression Young's modulus
E_t	Tangent Young's modulus
I_x, I_y	Moment of inertia about x-axis and y-axis
I_{xy}	product of inertia relative to x-axis and y-axis
$I_{\omega x}, I_{\omega y}$	warping moment of inertia relative to x-axis and y-axis,
G	Shear modulus of elasticity
$[K]$	Member global tangent stiffness matrix
K_T	St. Venant torsion
M_x, M_y	Bending moments
M_z	Torsional moment
M_{sv}	St. Venant torsion resisting moment
M_w	Resisting warping torsional moment
ω_n	Normlized unit warping
$\{M\}$	Moment vector
P	Applied axial load
δa	Elemental area
h	Distance between nodes

n	Total nodes
u	Deflection due to load in x-direction
v	Deflection due to load in y-direction
u_0	Initial member crookedness in x-direction
ϕ_0	Initial member crookedness in x-direction
u_{oi}	Midspan initial crookedness amplitude in x-direction
ϕ_{oi}	Midspan initial crookedness amplitude in x-direction
x, y, z	Global coordinates
X, Y	Centroid coordinates
z_i	Nodal distance from end of beam
Π	Total energy
$\{ \delta \}$	Cross-sectional deformation vector
ϵ	Normal strain
ϵ_t	Tensile strain
ϵ_c	Compression strain
ϵ_{ut}	Ultimate (fracture) tensile strain
ϵ_{uc}	Ultimate (fracture) compression strain
ϵ_{cr}	Tensile cracking strain
σ	Stress
σ_{uT}	Ultimate (fracture) tensile strength
σ_{uC}	Ultimate (fracture) compression strength
ϕ	Angle of twist
Φ_x, Φ_y	Bending curvatures

$\{\Delta\}$	Deformation vector
\int_A	Cross-sectional integration
e^*	Imperfection factor
e	eccentricity

LIST OF TABLES

<u>TABLE</u>	<u>PAGE</u>
Table 2.1 Tensile coupon tests results for Specimen 1 from flange of I-section (coupon cross-sectional dimensions: 0.8x0.25 in.)	44
Table 2.2 Tensile coupon tests results for Specimen 2 from flange of I-section (coupon cross-sectional dimensions: 0.8x0.25 in.)	45
Table 2.3 Tensile coupon tests results for Specimen 3 from web of I-section (coupon cross-sectional dimensions: 0.9x0.25 in.)	46
Table 2.4 Tensile coupon tests results for Specimen 4 from web of I-section (coupon cross-sectional dimensions: 0.8x0.25 in.)	47
Table 2.5 Summary of tensile test results for material of I-section	48
Table 2.6 Tensile coupon tests results for Specimen 5 from flange of channel section (coupon cross-sectional dimensions: 1.1x0.25 in.)	49
Table 2.7 Tensile coupon tests results for Specimen 6 from flange of channel section (coupon cross-sectional dimensions: 1.0x0.25 in.)	50
Table 2.8 Tensile coupon tests results for Specimen 7 from web of channel section (coupon cross-sectional dimensions: 1.0x0.25 in.)	51
Table 2.9 Tensile coupon tests results for Specimen 8 from web of channel section (coupon cross-sectional dimensions: 1.1x0.25 in.)	52
Table 2.10 Summary of tensile test results for material of channel section	53
Table 2.11 Minor axis bending test results for I-beam (in., L=30 in.)	54
Table 2.12 Results for FRP I-beam (in.) Test No. IFT3-1 with three-point loading (L=108 in.)	55
Table 2.13 Results for FRP I-beam (in.) Test No. IFT3-2 with three-point loading (L=96 in.)	56
Table 2.14 Results for FRP I-beam (in.) Test No. IFT3-3 with three-point loading (L=84 in.)	57
Table 2.15 Results for FRP I-beam (in.) Test No. IFT3-4 with three-point loading (L=72 in.)	58

Table 2.16	Results for FRP I-beam (in.) Test No. IFT4-1 with four-point loading (L=108 in.)	59
Table 2.17	Results for FRP I-beam (in.) Test No. IFT4-2 with four-point loading (L=96 in.)	60
Table 2.18	Results for FRP I-beam (in.) Test No. IFT4-3 with four-point loading (L=84 in.)	61
Table 2.19	Results for FRP I-beam (in.) Test No. IFT4-4 with four-point loading (L=72 in.)	62
Table 2.20	Results for FRP I-beam (in.) Test No. IFT4-5 with four-point loading (L=60 in.)	63
Table 2.21	Results for FRP channel beam (in.) Test No. CFT3-1 with three-point loading (L=108 in.)	64
Table 2.22	Results for FRP channel beam (in.) Test No. CFT3-2 with three-point loading (L=96 in.)	65
Table 2.23	Results for FRP channel beam (in.) Test No. CFT4-1 with four-point loading (L=108 in.)	66
Table 2.24	Results for FRP channel beam (in.) Test No. CFT4-2 with four-point loading (L=102 in.)	67
Table 2.25	Results for FRP channel beam (in.) Test No. CFT4-3 with four-point loading (L= 96 in.)	68
Table 2.26	Results for FRP channel beam (in.) Test No. CFT4-4 with four-point loading (L=84 in.)	69
Table 2.27	Results for FRP channel beam (in.) Test No. CFT4-5 with four-point loading (L=72 in.)	70
Table 2.28	Results for FRP channel beam (in.) Test No. CFT4-6 with four-point loading (L=60 in.)	71
Table 2.29	Results for FRP channel beam (in.) Test No. CFT4-7 with four-point loading (L=84 in.) (centroidal loading; x = -0.5675 in., y = -3.5 in.)	72

Table 2.30	Results for FRP channel beam (in.) Test No. CFT4-8 with four-point loading ($L=84$ in.) (loading between centroid and shear center ; $x = -0.2656$ in., $y = -3.5$ in.)	73
Table 2.31	Results for FRP channel beam (in.) Test No. CFT4-9 with four-point loading ($L=84$ in.) (loading to the right side of the shear center; $x=0.4531$ in., $y = -3.5$ in.)	74
Table 3.1	Minor axis bending theoretical results for I-beam (in., $L = 30$ in.)	75
Table 3.2	Results for FRP composite I-beam (in.) Test No. IFT3-1 with three-point loading ($L=108$ in., $e = -0.002$ in.)	76
Table 3.3	Results for FRP composite I-beam (in.) Test No. IFT3-2 with three-point loading ($L=96$ in., $e = -0.002$ in.)	77
Table 3.4	Results for FRP composite I-beam (in.) Test No. IFT3-3 with three-point loading ($L=84$ in., $e = -0.002$ in.)	78
Table 3.5	Results for FRP composite I-beam (in.) Test No. IFT3-4 with three-point loading ($L=72$ in., $e = +0.002$ in.)	79
Table 3.6	Results for FRP composite I-beam (in.) Test No. IFT4-1 with four-point loading ($L=108$ in., $e = -0.0002$ in.)	80
Table 3.7	Results for FRP composite I-beam (in.) Test No. IFT4-2 with four-point loading ($L=96$ in., $e = -0.00007$ in.)	81
Table 3.8	Results for FRP composite I-beam (in.) Test No. IFT4-3 with four-point loading ($L=84$ in., $e = -0.0005$ in.)	82
Table 3.9	Results for FRP composite I-beam (in.) Test No. IFT4-4 with four-point loading ($L=72$ in., $e = -0.0005$ in.)	83
Table 3.10	Results for FRP composite I-beam (in.) Test No. IFT4-5 with four-point loading ($L=60$ in., $e = -0.0005$ in.)	84
Table 3.11	Results for FRP composite I-beam (in.) Test No. CFT3-1 with three-point loading ($L=108$ in., $e = 0.0003$ in.)	85

Table 3.12	Results for FRP composite I-beam (in.) Test No. CFT3-2 with three-point loading ($L=96$ in., $e = 0.0003$ in.)	86
Table 3.13	Results for FRP composite I-beam (in.) Test No. CFT4-1 with four-point loading ($L=108$ in., $e = - 0.0003$ in.)	87
Table 3.14	Results for FRP composite I-beam (in.) Test No. CFT4-2 with four-point loading ($L=102$ in., $e = - 0.0005$ in.)	88
Table 3.15	Results for FRP composite I-beam (in.) Test No. CFT4-3 with four-point loading ($L=96$ in., $e = - 0.0001$ in.)	89
Table 3.16	Results for FRP composite I-beam (in.) Test No. CFT4-4 with four-point loading ($L=84$ in., $e = - 0.00009$ in.)	90
Table 3.17	Results for FRP composite I-beam (in.) Test No. CFT4-5 with four-point loading ($L=72$ in., $e = - 0.0009$ in.)	91
Table 3.18	Results for FRP composite I-beam (in.) Test No. CFT4-6 with four-point loading ($L=60$ in., $e = - 0.0005$ in.)	92
Table 3.19	Results for FRP composite I-beam (in.) Test No. CFT4-7 with four-point loading ($L=84$ in.; centroidal loading, $e = -0.5675$ in.)	93
Table 3.20	Results for FRP composite I-beam (in.) Test No. CFT4-8 with four-point loading ($L=84$ in.; loading between centroid and shear center $e = -0.2656$ in.)	94
Table 3.21	Results for FRP composite I-beam (in.) Test No. FT4-9 with four-point loading ($L=84$ in.; loading to the right side of the shear center $e = 0.4531$ in.)	95
Table 4.1	Summary of Comparison of Peak loads from Flexural-Torsional Experiment Theory	96
Table 5.1	Effect of load height on FRP channel beam buckling load	97

LIST OF FIGURES

<u>FIGURE</u>	<u>PAGE</u>
1a. Schematic view of FRP composite beam with three-point loading	98
1b. Schematic view of FRP composite beam with three-point loading	98
2. Cross-sectional dimensions of FRP composite I-section	98a
3. Cross-sectional dimensions of FRP composite channel section	98a
4. Tensile stress-strain relationship	99
5. Location and numbers of test specimens for I-section	100
6. Location and numbers of test specimens for channel section	101
7. Schematic of FRP composite tension test setup	102
8. Normal stress-strain relationship based on tensile coupon test for specimen 1 from flange of I-section (see table 2.1)	103
9. Normal stress-strain relationship based on tensile coupon test for specimen 2 from flange of I-section (see table 2.2)	104
10. Normal stress-strain relationship based on tensile coupon test for specimen 3 from web of I-section (see table 2.3)	105
11. Normal stress-strain relationship based on tensile coupon test for specimen 4 from web of I-section (see table 2.4)	106
12. Normal stress-strain relationship based on tensile coupon test for specimen 5 from flange of channel section (see table 2.5)	107
13. Normal stress-strain relationship based on tensile coupon test for specimen 6 from flange of channel section (see table 2.6)	108
14. Normal stress-strain relationship based on tensile coupon test for specimen 7 from web of I-section (see table 2.7)	109
15. Normal stress-strain relationship based on tensile coupon test for specimen 8 from web of I-section (see table 2.8)	110

16.	Cross-sectional schematic view at beam load application about minor axis . .	112
17.	Overall apparatus to conduct the flexural-torsional tests on FRP composite beams	113
18.	Loading setup with hydraulic jacks	114
19.	Tie rods connection of FRP composite beam	115
20.	Laboratory simulations of simple supports	116
21.	Load (P) at mid span about minor axis	117
22.	Load (P) versus midspan vertical deflection (v_c) about minor axis bending .	118
23.	Load (P) versus midspan vertical deflection (ϵ_c) about minor axis bending .	119
24.	Moment (M_y) versus (ϕ_y) about minor axis bending	120
25.	Cross-sectional schematic view at load application points for I-section beam	121
26.	Load (P) versus midspan vertical deflection (v_c) for test NO. IFT3-1	122
27.	Load (P) versus midspan lateral deflection (u_c) for test NO. IFT3-1	123
28.	Load (P) versus midspan angle of twist (ϕ_c) for test NO. IFT3-1	124
29.	Load (P) versus midspan vertical deflection (v_c) for test NO. IFT3-2	125
30.	Load (P) versus midspan lateral deflection (u_c) for test NO. IFT3-2	126
31.	Load (P) versus midspan angle of twist (ϕ_c) for test NO. IFT3-2	127
32.	Load (P) versus midspan vertical deflection (v_c) for test NO. IFT3-3	128
33.	Load (P) versus midspan lateral deflection (u_c) for test NO. IFT3-3	129
34.	Load (P) versus midspan angle of twist (ϕ_c) for test NO. IFT3-3	130
35.	Load (P) versus midspan vertical deflection (v_c) for test NO. IFT3-4	131

36.	Load (P) versus midspan lateral deflection (u_c) for test NO. IFT3-4	132
37.	Load (P) versus midspan angle of twist (ϕ_c) for test NO. IFT3-4	133
38.	Load (P) versus midspan vertical deflection (v_c) for test NO. IFT4-1	134
39.	Load (P) versus midspan lateral deflection (u_c) for test NO. IFT4-1	135
40.	Load (P) versus midspan angle of twist (ϕ_c) for test NO. IFT4-1	136
41.	Load (P) versus maximum strain (ϵ_c) for test NO. IFT4-1	137
42.	Load (P) versus midspan vertical deflection (v_c) for test NO. IFT4-2	138
43.	Load (P) versus midspan lateral deflection (u_c) for test NO. IFT4-2	139
44.	Load (P) versus midspan angle of twist (ϕ_c) for test NO. IFT4-2	140
45.	Load (P) versus maximum strain (ϵ_c) for test NO. IFT4-2	141
46.	Load (P) versus midspan vertical deflection (v_c) for test NO. IFT4-3	142
47.	Load (P) versus midspan lateral deflection (u_c) for test NO. IFT4-3	143
48.	Load (P) versus midspan angle of twist (ϕ_c) for test NO. IFT4-3	144
49.	Load (P) versus maximum strain (ϵ_c) for test NO. IFT4-3	145
50.	Load (P) versus midspan vertical deflection (v_c) for test NO. IFT4-4	146
51.	Load (P) versus midspan lateral deflection (u_c) for test NO. IFT4-4	147
52.	Load (P) versus midspan angle of twist (ϕ_c) for test NO. IFT4-4	148
53.	Load (P) versus maximum strain (ϵ_c) for test NO. IFT4-4	149
54.	Load (P) versus midspan vertical deflection (v_c) for test NO. IFT4-5	150
55.	Load (P) versus midspan lateral deflection (u_c) for test NO. IFT4-5	151
56.	Load (P) versus midspan angle of twist (ϕ_c) for test NO. IFT4-5	152

	<u>PAGE</u>
57. Load (P) versus maximum strain (ϵ_c) for test NO. IFT4-5	153
58. Cross-sectional schematic view at load application points (F and G) for channel section beam	154
59 Load (P) versus midspan vertical deflection (v_c) for test NO. CFT3-1	159
60. Load (P) versus midspan lateral deflection (u_c) for test NO. CFT3-1	160
61. Load (P) versus midspan angle of twist (ϕ_c) for test NO. CFT3-1	161
62. Load (P) versus midspan vertical deflection (v_c) for test NO. CFT3-2	162
63. Load (P) versus midspan lateral deflection (u_c) for test NO. CFT3-2	163
64. Load (P) versus midspan angle of twist (ϕ_c) for test NO. CFT3-2	164
65. Load (P) versus midspan vertical deflection (v_c) for test NO. CFT4-1	165
66. Load (P) versus midspan lateral deflection (u_c) for test NO. CFT4-1	166
67. Load (P) versus midspan angle of twist (ϕ_c) for test NO. CFT4-1	167
68. Load (P) versus midspan vertical deflection (v_c) for test NO. CFT4-2	168
69. Load (P) versus midspan lateral deflection (u_c) for test NO. CFT4-2	169
70. Load (P) versus midspan angle of twist (ϕ_c) for test NO. CFT4-2	170
71. Load (P) versus midspan vertical deflection (v_c) for test NO. CFT4-3	171
72. Load (P) versus midspan lateral deflection (u_c) for test NO. CFT4-3	172
73. Load (P) versus midspan angle of twist (ϕ_c) for test NO. CFT4-3	173
74. Load (P) versus midspan vertical deflection (v_c) for test NO. CFT4-4	174
75. Load (P) versus midspan lateral deflection (u_c) for test NO. CFT4-4	175
76. Load (P) versus midspan angle of twist (ϕ_c) for test NO. CFT4-4	176
77. Load (P) versus maximum strain (ϵ_c) for Test No. CFT4-4	177

PAGE

78.	Load (P) versus midspan vertical deflection (v_c) for test NO. CFT4-5	178
79.	Load (P) versus midspan lateral deflection (u_c) for test NO. CFT4-5	179
80.	Load (P) versus midspan angle of twist (ϕ_c) for test NO. CFT4-5	180
81.	Load (P) versus midspan vertical deflection (v_c) for test NO. CFT4-6	181
82.	Load (P) versus midspan lateral deflection (u_c) for test NO. CFT4-6	182
83.	Load (P) versus midspan angle of twist (ϕ_c) for test NO. CFT4-6	183
84.	Load (P) versus midspan vertical deflection (v_c) for test NO. CFT4-7	184
85.	Load (P) versus midspan lateral deflection (u_c) for test NO. CFT4-7	185
86.	Load (P) versus midspan angle of twist (ϕ_c) for test NO. CFT4-7	186
87.	Load (P) versus maximum strain (ϵ_c) for Test No. CFT4-7	187
88.	Load (P) versus midspan vertical deflection (v_c) for test NO. CFT4-8	188
89.	Load (P) versus midspan lateral deflection (u_c) for test NO. CFT4-8	189
90.	Load (P) versus midspan angle of twist (ϕ_c) for test NO. CFT4-8	190
91.	Load (P) versus maximum strain (ϵ_c) for Test No. CFT4-8	191
92.	Load (P) versus midspan vertical deflection (v_c) for test NO. CFT4-9	192
93.	Load (P) versus midspan lateral deflection (u_c) for test NO. CFT4-9	193
94.	Load (P) versus midspan angle of twist (ϕ_c) for test NO. CFT4-9	194
95.	Load (P) versus maximum strain (ϵ_c) for Test No. CFT4-9	195
96.	Discretized I-section	196
97.	Discretized channel section	197
98.	Maximum bending moment versus length curves for three-point loading	

PAGE

	of I-section FRP composite beams	198
99.	Maximum bending moment versus length curves for four-point loading of I-section FRP composite beams	199
100.	Maximum bending moment versus length curves for three-point loading of channel section FRP composite beams section	200
101.	Maximum bending moment versus length curves for four-point loading of channel section FRP composite beams	201

.

CHAPTER I.

INTRODUCTION

1.1 Background

Pultruded fiber reinforced plastic (FRP) structural members offer many advantages over conventional construction materials used in civil engineering application. One class of FRP construction materials which is currently used and commercially produced for civil engineering applications is the wide variety of structural shapes such as the I-section, channel section, angle section, and other symmetrical and unsymmetrical open sections. Whereas the existing body of both research and practice-oriented literature provides ample information to engineers for dealing with the analysis and design problems of structural members of most conventional materials such as steel, concrete, aluminum, and timber, there exists a substantial deficiency in the literature for members made from FRP materials. Specifically, engineers need practical analysis and design procedures similar to those recommended by and contained in practical construction specifications such as AISC Load and Resistance Factor Design (LRFD) Specification¹. In general, the procedures need to have a theoretical basis verified by laboratory tests. This dissertation represents a step in that direction.

Two of the cross-sectional shapes of practical importance are the I-section and the channel section. When a structural member with an I- or a channel section is subjected to a gradually increasing bending load about the cross-sectional major axis, the maximum load-carrying capacity may be governed by in-plane cracking moment or by a lateral-torsional

The journal model is *Elsevier*.

buckling mode at some critical level of loading. It may be possible to predict the behavior of such beams by means of an equilibrium and/or energy approach. The solution to the corresponding governing lateral and torsional differential equations of equilibrium together with a set of specified boundary conditions, may provide the expected beam response when subjected to gradually increasing static loads. Furthermore, the energy approach may provide a means for beam buckling load formula development. Material cracking can develop due to a fracture of fibers and/or the matrix material, whereafter the overall material stress-strain relationship becomes suddenly discontinuous.

Presented herein is the outcome of a theoretical and experimental study of the flexural and flexural-torsional behavior of I-section and channel section FRP beams subjected to gradually increasing static loads up to the maximum load-carrying capacity. Next, utilizing the procedures formulated, a Load and Resistance Factor Design (LRFD) approach is presented and its practical use demonstrated by means of analysis and design examples.

1.2 Literature Review

A considerable amount of research has been conducted in the past on flexural and flexural-torsional behavior of steel beams such as that by Razzaq and Galambos^{2,3,4}. In contrast, the amount of published research on flexural and flexural-torsional behavior of composite beams is relatively limited.

Baz and Chen (5) determined that the lateral buckling characteristics of flexible composite beams are actively controlled by activating sets of shape memory alloy (NATIONAL) fibers which are embedded along the mid-plane of these beams. This feature is invaluable in building light weight structures that have high resistance to failure due to buckling. Finite element models are developed to analyze the mechanical and thermal

characteristics of the composite beams. The models account for the individual contributions of the matrix, the NATIONAL fibers and the shape memory defect to the overall performance of the composite beams. A system is built to validate the finite element model. The system is used to control the lateral buckling of a composite beam which is 40.6 cm long, 5.1 cm wide and 0.25 cm thick, and reinforced with two 0.55 mm diameter NATIONAL-55 fibers. The results obtained confirm the validity of the developed theoretical model and indicate that the buckled beams can be brought back completely to their unbuckled configuration by proper activation of the shape memory effect. Also, the results obtained suggest that reinforcing the beams with NATIONAL fibers are effective in enhancing their lateral buckling characteristics.

Pollock, Zak, Hinton and Ahmad (6) presented an analysis to determine shear center for anisotropic elastic thin-walled composite beams, cantilevered and loaded transversely at the free end. It was found that twisting may occur for composite beams even if shear forces are applied at the shear center.

Kim and Dharan (7) presented the analysis of a beam under three-point and five-point bending using orthotropic plane elasticity to investigate the inter-laminar shear failure of unidirectional composites. The approach uses Fourier series expansions of the applied concentrated loads, together with Saint Venant's semi-inverse method in which the stresses are obtained by a non-dimensional stress function.

Xie and Steven (8) presented an explicit formula for correcting finite element predictions of buckling loads for beams. They found a simple formula for exact or very accurate buckling loads of beams with various end restraints at almost no computational cost. This method was also applied to two- and three-dimensional frames and it was found that the

errors in the original finite element predictions of buckling loads were significantly reduced after such a correction.

Beg (9) derived an accurate finite element model for the lateral buckling of closed thin-walled beams. Fourth-order polynomials were assumed for the bending and warping curvatures. The result was that the shape function for the transverse displacements was the polynomial of the sixth degree, and for the warping function the polynomial of the fifth degree. The shape function for torsional rotation was then automatically the polynomial of the sixth degree. Since a mixed variational principle was applied, the axial force became an independent variable and the shape function for a longitudinal tangential matrix and nodal forces were based on the selective Gaussian numerical integration with five nodes for the terms related to bending and warping, and with six nodes for the terms related to torsion.

Barbero and Raftoyiannis (10) studied the elastic buckling modes of pultruded I-beams subjected to various loading conditions. The coupling of lateral and distortional buckling for thin-walled members was investigated. The effect of fiber orientation in the matrix and volume fraction on beam response was investigated by a parametric study.

Craddock and Shing-Chung (11) examined the bending behavior of graphite-epoxy I-beams. The beams used in this study were made of T300/934 graphite-epoxy with three different layers. Short-beam shear tests, and bending deflection contributions were separated using Timoshenko Beam Theory. The equivalent bending stiffness was obtained from the deflection due to bending. The bending stiffness was calculated in transformed-section method developed especially for composites. A comparison of analytical and experimental results indicated that both methods are accurate tools for predicating the bending stiffness of composite material beams.

Chandrashekhara and Bangera (12) studied the flexural analysis of fiber-reinforced composite beams based on higher-order shear deformation theory. The geometric nonlinearity was incorporated in the formulation by considering the von Karman strains. The finite element method was used to solve the nonlinear governing equations by direct iteration. Unlike conventional beam models, the beam model accounts for y-direction strains. It was observed that the solution obtained from the two approaches differs slightly in the case of cross-ply laminates, but there exists a considerable difference in the case of angle-ply laminates. The influence of boundary conditions, beam geometries, and ply orientations on the deflections and stresses of laminated beams was shown both in tabular and graphical form.

Puspita, Barrau and Gay (13) presented the analytical calculation of homogeneous properties and stresses of a beam made up of several orthotropic materials. Tests had been realized with existing solutions such as: classic theory, three-dimensional finite elements and experimental data. It was shown that the proposed analytical method gives good results for beams with a close thin-walled, partitioned section unfilled or filled up with foam.

A review of the existing literature shows that practically little research work has been conducted in the past on the flexural and flexural-torsional response of FRP beams up to the maximum load-carrying capacity. Also, no practical Factor Load and Resistance Design (LRFD) procedures are presented in the past for FRP beams.

1.3 Problem Definition

The main thrust of the present research is to study the flexural and flexural-torsional response of thin-walled open section FRP beams subjected to gradually increasing static loads. The first part of the problem is to conceive, design and build an apparatus to conduct

full-scale flexural and flexural-torsional experiments on FRP I-section and channel section beams. An essential feature of the test setup must be that it should not restrain the possible development of lateral-torsional beam deformations. The second part of the problem is to carefully conduct a series of flexural and flexural-torsional beam experiments including any material cracking. The third part of the problem is to develop a numerical solution algorithm to solve the governing differential equations of flexural and flexural-torsional equilibrium for a beam whose material may exhibit cracking and maximum load-carrying capacity. Furthermore, the numerical analysis must predict the experimental response of the beams within a reasonable tolerance. The fourth and the last part of the problem is to use the analysis to develop a Load and Resistance Factor Design (LRFD) approach for practical analysis and design of FRP beams.

1.4 Objective and Scope

The objective of this research is to develop practical analysis and design procedures for dealing with the flexural and flexural-torsional problems of FRP beams. This objective is largely fulfilled by solving the four different parts of the global problem posed in Section 1.3.

A wide variety of types of beam materials, loading, and boundary conditions may be encountered in practical applications. Although the specific results of the study reported in this dissertation are based on specific materials, loading, and boundary conditions as described below, the LRFD procedure presented can readily be extended to handle other situations.

The experimental results reported are for specific I-section and channel section sizes with varying from 5 feet to 9 feet. The material of the beams is isophthalic polyester. The

loading conditions are shown in Figure 1 and consist of three- and four-point loads increase gradually until the member maximum load-carrying capacity reached. The ends of the test specimens are free to warp, that is, no end plates are used to restrain warping. The theoretical analysis is based on a central finite-difference algorithm for solving fourth-order coupled ordinary differential equations of flexural and flexural-torsional equilibrium including material cracking. A lateral torsional buckling load formula based on an energy formulation and verified experimentally is also presented. A possible LRFD procedure is outlined and its use explained by means of practical FRP beam examples.

1.5 Assumptions and Conditions

The following assumptions and conditions are adopted in this dissertation:

1. Small deflection theory is valid.
2. Beam section is thin-walled and open.
3. The beam ends are simply-supported.
4. Local buckling is neglected for the plate elements forming the beam sections.
5. The beams are slender, the sections are thin-walled, and transverse shear deformations are ignored.
6. The applied static loads are increased gradually up to the member maximum load-carrying capacity.
7. The member end warping is unrestrained.

CHAPTER II.

EXPERIMENTAL INVESTIGATION

2.1 Stability and Flexural-Torsional Tests

A series of experiments are conducted on I- and channel section FRP beams with various lengths. A number of major axis tests are performed on I-section beams which experienced lateral-torsional instability. Although these beams resulted in load-deflection relations which eventually became nonlinear, they did not develop any material cracking. Additional tests on relatively short beams also exhibited lateral-torsional behavior rather than develop any cracking. This was further verified with the help of theoretical analysis which also showed that in order to develop cracking with major-axis loading, the beam span would have to be so small that it could not be considered a regular beam; instead it would become a deep beam -- a problem outside the realm of the present study. A minor flexural test on a small span I-beam, however, exhibited considerable cracking. Next, several stability and flexural-torsional major axis tests are conducted on a channel section beam.

The experimental study is conducted with four main objectives. First, it is considered necessary to observe the experimental behavior of the beams including their response under external loads and possible material cracking at high loads. Second, based on the observed beam behavior, an appropriate theoretical model is established with the goal of capturing the actual response which is presented in Chapter III of this dissertation. Third, the experimental maximum bending moment versus beam clear span relations are compared to those obtained theoretically. Lastly, the results obtained from the study are used as a basis for demonstrating the formulation of a Load and Resistance Factor Design (LRFD) approach for practical problems. Although only I-section and channel section FRP beams are investigated in this

dissertation, the analysis presented can readily be applied, with some modifications, to beams with other types of open cross sections. Figures 1 (a) and 1 (b) show schematically three-point and four-point loading conditions, respectively, adopted for the beam tests. The static load P or the load pair (P, P) is applied gradually until the beam maximum load-carrying capacity is reached. Lateral bracing is provided at the ends A and B, indicated by X marks.

Tests are conducted on beams with clear spans, L , of 5, 6, 7, 8 and 9 ft. Figures 2 and 3 show the cross-sectional dimensions of the FRP I- and channel sections used in the experimental study. The cross-sectional principal centroidal major and minor axes, x and y are also shown in these figures. The tests are conducted with simply-supported flexural and torsionally pinned boundary conditions. For all of the tests with four-point loading, the distance between the loads P and P is kept constant at $b = 24$ in.

A $4 \times 2 \times \frac{1}{4}$ in. cross section is adopted for the I-beam and a $6 \times 1 \frac{5}{8} \times \frac{1}{4}$ in. for the channel section. These beams are manufactured, respectively, by IKG Industries, Nashville, TN, and Creative Pultrusions, Inc., Alum Bank, PA.

The experimental measurements consist of the applied load(s) and the resulting beam displacements, rotations, and strains at key locations. The load versus deflection and strain curves are compared, in Chapter IV, to those obtained theoretically.

2.2 Mechanical Properties of Materials

The mechanical properties of the FRP materials are found by conducting ASTM tension tests using a Tinius Olsen testing machine. Figure 4 shows a generic tensile stress-strain relationship for the type of beam FRP material used in this research. In this figure, E_T is the tensile Young's modulus; σ_{uT} is the ultimate (fracture) tensile strength and ϵ_{uT} is the

ultimate (fracture) tensile strain. The test specimens are cut from the flanges and the web, from the locations shown in Figures 5 and 6 for the I- and channel sections. The specimens numbered I-1 through I-4 are taken from the I-section whereas those numbered C-1 through C-4 are taken from the channel section. Figure 7 shows schematically the setup used to conduct the tension tests.

Tables 2.1 through 2.4 present the tensile coupon test results for Specimens I-1 through I-4 taken from the FRP I-section flanges and the web. Figures 8 through 11 show the tensile stress-strain relationships based on the data given in these tables. Table 2.5 presents a summary of the tensile test results for Specimens I-1 through I-4. Based on these results, the average tensile Young's modulus E_{11} written as E_T hereafter, the cracking strain ϵ_{cr} , and the tensile strength σ_{uT} are found to be 2.58×10^6 psi; 0.00999 in./in.; and 25,820 psi; respectively.

To determine the shear modulus, G_{12} written as G hereafter, for the material of the I-section, a torsional moment is applied at the midspan of an 8 ft. long beam by suspending a known weight through a lever arm clamped to the beam top flange while maintaining pinned boundary conditions. A pair of dial gages are used to measure the vertical deflection near the tip of the lever arm and at the beam midspan. This data is then used to obtain the midspan angle of twist. Finally, the value of G is found to be 0.42×10^6 psi based on an analytic relationship between the applied torsional moment and the midspan angle of twist.

Tables 2.6 through 2.9 present the tensile test results for Specimens C-1 through C-4 taken from the channel section flanges and web. The corresponding tensile stress-strain curves are drawn in Figures 12 through 15. Table 2.10 gives a summary of the tensile test results for Specimens C-1 through C-4. Based on these results, the average tensile Young's

modulus E_T , the cracking strain ϵ_{cr} , and the tensile strength σ_{uT} are found to be 3.27×10^6 psi; 0.01639 in./in.; and 53,639 psi, respectively.

2.3 Apparatus and Test Procedure

There are two different test setups used for conducting the experimental study. First, the beam flexural testing is carried out through direct utilization of the Tinius Olsen machine and specially fabricated beam end supports.

For flexural testing, the FRP beam ends are simply-supported by ‘gripping’ the beam end sections with a pair of round vertical bars. A two-part aluminum plate is used to ‘grip’ the midspan section and to subsequently serve as the loading plate for transmitting the machine load to the beam. The two parts of the loading plate are inter-connected by long screws. Figure 16 shows the load P transmitted to a steel bar which pushes a steel shaft against the loading plate. The flexural test procedure consists of gradually increasing the midspan load, allowing the readings to stabilize for approximately two minutes, and then recording the experimental data. The applied load is read from the load dial of the Tinius Olsen machine. The deflection is measured with a dial gage at the midspan while the tensile and compressive flange strains are measured with electrical resistance strain gages.

To conduct the stability and flexural-torsional tests on FRP beams, a full-scale apparatus is conceived, designed, fabricated, and finally utilized for a series of I- and channel section beam tests. One of the main criteria for the experimental load-application mechanism is that the lateral and torsional deflections not be constrained. This is successfully achieved by devising an apparatus.

Figure 17 shows the overall apparatus designed to conduct the stability and flexural-torsional tests on FRP beams. For the four-point loading, a pair of hydraulic jacks are placed

on top of a fixed-end steel beam, with their pistons pointing upward and pushing against steel plates to transfer the loads to a pair of tie rods attached to each of the plates, as shown in Figure 18. The loads are measured by means of calibrated load cells mounted between each jack and the plate assembly. The tie rods are connected to horizontal steel bars which, in turn, transmit the loads to the FRP beam through its bottom face as shown in Figure 19. The tie rod assemblies allow a test beam to develop lateral and torsional deflections as well as the vertical deflections. Each end of the beam is simply-supported by 'gripping' it with a pair of vertical round bars, as shown in Figure 20. In this figure, only the upper and a part of the lower horizontal bars at one of the beam supports are visible. The vertical bars are smaller in diameter and are mounted on the inside of the vertical supports. The distance between the beam end support fixtures can be adjusted to accommodate beams of various clear spans. The loading fixtures do not impose any warping restraints on the test beam. Deflections are measured using dial gages at beam midspan. To measure the vertical deflection, a dial gage is mounted atop the upper flange at the beam midspan. The midspan lateral deflection is measured with a dial gage mounted at web mid-depth. To measure the angle of twist, a 1 ft. long lever arm is clamped to the top flange at the beam midspan. A dial gage is used to measure the vertical deflection near the tip of the lever arm. This data is then used to obtain the midspan angle of twist. The measured dial gage readings are corrected for the unwanted coupling of the vertical, lateral, and torsional deflections. Additional strain gages are mounted at the beam end support locations to monitor any possible support-frame movements. These movements are found to be negligibly small.

The test procedure involves applying the external load (P) or the load pair (P, P) shown in Figure 1(a) and 1(b), through a common source of hydraulic pressure for both

hydraulic jacks shown in Figure 20, and then recording the deflections, strains, and the output from the load cells. The loads are applied in small increments in the linear portion of the load-deflection relationships. In the nonlinear range of these relationships, increments in the horizontal or twisting deflections are used to control the load increments. The FRP beams are allowed to stabilize after each load increment for a period of approximately 2 to 3 minutes before recording the data. For the three-point loading, a single hydraulic jack is utilized above the beam centerline.

2.4 Test Results and Discussion

2.4.1 Minor Axis Flexure

Table 2.11 presents the minor axis flexural test results for a 30.0-inch span I-beam with three-point loading. This table shows the applied load (P), the flexural compression and tension strains recorded using electrical resistance strain gages BSG1 and BSG2 whose locations are shown in Figure 21, and the midspan vertical deflection. The figure shows that the strain gages BSG1 and BSG2 are located at distance of $1/16$ in. from the top and bottom of the beam flange tips. The dashed curve in Figure 22 represent the experimental load (P) versus midspan vertical deflection. The load-deflection curve is found to be linear up to the maximum load-carrying capacity of the beam which corresponds to the initiation of cracking at the flange tips. The maximum recorded load is found to be 2,100 lbs. Once the cracking started the beam flexural resistance started to immediately drop as evidenced by the decrease in the load indicated on the Tinius Olsen machine dial. The dashed curve in Figure 23 represents the experimental load (P) versus the average flexural strain based on the absolute value of the compression and tension strains. The experimental M_y versus Φ_y curve for this

beam is shown in Figure 24. The experimental $M_y - \Phi_y$ curve is found to be linear up to the maximum load-carrying capacity, and is shown as the curve from point A to B in Figure 24.

2.4.2 Stability of I-Section Beams

2.4.2.1 Three-Point Loading Through Shear Center

The three-point loading tests (Figure 1a) are conducted using the load application setup shown schematically in Figure 25. A pair of steel tie rods are used to apply upward vertical loads (Q) placed symmetrically about the shear center S which coincides with the centroid C. The resultant, $P = 2Q$, shown in this figure acts at a distance $y_o' = -3.5$ in. above the x axis but passes through the S and C.

Table 2.12 presents the results for a 108-inch span I-beam for Test No. IFT3-1. This table shows the applied load, P, the midspan vertical deflection, lateral deflection, and the angle of twist. The dashed curve in Figure 26 shows the experimental load P versus midspan vertical deflection, v_c . The dashed curve in Figure 27 shows the experimental load P versus midspan lateral deflection, u_c . A reversal in the direction of u_c occurs in the load range from 78 lbs. to the maximum load of 99 lbs. The dashed curve in Figure 28 shows the load P versus midspan angle of twist, ϕ_c .

Tables 2.13 through 2.15 present the experimental results for I-beam test Nos. IFT3-2 through IFT3-4 with a clear span $L = 96, 84, 72$ in., respectively. Figures 29 through 37 show the midspan load P versus deflection curves based on the data given in these tables. The experimental peak loads for these three beams are found to be 147, 174, 265 lbs., respectively. During these experiments, any attempt to apply loads greater than the peak loads resulted in gradually increasing deflections, indicating beam instability.

2.4.2.2 Four-Point Loading Through Shear Center

The four-point loading tests (Figure 1b) are conducted using the load application setup shown schematically in Figure 25. For all of the experiments conducted, the distance between the loads P and P , is kept constant at $b = 24$ in. The value of y_o^* for these tests is -3.5 in.

Table 2.16 presents the results for a 108 in. span I-beam for Test No. IFT4-1. This table gives the experimental P , v_c , u_c , ϕ_c , and the longitudinal flange normal strain, ϵ_c , values at $(x,y) = (-0.1875 \text{ in.}, -2.0 \text{ in.})$. The dashed curve in Figures 38 through 40 show the experimental $P-v_c$, $P-u_c$, and $P-\phi_c$ curves, respectively. The dashed curve in Figure 41 shows the $P-\epsilon_c$ relationship. Similarly, Tables 2.17 through 2.20 present the experimental results for I-beam Test Nos. IFT4-2 through IFT4-5 with clear span $L = 96, 84, 72$ in., respectively. Figures 42 through 57 show the $P-v_c$, $P-u_c$, and $P-\phi_c$ curves based on the data given in these tables. The experimental peak load for these four beams are found to be 114, 125, 190 and 292 lbs., respectively. For these experiments, the beam instability was characterized by the development of relatively large deflections with practically no increase in the beam load resistance.

2.4.3 Stability of Channel Section Beams

2.4.3.1 Three-Point Loading through Shear Center

The three-point loading tests (Figure 1a) are conducted using the load application setup shown schematically in Figure 58. The loading apparatus is the same as described in Section 2.4.2.1. The value of y_o^* is still kept at -3.5 in.

Table 2.21 presents the results for a 108-inch span channel beam for Test No. CFT3-1. This table shows P , v_c , u_c , and ϕ_c values. The dashed curve in Figure 59 shows the

experimental load P - v_c curve. The dashed curve in Figure 60 results the experimental load P - u_c curve. An initial reversal in the direction of u_c is noted in this figure at around 160 lbs. whereafter the beam returns to its original direction of motion. The dashed line in Figure 61 dashed shows the experimental P - ϕ_c curve. Table 2.22 presents the experimental results for a 96-inch span channel beam for Test No. CFT3-2. Figures 62 through 64 show the P - v_c , P - u_c , and P - ϕ_c curves.

2.4.3.2 Four Point Loading Through Shear Center

The four-point loading tests (Figure 1b) are also conducted using the load application setup shown schematically in Figure 58. For these experiments $b = 24$ in. and $y_o = -3.5$.

Table 2.23 presents the results for a 108 in. span channel beam for Test No. CFT4-1. give the experimental P , v_c , u_c , and ϕ_c values. The dashed curves in Figures 65 through 67 the experimental P - v_c , P - u_c , and P - ϕ_c curves. The maximum load is found to be 136 lbs.

Tables 2.24 through 2.26 present the experimental results for channel beam Test Nos. CFT4-2 through CFT4-4, for $L = 102, 96$, and 84 in., respectively. The dashed curves in Figures 68 through 76 show the midspan load-deflection curves. Based on the data given in these tables, the experimental peak load for these three beams is found to be 160, 198, 300 lbs., respectively. The dashed curve in Figure 77 shows the relationship between P , and the midspan longitudinal normal flange strain, ϵ_c , near upper flange tip. With reference to the coordinate system, the gage is located at $(x,y) = (0.185 \text{ in.}, y = -3.5 \text{ in.})$.

Tables 2.27 through 2.28 present the experimental results for channel beam Test Nos. CFT4-5 and CFT4-6 with clear span $L = 72$, and 60 in., respectively. Figures 78 through 83 show the midspan load-deflection curves. Based on the data given in these

tables, the experimental peak load for these two beams is found to be 452, and 701 lbs., respectively.

2.4.3.3 Four-Point Loading Away from Shear Center

Three tests are conducted on a 84.0 in. span beam with four-point loading away from the shear center. For each of these tests, the vertical location of the applied load pair (P,P) is defined by $y = y_o = -3.5$ in. The horizontal location of the load pair (P,P) is defined by $x = -0.5675$ in., -0.2656 in., and 0.4531 in., Respectively, for Test Nos. CFT4-7 through CFT4-9. These x values correspond, respectively, to the cross section centroid; a location half-way between the centroid and the shear center; and another location to the right of the shear center as shown in Figure 58.

Table 2.29 presents the results for Test No. CFT4-7. It gives the experimental value of P , v_c , u_c , ϕ_c , and ϵ_c at $(x,y) = (-0.185$ in., -3.0 in.). The dashed curves in Figures 84 through 87 present the $P-v_c$, $P-u_c$, $P-\phi_c$, and $P-\epsilon_c$ curves. The maximum load is found to be 203 lbs. Similarly, Tables 2.30 and 2.31 give the results for Test Nos. CFT4-8, and CFT4-9, respectively. Figure 88 through 95 present the load-deflection and load-strain curves for these tests.

CHAPTER III.

THEORETICAL ANALYSES

3.1 Prologue

In order to formulate an appropriate mathematical model for the predication of the behavior of FRP composite beams, a careful study of their experimental response to gradually increasing load(s) is necessary. Three main types of experimental loading conditions and corresponding beam responses are presented in this chapter, namely, in-plane bending with a midspan concentrated load resulting in in-plane deflections involving material cracking, three- and four-point major axis loading through the shear center eventually culminating into flexural-torsional instability, and four-point major axis loading through locations other than the shear center producing in-plane as well as flexural-torsional deflections for the entire range of the applied loading.

For the in-plane bending with resulting in-plane deflections, a single differential equation of equilibrium together with the boundary conditions is found to be sufficient to predict the load-deflection curve. For the flexural-torsional problems, a total of three differential equations of equilibrium are needed together with appropriate flexural and torsional boundary conditions. The first and the second of these equations represent flexural equilibrium in the vertical and horizontal planes while the third equation represents the torsional equilibrium of the beam. For a beam with a general cross section, these three equations of equilibrium are coupled. For singles-symmetric or doubly-symmetric sections of the type considered in this dissertation, the first differential equation becomes decoupled from the remaining two. However, the remaining two equations remain coupled. The main portion of the theoretical solution presented herein is based on a finite-difference scheme.

For the case of four-point loading, an energy based Rayleigh-Ritz procedure is also used to develop an elastic buckling load formula. A comparison of the experimental and theoretical results is presented Chapter IV of this dissertation.

3.2 Cross-Sectional Equilibrium Equations

Figures 96 and 97 show a discretized I- and channel sections, respectively, each with a width B, depth D, and a wall thickness t. Each wall of the cross section is divided into elemental areas. The term δa represents a typical elemental area. For the flexural-torsional problems, a typical cross section is subjected to an in-plane bending moment about the major axis (x), and with or without a torsional moment about the longitudinal axis (z). In addition, the cross section has induced minor axis (y) curvature, and torsional curvature about a centroidal axis, z, normal to the xy plane, giving rise to both minor axis bending strains as well as warping strain. The total normal ϵ at a point (x, y) of the cross section is then given by [10]:

$$\epsilon = \Phi_x y - \Phi_y x + \Phi_z \omega_n \quad (1)$$

in which Φ_x and Φ_y are the bending curvatures about the x and y axes, respectively, and Φ_z is the torsional curvature about the cross-sectional centroid.

The stress-strain relationship is given by:

$$\begin{aligned} \sigma &= E\epsilon, \quad \text{for } 0 \leq \epsilon \leq \epsilon_{cr} \\ \sigma &= 0 \quad \text{for } \epsilon > \epsilon_{cr} \end{aligned} \quad (2)$$

in which , E is the Young's modulus and ϵ is the normal strain.

If M_x and M_y represent bending moments about the x and y axis, respectively, and M_z the torsional moment, then the cross-sectional equilibrium equations can be written as follows [10]:

$$M_x = \int_A \sigma y dA \quad (3)$$

$$M_y = - \int_A \sigma x dA \quad (4)$$

$$M_z = M_{sv} + M_w \quad (5)$$

in which dA is an elemental area of the cross section, σ is the normal stress on the area, \int_A is cross-sectional integration, M_{sv} is St. Venant torsion resisting torsional moment, and M_w is resisting warping torsional moment. The M_{sv} and M_w are given by following expressions [10]:

$$M_{sv} = GK_T \frac{d\phi}{dz} \quad (6)$$

$$M_w = -EI_\omega \phi''' \quad (7)$$

in which K_T is the St. Venant torsion constant given by:

$$K_T = \frac{1}{3} \sum_{i=1}^n B_i t_i^3 \quad (8)$$

in which B_i and t_i are the width and thickness of the i -th plate component of the cross section, and the summation is over all n plates of the section. The item I_ω is called the warping moment of inertia and is given by:

$$I_\omega = \int_A \omega_n^2 t ds \quad (9)$$

$$M_z = GK_T \phi' - EI_\omega \phi''' \quad (10)$$

Substituting Equations 6 and 7 into 5 gives:

The specific differential equations of equilibrium for three-point and four-point loading are presented in Section 3.2.1, and 3.2.2, respectively.

3.2.1 Governing Differential Equations for Three-Point Loading

For the three-point loading, the external bending moments $(M_x)_{ext}$ and $(M_y)_{ext}$, and the torsional moment $(M_z)_{ext}$ in the presence of an eccentricity “e” relative to the shear center S of the applied load P, for $0 \leq z \leq \frac{L}{2}$, are given by:

$$(M_x)_{ext} = Pz_i \quad (11)$$

$$(M_y)_{ext} = 0 \quad (12)$$

$$(M_z)_{ext} = P(u_{max} - y_o^* \phi_{max} - u) - Pe \quad (13)$$

Equations 1 through 10 combined with Equations 11 through 13 and the second-order effects given in Reference 10 finally result in the following differential equations governing the behavior of beam s subjected to three-point loading:

$$B_x v'' + B_{xy} u'' + B_{\omega y} \phi'' + Pz = 0 \quad (14)$$

$$B_y u'' + B_{xy} v'' + B_{\omega x} \phi'' + Pz \phi = 0 \quad (15)$$

$$C_T \phi' - C_\omega \phi''' - B_{\omega x} u''' - B_{\omega y} v''' - Pzu' - P(u_{max} - y_o^* \phi_{max} - u) = Pe \quad (16)$$

where :

u_{max} = maximum lateral deflection

ϕ_{max} = maximum angle of twist

$$B_x = EI_x$$

$$B_y = EI_y$$

$$B_{xy} = E I_{xy}$$

$$B_{\omega x} = E I_{\omega x}$$

$$B_{\omega y} = E I_{\omega y}$$

$$C = G K_t$$

$$C_w = E I_\omega$$

I_x, I_y = moment of inertia about x- and y-axis and y-axis

I_{xy} = product of inertia relative to x-axis and y-axis

$I_{\omega x}, I_{\omega y}$ = warping moment of inertia relative to x- and y-axis, respectively

G = shearing modulus

For evaluating these cross-sectional properties, the cracked portions of a beam cross section are considered to be non-existent as implied by the use of Equation 2.

If a beam does not develop any cracking up to its maximum load-carrying capacity, and if the cross section is mono- or doubly-symmetric, the terms B_{xy} , $B_{\omega x}$, and $B_{\omega y}$ in Equations 14-16 become zero. Setting these terms equal to zero in these equations and differentiating Equation 16 once results in:

$$B_x v'' + P z_i = 0 \quad (17)$$

$$B_y u'' + P z_i \phi = 0 \quad (18)$$

$$C_T \phi'' - C_\omega \phi''' - P z_i u'' = e^* \quad (19)$$

in which an imperfection factor e^* is introduced on the right side of Equation 19 to account for the imperfections in the laboratory beams as well as in the loading mechanisms described in Chapter II. An advantage of the e^* factor is that it converts Equations 18 and 19 to nonhomogeneous differential equations thus providing a load-deflection type of output which can more meaningfully be compared with the experimental curves indicating some u and ϕ

deflections even at small values of the load P . As described in Section 5.1 of this dissertation, e^* was generally found to be relatively small.

3.2.2 Governing Differential Equations for Four-Point Loading

For the case of four-point loading, Equation 17-19 are applicable for the range $0 \leq z \leq a$, where a is defined in Figure 1 (b). In addition, three more differential equations are needed for the range $0 \leq z \leq \frac{L}{2}$. For this latter range, Equations 17-19 can again be utilized by setting $z = a$.

3.3 Boundary and other Conditions

For both the three- and four-point loading cases, the following flexural boundary and

$$u(0) = u''(0) = v(0) = v''(0) = 0 \quad (20)$$

symmetry conditions are used:

$$u'(\frac{L}{2}) = v'(\frac{L}{2}) = 0 \quad (21)$$

Also, the torsionally pinned boundary and symmetry conditions are written as:

$$\phi(0) = \phi''(0) = 0 \quad (22)$$

$$\phi'(\frac{L}{2}) = 0 \quad (22b)$$

$$-C_w \phi'''(\frac{L}{2}) - P y_o \phi(\frac{L}{2}) = 0 \quad (23)$$

For the four-point loading, the following condition can be obtained by applying Equation 16 at $z = a$ resulting in:

$$C_T \phi'(a) - C_w \phi'''(a) - P a u'(a) - P \left[u\left(\frac{L}{2}\right) - y_o \phi\left(\frac{L}{2}\right) - u(a) \right] = P e \quad (24a)$$

Lastly, the following symmetry condition is also applicable for the four-point loading:

$$\phi'''(\frac{L}{2}) = 0 \quad (24b)$$

3.4 Finite-Difference Formulation

The numerical procedure is based on a central finite-difference scheme applied to the differential equations and the boundary conditions presented in Sections 3.2 and 3.3. For example, Equations 17-19 for the three-point loading are written in the following finite-difference form:

$$\frac{B_x}{h^2} (v_{i-1} - 2v_i + v_{i+1}) = -P z_i \quad (25)$$

$$\frac{B_y}{h^2} (v_{i-1} - 2v_i + v_{i+1}) - P z_i \phi_i = 0 \quad (26)$$

$$\begin{aligned} \frac{C_T}{h^2} (\phi_{i-1} - 2\phi_i + \phi_{i+1}) - \frac{C_w}{h^4} (\phi_{i-2} + 4\phi_{i-1} + 6\phi_i - 4\phi_{i+1} + \phi_{i+2}) \\ - \frac{P z_i}{h^2} (u_{i-1} - 2u_i + u_{i+1}) = e \end{aligned} \quad (27)$$

For the four-point loading, Equations 25-27 are first applied in the range $0 \leq z \leq a$. Next, Equations 25-27 are modified by replacing the z_i term by 'a' shown in Figure 1(b), and then applied in the range $a \leq z \leq \frac{L}{2}$.

The boundary and other conditions in Section 3.3 are similarly expressed in the finite-difference form.

Applying the appropriate governing finite-difference equations at nodes $I = 1, 2, 3, \dots, n$ over the range $0 \leq z_i \leq \frac{L}{2}$, together with the boundary and other conditions for the three- or four-point loading condition finally results in the following equation:

$$[K]\{\Delta\} = \{M\} \quad (28)$$

in this equation, $[K]$ is the global stiffness matrix of the order $3(n+2)$. The vector $\{\Delta\}$ contains the beam deflections defined as follows:

$$\{\Delta\} = \{v_1 \ u_1 \ \phi_1 \ v_2 \ u_2 \ \phi_2 \ \dots \ v_{n-1} \ u_{n-1} \ \phi_{n-1} \ v_n \ u_n \ \phi_n\}^T \quad (29)$$

and $\{M\}$ is the applied nodal load vector

The solution procedure involves specifying a load P or a load pair (P,P) and solving Equation 28 for the deflection vector $\{\Delta\}$ directly if no cracking of the beam occurs. If cracking develop, $[K]$ becomes a function of the extent of cracking in which case Equation 28 must be solved iteratively for each load level, for the flexural-torsional experiments conducted, the maximum load-carrying capacity is governed by elastic instability rather than cracking. To determine the instability load, a dimensionally determinant, \bar{D} , of the matrix $[K]$ is first defined as follows:

$$\bar{D}_P = \frac{D_P}{D_o} \quad (30)$$

in which :

$$D_o = |[K]_o| \quad (31)$$

$$D_P = |[K]_P| \quad (32)$$

A finite-difference computer program is developed and is presented in Appendix A of this dissertation. In the program, a beam is considered unstable when \bar{D}_p becomes nearly equal to zero.

For the beams analyzed in this dissertation, “h” was taken as 3 in. A convergence study showed that this value of h was more than adequate.

For the minor axis flexural test described in section 2.4.1 of this dissertation material cracking eventually controls the member load-carrying capacity. The procedure for generally the in-plane moment-curvature and load-deflection curves when material cracking is present is given in the next section. The experimental results for the 30 in. beam described in Section theoretically.

3.5 Moment-Curvature and Load-Deflection Curves Including Material Cracking

The minor axis experimental moment-curvature curve for the I-section is presented previously in Section 2.4.1 of this dissertation. In order to obtain a minor axis theoretical moment-curvature relation including the effect of material cracking, Equation 1 is need with $\Phi_x = 0$ and $\Phi_z = 0$, to define the total normal strain ϵ . The normal stress is then obtained form Equation 2. The following steps are used for generating the $M_y - \Phi_y$ relationship:

1. Specify a value of Φ_y .
2. Determine cross-sectional strain distribution using Equation 1.
3. Determine the normal stress using Equation 2.
4. Compute the internal resisting bending moment by using a discretized section and by summing up moment contributions of individual discrete elements.

In the above procedure, elemental cross-sectional areas with $|\epsilon| > \epsilon$ are not included in the moment summation process. This is due to the nature of the prescribed Equation 2 which physically means that the cracked portion of the section does not resist any loads.

The 30.0-inch span minor axis flexural test described in Section 2.4.1 resulted in a tensile cracking strain, ϵ_{crb} , of 0.0134 in./in. extrapolated from the strain gage reading on the specimen tension side at the instant of cracking. Whereas the experimental $M_y - \Phi_y$ curve (AB) in Figure 24 is terminated at B, the theoretical curve obtained using the above procedure has both an ascending as well as a descending part based on using $\epsilon_{cr} = \epsilon_{crb}$. This is shown as the curved ABC in the figure. Furthermore, when ϵ_{cr} from the tension tests described in Section 2.2, that is, with $\epsilon_{cr} = \epsilon_{crb} = 0.00999$ in./in., $M_y - \Phi_y$ curve with a lower peak moment is obtained. This is shown as the curve ADE in the figure. For obvious reasons, the experimental peak moment is in agreement with the theory up to point B in Figure 24 when ϵ_{crb} is used.

To obtain the theoretical load versus midspan deflection curve, the moment-curvature curve ABC in Figure 24 is used together with the following equation:

$$\phi_i = v_i'' \quad (33)$$

which takes the following finite-difference form:

$$v_{i-1} - 2v_i + v_{i+1} = h^2 \phi_i \quad (34)$$

The boundary and symmetry conditions are

$$v(0) = v'(\frac{L}{2}) = 0 \quad (35)$$

Applying Equation 34 and nodes $I=1,2,3,\dots,n$, and utilizing the finite-difference version of Equations 35 leads to a simultaneously system of equations which is solved for the noded v_i deflections. Figure 22 shows the theoretical load-deflection curve based on this procedure.

3.6 Buckling Load Formula for Four-Point Loading with Energy Approach

An approximate theoretical buckling load formula is developed for the beam problem with four-point loading. The total potential for a thin-walled beam is given by [13]:

$$\begin{aligned} \Pi = \frac{1}{2} \int_0^{\frac{L}{2}} \left[E I_y (u'')^2 + E I_\omega (\phi'')^2 \right] dz + \int_0^a P z u'' \phi dz \\ + \int_0^{\frac{1}{2}(L-2a)} P a u'' \phi dz - \frac{1}{2} P y_o \phi_p^2 \end{aligned} \quad (36)$$

where ϕ_p is the angle of twist at $z = a$, that is, at the location of the left side load P shown in Figure 1(b). The following assumed beam buckled shape satisfies the flexural and torsionally pinned boundary conditions:

$$u = A \sin \frac{\pi z}{L} \quad (37)$$

$$\phi = B \sin \frac{\pi z}{L} \quad (38)$$

Substituting these expression into Equation 36 and using Raleigh-Ritz procedure leads to the following approximate buckling load, P_{cr} , formula:

$$P_{cr} = \frac{0.5 \left[-f_2 + \sqrt{f_2^2 + 4 f_1 f_3} \right]}{f_1} \quad (39)$$

$$f_1 = \frac{1}{16} \left[f(a) - \frac{\pi^2 a^2}{L^2} - \frac{2 \pi a}{L} g(a) \right]^2 \quad (40)$$

$$f_2 = \frac{\pi^4 E_{11} I_y}{4 L^3} y_o^* \sin^2 \left(\frac{\pi a}{L} \right) \quad (41)$$

$$f_3 = \frac{\pi^6 E_{11} I_y}{16 L^4} \left[\frac{\pi^2 E_{11} I_\omega}{L^2} + G_{12} K_T \right] \quad (42)$$

$$f(a) = \frac{\pi a}{L} \sin \left(\frac{2 \pi a}{L} \right) - \sin^2 \left(\frac{\pi a}{L} \right) \quad (43)$$

$$g(a) = \frac{1}{2} \left[\pi \left(1 - \frac{2a}{L} \right) - \sin \pi \left(1 - \frac{2a}{L} \right) \right] \quad (44)$$

in which I_y , I_ω , and K_T are the beam minor axis moment of inertia, warping moment of inertia, and St. Venant torsion constant, respectively. Also, E_{11} and $G_{12} = G$. The procedure and formulas for calculating I_ω and K_T are given in standard textbooks dealing with stability of structures such as that by Galambos [10]. The term y_o^* accounts for the height of each load P above or below the shear center S. The sign of y_o^* must be taken with reference the x,y coordinate system defined previously in this dissertation.

Although the I- and the channel sections of the beams analyzed are divided into 120 and 144 elemental areas, respectively, for the purpose of evaluating the total normal bending and warping strains in order to ascertain whether or not an element is cracked, no material cracking developed either in the laboratory tests or in the theoretical analysis since the normal strains at instability are relatively small compared with ϵ_{cr} .

The theoretical results presented in the following sections are based on the finite-differences procedure outlined in Section 3.4. A very small eccentricity e relative to the shear center is also introduced in the theoretical formulation in order to simulate the unavoidable tiny eccentricity of the applied load P or the load pair (P,P).

3.7 Beam Stability

3.7.1 I-Section Beams

3.7.1.1 Three-Point Loading

Table 3.2 presents the theoretical results for the I-beam with three-point loading for Test No. IFT3-1. This table presents the P , v_c , u_c , and ϕ_c . The load is applied through the shear center with an $e = -0.002$ in. The solid curve in Figure 26-28 show the theoretical P - v_c , P - u_c , and P - ϕ_c relations. Tables 3.3 through 3.5 present the theoretical results for the I-beam for Test Nos. IFT3-2 through IFT3-4. Figures 29 through 34 show the theoretical load-deflection curves for these tests.

3.7.1.2 Four-Point Loading

Table 3.6 presents the theoretical results for the I-section beam with four-point loading for Test No. IFT4-1. This table presents the P , v_c , u_c , and ϕ_c values. The value of e is taken as -0.002 in. Figures 38-41 show the theoretical P - v_c , P - u_c , P - ϕ_c , and P - ϵ_c curves. Similarly Tables 3.6 through 3.10 present the theoretical results for the I-beam Test Nos. IFT4-2 through IFT4-5. Figures 42 through 57 show the theoretical the load-deflection and load-strain curves for these tests.

3.7.2 Channel Section Beams

3.7.2.1 Three-point loading

Table 3.11 presents the theoretical results for the channel section beam with three-point loading for Test No. CFT3-1. This table presents P , v_c , u_c , and ϕ_c values. The value of $e = -0.0003$ in. Figure 59-61 show the theoretical Figure 61 shows the theoretical P - v_c , P - u_c , P - ϕ_c , and P - ϵ_c curves. Similarly, Table 3.12 presents the theoretical results for the

channel section beam for Test No. CFT3-2. Figures 62 through 64 show the theoretical load-deflection curves.

3.7.2.2 Four-Point Loading

Table 3.13 presents the theoretical results for the channel section beam with four-point loading for Test No. CFT4-1. This table presents P , v_c , u_c , and ϕ_c values. The value of $e = -0.0003$ in. Figure 65-67 show the theoretical $P-v_c$, $P-u_c$ and $P-\phi_c$ curves. Similarly, Tables 3.14 through 3.18 presents the theoretical results for the channel section beam for Test Nos. CFT4-2 through CFT4-6. Figures 68 through 83 show the theoretical $P-v_c$, $P-u_c$, $P-\phi_c$, and $P-\epsilon_c$ curves.

3.7.3 Flexural-Torsional Behavior of Channel Beam

Table 3.19 presents the theoretical results for an 84.0 in. span channel beam section with four-point loading applied through the centroid for Test No. CFT4-7. Figure 85-88 show the load-deflection and load-strain curves.

Table 3.20 presents the theoretical results for the 84 in. channel beam section with Test No. CFT4-8 with four-point loading applied between the section centroid and the shear center as described in Section 2.4.3.3. Figure 89-92 show the load-deflection and load-strain curves.

Table 2.21 presents the theoretical results for the 84 in. channel section beam Test No. CFT4-9 loading applied at $x = 0.4531$ in. as described in Section 2.4.3.3. Figure 93-96 show the theoretical load-deflection and load-strain curves.

CHAPTER IV.
LOAD AND RESISTANCE FACTOR DESIGN APPROACH
FOR FRP BEAM STABILITY

4.1 LRFD Philosophy for FRP Composite Beams

The Load and Resistance Factor Design (LRFD) is a probability-based design procedure which requires that none of a prescribed set of limit states be exceeded. For an FRP beam to be used in a routine structural application, the following serviceability limit states must be satisfied:

1. The beam should not develop an overall instability.
2. The maximum beam deflection should be less than a prescribed limit, such as $L/360$.
3. The beam should not develop material cracking.
4. The beam flange and web should not develop any local buckling.

Additional limit states must be defined if other factors such as fatigue, low or high temperatures, and creep are present. In this dissertation, considerations is given only to the first three limit states. As mentioned in Chapter I, it is assumed that no local buckling occurs. For the beams tested in the laboratory, this assumption was found to be true.

The series loads are converted to the design (fractured) loads by multiplying the service loads by load factors obtained using statistical averages based on measured variations of the loads. Obviously, if a mean value of a type of load, such as the live load, is used in addition to a standard deviation, there will be an associated likelihood or probability of the load not exceeding a certain value. In LRFD, the thought and the computational processes are simplified by establishing a separate load factor for each different load type in such a way that the probability of the actual loads exceeding the factored loads is quite small. Based

on the investigations that eventually led to the LRFD specification for steel structures [11], the dead and live load factors were found to be 1.2 and 1.6, respectively.

The LRFD procedure also requires the use of a set of “ resistance factors ” to account for the statistical variation in the material mechanical properties as well as the possible structural failure modes such as overall instability, cracking, etc. For steel beams, the resistance factor, ϕ_b , for flexure is found to be 0.9.

It should be recognized that the load factors are applied to the external loads, that is, they are not material dependant. Thus, the dead and live load factors of 1.2 and 1.6 are adopted herein. On the other hand, a large number of tests must be conducted on FRP composite beams with a variety of practical loading and boundary conditions in order to ascertain an appropriate resistance factor (ϕ_b) value. The results summarized in Table 4.1 show that the experimental maximum loads are generally higher than the predicted ones. Based on the limit number of tests conducted in this investigation, a resistance factor ϕ_b of 0.9 seems to be both reasonable and generally conservative, and is adopted in this chapter.

Before formulating a LRFD approach for FRP composite beams, it is necessary to first review the beam maximum bending moment (M_{max}) versus the beam clear span (L) relations based on both theory and experiments presented in Chapters II and III.

4.2 Maximum Bending Moment versus Beam Length Relations

Figures 4.1 and 4.2 present the maximum bending moment (M_{max}) versus unsupported length (L) relations for three- and four-point of I-section beams loading, respectively. For these figures $y_o^* = -3.5$ in.; $E = 2.55 \times 10^6$ psi; $G = 0.42 \times 10^6$ psi ; $I_x = 4.41$ in⁴; $I_y = 0.3345$ in⁴; $K_t = 0.0403$ in⁴; $I_\omega = 1.17$ in⁴, $e = -0.002$ f or a $4 \times 2 \times \frac{1}{4}$ in. I-section beam.

The solid curve in Figure 98 for the three-point loading is based on the finite-difference analysis presented in Chapter III, the dashed curve in this figure gives the M_{\max} - L relations corresponding to limiting midspan vertical deflection of $L/360$. The experimental M_{\max} versus L values for Test Nos. IFT3-1 through IFT3-4 given in Table 4.1 are also plotted in this figure. The experimental results from these test are in good agreement with the finite-difference curve.

Figure 99 shows the M_{\max} - L relations for four-point loading obtained using the finite-difference analysis, the limiting midspan vertical deflection of $L/360$ using the finite-difference method again, the buckling load formula given by Equation 39, and the experimental results from Test Nos. IFT4-1 through IFT4-5. The finite-difference, buckling load formula, and the experimental results are in good agreement. The theoretical results are found to be on the conservative side as compared with the experimental ones.

Figures 100 and 101 present the M_{\max} - L relations for three- and four-point loading, of channel section beams, respectively. For these figures $y_o^* = -3.5$ in.; $E = 3.23 \times 10^6$ psi; $G = 0.42 \times 10^6$ psi; $I_x = 10.18$ in⁴; $I_y = 0.43$ in⁴; $K_t = 0.0455$ in⁴; $I_\omega = 2.52$ in⁴ and $e = -0.003$ f or a $6 \times 1 \frac{5}{8} \times \frac{1}{4}$ in. I-section beam.

Figure 100 shows the M_{\max} - L relation for three-point loading. The curve corresponding to the limiting midspan vertical deflection of $L/360$ does not exist for this case since for the range of L shown in this figure, the beam instability occurs before a deflection of $L/360$ is developed. The two experimental results from Test Nos. CFT3-1 and CFT3-2 are in excellent agreement with the finite-difference curve.

Figure 101 shows the M_{\max} - L relations for four-point loading obtained using the finite-difference analysis, the buckling load formula given by Equation 39, and the

experimental results from Test Nos. CFT4-1 through CFT4-6. All of these results are in good agreement, although the experimental results are closer to those calculated using the buckling load formula.

In summary, the theoretical M_{\max} -L relations are in good agreement with the test results.

4.3 LRFD Approach for FRP Composite Beams

As mentioned in Section 4.1, the stability, in-plane deflection, and material cracking are considered as the main LRFD limit states for the beam problem considered in this dissertation. The beam stability limit state is given by:

$$M_u \leq M_R \quad (44)$$

in which M_u is the factored (ultimate) design buckling moment given by:

$$M_u = \Upsilon_{DL} M_{DL} + \Upsilon_{LL} M_{LL} \quad (45)$$

in which Υ_{DL} and Υ_{LL} are dead and live load factors, M_{DL} and M_{LL} are the bending moments due to dead and live loads, respectively, and M_R is the internal resisting bending moment given by:

$$M_R = \phi_b M_{\max} \quad (46)$$

In this equation ϕ_b is taken as 0.9, and M_{\max} is the buckling or instability bending moment obtained from appropriate M_{\max} versus L relations of the type given in Figure 98 through 101 the Υ_{DL} and Υ_{LL} values are taken as 1.2 and 1.6.

The given cracking limit state is given by:

$$M_u \leq M_c \quad (47)$$

in which M_c is the beam cracking bending moment given by:

$$M_c = \frac{\sigma_c}{S} \quad (48)$$

in which σ_c is the material cracking stress and S is the elastic sectional modulus.

The beam in-plane deflection limit state is given by:

$$v_{\max} \leq L/360 \quad (49)$$

The above LRFD approach may be used for beams with various types of loading and boundary conditions although the discussions in this chapter are related primarily to the specific cases of three- and four-point loading of I- and channel sections with pinned boundary conditions.

In order to demonstrate the use of the LRFD approach described in this section, practical analysis and design examples are presented in the next two sections for the case of four-point loading (Figure 101) on the channel section beam. A study of Figure 101 indicated that the buckling formula given by Equation 39 is in excellent agreement with the experimental results. Although this figure also shows that the finite-difference M_{\max} -L relation is more conservative, in the two sections to follow, Equation 39 is adopted due to its close agreement with the experiments.

4.4 LRFD Analysis Example

With reference to Figure 1b, the following analysis problem is posed herein:

Determine the buckling load (P_{cr}) and the buckling moment (M_R) of a FRP composite channel beam with the following data.

Section size: 10 x 2 3/4 x 1/2 in.

Span, $L = 144$ in.

End distance, $a = 20$ in.

Load height, $y_o^* = 5.0$ in.

$$E = 2.5 \times 10^6 \text{ psi}$$

$$G = 0.42 \times 10^6 \text{ psi}$$

$$I_y = 3.97 \text{ in}^4$$

$$I_w = 63.5530 \text{ in}^6$$

$$K_T = 0.604167 \text{ in}^4$$

Solution:

Using Equations 40 through 42:

$$f_1 = 0.0297993$$

$$f_2 = 72.2852$$

$$f_3 = 456822.0$$

and using Equation 39, the buckling load is:

$$P_{cr} = 2886.04 \text{ lbs.}$$

The buckling moment is found by combining Equations 39 and 46=

$$M_R = \phi_b a P_{cr}$$

in which $a P_{cr} = M_{\max}$. Assuming a resistance factor $\phi_b=0.9$, the buckling moment is:

$$M_R = 51948.72 \text{ lb-in.}$$

It should be noted that the buckling load P_{cr} can be increased to 3915.35 lbs, an increase in the buckling load capacity of 35%, if the loads could be applied right at the shear center, i.e.,

with $y_o^* = 0$. The P_{cr} value can be increased to 5311.77 lbs (assuming elastic behavior), an increase in the buckling load capacity of 84.0%, if the load could be applied at $y_o^* = -5.0$ in.

4.5 LRFD Design Example

With reference to Figure 1b, the following design problem is posed herein:

Select a FRP composite channel beam section for service dead and live loads P_D and P_L , respectively, of 208.33 lbs. and 500 lbs. and with the following data:

Span, $L = 120$ in.

End distance, $a = 25$ in.

Load height, $y_o^* = 4.0$ in.

$E = 2.5 \times 10^6$ psi

$G = 0.42 \times 10^6$ psi

Solution:

Using dead and live load factors of 1.2 and 1.6, respectively, the buckling load capacity should equal:

$$P_{cr} = 1.2(208.33) + 1.6(500) = 1050 \text{ lbs.}$$

Try $6 \times 11/16 \times 3/8$ in. channel section for which:

$$I_y = 0.52 \text{ in}^4$$

$$I_w = 3.5938 \text{ in}^6$$

$$K_T = 0.151611 \text{ in}^4$$

Using Equations 40 through 42:

$$f_1 = 0.0336719$$

$$f_2 = 27.1577$$

$$f_3 = 26306.8$$

and using Equation 39, the buckling load of the trial section is:

$$P_{cr} = 568.27 \text{ lbs}$$

which is well below the design load of 1050 lbs. Even if the design load is applied at the shear center ($y_o^* = 0$), this section would carry only 883.89 lbs and would, therefore, be deemed inadequate. However, if the load is applied at $y_o^* = -4.0$ in., The P_{cr} value will be 1374.81 lbs which is greater than the design load of 1050 lbs and the same section size would be adequate.

Try 8 x 2 3/16 x 3/8 in. channel section for which:

$$I_y = 1.52 \text{ in}^4$$

$$I_w = 15.7387 \text{ in}^6$$

$$K_T = 0.204346 \text{ in}^4$$

Using Equations 40 through 42:

$$f_1 = 0.0336719$$

$$f_2 = 79.3841$$

$$f_3 = 124200.0$$

and using Equations 39, the buckling load is:

$$P_{cr} = 1074.67 \text{ lbs}$$

which is slightly greater than the design load of 1050 lbs. Therefore, use 8 x 2 3/16 x 3/8 in. FRP. channel section. This section would carry $P_{cr} = 1920.55$ lbs. at buckling, if the load height is kept at zero, i.e. if $y_o^* = 0$. The same section will provide $P_{cr} = 3432.25$ lbs if $y_o^* = -4.0$ in. Of course, it is assumed herein that the beam material will remain elastic.

CHAPTER V.

COMPARISON OF RESULTS AND CONCLUSIONS

5.1 Comparison of Theory and Experiments

The experimental results from the FRP composite beam tests presented in Chapter II are in good general agreement with those predicted theoretically in Chapter III. As evident from the maximum bending moment versus the beam length relations summarized in Chapter IV, the peak loads from the theory and experiment also exhibit good general agreement. The theoretical load-deflection and load-strain curves are generally in excellent agreement in the linear range. In the nonlinear range, the equilibrium-based finite-difference results tend to be on the conservative side in comparison with those from the experiments.

For the I-section beam bent about the minor axis, the peak loads from the theory and experiment differ by about 5%. Table 4.1 summarizes the comparison of experimental and theoretical peak loads, P_{emax} and P_{tmax} . The value of the imperfection factor e^* is also listed in this table and is found to be generally small. For the three-point loading of the I-section beams, the $P_{\text{tmax}}/P_{\text{emax}}$ ratio varies between 0.95 and 1.25 with an average of 1.04. For the four-point loading of the I-section beams, the ratio varies from 0.77 to 1.00 with an average of 0.88.

For the three-point loading of the channel section beams, the $P_{\text{tmax}}/P_{\text{emax}}$ ratios are 0.89 and 0.93. For the four-point loading of the channel section beams, the $P_{\text{tmax}}/P_{\text{emax}}$ ratio varies from 0.75 to 0.80. For the flexural-torsional loading, the ratio varies from 0.87 to 0.95.

For the four-point loading of the channel section beams, the ratio of the buckling load from Equation 39 to that obtained experimentally, for Test CFT4-1 through CFT4-6 is approximately in the range from 0.89 to 0.98.

In summary, therefore, a good agreement between the theoretical and the experimental results is found thus making it feasible to use the theory for the formulation of a Load and Resistance Factor Design (LRFD) approach for practical use.

5.2 Load Height Effect

Table 5.1 presents the buckling load P_{cr} obtained using Equation 39, for a $6 \times 1 \frac{5}{8} \times \frac{1}{4}$ in. FRP channel section beam for various values of the load height accounted for by the vertical distance y_o^* from the shear center S. The values of L and “a” are taken in the range from 108 in. to 84 in., and 42 in. to 30 in., respectively. The results in this table show that the buckling load P_{cr} is seriously altered by changing y_o^* .

5.3 Conclusions

The following principal conclusions are drawn from the study of the FRP composite I- and channel section beams:

1. The experimental results are in good agreement with those based on the finite-difference solution to the coupled system of differential equations for flexural and torsional equilibrium.
2. The energy-based elastic buckling formula presented in this dissertation is in excellent agreement with the experimental results from the four-point loading tests on channel section beams.
3. For loading through locations other than the shear center, such as through the centroid, the warping normal strains or stresses could be substantial in comparison with the flexural stresses. For the tests conducted, the warping stresses were found to be over 20% of the flexural stresses.

4. The buckling load of the beam is seriously altered by changing the height of the applied load relative to the shear center. The most disadvantageous loading is on the side of the compression flange, resulting in decreasing buckling loads as the load height is increased above it. The most advantageous loading is on the side of the tension flange, resulting in increasing buckling loads as the load distance is increased by moving away from it. Thus, the FRP structural designers should develop the structural details such that the I-beams and channel beams get loaded on the side of the tension flange, whenever possible.
5. The beam buckling load is very sensitive to the minor axis slenderness ratio.
6. For the major axis beam tests conducted, overall elastic instability dictated the load-carrying capacity.
7. For the flexural-torsional tests, no cracking or local buckling is observed.
8. Based on the experimental and theoretical results presented, a Load and Resistance Factor Design (LRFD) approach is proposed for possible practical use.

Extensive testing on a commercial scale needs to be conducted to develop an appropriate statistical data base for establishing a refined value of the resistance factor ϕ .

5.4 Future Research

Additional research needs to be conducted on FRP beams with various other types of the loading and boundary conditions. Also, a wide variety of FRP materials are being produced by the manufacturers in USA and from around the world. Thus, extensive testing of beams made from various FRP materials should be conducted in order to correlate with theory and to develop general LRFD procedures.

REFERENCES

1. American Institute of Steel Construction Inc. "Load & Resistance Factor Design"; Vol.1, Chicago, Illinois, 1994
2. Razzaq Z. And Galambos, T.V. Biaxial bending of beams with or without torsion. J. Structural Division, ASCE, 1979, 105
3. Razzaq Z. And Galambos, T.V. Biaxial bending tests with or without torsion. J. Structural Division, AscE, 1979. 105
4. Galambos, T.V., *Structural Members and Frames*, Prentice Hall, Inc., Englewood Cliffs, New Jersey, 1968.
5. Baz, A.; Chen, T., "Proceeding of the SPIE- the International Society for Optical Engineering", Vol. 2427, 1995.
6. Pollock, G.D; Zak, A. R.; Hinton, H. H; Ahmad, M. F., " Structural Engineering and Mechanics," Vol. 3, Jan. 1995.
7. Kim, W. C. ; Dharan, C. K. H., "Composite Structures," Vol. 30, 1995.
8. Xie, Y.M.; Steven, G.P., "Computer and Structures," Vol. 52, July 1994.
9. Beg, D. , "Zeitschrift Fur Angewandte Mathematik and Mechanik," Vol. 74, 1994.
10. Barbero, E. J. ; Raftoyiannis, I. G; "Composite Structures," Vol. 27, 1994.
11. Craddock, J. N. ; Shing-Chung, Yen., "Composites Engineering," Vol. 3. 1994.
12. Chandrashekhara, K.; Bangera, K. M., "Composite Science and Technology," Vol. 47, 1993.
13. Puspita, G.; Barrau, J.J.; Gay, D., "Composite Structures," Vol. 24, 1993.
14. Chen, Wai-Fah; Atsuta, Toshio., "Theory of Beam-Columns," Vol. 2, 1977

Table 2.1. Tensile coupon tests results for Specimen 1 from flange of I-section
(coupon cross-sectional dimensions: 0.8x0.25 in.)

Obs. No.	Load P (lbs)	Axial Stress (psi)	Axial Strain (in./in.)
0	400	2000	0.000725
1	800	4000	0.001488
2	1200	6000	0.002256
3	1600	8000	0.003114
4	2000	10000	0.003929
5	2400	12000	0.004754
6	2800	14000	0.005604
7	3200	16000	0.006470
8	3600	18000	0.007314
9	4000	20000	0.008185
10	4400	22000	0.009083
11	4800	24000	0.009979
12	5200	26000	0.010902
13	5600	28000	0.011843

Table 2.2. Tensile coupon test results for Specimen 2 from flange of I-section
(coupon cross-sectional dimensions: 0.8x0.25 in.)

Obs. No.	Load/P (lbs.)	Avail. Stress (psi)	Avail. Strain (in./in.)
0	400	2000	0.000795
1	800	4000	0.001424
2	1200	6000	0.002199
3	1600	8000	0.002975
4	2000	10000	0.003748
5	2400	12000	0.004580
6	2800	14000	0.005412
7	3200	16000	0.006275
8	3600	18000	0.007145
9	4000	20000	0.008012
10	4400	22000	0.008900
11	4800	24000	0.009780
12	5200	26000	0.010653
13	5600	28000	0.011545
14	6000	30000	0.012475
15	6140	30700	-

Table 2.3. Tensile coupon test results for Specimen 3 from web of I-section
(coupon cross-sectional dimensions: 0.9x0.25 in.)

Obs. No.	Load P (lbs)	Axial Stress (ksi)	Axial Strain (in./in.)
0	400	1778	0.000500
1	800	3556	0.001170
2	1200	5333	0.001783
3	1600	7111	0.002405
4	2000	8889	0.003070
5	2400	10667	0.003726
6	2800	12444	0.004407
7	3200	14222	0.005086
8	3600	16000	0.005765
9	4000	17778	0.006453
10	4400	19556	0.007154
11	4800	21333	0.007772
12	4900	21778	-

Table 2.4. Tensile coupon test results for Specimen 4 from web of I-section
(coupon cross-sectional dimensions: 0.9x0.25 in.)

Obs. No.	Load P (lbs)	Axial Stress (psi)	Axial Strain (in./in.)
0	400	1778	0.000600
1	800	3556	0.001270
2	1200	5333	0.001888
3	1600	7111	0.002508
4	2000	8889	0.003170
5	2400	10667	0.003827
6	2800	12444	0.004508
7	3200	14222	0.005187
8	3600	16000	0.005868
9	4000	17778	0.006558
10	4400	19556	0.007250
11	4800	21333	0.007890
12	5200	23111	-

Table 2.5. Summary of tensile test results for material of I-section

Specimen No.	Section (in.)	Location	Young's Modulus, E_T (psi)	ϵ_T (in./in.)
I1	I-4x2x0.25	Flange	2,452,182	0.011843
I2	I-4x2x0.25	Flange	2,328,448	0.012475
I3	I-4x2x0.25	Web	2,813,281	0.007772
I4	I-4x2x0.25	web	2,744,572	0.007890

Table 2.6. Tensile coupon test results for Specimen 5 from flange of channel section
(coupon cross-sectional dimensions: 1.1x0.25 in.)

Obs. No.	Load P (lbs)	Axial Stress (psi)	Axial Strain (in./in.)
0	1000	3636	0.001143
1	2000	7273	0.002180
2	3000	10910	0.003310
3	4000	14545	0.004339
4	5000	18182	0.005473
5	6000	21818	0.006613
6	7000	25455	0.007815
7	8000	29091	0.008984
8	9000	32727	0.010212
9	10000	36364	0.011410
10	11000	40000	0.012595
11	12000	43636	0.013755
12	13000	47273	0.014940
13	14000	50909	0.016250
14	15000	54545	0.017516
15	15500	56364	0.018235

Table 2.7. Tensile coupon test results for Specimen 6 from flange of channel section
(coupon cross-sectional dimensions: 1x0.25 in.)

Obs. No.	Load P (lbs.)	Axial Stress (psi)	Axial Strain (in./in.)
0	1000	4000	0.001132
1	2000	8000	0.002325
2	3000	12000	0.003520
3	4000	16000	0.004780
4	5000	20000	0.006096
5	6000	24000	0.007328
6	7000	28000	0.008696
7	8000	32000	0.009984
8	9000	36000	0.011332
9	10000	40000	0.012675
10	11000	44000	0.014000
11	12000	48000	0.015345
12	13000	52000	0.016722
13	13500	54000	0.017502

Table 2.8. Tensile coupon test results for Specimen 7 from web of channel section
(coupon cross-sectional dimensions: 1x0.25 in.)

Obs. No.	Load P (lbs.)	Axial Stress (psi)	Axial Strain (in./in.)
0	800	3200	0.000860
1	1600	6400	0.001776
2	2400	9600	0.002718
3	3200	12800	0.003693
4	4000	16000	0.004661
5	4800	19200	0.005663
6	5600	22400	0.006658
7	6200	24800	0.007392
8	7000	28000	0.008395
9	7800	31200	0.009437
10	9200	36800	0.011005
11	10000	40000	0.011988
12	10800	43200	0.012983
13	11600	46400	-

Table 2.9. Tensile coupon test results for Specimen 8 from web of channel section
(coupon cross-sectional dimensions: 1x0.25 in.)

Obs. No.	Load P (lbs)	Axial Stress (psi)	Axial Strain (in./in.)
0	1000	4000	0.001153
1	2000	8000	0.002317
2	3000	12000	0.003500
3	4000	16000	0.004658
4	5000	20000	0.005878
5	6000	24000	0.007056
6	7000	28000	0.008291
7	8000	32000	0.009496
8	9000	36000	0.010743
9	10000	40000	0.011929
10	11000	44000	0.013165
11	12000	48000	0.014365
12	13000	52000	0.015583
15	14000	56000	0.016858

Table 2.10. Summary of tensile test results for material of channel section

Specimen No.	Section (in.)	Location	Young's Modulus, E_T (psi)	E_T (in./in.)
C1	C6x1.625x0.25	Flange	3,183,774	0.018235
C2	C6x1.625x0.25	Flange	3,180,111	0.017502
C3	C6x1.625x0.25	Web	3,366,224	0.012983
C4	C6x1.625x0.25	Web	3,360,470	0.016858

Table 2.11. Minor axis bending test results for I-beam (4x2x1/4 in., L=30 in.)

Obs. No.	Load P (lbs)	Bending Strain (in./in.)		Midspan Vertical Deflection (in.)
		BSC1	BSC2	
0	200	-0.001162	0.001211	0.120
1	400	-0.00238	0.002519	0.240
2	600	-0.003628	0.003862	0.360
3	800	-0.004905	0.005233	0.480
4	1000	-0.006103	0.006533	0.600
5	1200	-0.007297	0.007780	0.720
6	1400	-0.008623	0.009169	0.850
7	1600	-0.009912	0.010519	0.975
8	1800	-0.011196	0.011802	1.100
9	2000	-0.012555	0.012977	1.225
10	2100	-0.013165	0.013488	1.290
11	2180	-	-	-

Table 2.12. Results for FRP I-beam (4"x2"x0.25") Test No. IFT3-1
with three-point loading (L=108in.)

Obs. No.	Load P (lbs.)	Midspan Vertical Deflection (in.)	Midspan Lateral Deflection (in.)	Midspan Angle of Twist (rad)
0	0	0.43477	0.26065	0.027199
1	35	0.52633	0.24601	0.036671
2	62	0.59018	0.22118	0.041522
3	78	0.64805	0.17759	0.039815
4	99	0.746877	0.91167	0.013170

Table 2.13. Results for FRP I-beam (4"x2"x0.25") Test No. IFT3-2
with three-point loading (L= 96 in.)

Obs. No.	Load P (lb)	Midspan Vertical Deflection(in.)	Midspan Lateral Deflection(in.)	Midspan Angle of Twist(in.)
0	0	0.49235	0.12125	0.043470
1	29	0.53544	0.11695	0.048788
2	62	0.58726	0.10989	0.054595
3	88	0.62789	0.08591	0.058924
4	110	0.66791	0.05431	0.057295
5	142	0.78980	0.44303	0.006399
6	147	0.82587	0.34063	-0.01725

Table 2.14. Results for FRP I-beam (4"x2"x0.25") Test No. IFT3-3
with three-point loading ($L = 84$ in.)

Obs. No.	Load P (lb.)	Midspan Vertical Deflection (in.)	Midspan Lateral Deflection (in.)	Midspan Angle of Twist (in.)
0	0	0.362000	0.074235	0.014482
1	13	0.375123	0.074180	0.016502
2	43	0.413392	0.077311	0.020147
3	83	0.466050	0.053625	0.024964
4	110	0.504537	0.033903	0.025561
5	136	0.543047	0.014821	0.023570
6	158	0.597874	0.918848	0.011668
7	174	0.611995	0.939279	-0.01080

Table 2.15. Results for FRP I-beam (4"x2"x0.25") Test No. IFT3-4
with three-point loading ($L = 72$ in.)

Obs. No.	Load P (lbs.)	Midspan Vertical Deflection (in.)	Midspan Lateral Deflection (in.)	Midspan Angle of Twist (rad.)
0	0	0.414212	0.45874	0.031848
1	59	0.468665	0.455119	0.038027
2	110	0.505830	0.445474	0.041930
3	158	0.548825	0.424267	0.418127
4	201	0.583471	0.396016	0.038664
5	219	0.600530	0.370348	0.037823
6	238	0.617770	0.328133	0.021476
7	249	0.628565	0.286714	0.009120
8	254	0.641266	0.2333175	-0.007274
8	262	0.658012	0.1616291	-0.027677
10	265	0.673112	0.101714	-0.044547

Table 2.16. Results for FRP I-beam (4"x2"x0.25") Test No. IFT4-1
with four-point loading ($L = 108$ in.)

Obs. No.	Midspan Deflection				
	Load P (lbs.)	v_c (in.)	v_t (in.)	ϕ_c (in.)	ϵ_c (in./in.)
0	13	0.03199	0.00397	0.00092	0.000065
1	27	0.06099	0.00792	0.00120	0.000121
2	38	0.13998	0.00447	0.00378	0.000261
3	48	0.17992	0.01300	0.00553	0.000335
4	62	0.24682	0.01891	0.00847	0.000455
5	70	0.32635	0.03812	0.01493	0.000594
6	72	0.37402	0.06624	0.02601	0.000688
7	75	0.39189	0.09996	0.02801	0.000763
8	78	0.41735	0.20025	0.06446	0.000838

Table 2.17. Results for FRP I-beam (4"x2"x0.25") Test No. IFT4-2
with four-point loading (L = 96 in.)

Obs. No.	Midspan Deflection				
	Load P (lbs.)	v_x (in.)	v_y (in.)	ϕ (in.)	ϵ (in./in.)
0	19	0.01799	0.00098	0.00092	0.000044
1	34	0.03499	0.00296	0.00110	0.000085
2	50	0.09499	0.00381	0.00194	0.000213
3	66	0.13998	0.00467	0.00231	0.000313
4	77	0.17998	0.00541	0.00323	0.000396
5	82	0.24494	0.00971	0.00525	0.000538
6	101	0.31275	0.02189	0.00993	0.000683
7	106	0.33957	0.02748	0.01331	0.000797
9	114	0.37539	0.09979	0.04012	0.000853

Table 2.18. Results for FRP I-beam (4"x2"x0.25") Test No. IFT4-3
with four-point loading (L = 84 in.)

Obs. No.	Midspan Deflection				
	Load P (lbs.)	v_z (in.)	w_z (in.)	ϕ (in.)	ϵ_z (in./in.)
0	29	0.02499	0.00397	0.00120	0.000072
1	50	0.08496	0.00760	0.00461	0.000233
2	72	0.12985	0.01698	0.00783	0.000361
3	93	0.17468	0.02600	0.01139	0.000486
4	103	0.21723	0.04343	0.01638	0.000602
5	114	0.25599	0.06919	0.02646	0.000722
6	119	0.27734	0.10688	0.03954	0.000794
9	125	0.28840	0.14953	0.05224	0.000863

Table 2.19. Results for FRP I-beam (4"x2"x0.25") Test No. IFT4-4
with four-point loading ($L = 72$ in.)

Obs. No.	Midspan Deflection				
	Load P (lbs.)	v_c (in.)	u_c (in.)	ϕ_c (in.)	ϵ_c (in./in.)
0	24	0.01400	0.00001	0.00129	0.000048
1	56	0.08199	0.00172	0.00342	0.000217
2	78	0.11597	0.00436	0.00544	0.000326
3	99	0.13995	0.00604	0.00683	0.000408
4	120	0.17986	0.01226	0.00967	0.000544
5	141	0.22567	0.02095	0.01351	0.000712
6	158	0.24643	0.02988	0.01666	0.000782
7	177	0.27729	0.05656	0.02670	0.000910
8	185	0.29534	0.08572	0.03781	0.000988
9	190	0.30162	0.11600	0.048827	0.001035

Table 2.20. Results for FRP I-beam (4"x2"x0.25") Test No. IFT4-5
with four-point loading (L = 60 in.)

Obs. No.	Midspan Deflection				
	Load P (lbs.)	v_m (in.)	z_m (in.)	ϕ_m (in.)	ϵ_m (in./in.)
0	32	0.01200	0.00001	0.00111	0.000056
1	56	0.03799	0.00091	0.00221	0.000175
2	88	0.06099	0.00076	0.00379	0.000280
3	120	0.09099	0.00052	0.00526	0.000403
4	158	0.12395	0.00513	0.00701	0.000551
5	190	0.15985	0.01239	0.01004	0.000725
6	217	0.18071	0.01967	0.01287	0.000821
7	243	0.20816	0.03672	0.02051	0.000955
8	260	0.22100	0.07229	0.02563	0.001033
9	270	0.22721	0.06977	0.03585	0.001079
10	278	0.23589	0.08683	0.04247	0.001119
11	286	0.23836	0.11420	0.05240	0.001168
12	292	0.24180	0.13462	0.06148	0.001239
13	292	0.24348	0.16000	0.07056	0.001239
14	292	0.24226	0.18914	0.08438	0.001239

Table 2.21. Results for FRP channel beam ($6 \times 1\frac{5}{8} \times \frac{1}{4}$ in.) Test No. CFT3-1 with three-point loading ($L = 108$ in.)⁸

Obs. No.	Load (lbs.)	Midspan Vertical Deflection (in.)	Midspan Lateral Deflection (in.)	Midspan Angle of Twist (rad.)
0	0	0	0	0
1	35	0.019594	0.008848	-0.005334
2	86	0.078041	0.008838	-0.007354
3	131	0.078041	0.003774	-0.007729
4	163	0.155357	-0.010629	-0.004958
5	193	0.274455	0.064145	0.001781
6	209	0.293831	0.040911	0.008651
7	222	0.321353	0.008292	0.018370
8	238	0.359076	-0.044736	0.035747
9	241	0.407363	-0.044736	0.043101
10	243	0.429363	-0.044736	0.055848
11	248	0.460037	-0.0146961	0.070790
12	257	0.480530	-0.193147	0.085881
13	260	0.500533	-0.234303	0.098771

Table 2.22. Results for FRP channel beam ($6 \times 1 \frac{5}{8} \times \frac{1}{4}$ in.) Test No. CFT3-2
with three-point loading ($L = 96$ in.)

Obs. No.	Load (lbs.)	Midspan Vertical Deflection (in.)	Midspan Lateral Deflection (in.)	Midspan Angle of Twist (rad)
0	0	0	0	0
1	46	0.034854	0.004146	-0.000382
2	96	0.664230	0.007413	-0.000735
3	155	0.101245	0.011315	-0.001075
4	203	0.129721	0.112530	-0.001272
5	243	0.144385	0.002922	-0.001294
6	270	0.156382	-0.008866	-0.002495
7	297	0.183497	-0.030791	-0.002795
8	310	0.190234	-0.057975	0.003785
9	318	0.197532	-0.073204	0.008202
10	324	0.199452	-0.095082	0.014085
11	334	0.202454	-0.129202	0.024486
12	340	0.205380	-0.014660	0.034592
13	345	0.217984	-0.192992	0.042605

Table 2.23. Results for FRP channel beam ($6 \times 1\frac{5}{8} \times \frac{1}{4}$ in.) Test No. CFT4-1
with four-point loading ($L = 108$ in.)

Obs. No.	Load (lbs.)	Midspan Vertical Deflection (in.)	Midspan Lateral Deflection (in.)	Midspan Angle of Twist (rad)
0	32	0.04799	0.00598	0.00025
1	64	0.08397	0.01487	0.00143
2	80	0.10895	0.02177	0.00202
3	96	0.12388	0.02850	0.00396
4	115	0.14859	0.04777	0.00823
5	131	0.16071	0.07842	0.01590
6	136	0.15972	0.11969	0.02645

Table 2.24. Results for FRP channel beam ($6 \times 1\frac{5}{8} \times \frac{1}{4}$ in.) Test No. CFT4-2
with four-point loading ($L = 102$ in.)

Obs. No.	Load (lbs.)	Midspan Vertical Deflection (in.)	Midspan Lateral Deflection (in.)	Midspan Angle of Twist (rad)
0	30	0.02999	0.00195	0.00152
1	56	0.05499	0.00283	0.00296
2	85	0.08597	0.00457	0.00399
3	109	0.11296	0.00531	0.00489
4	135	0.14495	0.00751	0.00577
5	156	0.17495	0.00980	0.00645
6	160	0.18395	0.01195	0.00710

Table 2.25. Results for FRP channel beam ($6 \times 1\frac{5}{8} \times \frac{1}{4}$ in.) Test No. CFT4-3 with four-point loading ($L = 96$ in.)

Obs. No.	Load (lb.)	Midspan Vertical Deflection (in.)	Lateral Deflection (in.)	Midspan Angle of Twist (rad)
0	32	0.03099	0.00299	0.00008
1	63	0.05998	0.01092	0.00126
2	96	0.09090	0.02467	0.00362
3	128	0.11465	0.04413	0.00757
4	160	0.14355	0.08252	0.01706
5	181	0.15875	0.14738	0.03430
6	198	0.15990	0.22365	0.04775

Table 2.26. Results for FRP channel beam ($6 \times 1\frac{5}{8} \times \frac{1}{4}$ in.) Test No. CFT4-4 with four-point loading ($L = 84$ in.)

Obs. No.	Midspan Deflection				
	Load P (lbs.)	v_z (in.)	w (in.)	ϕ_z (in.)	ϵ (in./in.)
0	102	0.05299	0.00186	0.00262	0.000253
1	185	0.10499	0.00201	0.00396	0.000457
2	243	0.14300	0.00336	0.00425	0.000582
3	273	0.16199	0.00475	0.00452	0.000650
4	281	0.18699	0.00495	0.00470	0.000674
5	297	0.19799	0.00696	0.00480	0.000740
6	300	0.211800	0.01009	0.00520	0.000757

Table 2.27. Results for FRP channel beam ($6 \times 1\frac{5}{8} \times \frac{1}{4}$ in.) Test No. CFT4-5 with four-point loading ($L = 72$ in.)

Obs. No.	Load (lbs.)	Midspan Vertical Deflection (in.)	Midspan Lateral Deflection (in.)	Midspan Angle of Twist (rad)
0	51	0.01599	0.00298	0.00101
1	107	0.03498	0.00592	0.00211
2	161	0.05796	0.01082	0.00305
3	214	0.08194	0.01468	0.00381
4	243	0.09492	0.01657	0.00449
5	268	0.10689	0.01943	0.00526
6	302	0.12184	0.02422	0.00637
7	324	0.13378	0.02903	0.00722
8	342	0.14170	0.03379	0.00850
9	353	0.14565	0.03665	0.00919
10	361	0.15159	0.03948	0.00996
11	375	0.15752	0.04227	0.01090
12	385	0.16539	0.04797	0.01218
13	400	0.17127	0.05116	0.01338
14	412	0.17806	0.05825	0.01536
15	425	0.18869	0.06751	0.01837
16	436	0.19440	0.07293	0.02077
17	447	0.21358	0.10290	0.06177
18	452	0.22096	0.12115	0.07554

Table 2.28. Results for FRP channel beam ($6 \times 1 \frac{5}{8} \times \frac{1}{4}$ in.) Test No. CFT4-6 with four-point loading ($L = 60$ in.)

Obs. No.	Load (lb.)	Midspan Vertical Deflection (in.)	Midspan Lateral Deflection (in.)	Midspan Angle of Twist (rad)
0	59	0.01199	0.00098	0.00101
1	115	0.02399	0.00195	0.00203
2	163	0.03498	0.00389	0.00304
3	217	0.04896	0.00879	0.00415
4	279	0.06391	0.01465	0.00534
5	314	0.07785	0.02147	0.00679
6	377	0.09275	0.02923	0.00824
7	431	0.10859	0.03786	0.01038
8	530	0.12312	0.05611	0.01518
9	556	0.13286	0.06265	0.01750
10	578	0.013965	0.06729	0.01922
11	589	0.14449	0.07102	0.02042
12	607	0.15027	0.07568	0.02181
13	618	0.15509	0.07939	0.02301
14	629	0.15985	0.08405	0.02440
15	642	0.16457	0.08864	0.02613
16	655	0.17025	0.09315	0.02802
17	669	0.17476	0.10057	0.03054
18	682	0.18110	0.10873	0.03392
19	693	0.18733	0.11782	0.03739
20	701	0.19318	0.12855	0.04251
21	701	0.19861	0.13385	0.04468
22	701	0.20617	0.14633	0.04992

Table 2.29. Results for FRP channel beam ($6 \times 1 \frac{5}{8} \times \frac{1}{4}$ in.) Test No. CFT4-7 with four-point loading ($L = 84$ in.) (centroidal loading; $x = -0.5675$, $y = -3.0$)

Obs. No.	Midspan Deflection				
	Load P (lbs.)	v_z (in.)	w_z (in.)	ϕ_z (in.)	ϵ_z (in./in.)
0	27	0.02701	-0.00225	0.00946	0.000084
1	62	0.05802	-0.00218	0.02042	0.000162
2	88	0.08962	0.00916	0.03161	0.000239
3	115	0.11860	0.026767	0.04377	0.000311
4	142	0.14827	0.05400	0.05940	0.000391
5	169	0.17641	0.09556	0.07834	0.000466
6	187	0.20361	0.15054	0.10613	0.000560
7	203	0.24860	0.22436	0.15370	0.000653

Table 2.30. Results for FRP channel beam ($6 \times 1 \frac{5}{8} \times \frac{1}{4}$ in.) Test No. CFT4-8 with four-point loading ($L = 84$ in.)
(loading between centroid and shear center; $x = -0.2656$, $y = -3.0$)

Obs. No.	Midspan Deflection				
	Load P (lbs)	ψ (in)	u_x (in)	ϕ (in)	ϵ_x (in/in)
0	35	0.02300	-0.00015	0.00682	0.000092
1	72	0.04889	0.00626	0.01507	0.000164
2	104	0.07769	0.01119	0.02321	0.000255
3	136	0.10615	0.02251	0.03271	0.000324
4	177	0.14588	0.05563	0.04961	0.000439
5	211	0.18407	0.10787	0.07348	0.000552
6	243	0.23832	0.21494	0.11344	0.000702

Table 2.31. Results for FRP channel beam ($6 \times 1 \frac{5}{8} \times \frac{1}{4}$ in.) Test No. CFT4-9 with four-point loading ($L = 84$ in.)
(loading to right side of the shear center; $x = 0.4531$, $y = -3.0$)

Obs. No.	Midspan Deflection				
	Load P (lbs.)	v_z (in.)	v_y (in.)	ϕ_x (in.)	ϵ_x (in./in.)
0	32	0.01805	0.00104	-0.01235	0.000073
1	64	0.032815	0.00617	-0.01843	0.000130
2	104	0.054520	0.00457	-0.03123	0.000210
3	131	0.073995	-0.00793	-0.03754	0.000273
4	158	0.093382	-0.02922	-0.04232	0.000335
5	182	0.111590	-0.06401	-0.03765	0.000375
6	195	0.122299	-0.10265	-0.02765	0.000404
7	201	0.133494	-0.13601	-0.01543	0.000407
8	209	0.140133	-0.16553	-0.00232	0.000408
9	211	0.147355	-0.20652	0.014543	0.000411
10	217	0.159112	-0.25060	0.041231	0.000406
11	222	0.170324	-0.29283	0.08565	0.000400
12	225	0.181351	-0.35453	0.08765	0.000392
13	233	0.193733	-0.39980	0.11067	-

Table 3.1 Minor axis bending theoretical results for I-beam
(4×2×0.25 in., L=30 in.)

Obs. No.	Load P (lbs)	Bending Strain (in./in.)	Midspan Deflection v_c (in.)
0	200	0.001253	0.115823
1	400	0.002607	0.231645
2	600	0.003997	0.347528
3	800	0.005416	0.463682
4	1000	0.006761	0.579472
5	1200	0.008052	0.694845
6	1400	0.009489	0.820251
7	1600	0.010887	0.940875
8	1800	0.012215	1.061523
9	2000	0.0134311	1.182125
10	2240	0.034566	1.244830

Table 3.2 Results for FRP composite I-beam (4×2×0.25 in.) Test No. IFT3-1 with three- point loading (L =108 in. e =-0.002 in.)

Obs. No.	Load P (lbs)	Midspan Deflection		
		u_c (in.)	u_e (in.)	ϕ_e (in.)
0	0	0	0	0
1	35	0.084202	0.032273	0.003288
2	62	0.149158	0.132173	0.007682
3	78	0.187650	0.26673	0.012411
4	99	0.238172	0.731265	0.027078
5	124	0.298316	0.782324	0.455208

Table 3.3 Results for FRP composite I-beam (4×2×0.25 in.) Test No. IFT3-2 with three- point loading (L = 96 in. e =-0.002 in.)

Obs. No.	Load P (lbs.)	Midspan Deflection		
		δ_c (in.)	δ_{cr} (in.)	ϕ_c (in.)
0	0	0	0	0
1	29	0.048999	0.0011043	0.00192
2	62	0.010475	0.0062660	0.00515
3	88	0.148689	0.0164246	0.00960
4	110	9.185862	0.0376788	0.01709
5	140	0.236551	0.164499	0.06159

Table 3.4 Results for FRP composite I-beam (4×2×0.25 in.) Test No. IFT3-3 with three- point loading (L = 84 in. e =-0.002 in.)

Obs. No.	Load P (lbs)	Midspan Deflection		
		u_z (in.)	u_y (in.)	ϕ_z (in.)
0	0	0	0	0
1	13	0.015847	0.000999	0.000578
2	43	0.048673	0.012272	0.000215
3	83	0.093950	0.057219	0.000523
4	110	0.124513	0.124412	0.000867
5	136	0.153943	0.257112	0.001458
6	158	0.178846	0.515028	0.002528
7	170	0.196957	0.828617	0.004484

Table 3.5 Results for FRP composite I-beam (4×2×0.25 in.) Test No. IFT3-4 with three-point loading (L = 72 in. e =+0.002 in.)

Obs. No.	Load P (lbs.)	Midspan Deflection		
		u_c (in.)	v_c (in.)	ϕ_c (in.)
0	0	0	0	0
1	59	0.042056	-0.00101	0.0002061
2	110	0.078410	-0.00436	0.0004804
3	158	0.112626	-0.01226	0.0009457
4	201	0.143277	-0.03132	0.0019112
5	219	0.156821	-0.05033	0.0028267
6	238	0.169512	-0.09743	0.0050509
7	249	0.177492	-0.17281	0.0085791
8	254	0.181057	-0.25225	0.0122866
9	260	0.186759	-0.32564	0.0246490

Table 3.6 Results for FRP composite I-beam (4×2×0.25 in.) Test No. IFT4-1 with four-point loading (L = 108 in. e = 0.0002 in.)

Obs. No.	Load P (lbs.)	Midspan Deflection			ϵ (in./in.)
		v_c (in.)	Δ_c (in.)	ϕ_c (in.)	
0	0	0	0	0	0
1	13	0.042641	0.0001079	0.0002253	0.000118
2	27	0.088570	0.0005550	0.0005945	0.000246
3	38	0.124663	0.0013279	0.0009679	0.000347
4	48	0.157459	0.0026763	0.0015575	0.000440
5	62	0.203397	0.0075414	0.0034399	0.000573
6	70	0.229623	0.0168320	0.0068500	0.000659
7	72	0.236203	0.0221151	0.0087663	0.000685
8	75	0.246045	0.0380550	0.0145222	0.000736
9	78	0.259167	0.2118480	0.0377166	0.000859

Table 3.7 Results for FRP composite I-beam (4×2×0.25 in.) Test No. IFT4-2 with four-point loading (L = 96 in. e = -0.00007 in.)

Obs. No.	Load P (lbs.)	Midspan Deflection			ϵ_f (in./in.)
		v_c (in.)	w_c (in.)	ϕ_c (in.)	
0	0	0	0	0	0
1	19	0.099480	0.000447	0.000091	0.000122
2	34	0.088544	0.000169	0.000194	0.000220
3	50	0.130212	0.000465	0.000367	0.000325
4	66	0.171880	0.001164	0.000704	0.000435
5	77	0.200527	0.002351	0.001227	0.000518
6	82	0.213548	0.003464	0.001704	0.000516
7	91	0.236899	0.009700	0.004327	-

Table 3.8 Results for FRP composite I-beam (4×2×0.25 in.) Test No. IFT4-3 with four-point loading (L = 84 in. e = -0.0005 in.)

Obs. No.	Load P (lb.)	Midspan Deflection			ϵ (in./in.)
		v_c (in.)	v_f (in.)	ϕ_c (in.)	
0	0	0	0	0	0
1	29	0.044762	0.000382	0.000765	0.000126
2	50	0.071775	0.001397	0.001630	0.000220
3	72	0.111135	0.003956	0.003248	0.000321
4	93	0.143550	0.010730	0.006890	0.000429
5	103	0.158985	0.019311	0.011250	0.000494
6	114	0.175964	0.051026	0.027003	0.000626
7	119	0.185226	0.121519	0.061799	0.000836
8	123	0.189856	3.842665	1.893306	0.001751

Table 3.9 Results for FRP composite I-beam (4×2×0.25 in.) Test No. IFT4-4 with four-point loading (L = 72 in. e = 0.0005 in.)

Obs. No.	Load P (lbs.)	Midspan Deflection			ϵ_c (in./in.)
		v_c (in.)	v_s (in.)	ϕ_c (in.)	
0	0	0	0	0	0
1	24	0.023328	0.000104	0.000400	0.000066
2	56	0.054433	0.000707	0.001170	0.000156
3	78	0.075818	0.001679	0.002007	0.000220
4	99	0.096231	0.003504	0.003221	0.000285
5	120	0.116643	0.007520	0.005919	0.000358
6	141	0.137056	0.020326	0.013709	0.000467
7	158	0.153580	0.139320	0.084328	0.00100
8	161	0.156497	0.753149	0.447825	0.00353

Table 3.10 Results for FRP composite I-beam (4×2×0.25 in.) Test No. IFT4-5 with four-point loading (L = 60 in. e = -0.0005 in.)

Obs. No.	Load P (lbs.)	Midspan Deflection			ϵ_s (in./in.)
		v_c (in.)	v_s (in.)	ϕ_s (in.)	
0	0	0	0	0	0
1	32	0.018000	0.000067	0.000033	0.000051
2	56	0.031501	0.000230	0.000065	0.000090
3	88	0.050064	0.000678	0.000123	0.000144
4	120	0.067502	0.001599	0.000214	0.000200
5	158	0.088877	0.004178	0.000429	0.000276
6	190	0.106878	0.011098	0.000954	0.000368
7	217	0.122066	0.056323	0.004263	0.000682
8	226	0.127129	8.724050	0.635219	0.003436

Table 3.11 Results for FRP composite channel beam ($6 \times 1 \frac{5}{8} \times 0.25$ in.) Test CFT3-1 with three-point loading ($L = 108$ in. $e = 0.0003$ in.)

Obs. No.	Load P (lb.)	Midspan Deflection		
		v_x (in.)	v_y (in.)	ϕ_z (in.)
0	0	0	0	0
1	35	0.028798	-0.000186	0.000301
2	86	0.070761	-0.001290	0.000855
3	131	0.107788	-0.003745	0.001636
4	163	0.134118	-0.007508	0.002645
5	193	0.158802	-0.015597	0.004660
6	209	0.171967	-0.025601	0.007080
7	222	0.182664	-0.044136	0.011511
8	233	0.191715	-0.091466	0.022774
9	238	0.195829	-0.162696	0.039691
10	241	0.198297	-0.292341	0.070468
11	243	0.199943	-0.602048	0.298558

Table 3.12 Results for FRP composite channel beam ($6 \times 1 \frac{5}{8} \times 0.25$ in.) Test No. CFT3-2 with three-point loading ($L = 96$ in. $e = 0.0003$ in.)

Obs. No.	Load P (lbs.)	Midspan Deflection		
		w_c (in.)	u_c (in.)	ϕ_c (in.)
0	0	0	0	0
1	46	0.026582	-0.000165	0.000291
2	96	0.055477	-0.000796	0.000972
3	155	0.089572	-0.002524	0.001325
4	203	0.117311	-0.005635	0.002267
5	243	0.140426	-0.011552	0.003896
6	270	0.156029	-0.021210	0.006456
7	297	0.171632	-0.054280	0.015201
8	310	0.179145	-0.142142	0.037841

Table 3.13 Results for FRP composite channel beam (6×1 5/8×0.25 in.) Test No. CFT4-1 with four-point loading (L = 108 in.; e = -0.0003 in.)

Obs. No.	Load P (lbs.)	Midspan Deflection		
		δ_p (in.)	δ_c (in.)	ϕ_c (in.)
0	0	0	0	0
1	32	0.035904	0.000490	0.000671
2	64	0.071804	0.002904	0.002008
3	80	0.089761	0.006256	0.003480
4	96	0.107713	0.015297	0.007551
5	115	0.129031	0.218289	0.085593
6	117	0.131275	16.86569	6.505250

Table 3.14 Results for FRP composite channel beam ($6 \times 1 \frac{5}{8} \times 0.25$ in.) Test No. CFT4-2 with four-point loading ($L = 102$ in.; $e = -0.0005$ in.)

Obs. No.	Load P (lbs.)	Midspan Deflection		
		v_c (in.)	v_s (in.)	ϕ_c (in.)
0	0	0	0	0
1	30	0.028356	0.000499	0.000864
2	56	0.052931	0.002215	0.002067
3	85	0.081288	0.007844	0.004865
4	109	0.103027	0.025830	0.012587
5	130	0.12287	0.952344	0.391809

Table 3.15 Results for FRP composite channel beam ($6 \times 1 \frac{5}{8} \times 0.25$ in.) Test No. CFT4-3 with four-point loading ($L = 96$ in.; $e = -0.0001$ in.)

Obs. No.	Load P (lbs.)	Midspan Deflection		
		Δ_c (in.)	Δ_t (in.)	ϕ_c (in.)
0	0	0	0	0
1	32	0.025216	0.007192	0.000155
2	63	0.055643	0.003593	0.000397
3	96	0.075650	0.012908	0.000944
4	128	0.100864	0.057465	0.003179
5	148	0.116628	3.079524	0.149144

Table 3.16 Results for FRP composite channel beam (6×1 5/8×0.25 in.) Test No. CFT4-4 with four-point loading (L = 84 in.; e = -0.00009 in.)

Obs. No	Load P (lbs)	Midspan Deflection			ϵ (in/in)
		v_c (in.)	w_c (in.)	ϕ_c (in.)	
0	0	0	0	0	0
1	50	0.018943	0.000282	0.000131	0.000038
2	100	0.037892	0.001477	0.000346	0.000076
3	150	0.056839	0.005076	0.000798	0.000115
4	200	0.075785	0.021639	0.002569	0.000153
5	233	0.088290	8.303214	0.850028	0.000215

Table 3.17 Results for FRP composite channel beam ($6 \times 1 \frac{5}{8} \times 0.25$ in.) Test No. CFT4-5 with four-point loading ($L = 72$ in.; $e = -0.0009$ in.)

Obs. No.	Load P (lbs)	Midspan Deflection		
		u_c (in.)	u_g (in.)	ϕ_c (in.)
0	0	0	0	0
1	51	0.010952	0.000164	0.000737
2	107	0.022979	0.000862	0.001843
3	161	0.034576	0.002423	0.003458
4	214	0.045959	0.005740	0.006187
5	243	0.052187	0.009207	0.008759
6	268	0.057556	0.014305	0.012363
7	302	0.064858	0.029783	0.022901
8	324	0.069582	0.059811	0.042942
9	344	0.073878	0.219308	0.148537

Table 3.18 Results for FRP composite channel beam (6×1 5/8×0.25 in.) Test No. CFT4-6 with four-point loading (L = 60 in.; e = -0.0005 in.)

Obs. No.	Load P (lbs.)	Midspan Deflection		
		δ_c (in.)	δ_c (in.)	ϕ_c (in.)
0	0	0	0	0
1	59	0.007332	0.000227	0.000151
2	115	0.014292	0.000955	0.000327
3	163	0.020258	0.002124	0.000515
4	217	0.026969	0.004299	0.000785
5	279	0.034675	0.008570	0.001220
6	314	0.039025	0.012343	0.001564
7	377	0.046854	0.023907	0.002530
8	431	0.053566	0.045082	0.004184
9	530	0.065870	0.468884	0.037945
10	548	0.067858	1.874874	2.592340

Table 3.19 Results for FRP composite channel beam (6×1 5/8×0.25 in.) Test No. CFT4-7 with four-point loading (L = 84 in.; centroidal loading, e = -0.5675 in.)

Obs. No.	Load P (lbs)	Midspan Deflection			ϵ_x (in./in.)
		v_x (in.)	v_z (in.)	ϕ_x (in.)	
0	0	0	0	0	0
1	27	0.014253	0.000139	0.000480	0.000029
2	62	0.032730	0.000890	0.001338	0.000067
3	88	0.046567	0.002162	0.002299	0.000095
4	115	0.607105	0.004797	0.003922	0.000124
5	142	0.749642	0.010791	0.007180	0.000153
6	169	0.089218	0.031173	0.017515	0.000182
7	187	0.098720	0.142312	0.072509	0.000200
8	193	0.010188	0.677596	1.159608	0.003982

Table 3.20 Results for FRP composite channel beam (6×1 5/8×0.25 in.) Test
 No. CFT4-8 with four-point loading
 (L = 84 in.; loading between centroid and shear center $e = -0.2656$)

Obs. No.	Load P (lbs.)	Midspan Deflection			ϵ (in./in.)
		v_z (in.)	v_y (in.)	ϕ_z (in.)	
0	0	0	0	0	0
1	35	0.018477	0.000111	0.000296	0.000032
2	72	0.038010	0.000568	0.000735	0.000067
3	104	0.054903	0.001474	0.001327	0.000097
4	136	0.071796	0.003446	0.002384	0.000127
5	177	0.093441	0.012198	0.006527	0.000150
6	211	0.111390	3.157672	1.425375	0.002638

Table 3.21 Results for FRP composite channel beam ($6 \times 1 \frac{5}{8} \times 0.25$ in.) Test
 No. CFT4-9 with four-point loading
 (L = 84 in.; loading to right side of the shear center from wall, $e = 0.4531$ in.)

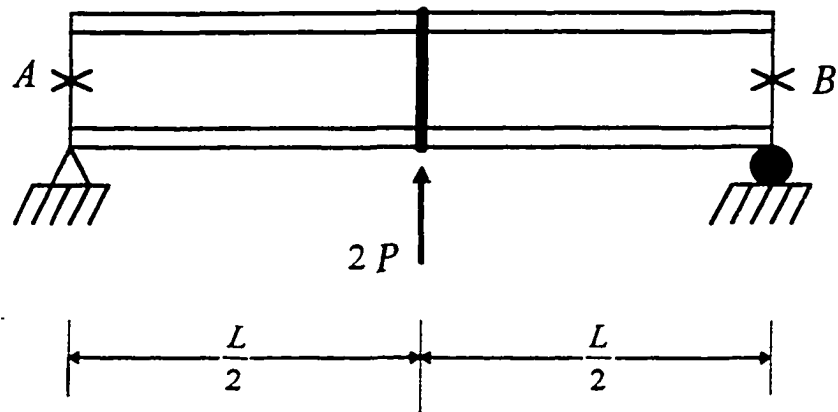
Obs. No.	Load P (lbs.)	Midspan Deflection			ϵ_s (in./in.)
		v_s (in.)	z_s (in.)	ϕ_s (in.)	
0	0	0	0	0	0
1	32	0.016893	-0.000158	0.000459	0.000033
2	64	0.033786	-0.000746	0.001085	0.000066
3	104	0.054903	-0.002616	0.002357	0.000107
4	131	0.069157	-0.005497	0.003950	0.000135
5	158	0.083410	-0.012294	0.007357	0.000164
6	182	0.096080	-0.033309	0.017376	0.000190
7	203	0.107167	-1.128954	-0.52998	0.002833

Table 4.1 Summary of Comparison of Peak loads from Flexural-Torsional
Experiment Theory

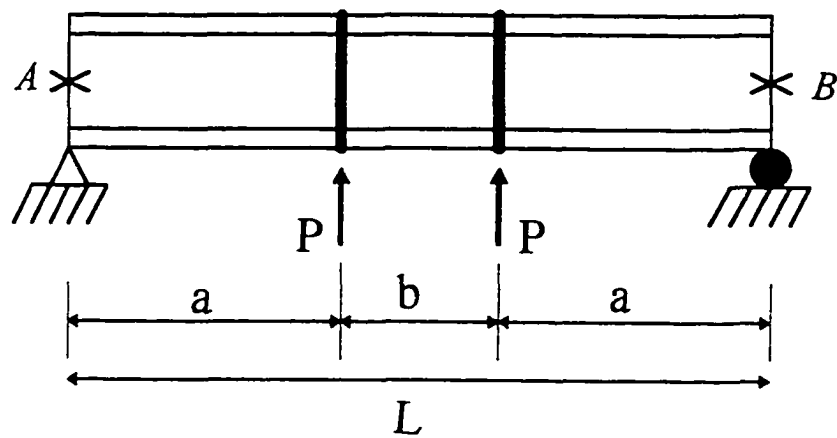
Serial No.	Test No.	Length (in.)	e	$P_{\text{exp.}}$ (lbs.)	$P_{\text{theor.}}$ (lbs.)	$P_{\text{theor.}}/P_{\text{exp.}}$
1	IFT3-1	108	-0.002	99	124	1.25
2	IFT3-2	96	-0.002	147	140	0.95
3	IFT3-3	84	-0.002	174	170	0.97
4	IFT3-4	72	+0.002	265	260	0.98
5	IFT4-1	108	-0.0002	78	78	1.00
6	IFT4-2	96	-0.00007	114	91	0.80
7	IFT4-3	84	-0.0005	125	123	0.98
8	IFT4-4	72	-0.0005	190	161	0.85
9	IFT4-5	60	-0.0005	292	226	0.77
10	CFT3-1	108	+0.0003	260	244	0.93
11	CFT3-2	96	+0.0003	345	310	0.89
12	CFT4-1	108	-0.0003	136	117	0.86
13	CFT4-2	102	-0.0005	160	130	0.80
14	CFT4-3	96	-0.0001	198	148	0.75
15	CFT4-4	84	-0.00009	300	233	0.78
16	CFT4-5	72	-0.0009	452	344	0.76
17	CFT4-6	60	-0.0003	701	548	0.78
18	CFT4-7	84	-0.5675	203	193	0.95
19	CFT4-8	84	-0.2656	243	211	0.87
20	CFT4-9	84	0.4531	233	203	0.87

Table 5.1 Effect of load height on FRP channel beam buckling load

y_o (in)	P_{cr} (lbs)			
	For $(+y_o)$			For $(-y_o)$
	$L = 108\text{in}$ $a = 42\text{in}$	$L = 84\text{in}$ $a = 30\text{in}$	$L = 60\text{in}$ $a = 18\text{in}$	$L = 84\text{in}$ $a = 30\text{in}$
0.0	304.87	683.84	2212.11	638.42
0.5	272.32	586.17	1791.88	797.79
1.50	218.46	436.49	1213.95	1071.37
2.50	177.19	335.54	878.04	1393.67
3.50	147.43	267.41	675.12	1748.78
4.50	124.65	220.09	544.01	2124.72
5.50	107.29	186.02	453.81	2513.89
6.50	93.81	160.60	388.50	2911.72
10.50	61.53	102.85	245.11	4546.96
100.00	6.53	11.05	26.05	42335.90
1000.00	0.67	1.11	2.65	423250.00
10^{10}	0.00	0.00	0.00	423249×10^9



(a)



(b)

Figure 1. (a) Schematic view of FRP composite beam with three-point loading
 (b) Schematic view of FRP composite beam with four-point loading

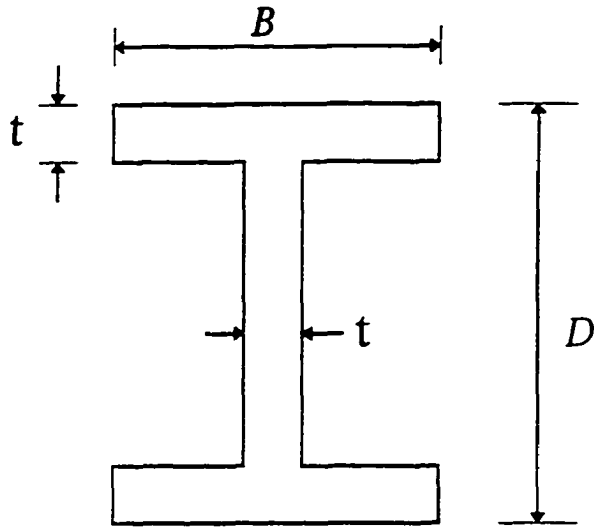


Figure 2. Cross-sectional dimensions of FRP composite I-section

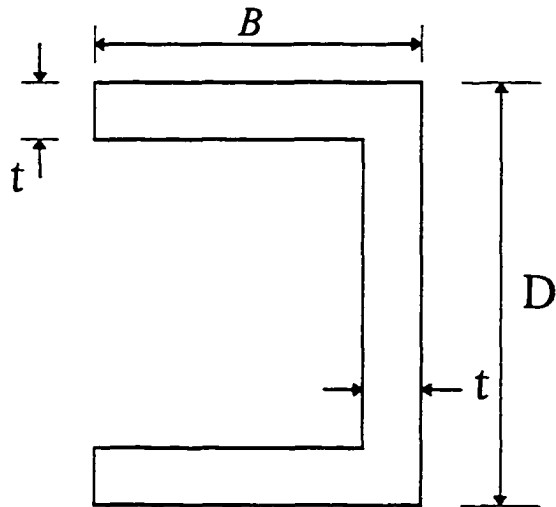


Figure 3. Cross-sectional dimensions of FRP channel section

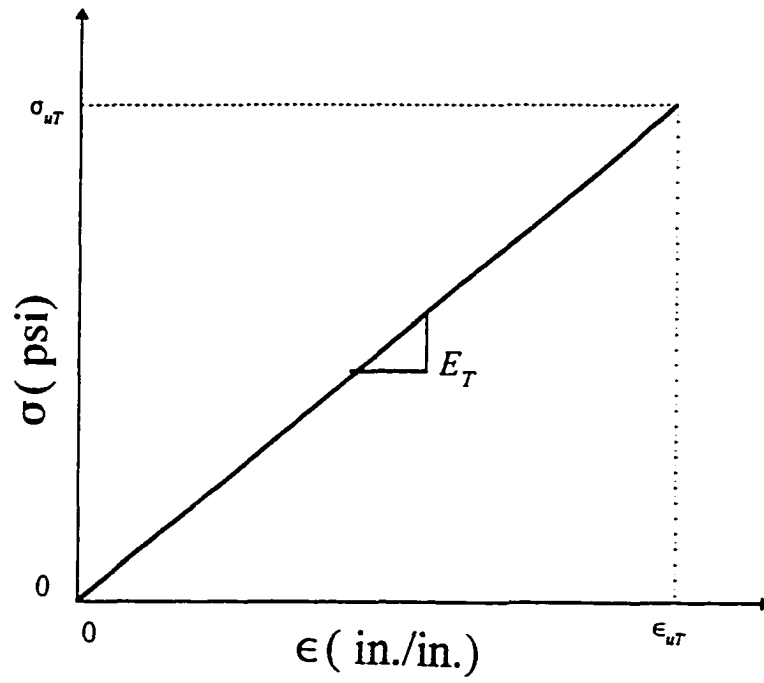


Figure 4. Tensile stress-strain relationship

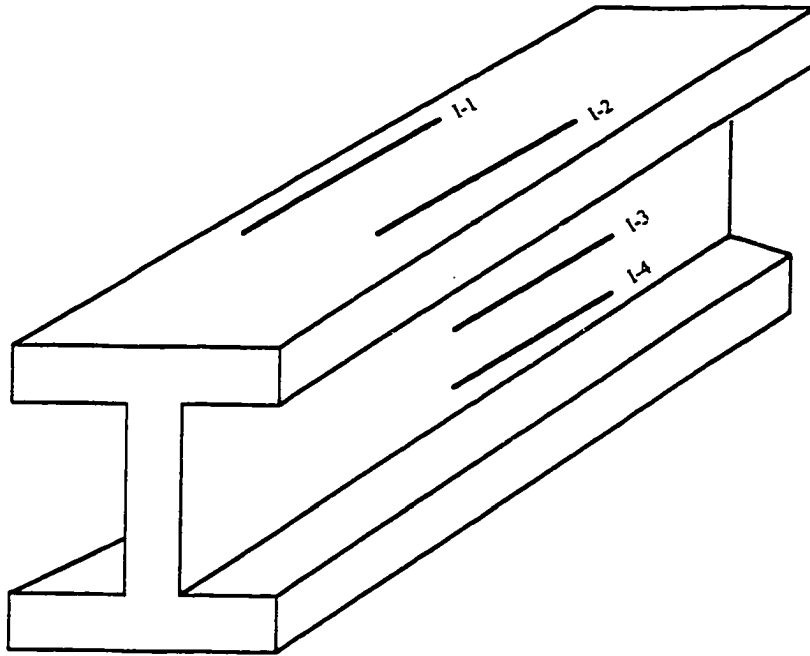


Figure 5. Location and numbers of test specimens for I-section

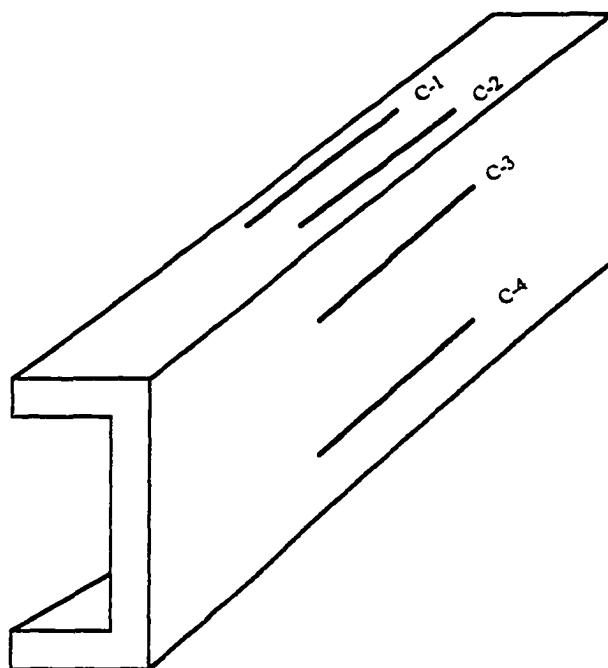


Figure 6. Location and numbers of test specimens for channel section

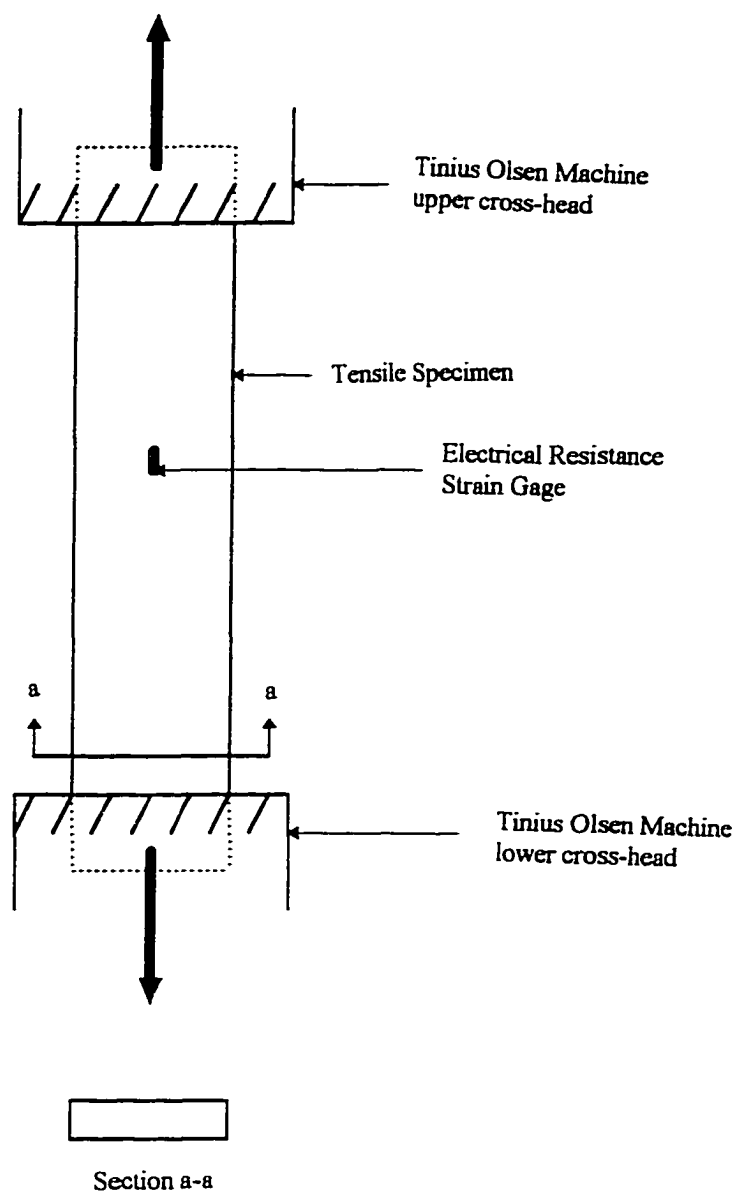


Figure 7. Schematic of FRP composite tension test set up

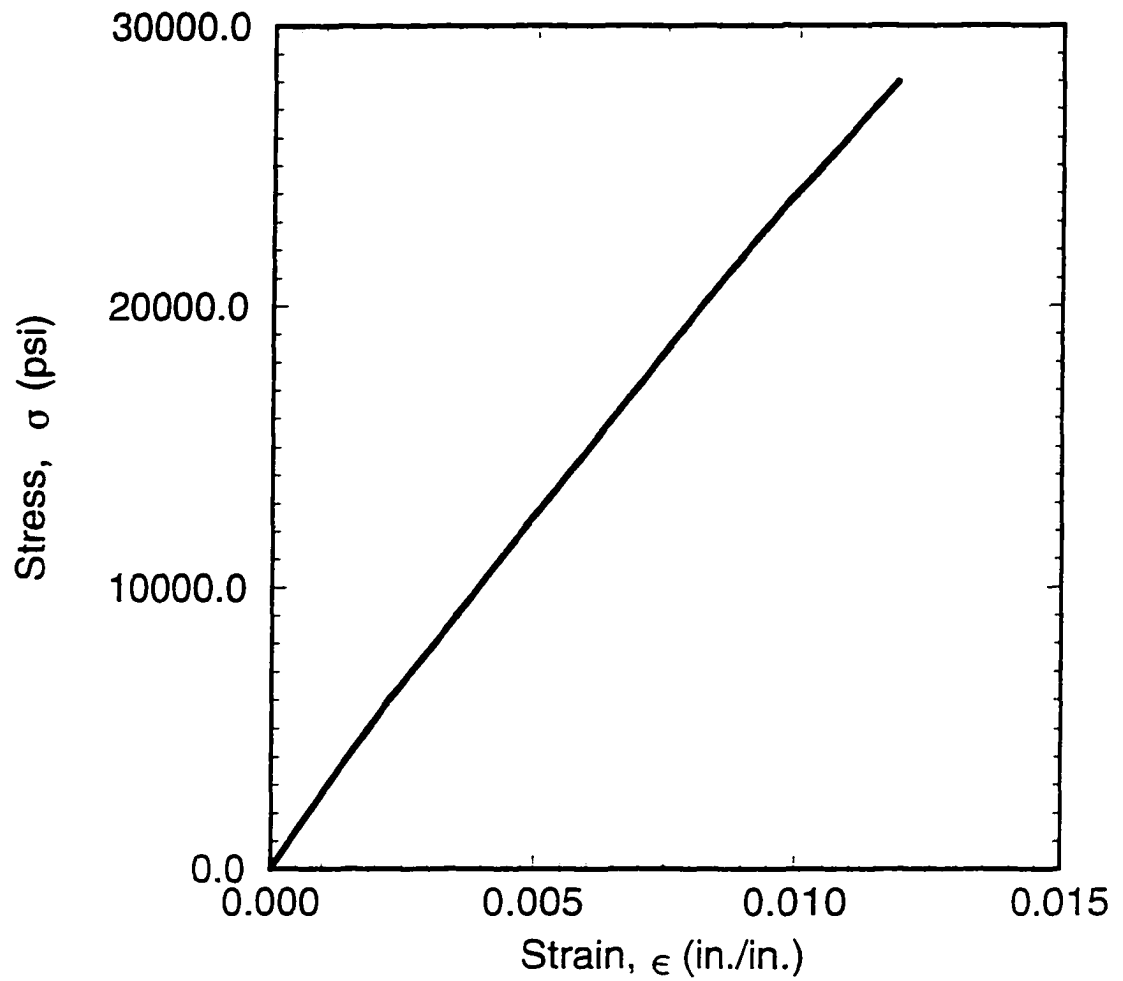


Figure 8. Normal stress-strain relationship based on tensile coupon test for specimen 1 from flange of I-section (see table 2.1)

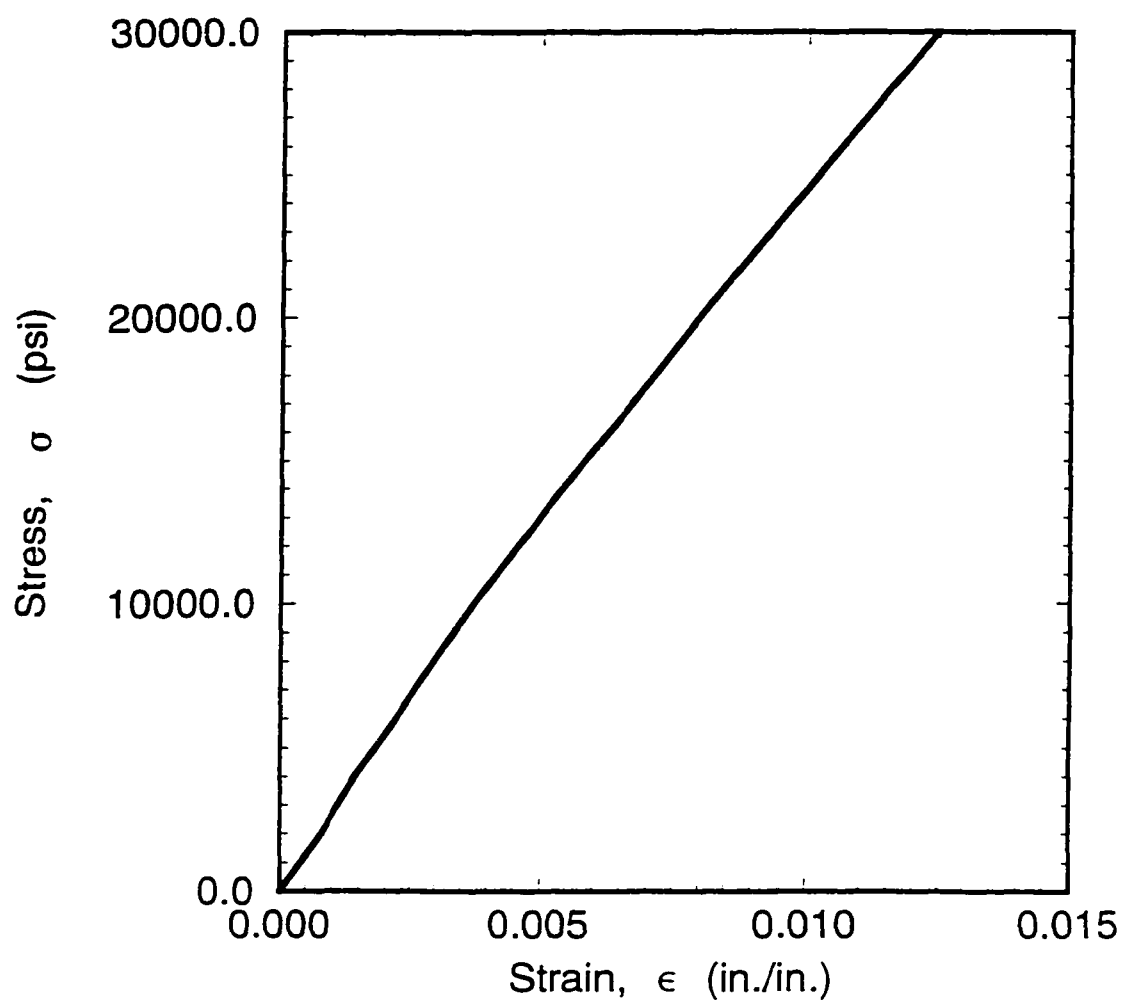


Figure 9. Normal stress-strain relationship based on tensile coupon test for specimen 2 from flange of I-section (see table 2.2)

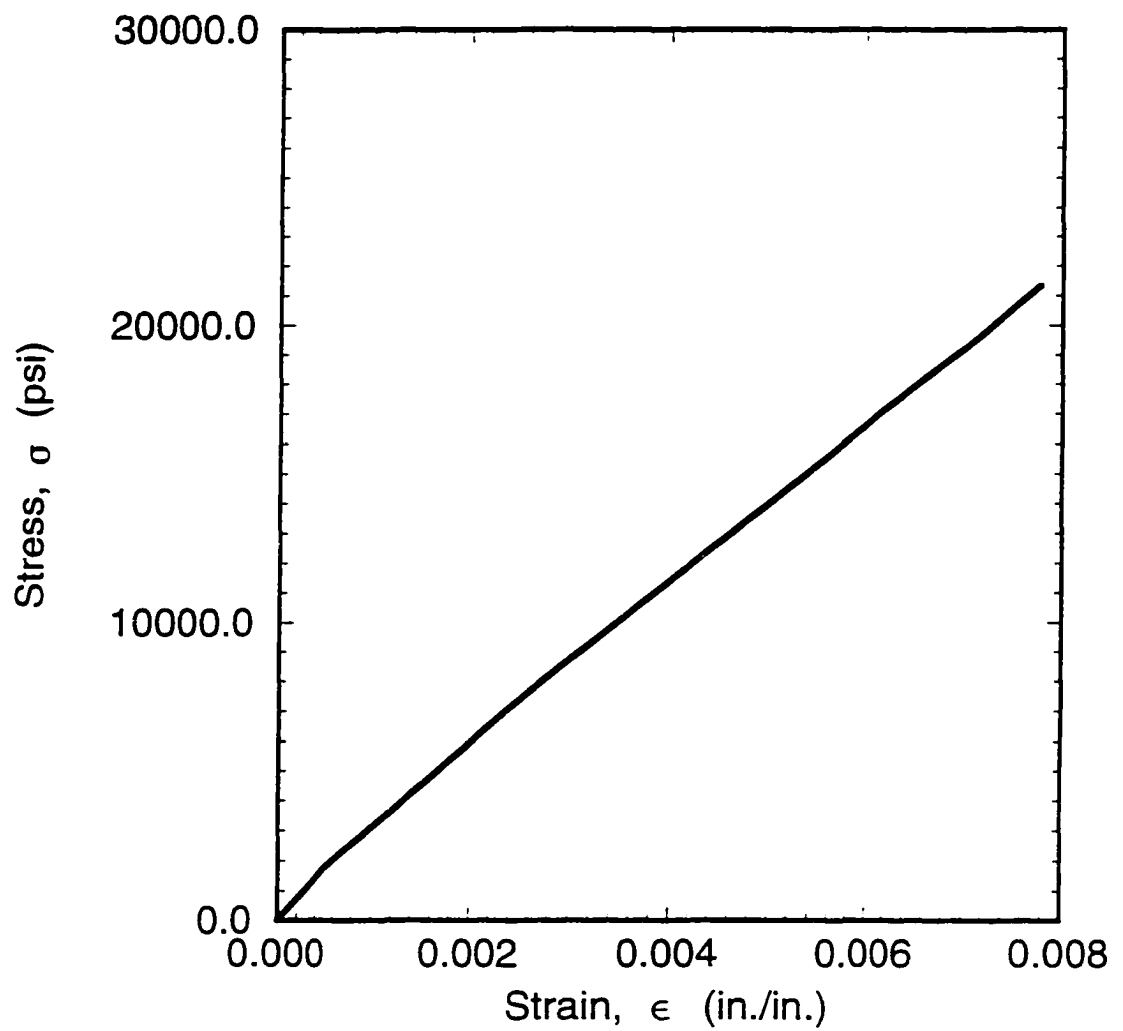


Figure 10. Normal stress-strain relationship based on tensile coupon test for specimen 3 from web of I-section (see table 2.3)

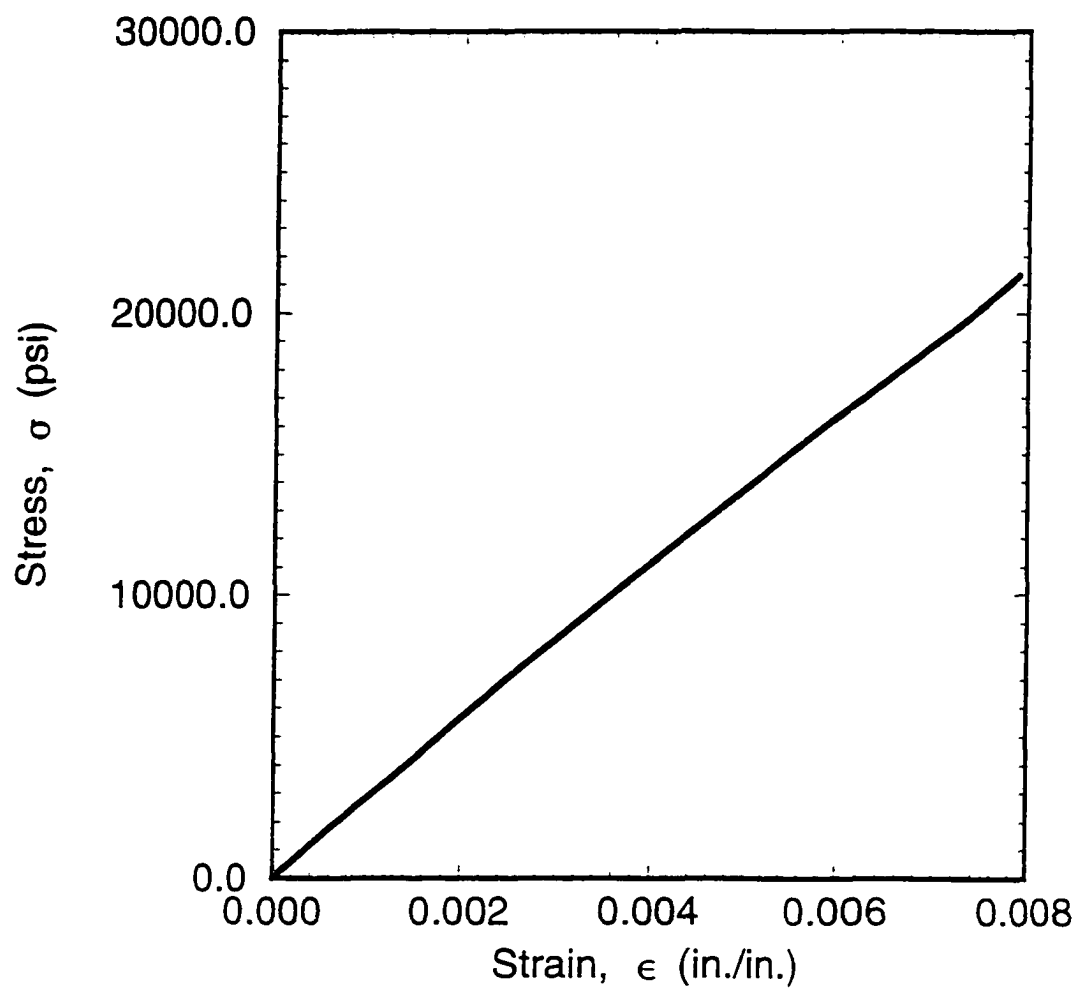


Figure 11. Normal stress-strain relationship based on tensile coupon test for specimen 4 from web of I-section (see table 2.4)

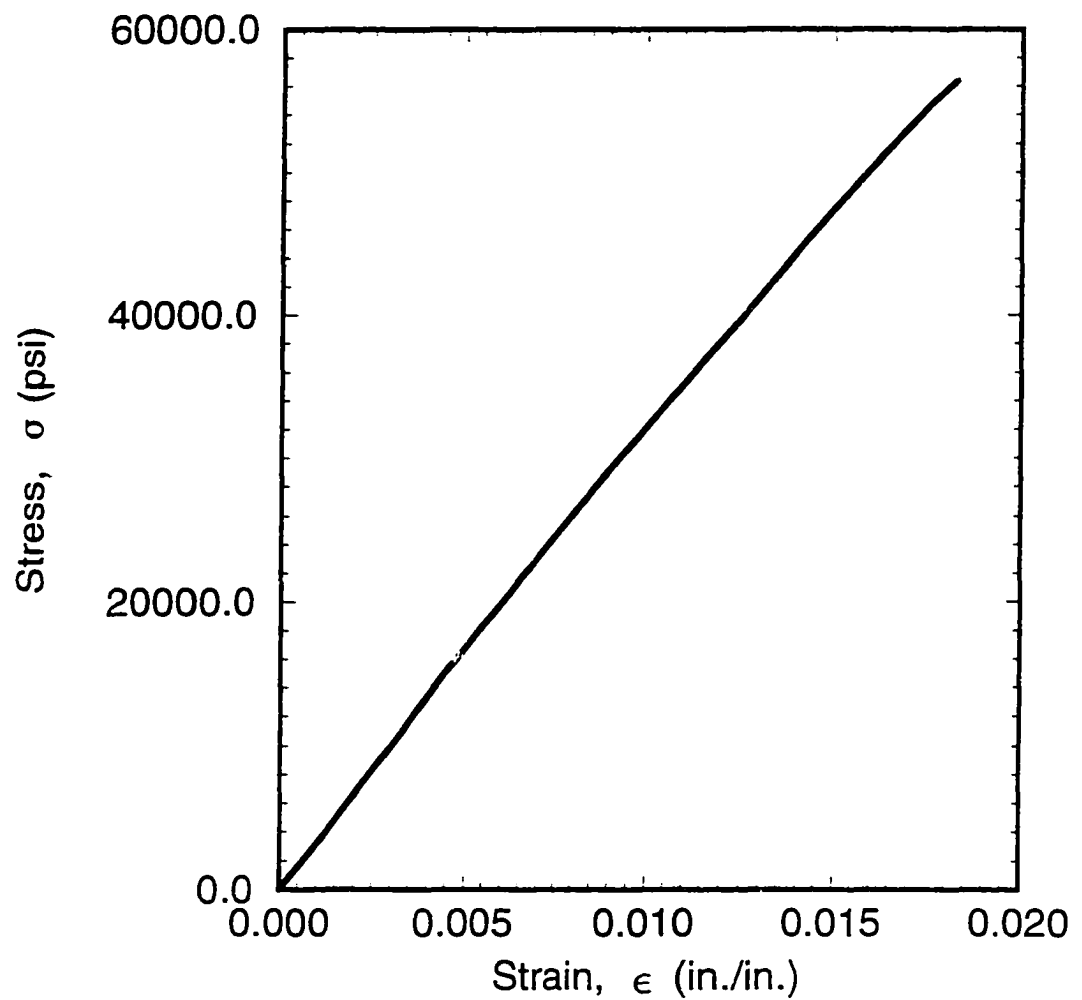


Figure 12. Normal stress-strain relationship based on tensile coupon test for specimen 5 from flange of channel section (see table 2.5)

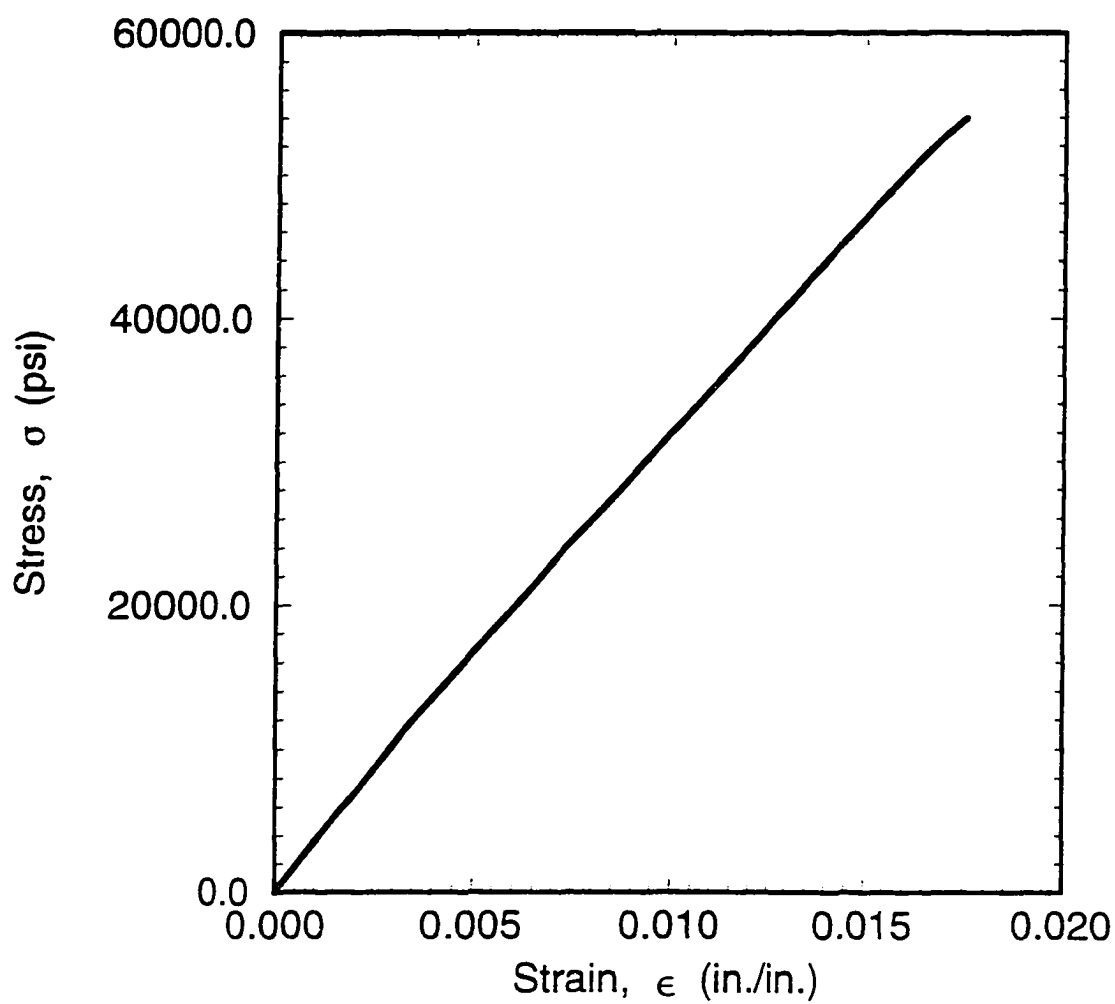


Figure 13. Normal stress-strain relationship based on tensile coupon test for specimen 6 from flange of channel section (see table 2.6)

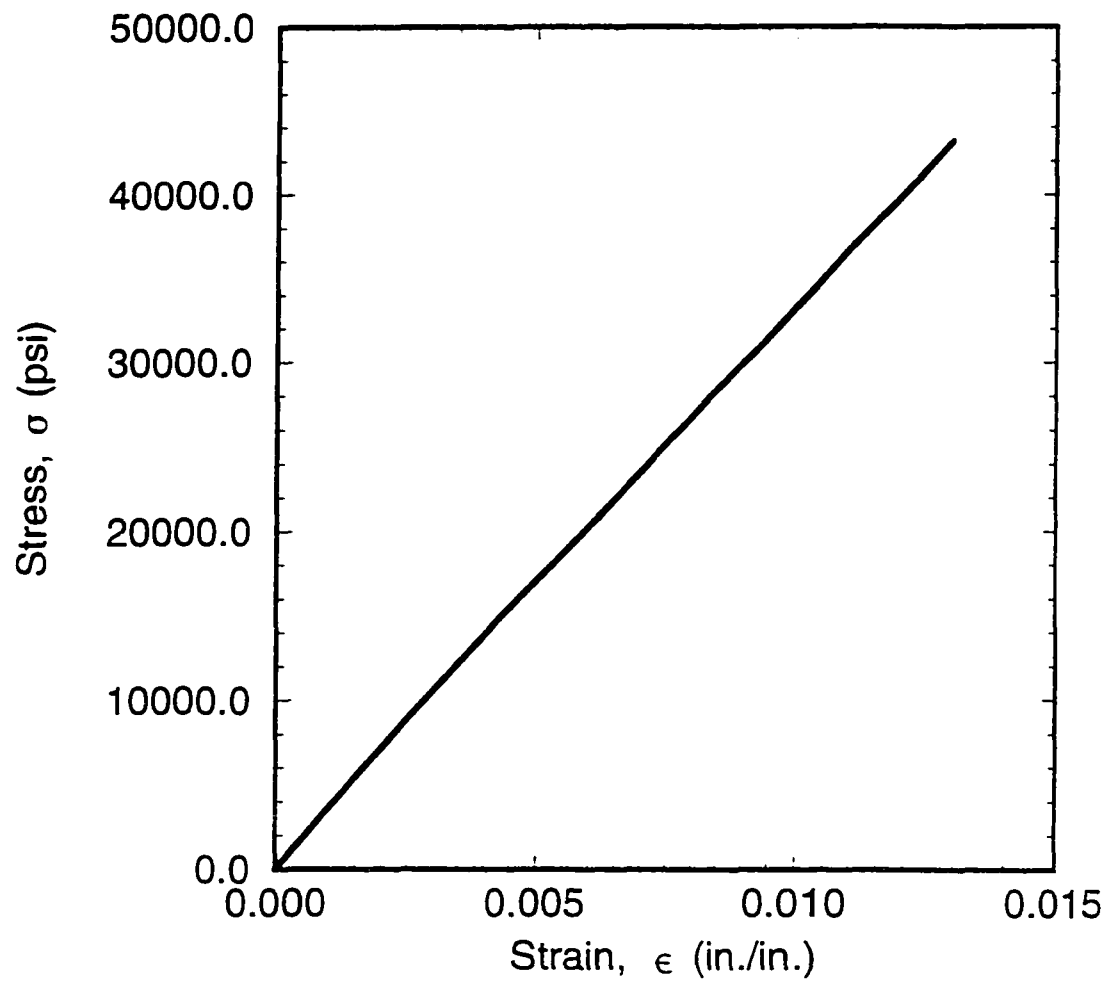


Figure 14. Normal stress-strain relationship based on tensile coupon test for specimen 7 from web of channel section (see table 2.7)

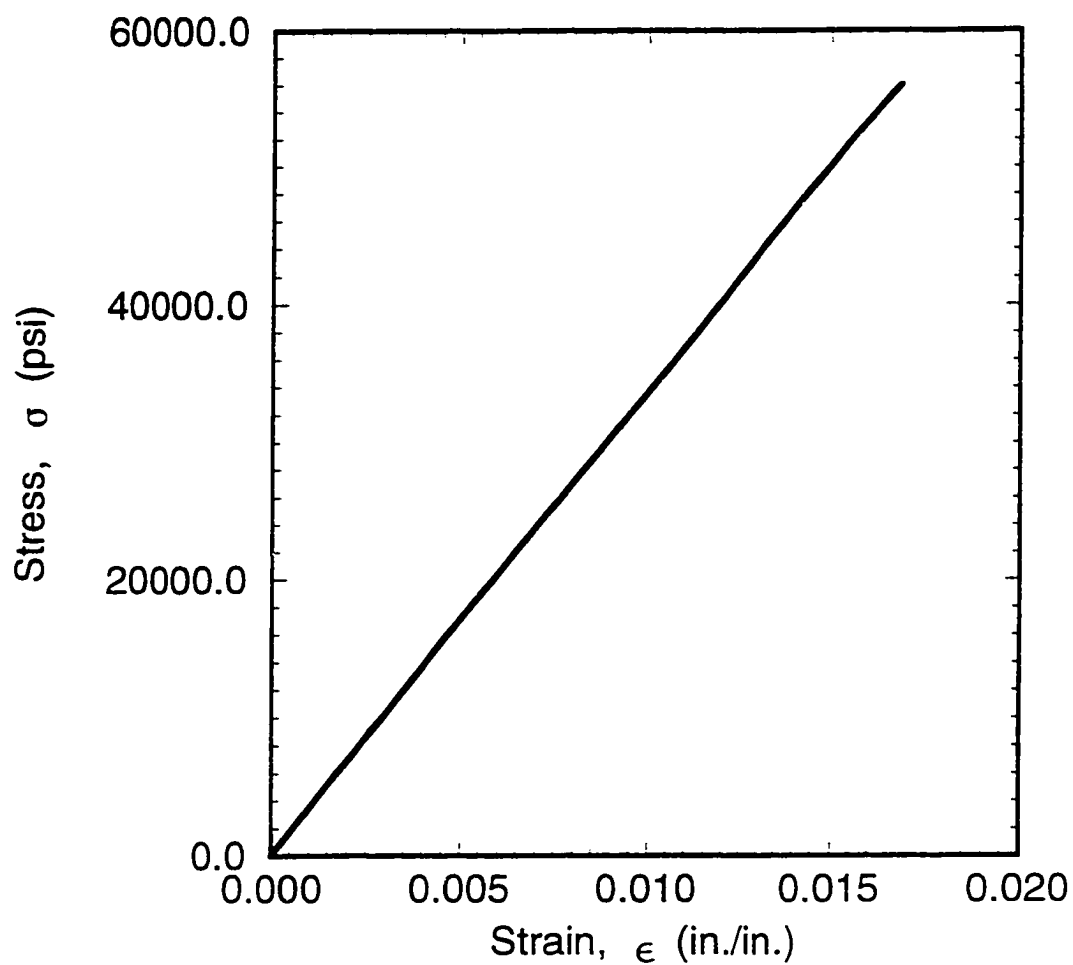


Figure 15. Normal stress-strain relationship based on tensile coupon test for specimen 5 from web of channel section (see table 2.8)

NOTE TO USERS

Page(s) missing in number only; text follows. Microfilmed as received.

UMI

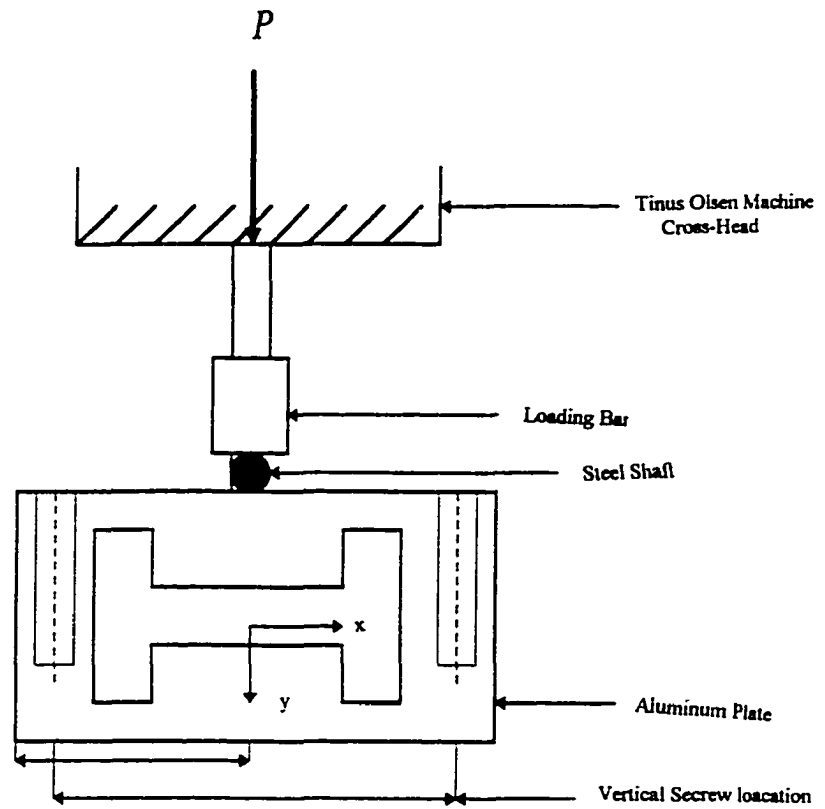


Figure 16. Cross-sectional schematic view at beam load application about minor axis



Figure 17. Apparatus for testing FRP beam



Figure 18. Loading setup with hydraulic jacks

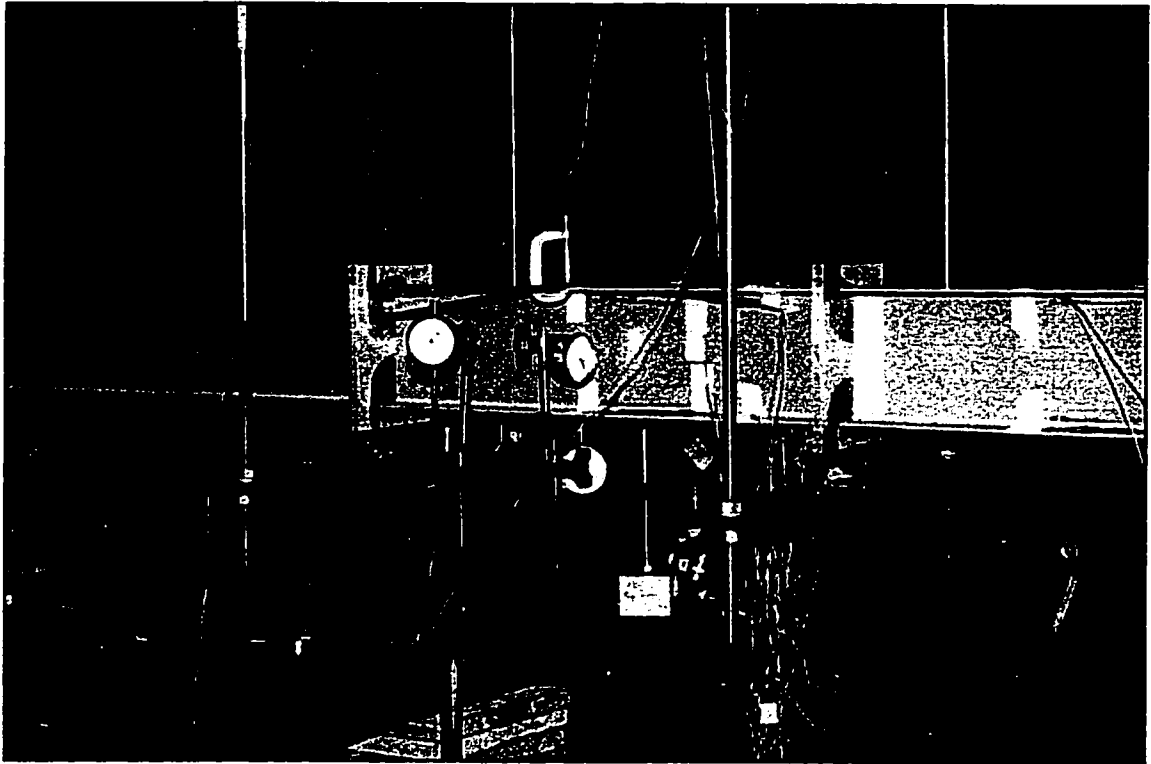


Figure 19. Tie rods connection of FRP beam

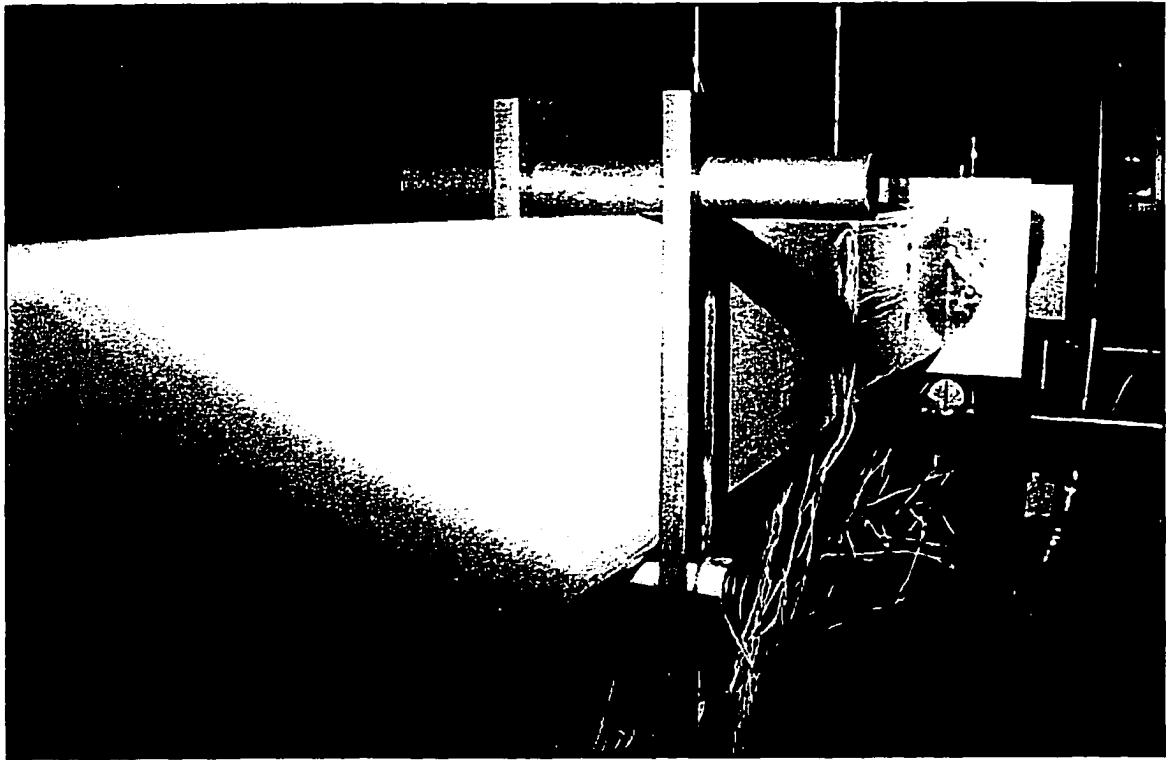


Figure 20. Laboratory simulations of simple supports

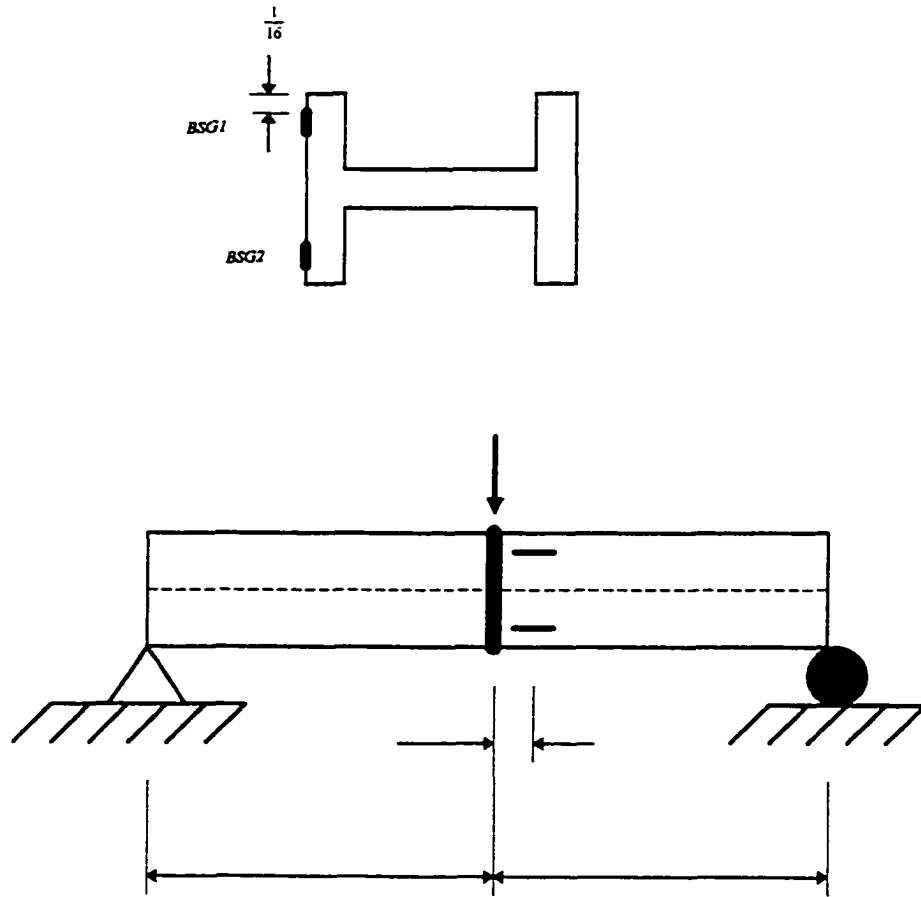


Figure 21. Load (P) at midspan about minor axis

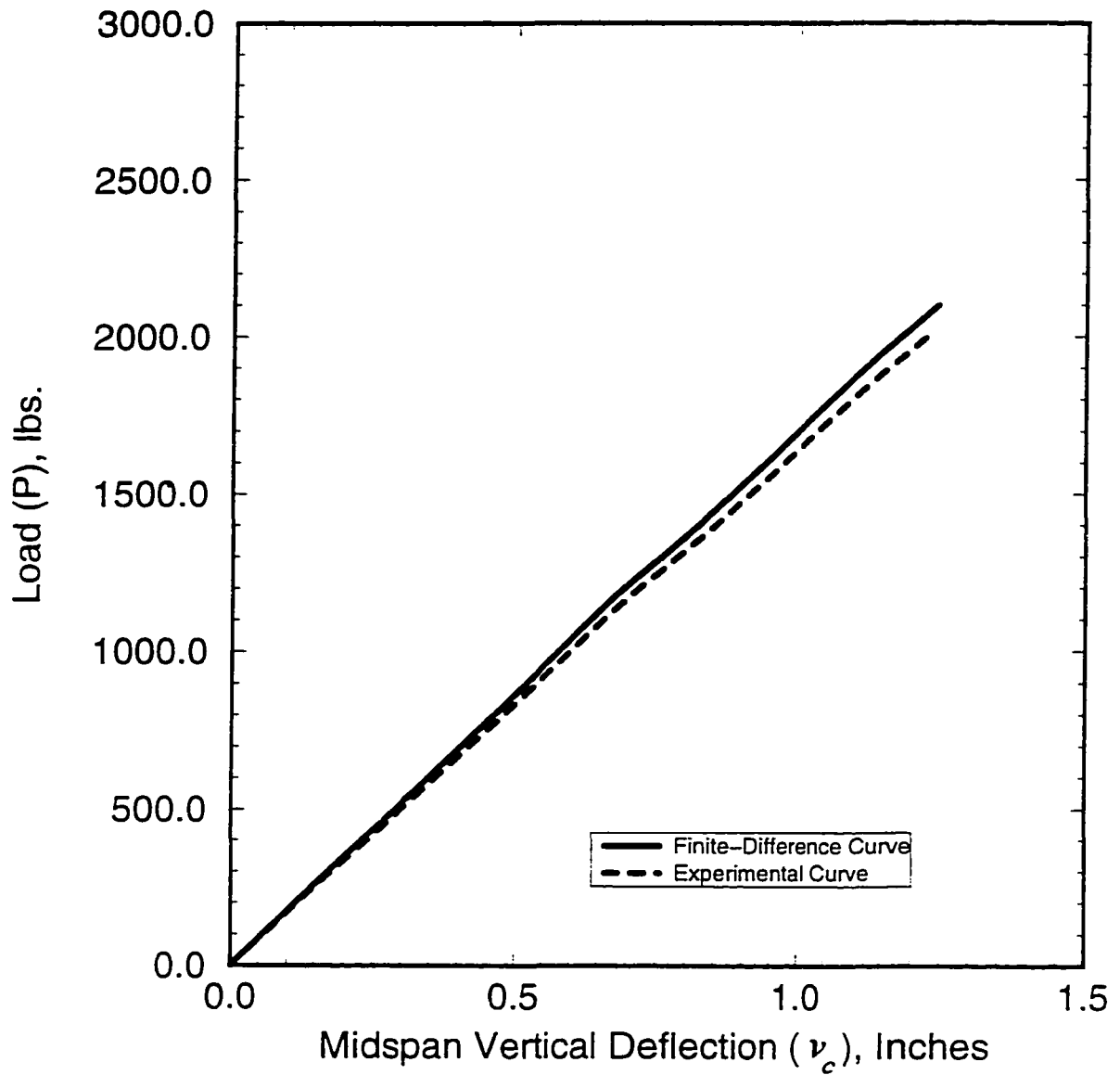


Figure 22. Load (P) versus midspan vertical deflection (v_c), about the minor axis bending

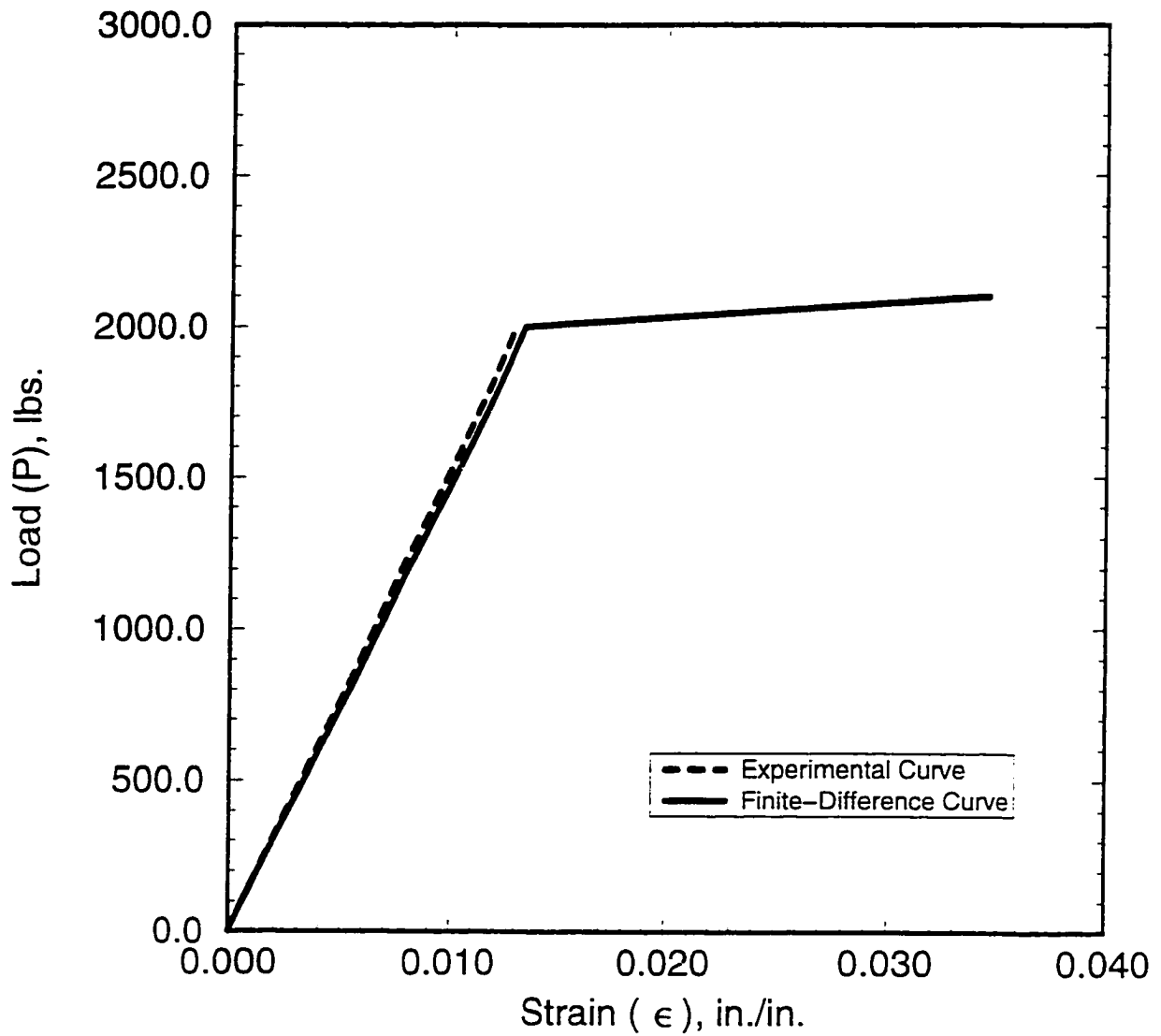


Figure 23. Load (P) versus midspan strain (ϵ_c), about the minor axis bending

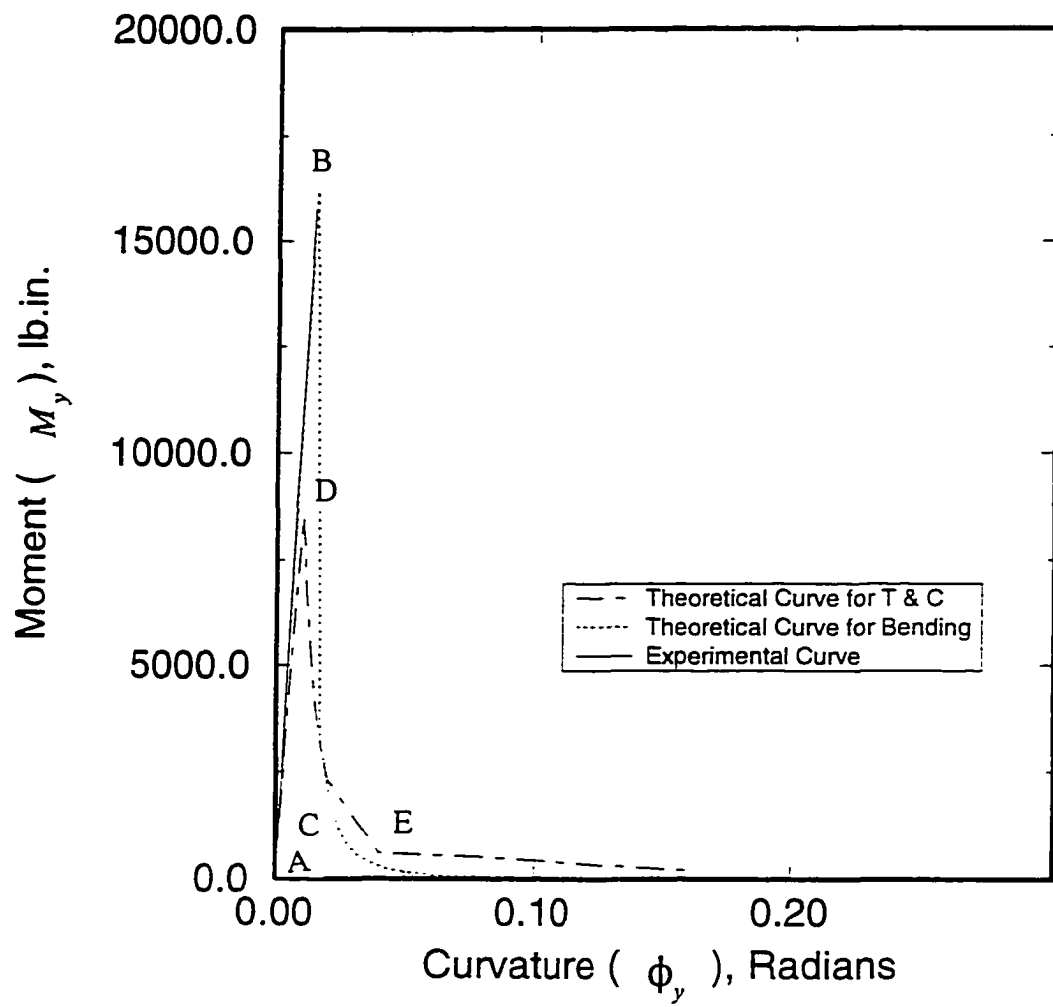


Figure 24. Moment (M_y) versus (ϕ_y) about minor axis bending

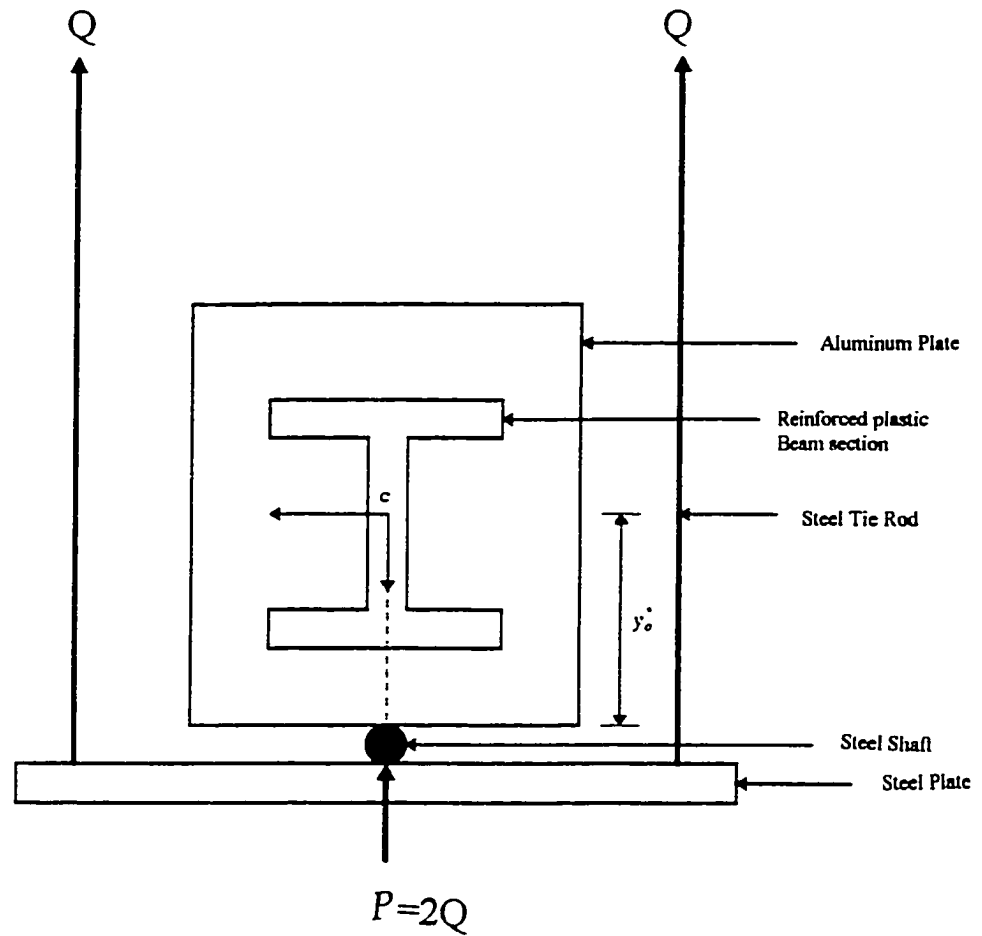


Figure 25. Cross-sectional schematic view at load application points for I-section beam

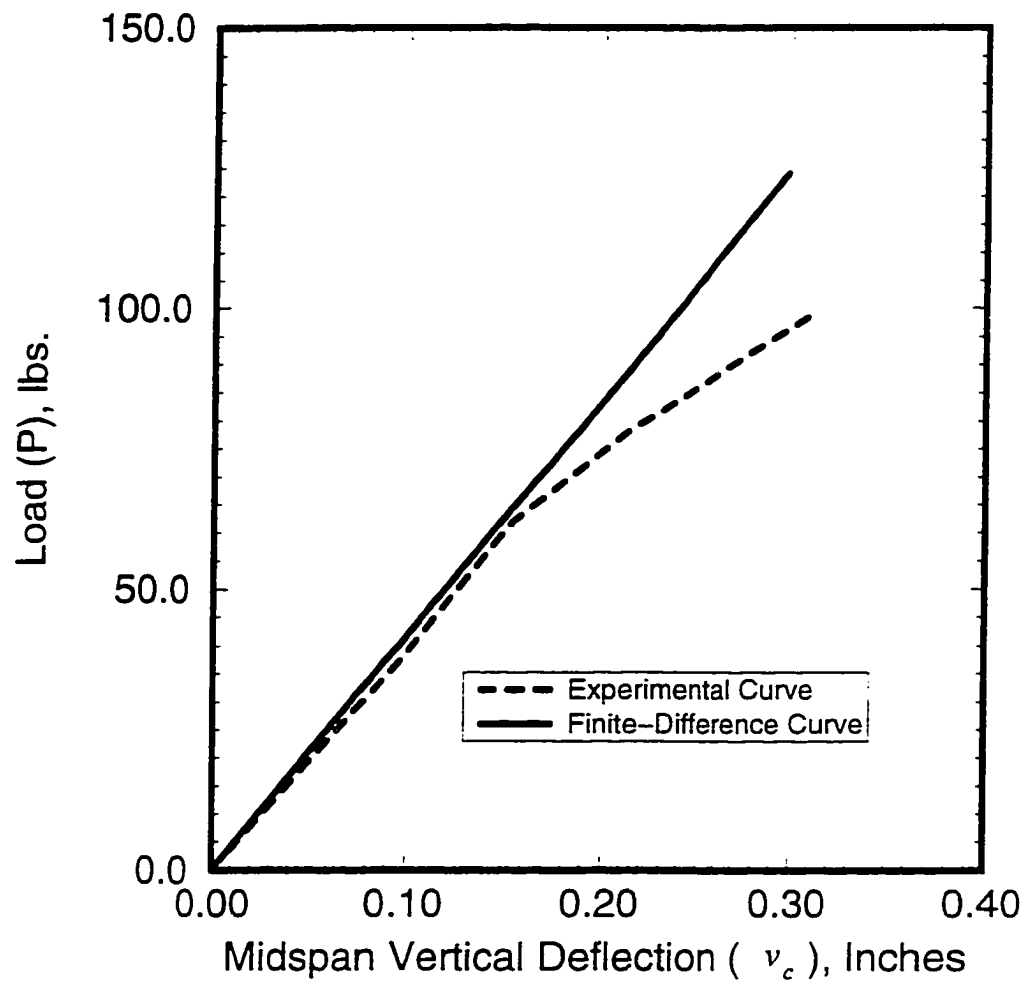


Figure 26. Load (P) versus midspan vertical deflection (v_c) for Test No. IFT3-1

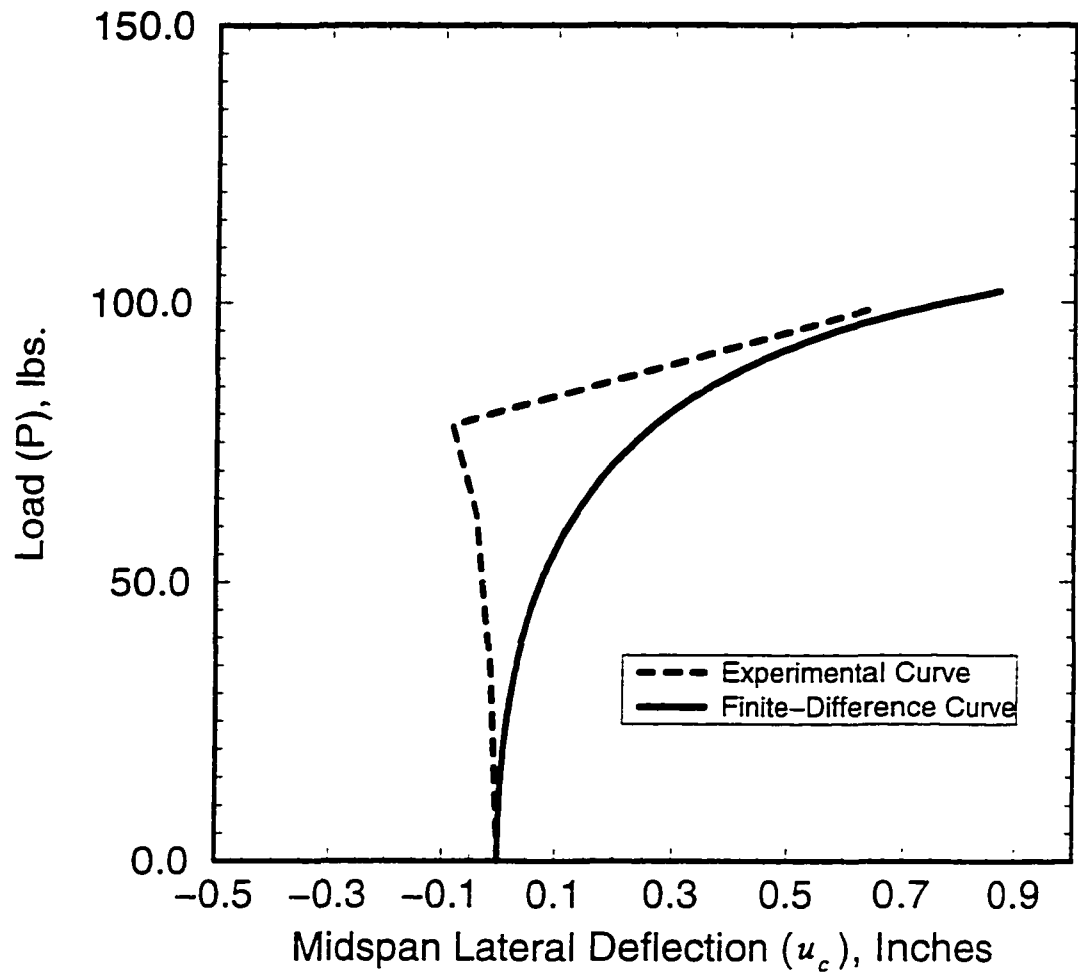


Figure 27. Load (P) versus midspan lateral deflection (u_c) for Test No. IFT3-1

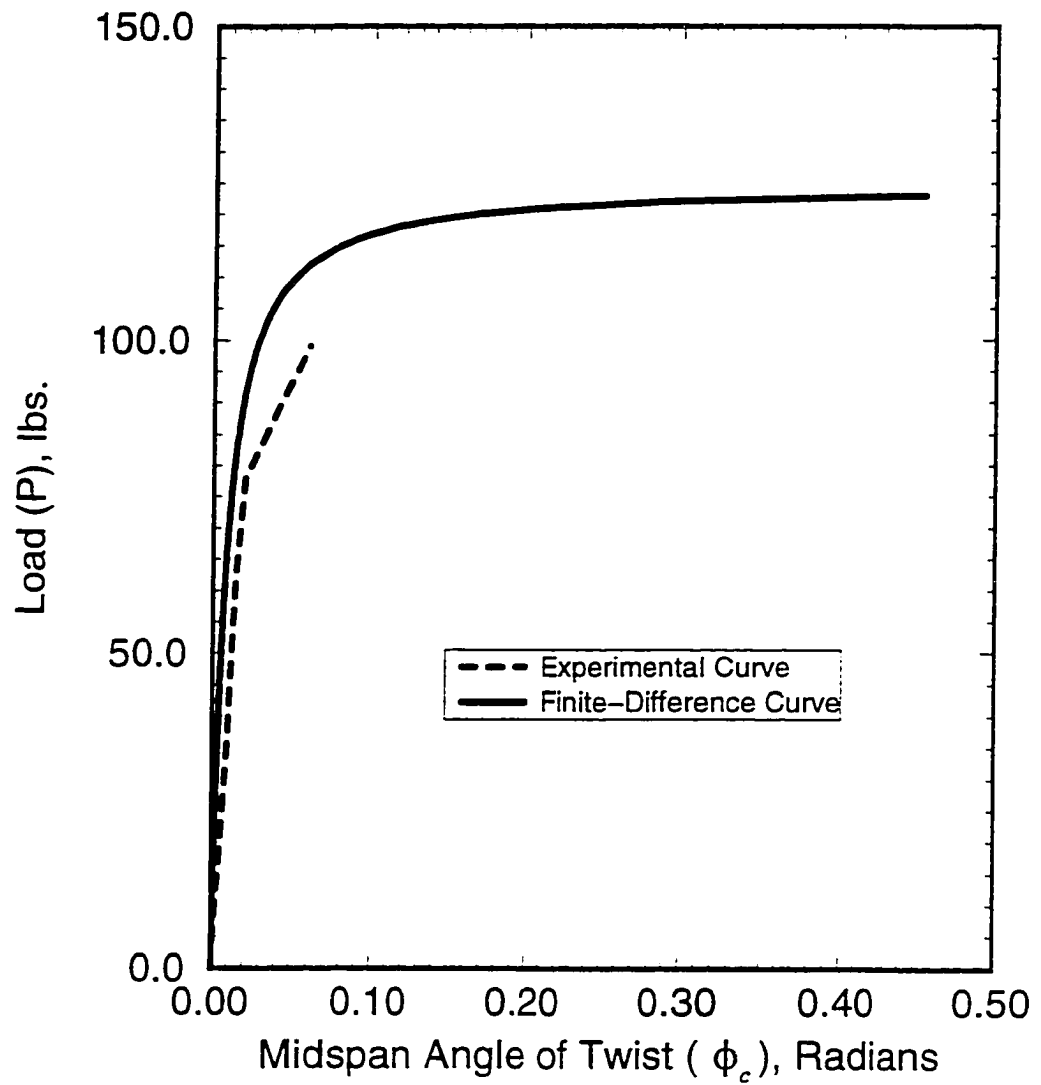


Figure 28. Load (P) versus midspan angle of twist (ϕ_c) for Test No. IFT3-1

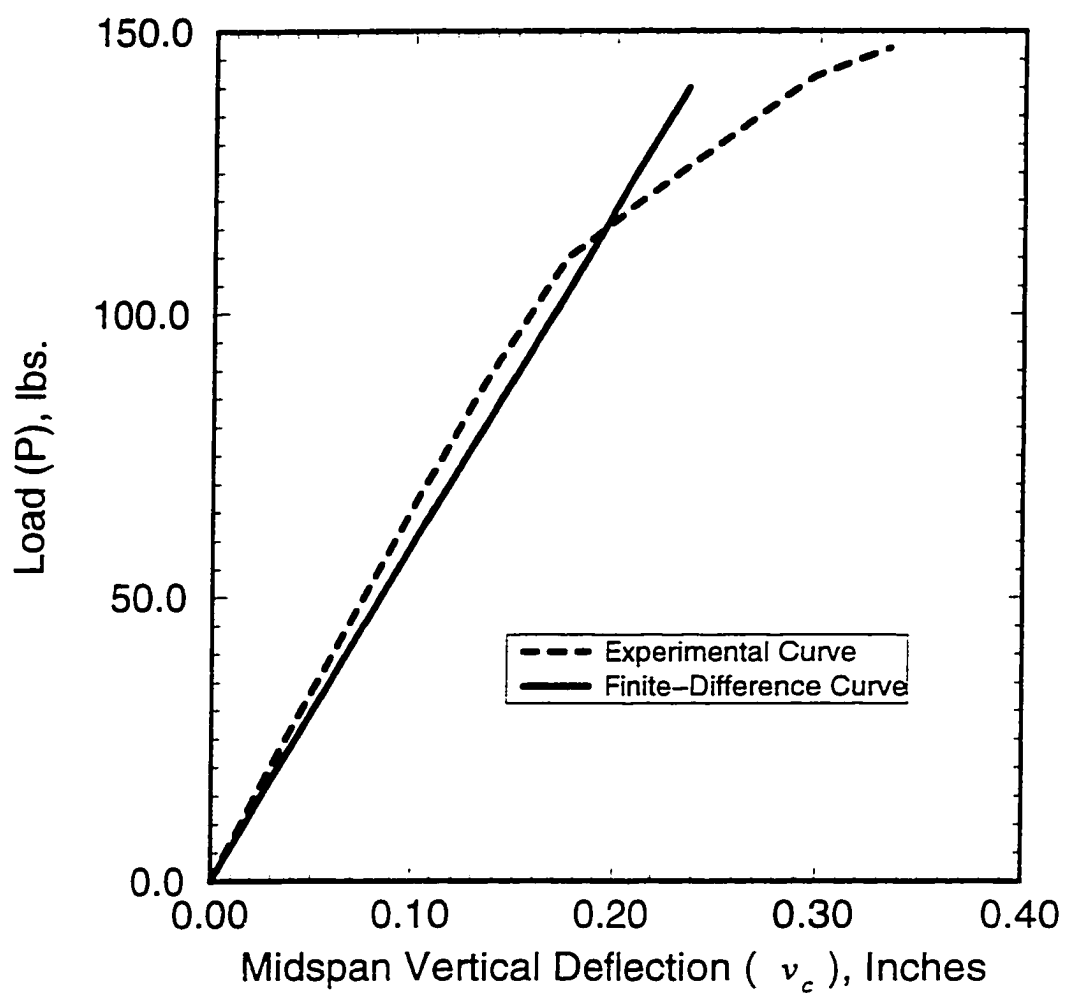


Figure 29. Load (P) versus midspan vertical deflection (v_c) for Test No. IFT3-2

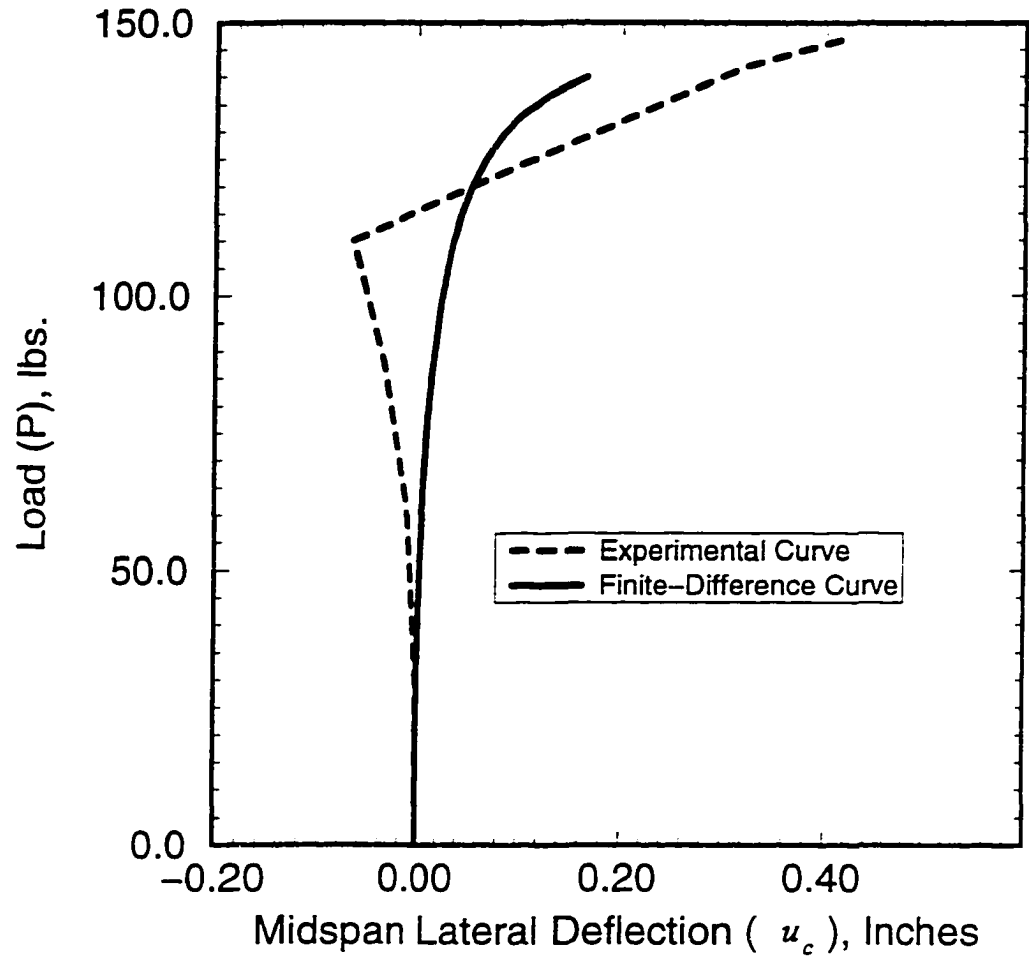


Figure 30. Load (P) versus midspan lateral deflection (u_c) for Test No. IFT3-2

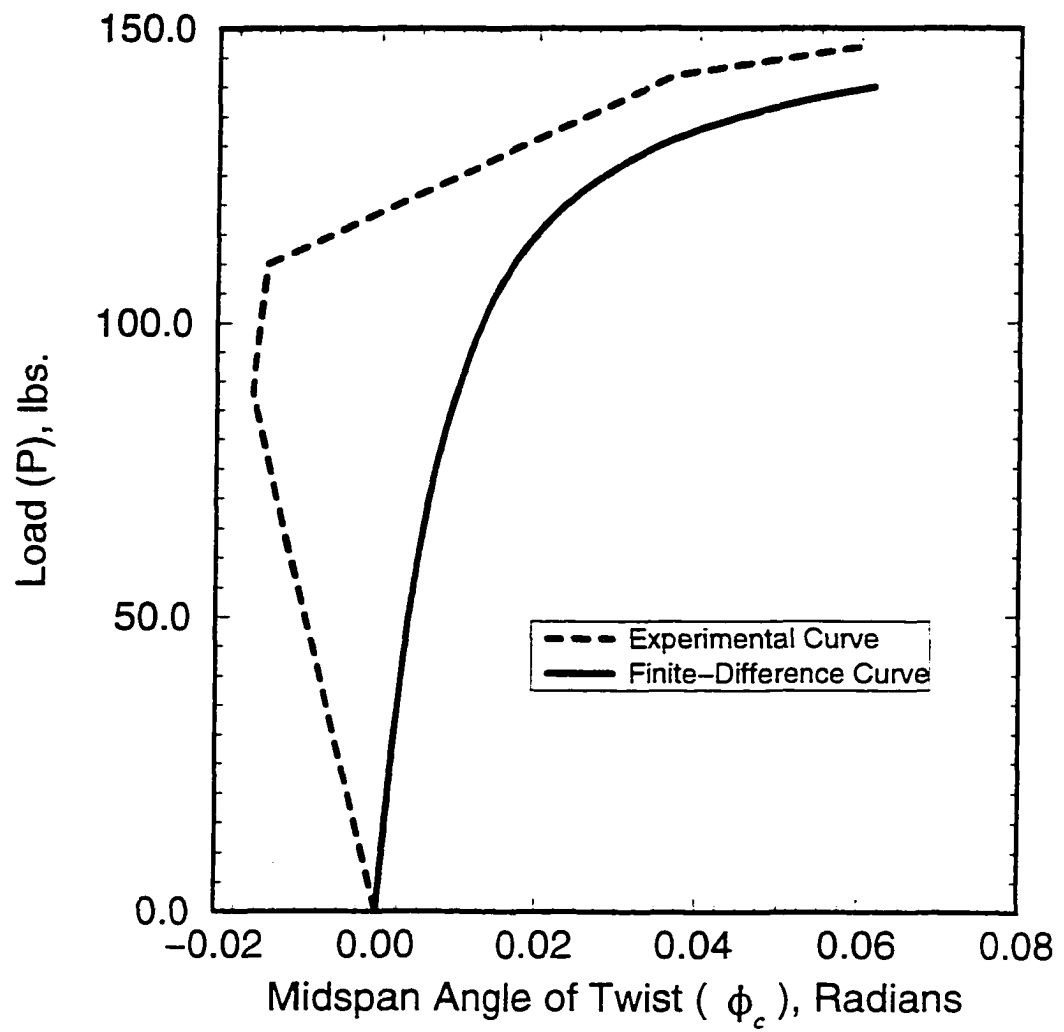


Figure 31. Load (P) versus midspan angle of twist (ϕ_c) for Test No. IFT3-2

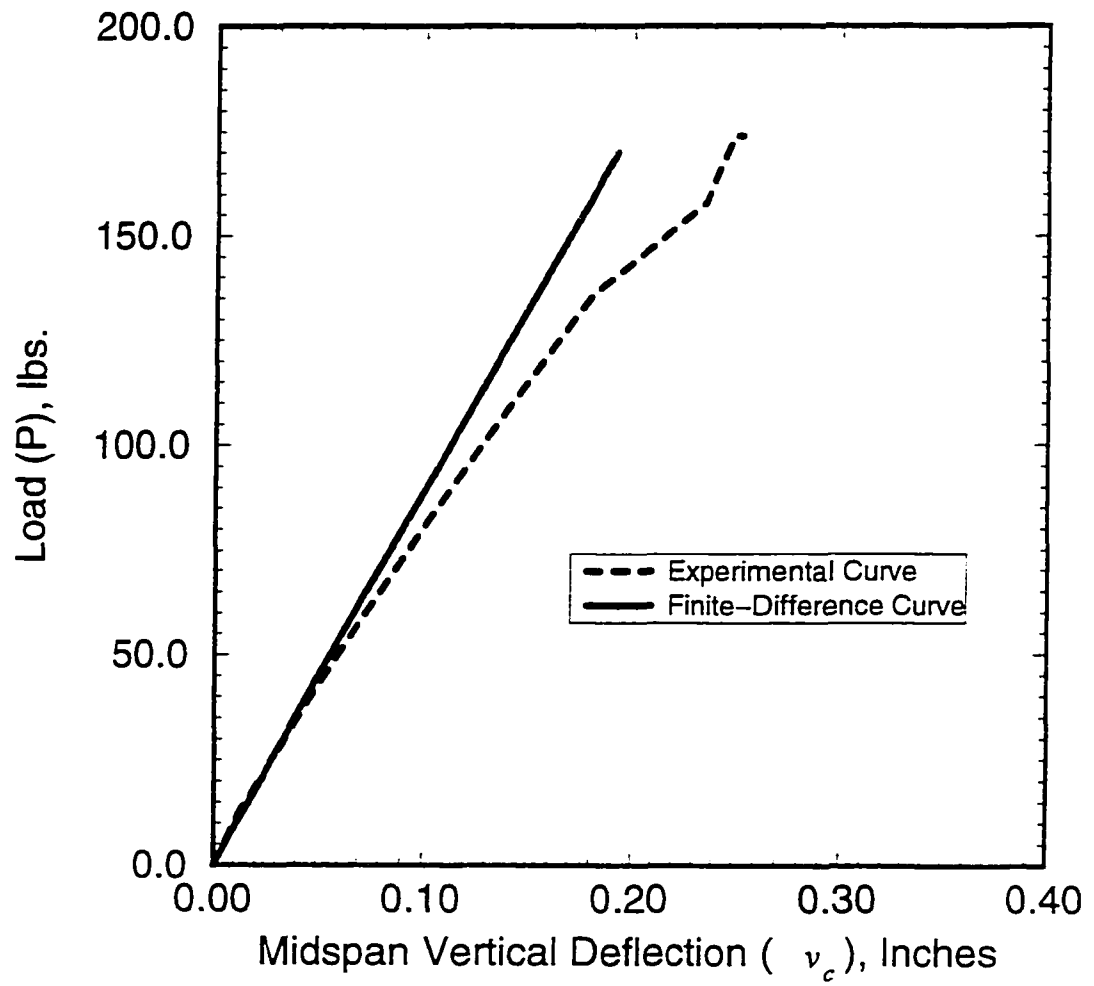


Figure 32. Load (P) versus midspan vertical deflection (v_c) for Test No. IFT3-3

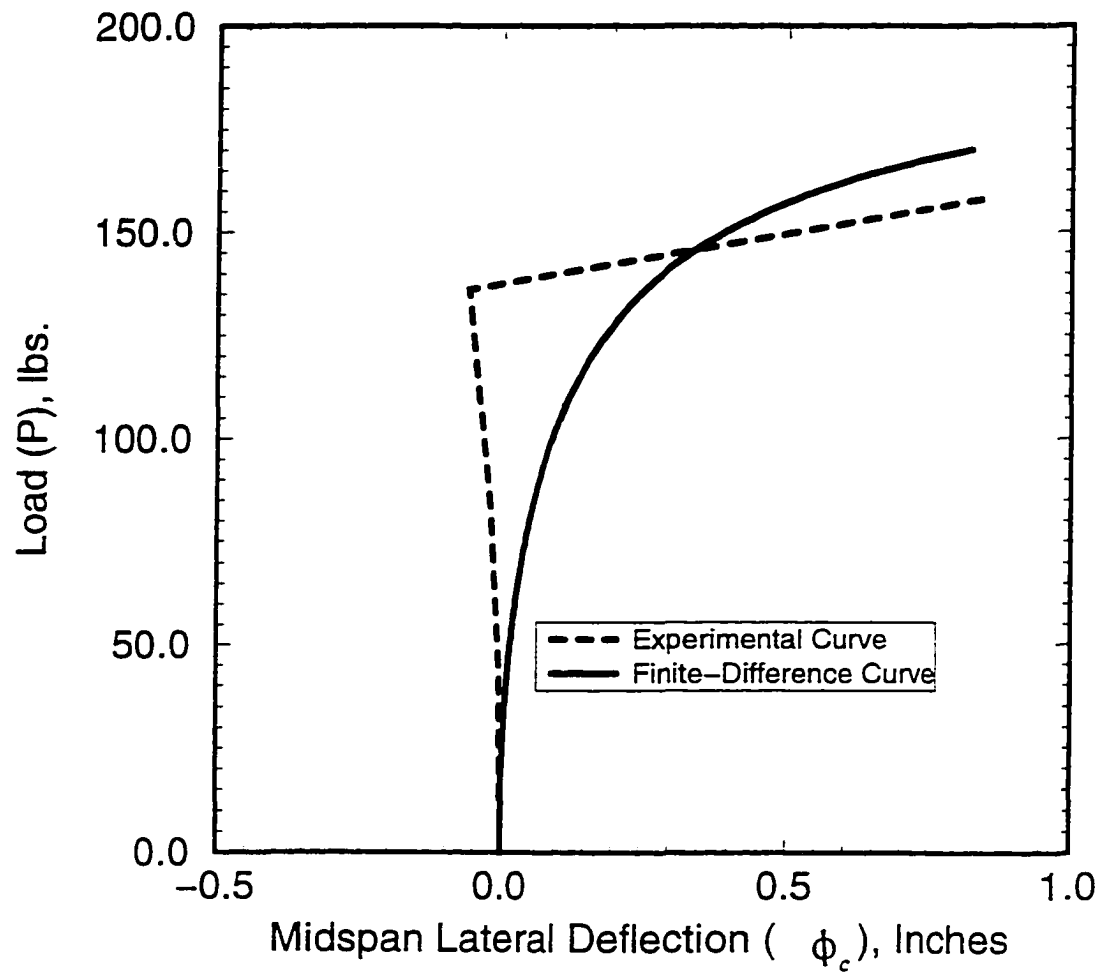


Figure 34. Load (P) versus midspan angle of twist (ϕ_c) for Test No. IFT3-3

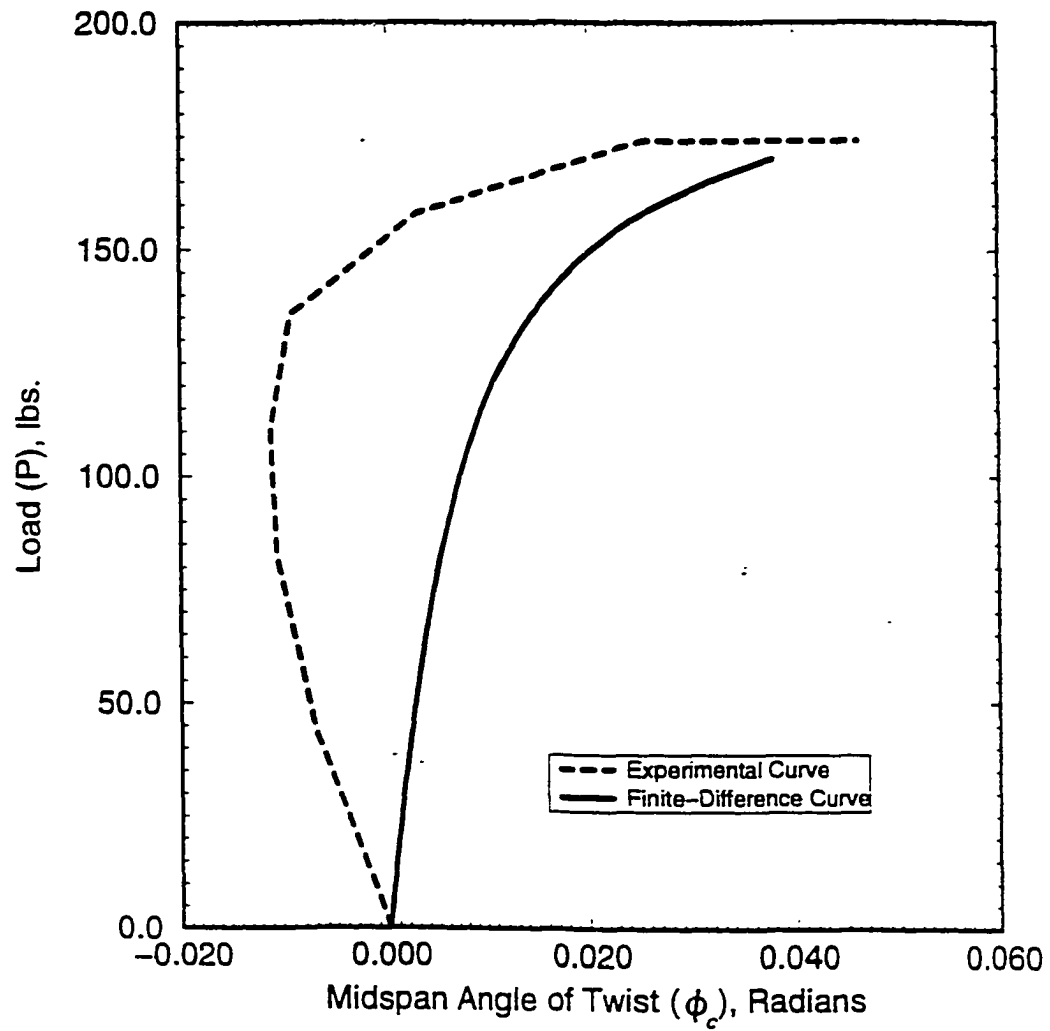


Figure 34. Load (P) versus midspan angle of twist (ϕ_c) for Test No. IFT3-3

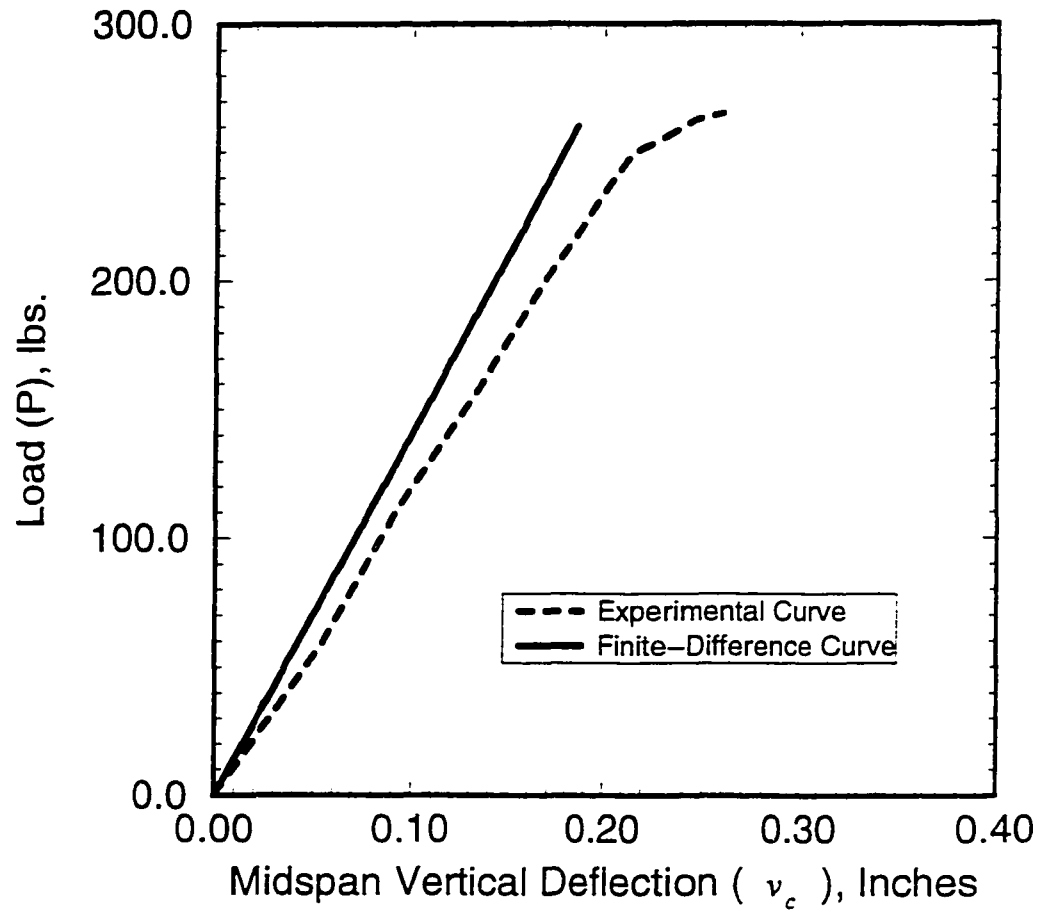


Figure 35. Load (P) versus midspan vertical deflection (v_c) for Test No. IFT3-4

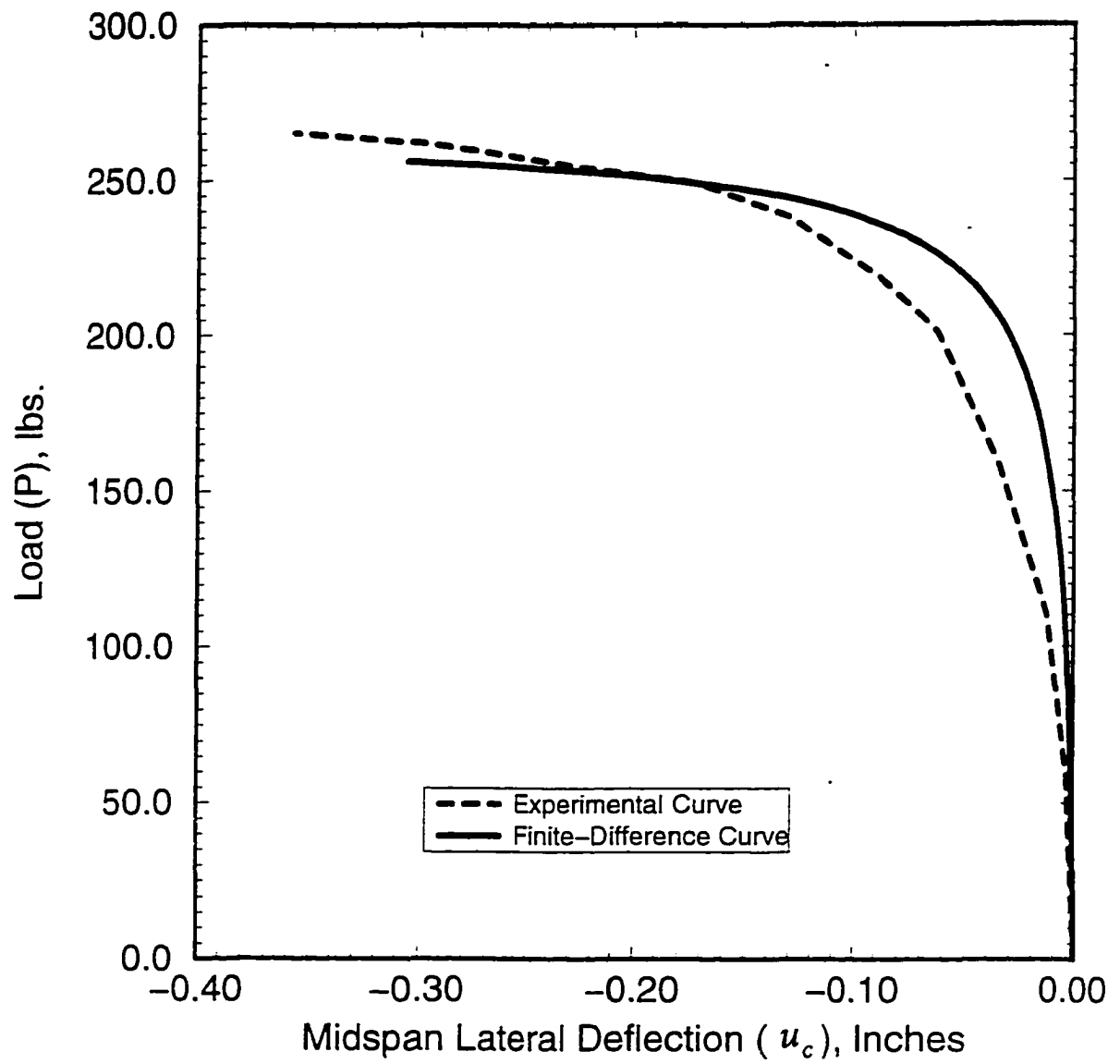


Figure 36. Load (P) versus midspan lateral deflection (u_c) for Test No. IFT3-4

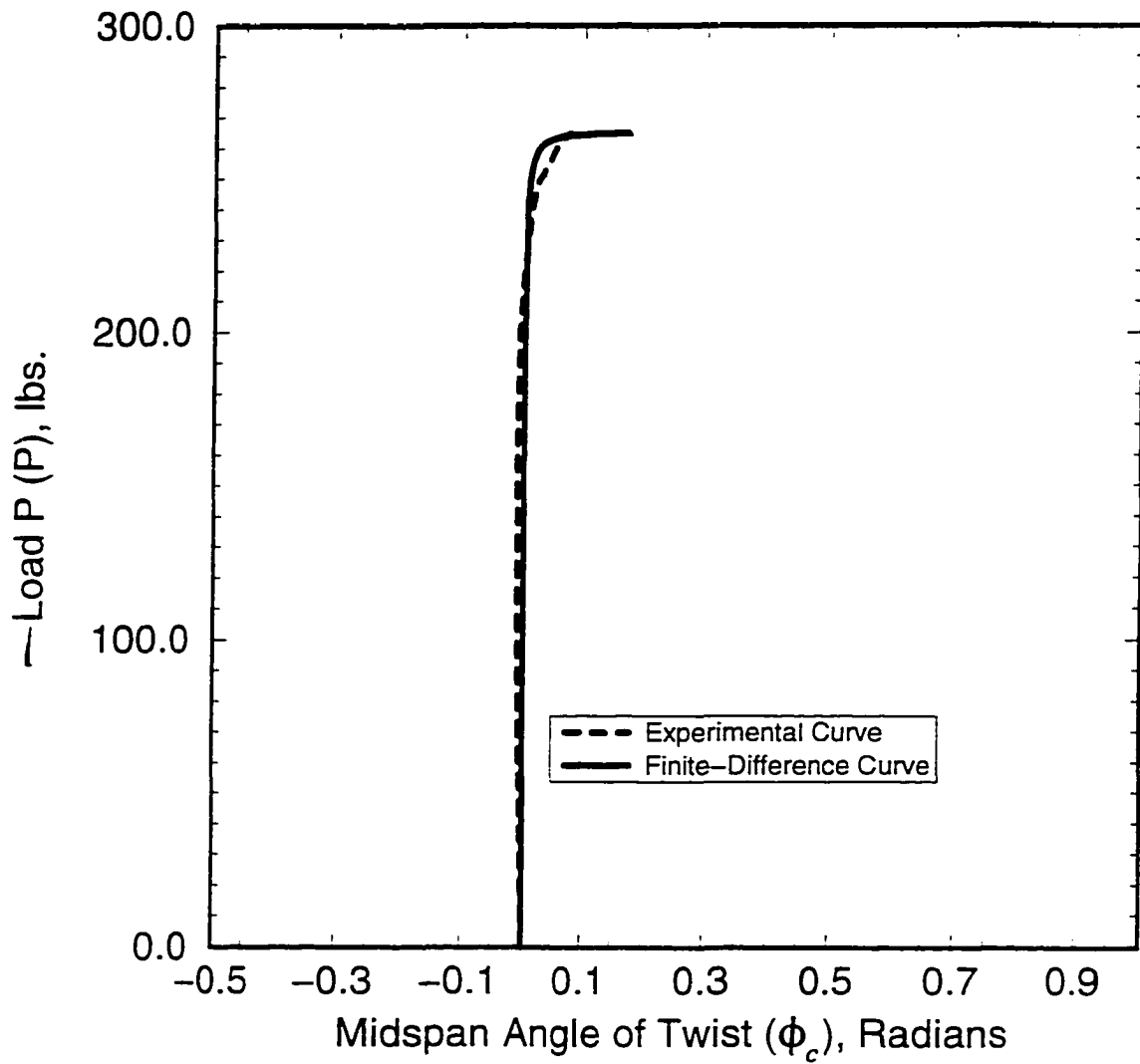


Figure 37. Load (P) versus midspan angle of twist (ϕ_c) for Test No. IFT3-4

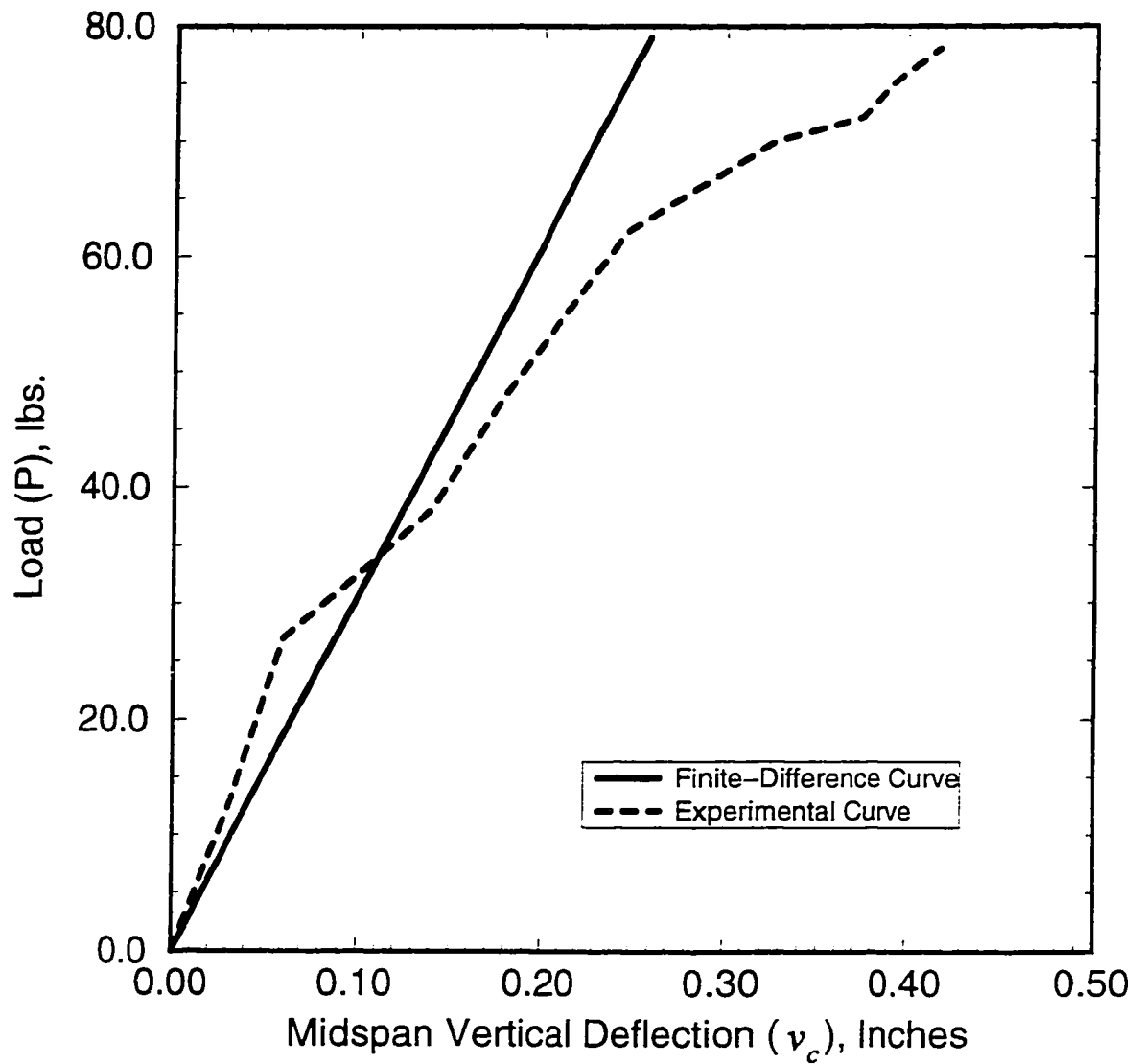


Figure 38. Load (P) versus midspan vertical deflection (v_c) for Test No. IFT4-1

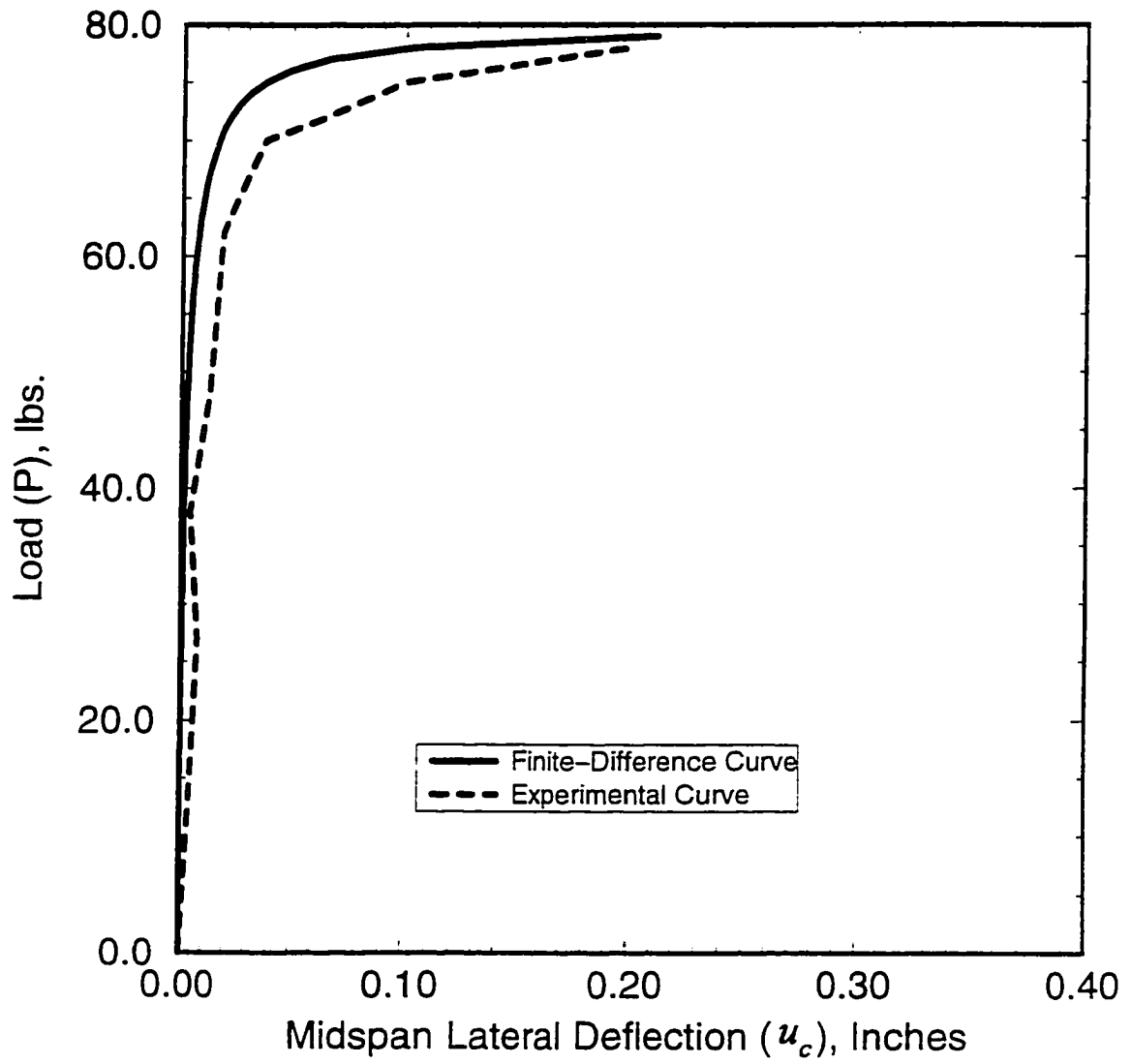


Figure 39. Load (P) versus midspan lateral deflection (u_c) for Test No. IFT4-1

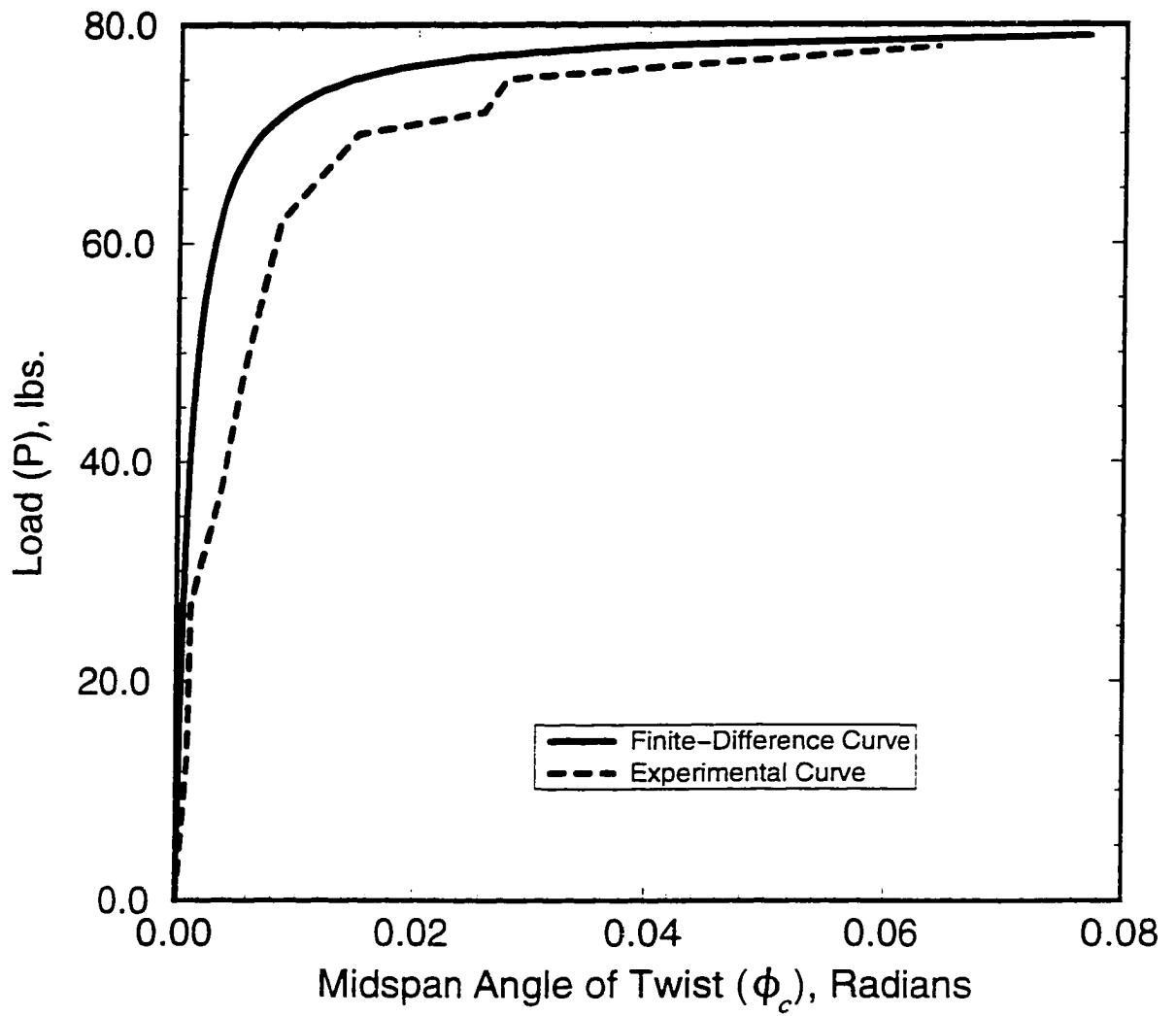


Figure 40. Load (P) versus midspan angle of twist (ϕ_c) for Test No. IFT4-1

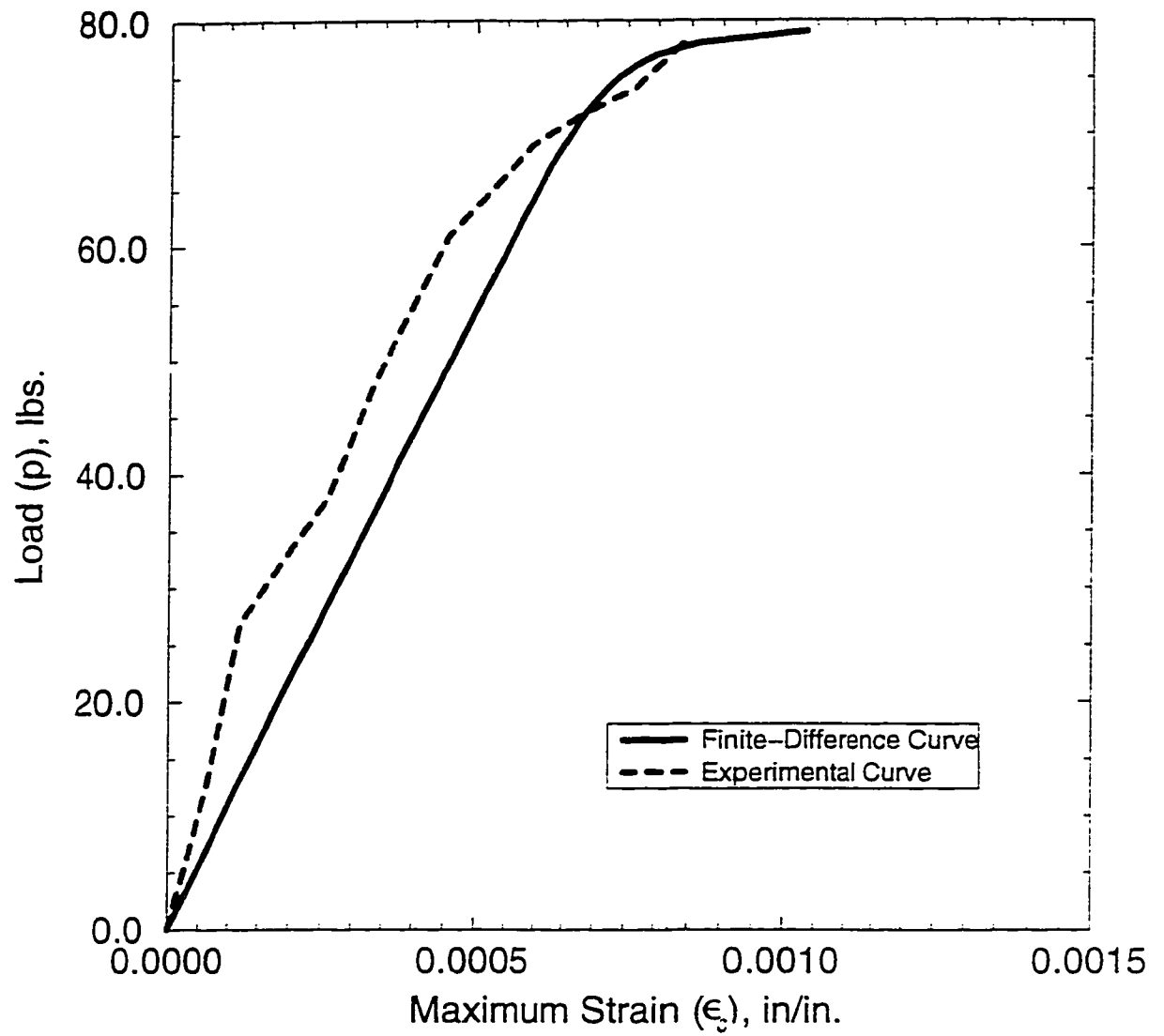


Figure 41. Load (P) versus maximum strain (ϵ_c) for Test No. IFT4-1

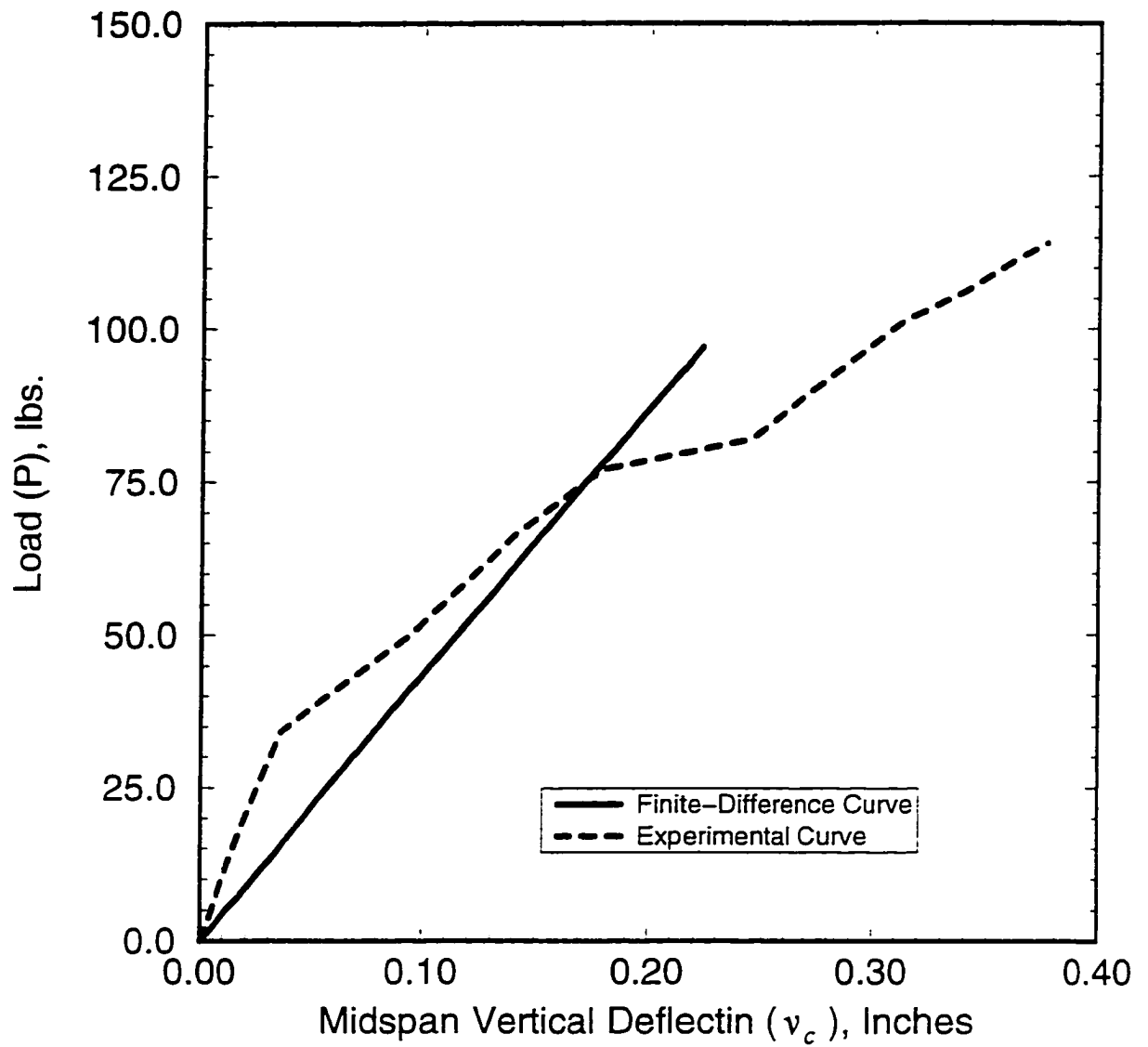


Figure 42. Load (P) versus midspan vertical deflection (v_c) for Test No. IFT4-2

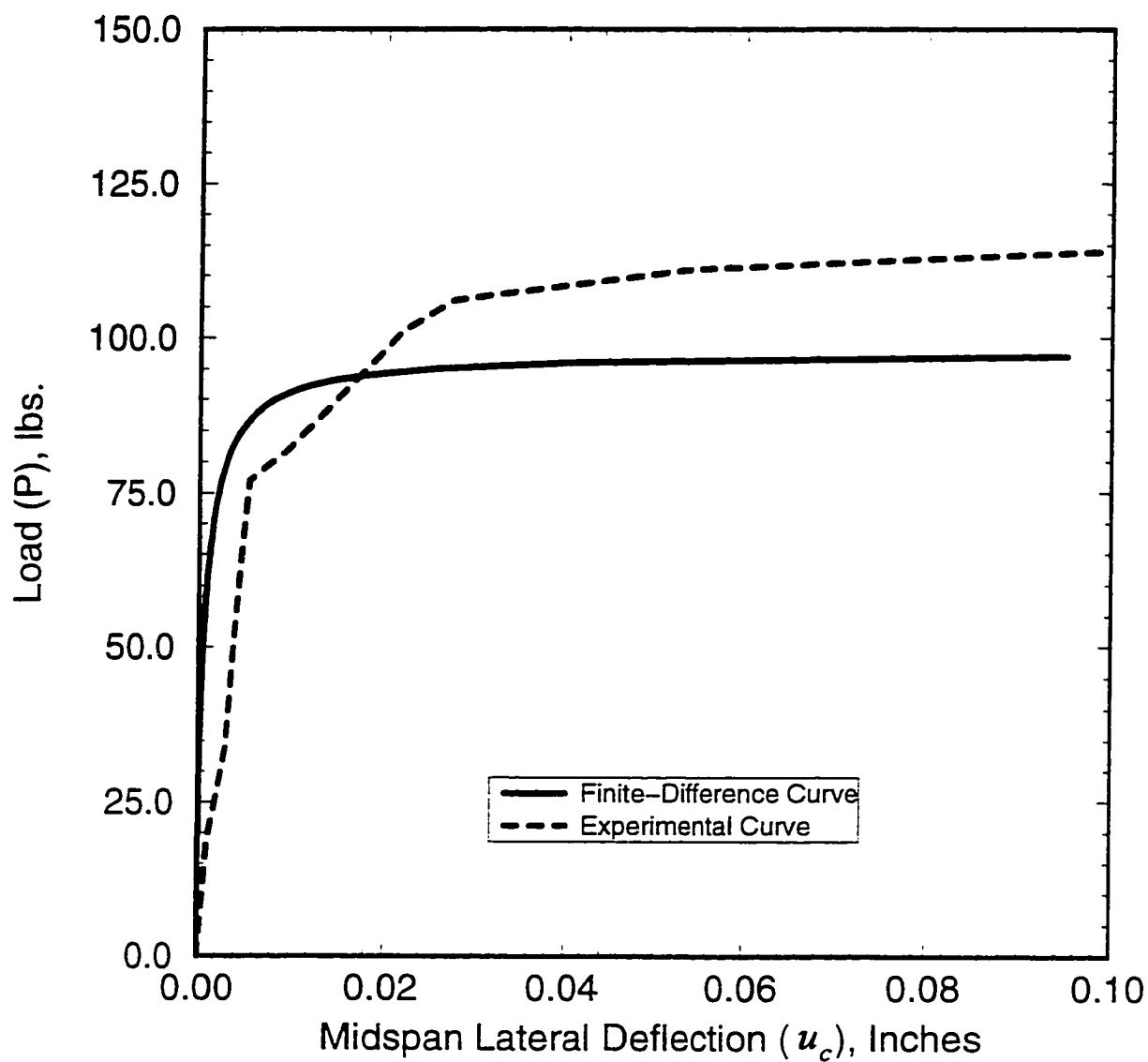


Figure 43. Load (P) versus midspan lateral deflection (u_c) for Test No. IFT4-2

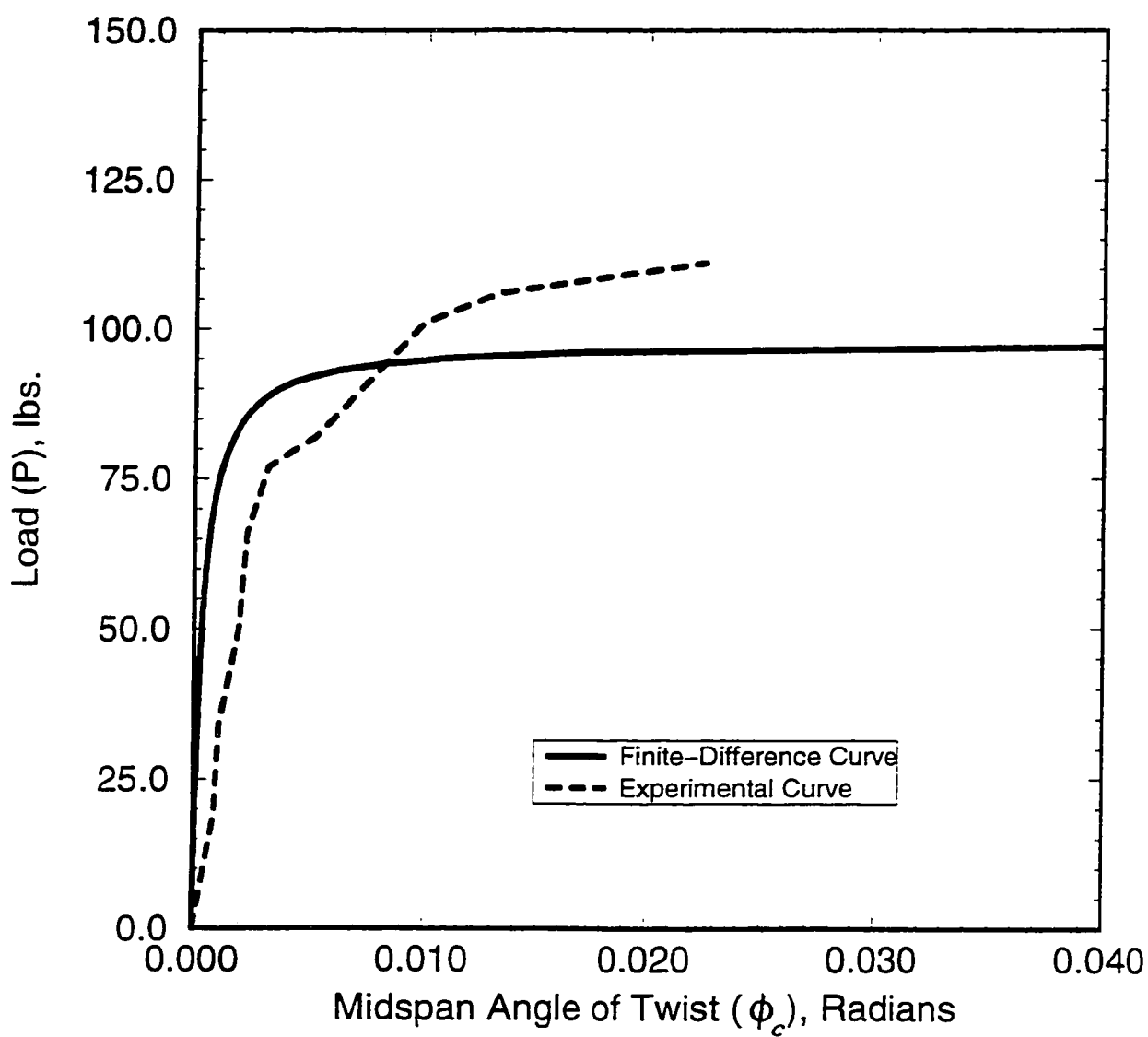


Figure 44. Load (P) versus midspan angle of twist (ϕ_c) for Test No. IFT4-2

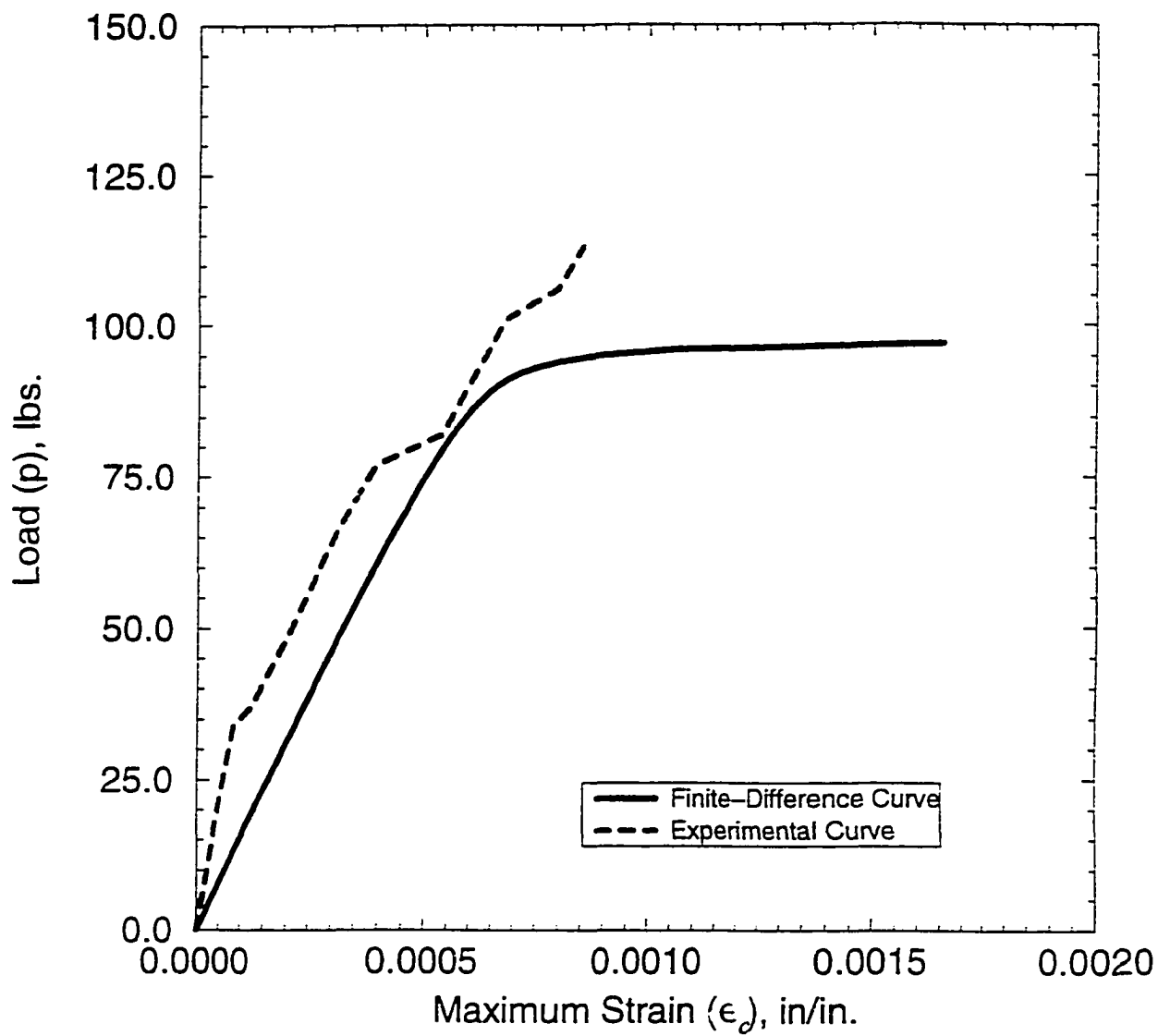


Figure 45. Load (P) versus maximum strain (ϵ_c) for Test No. IFT4-2

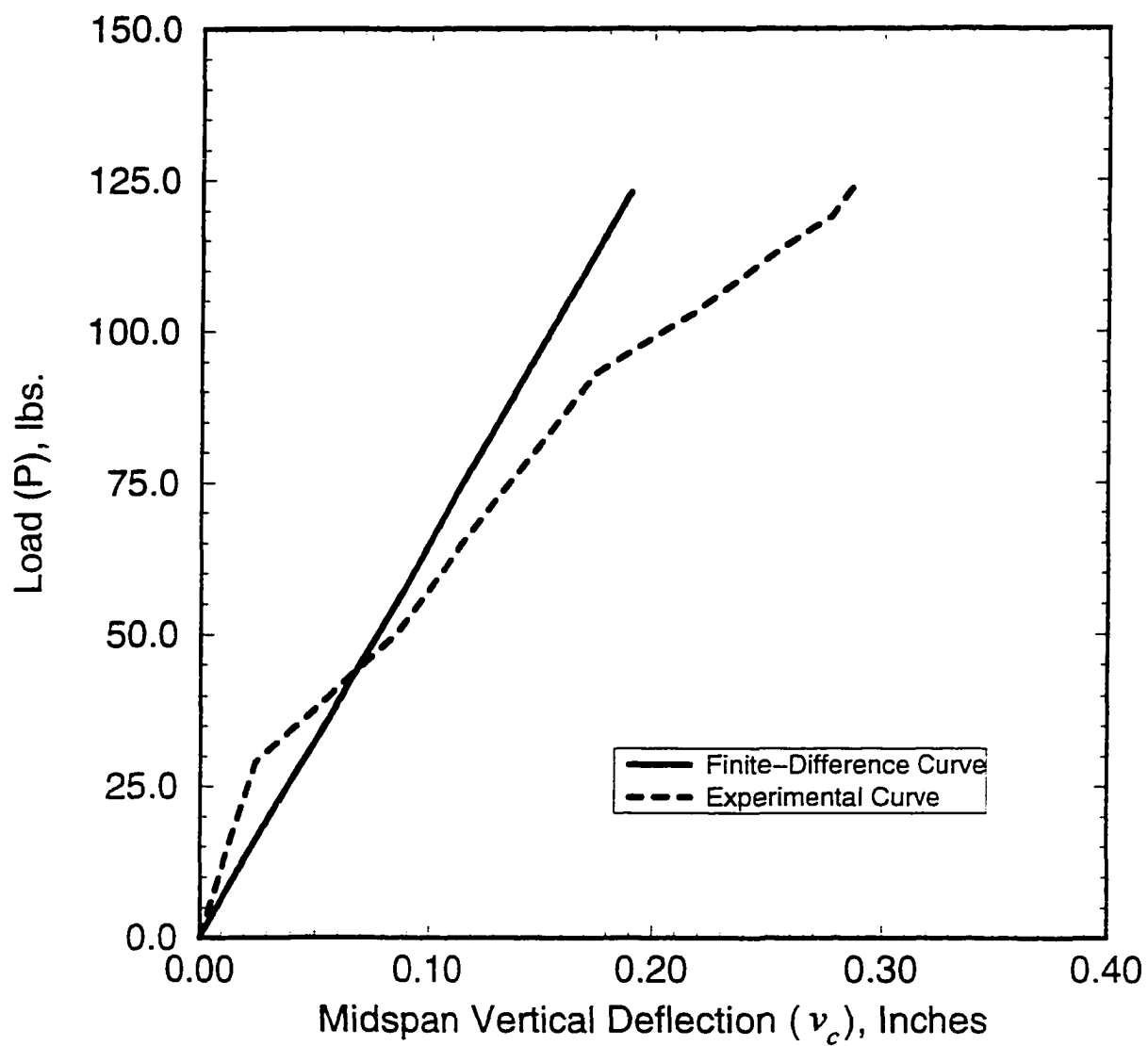


Figure 46. Load (P) versus midspan vertical deflection (v_c) for Test No. IFT4-3

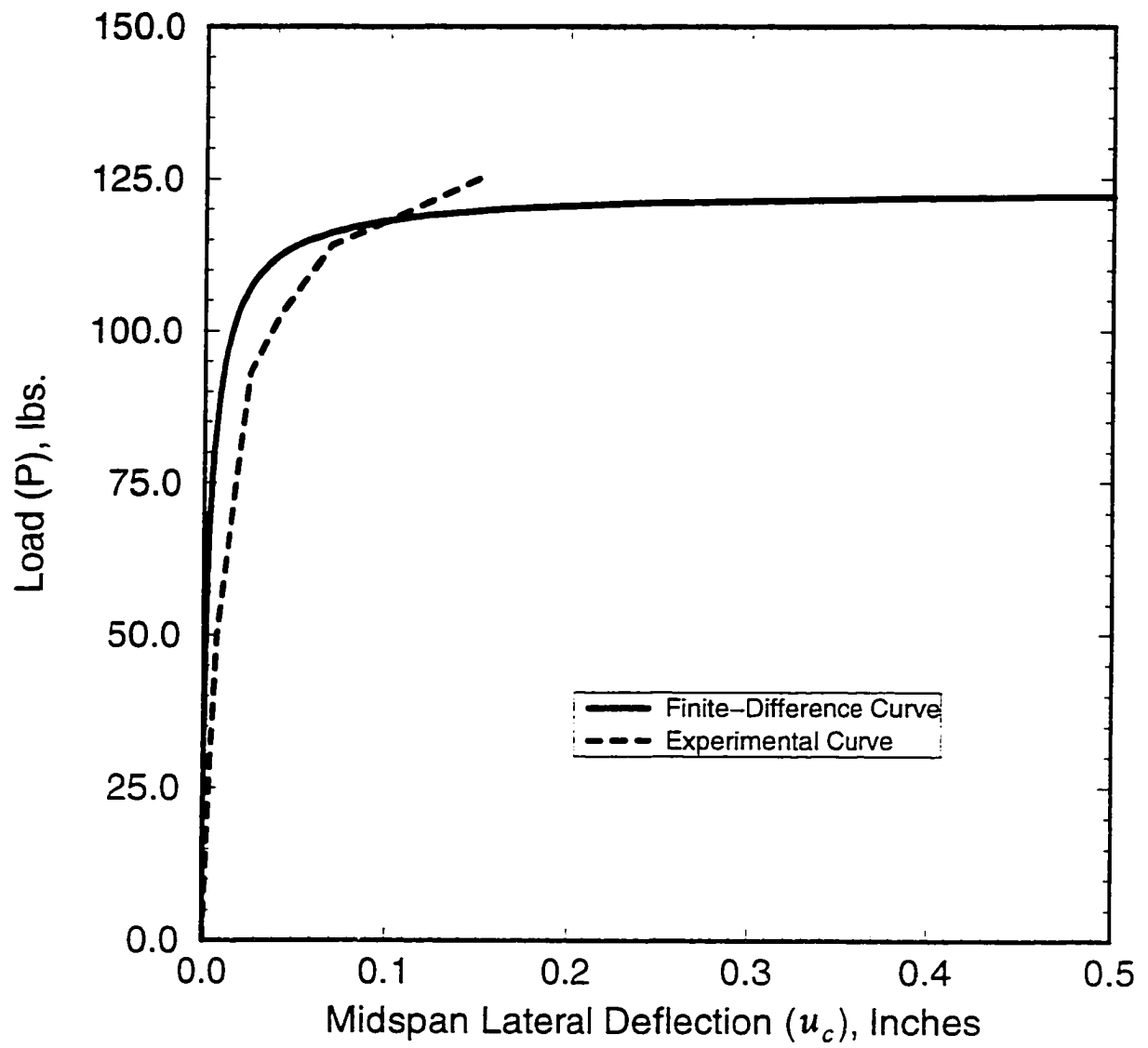


Figure 47. Load (P) versus midspan lateral deflection (u_c) for Test No. IFT4-3

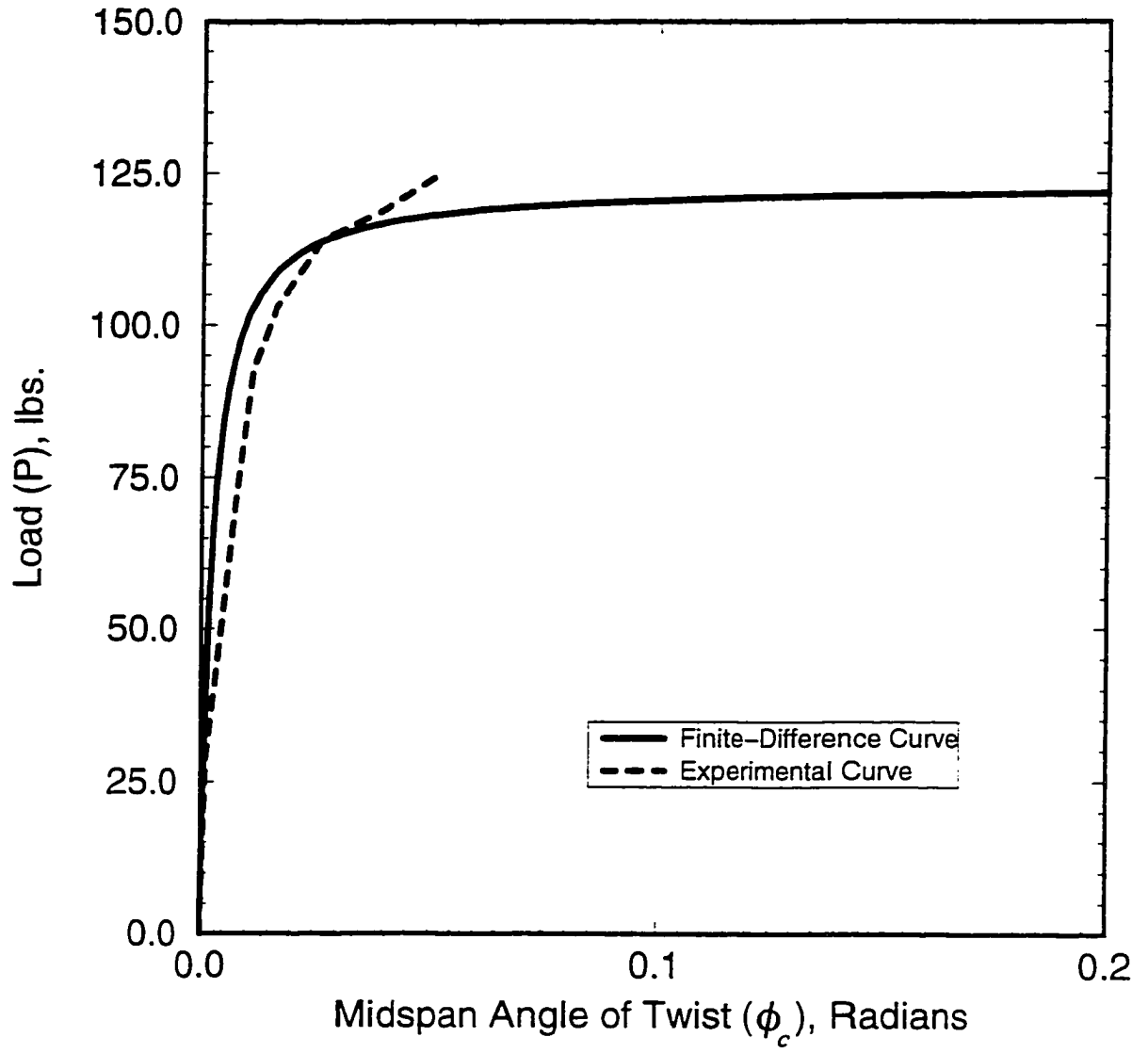


Figure 48. Load (P) versus midspan angle of twist (ϕ_c) for Test No. IFT4-3

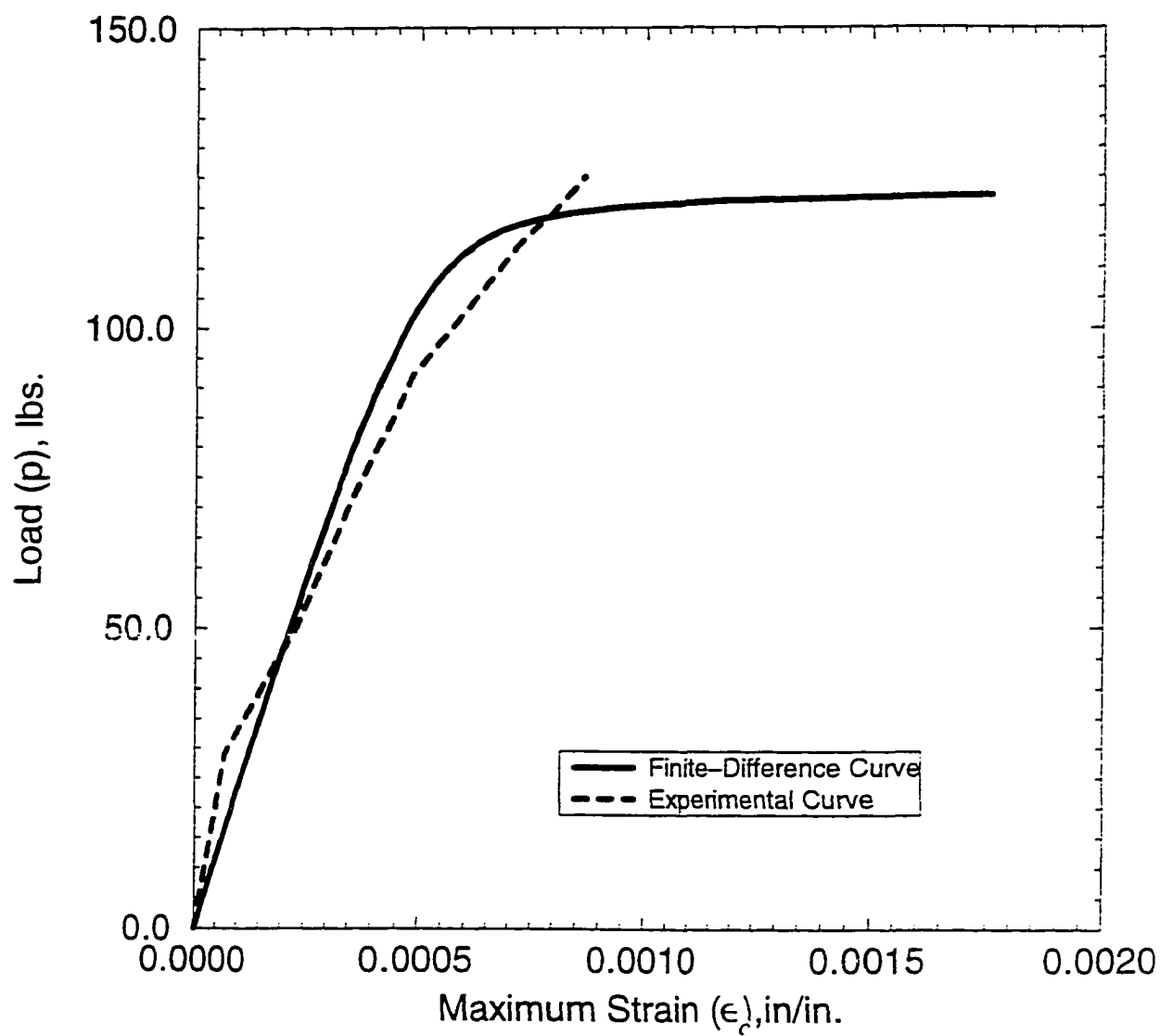


Figure 49. Load (P) versus maximum strain (ϵ_c) for Test No. IFT4-3

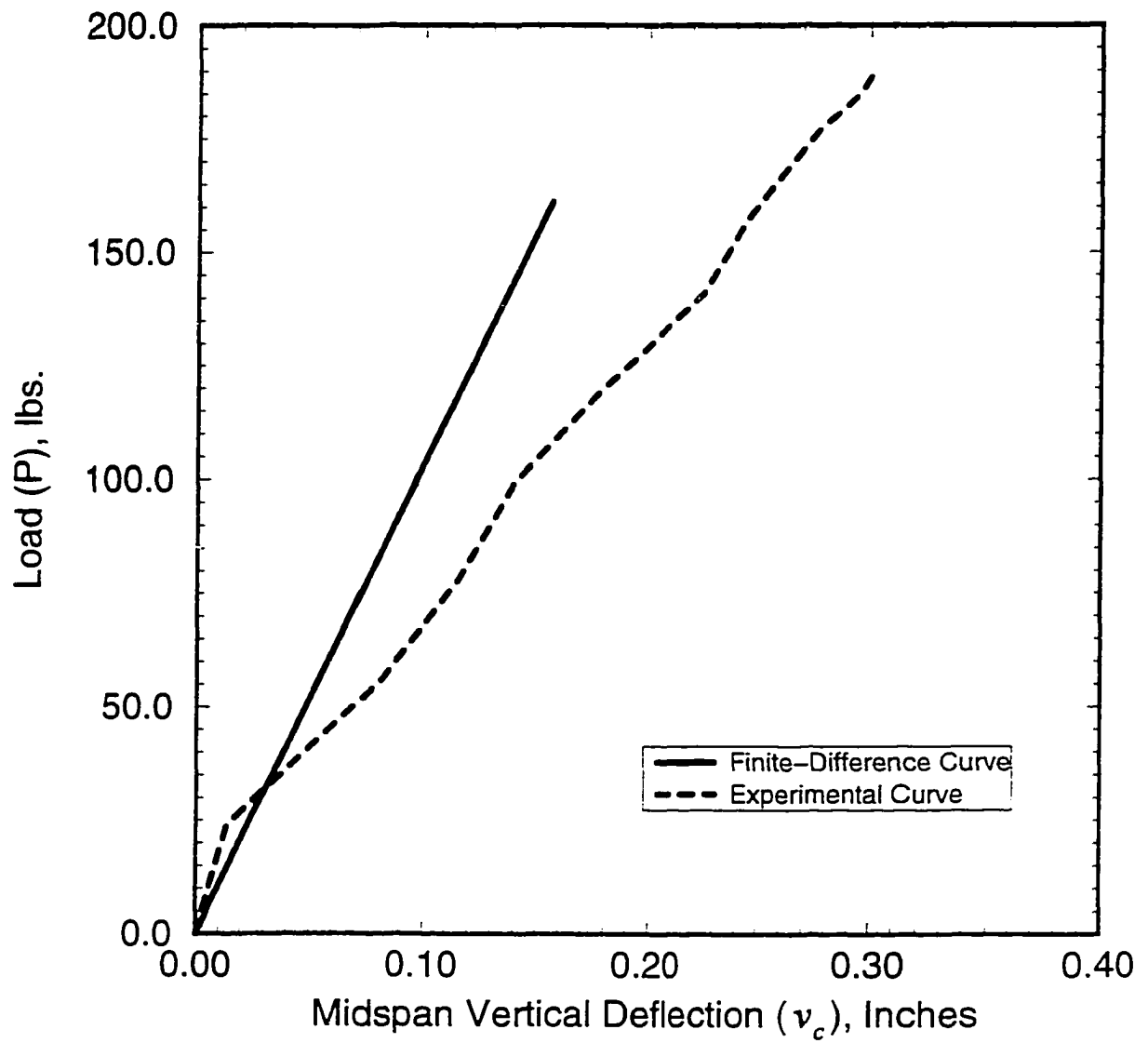


Figure 50. Load (P) versus midspan vertical deflection (v_c) for Test No. IFT4-4

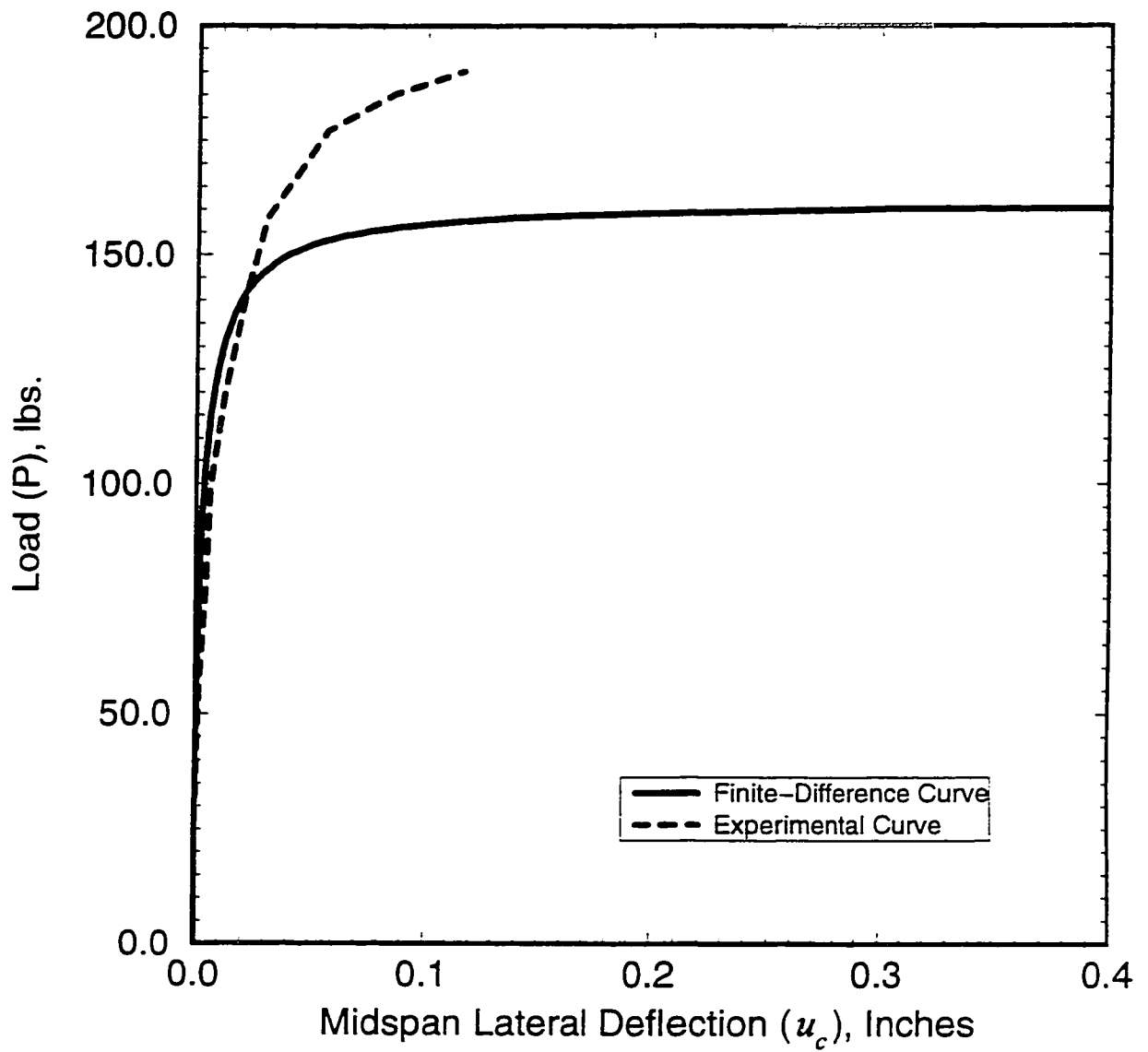


Figure 51. Load (P) versus midspan lateral deflection (u_c) for Test No. IFT4-4

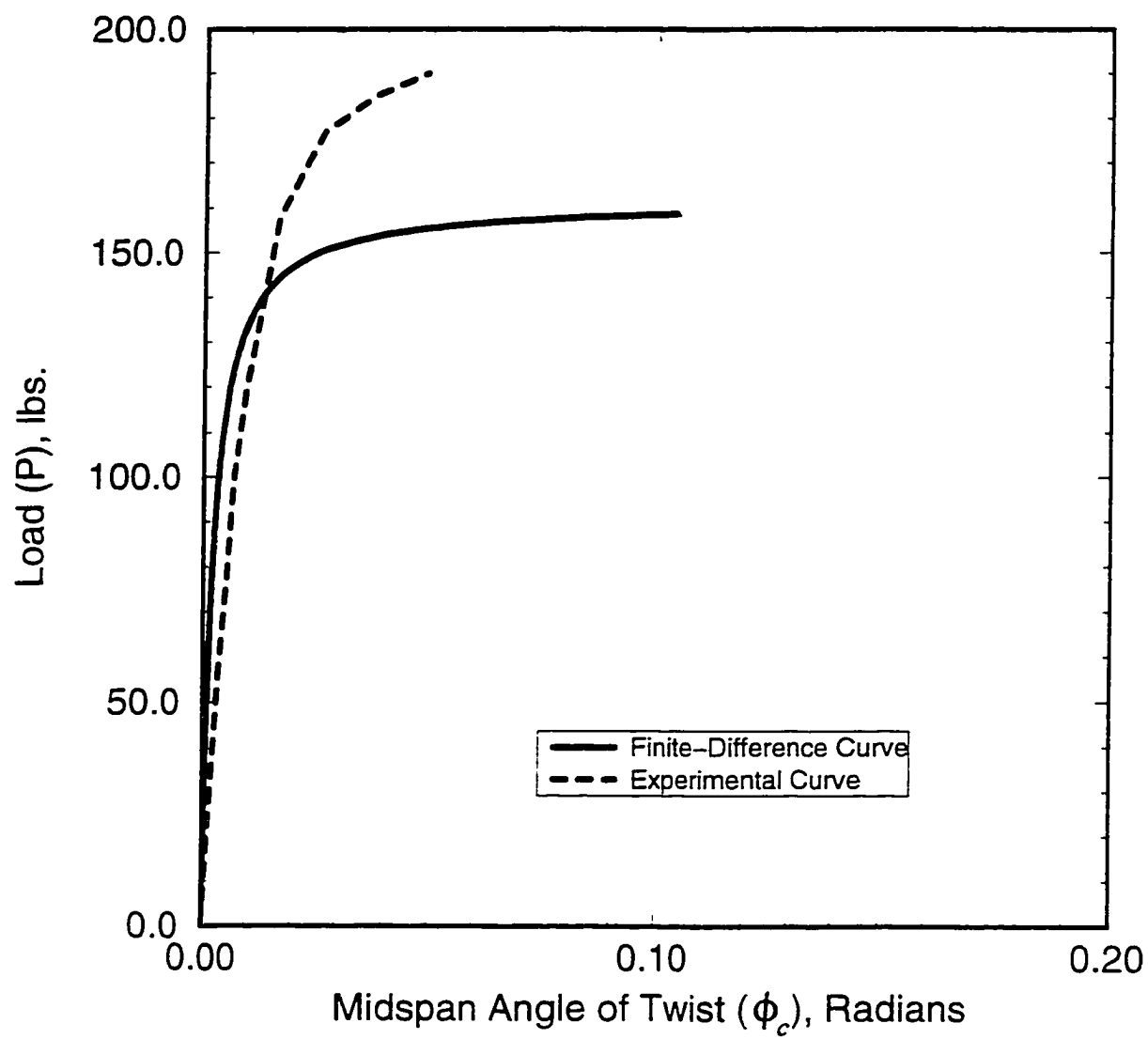


Figure 52. Load (P) versus midspan angle of twist (ϕ_c) for Test No. IFT4-4

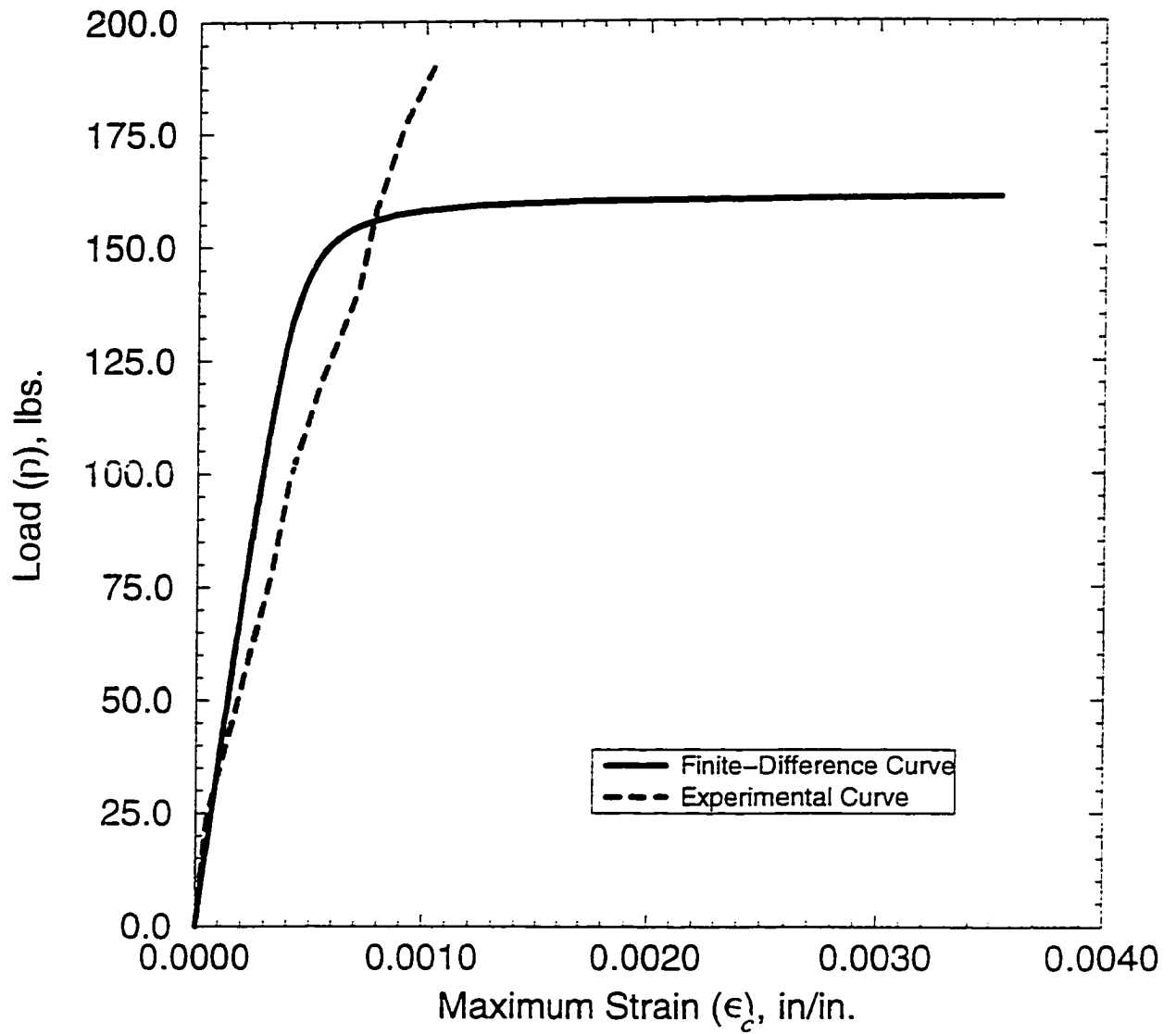


Figure 53. Load (P) versus maximum strain (ϵ_c) for Test No. IFT4-4

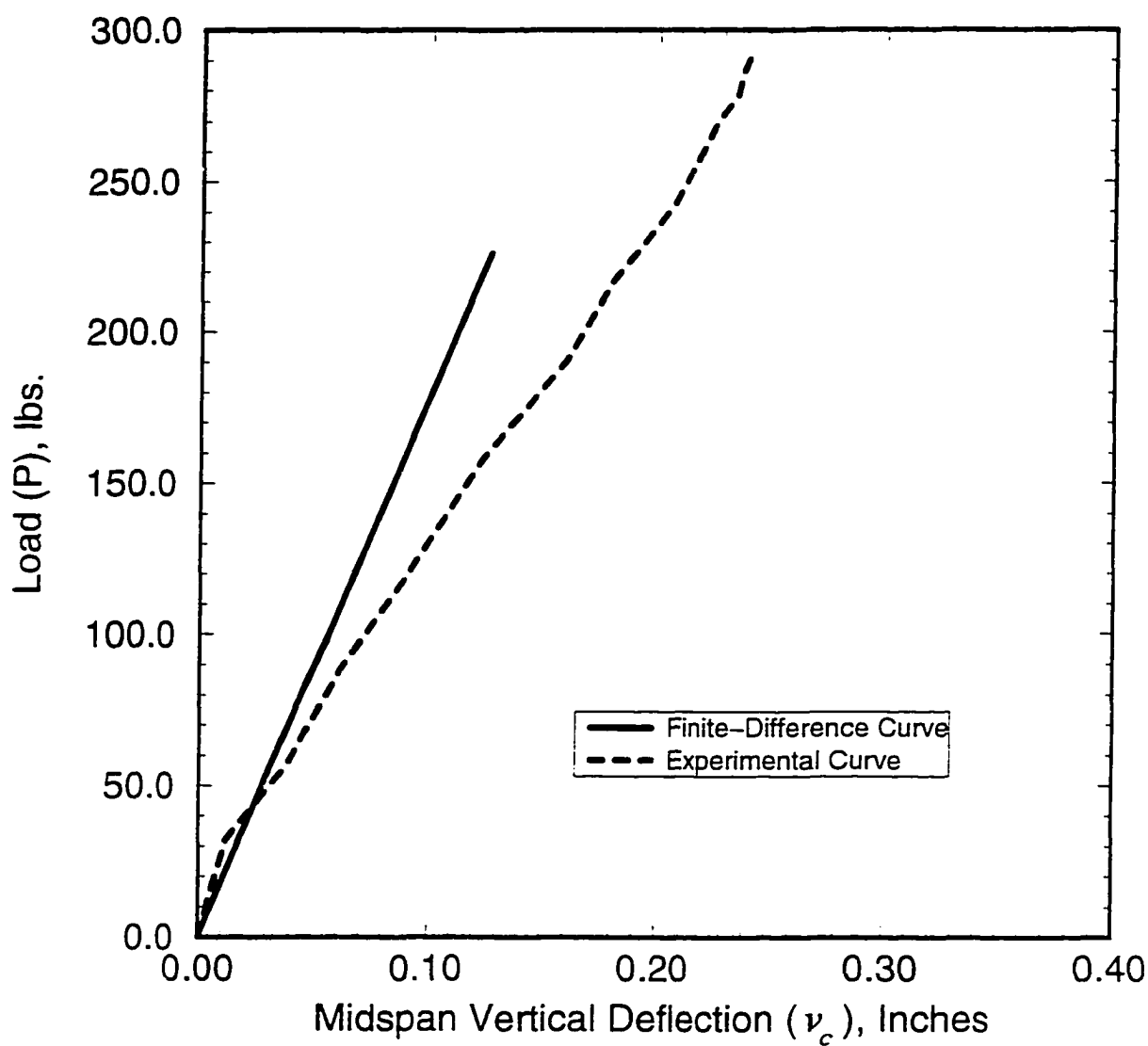


Figure 54. Load (P) versus midspan vertical deflection (v_c) for Test No. IFT4-5

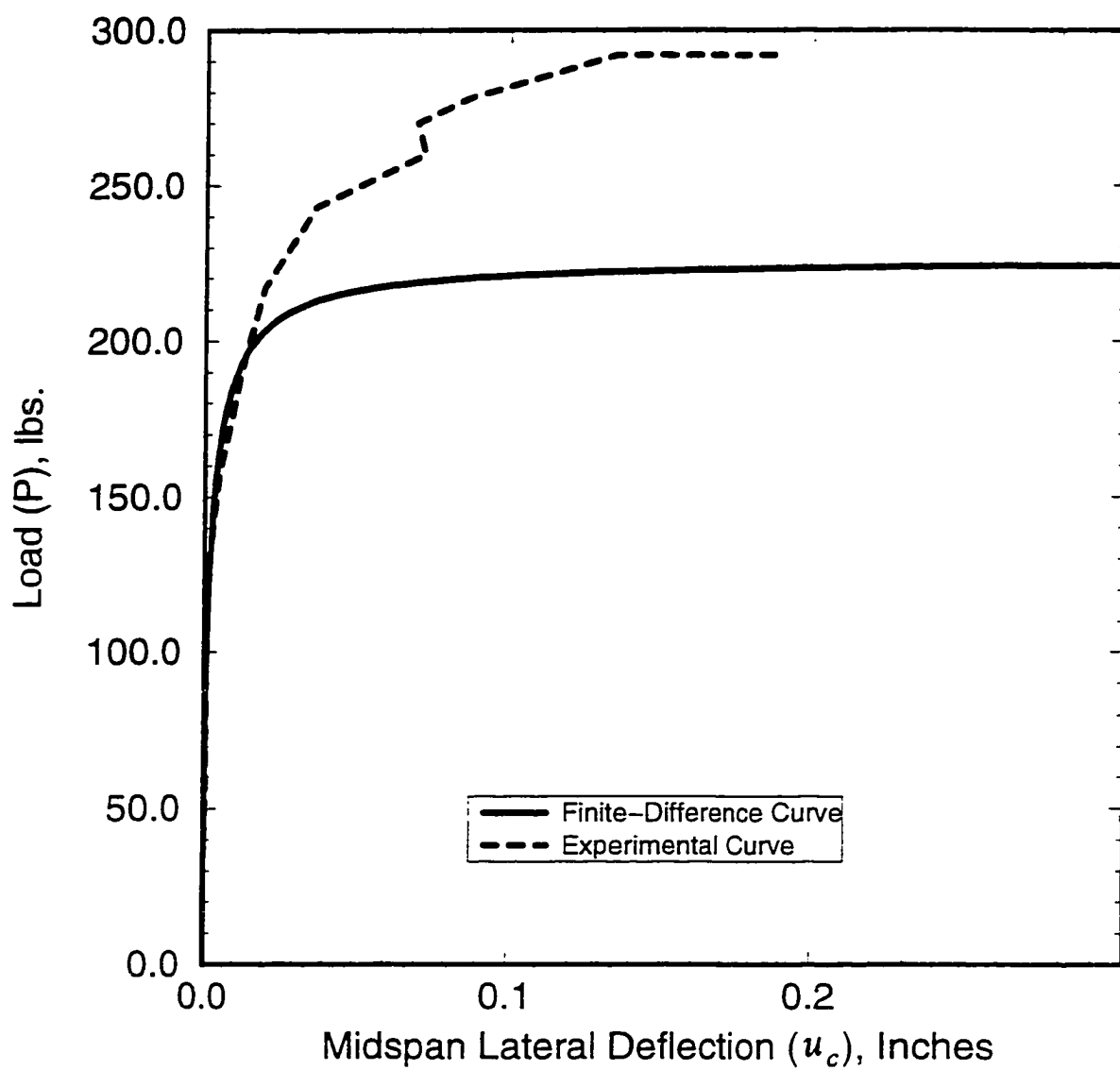


Figure 55. Load (P) versus midspan lateral deflection (u_c) for Test No. IFT4-5

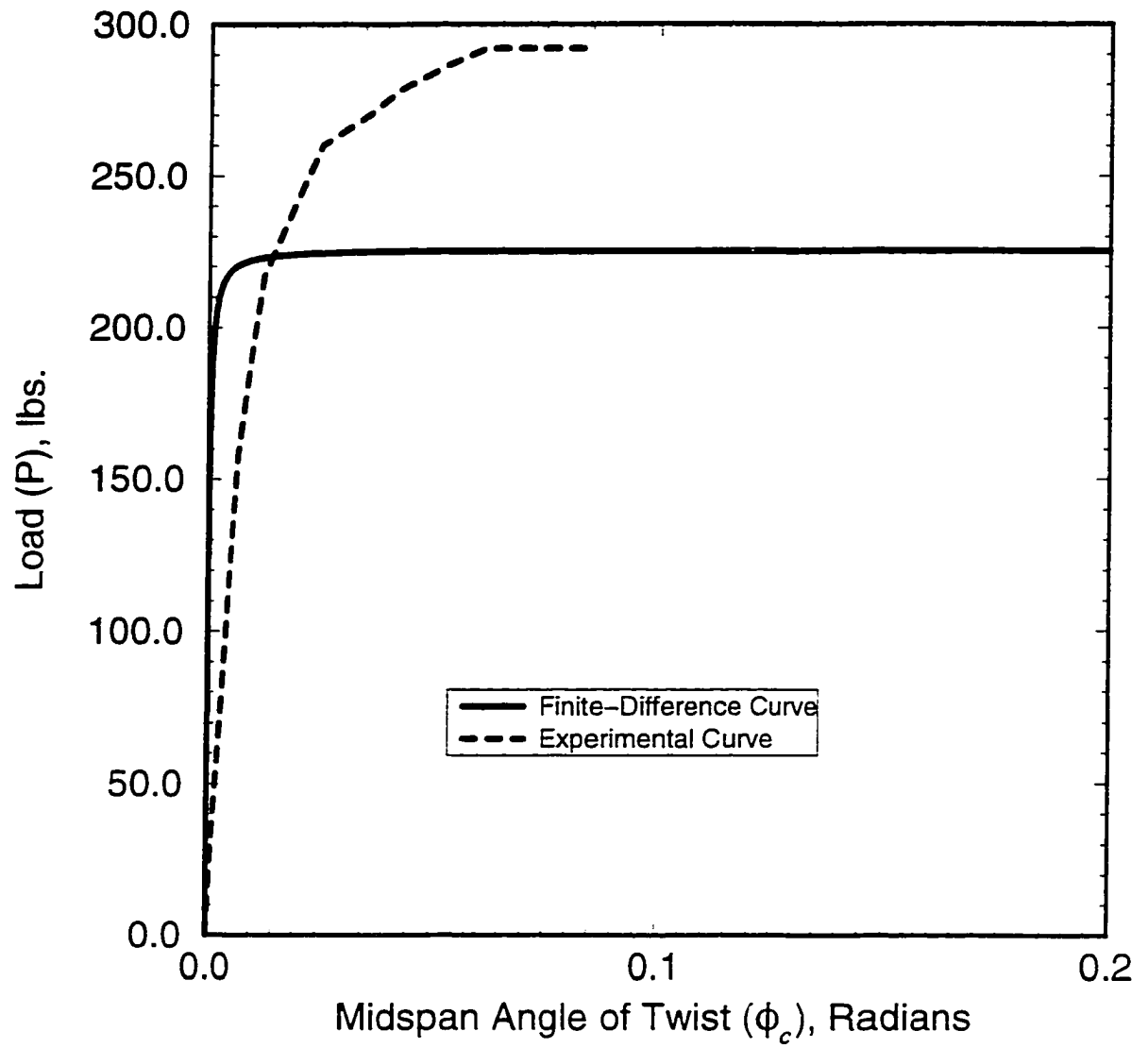


Figure 56. Load (P) versus midspan angle of twist (ϕ_c) for Test No. IFT4-5

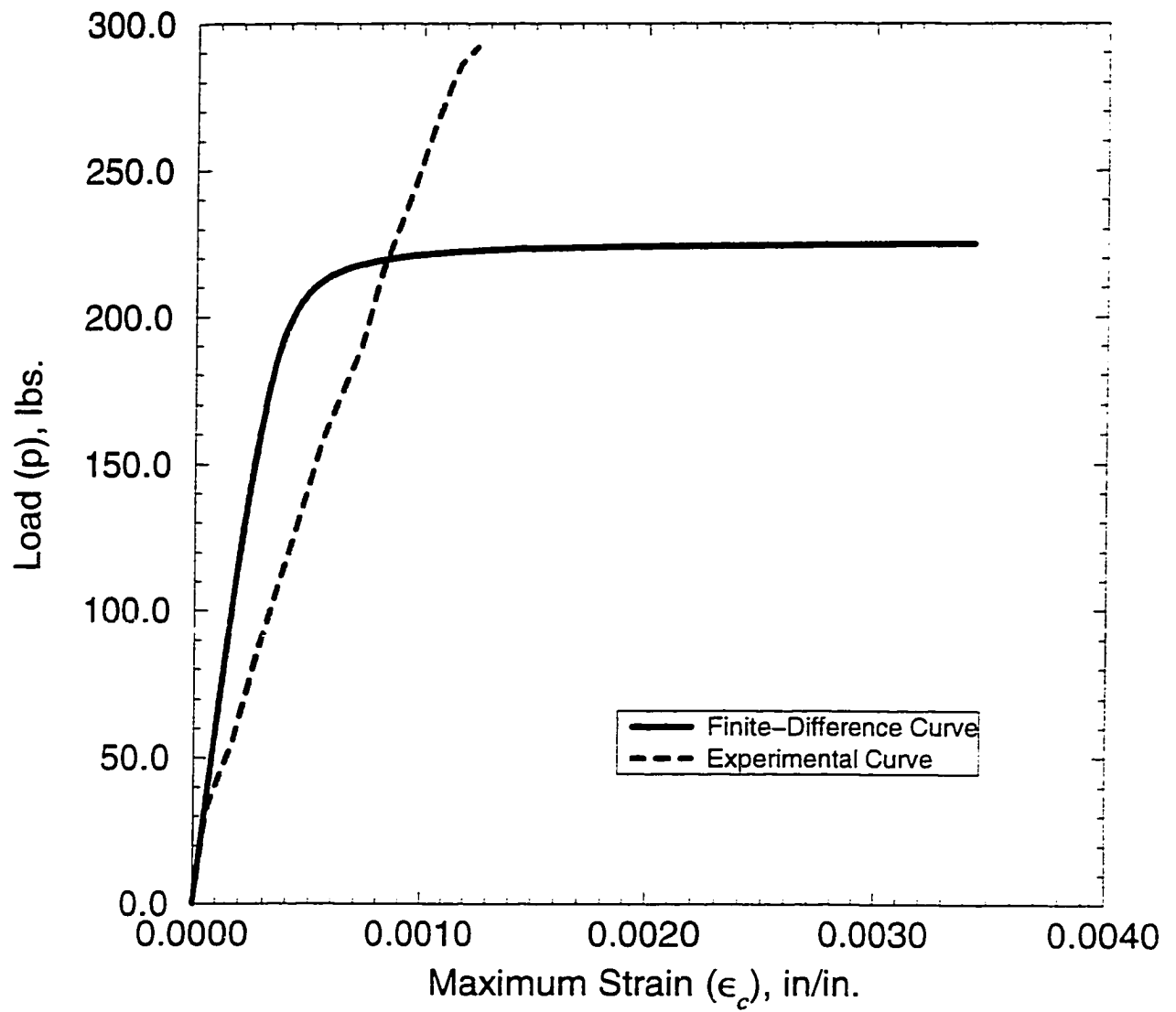


Figure 57. Load (P) versus maximum strain (ϵ_c) for Test No. IFT4-5

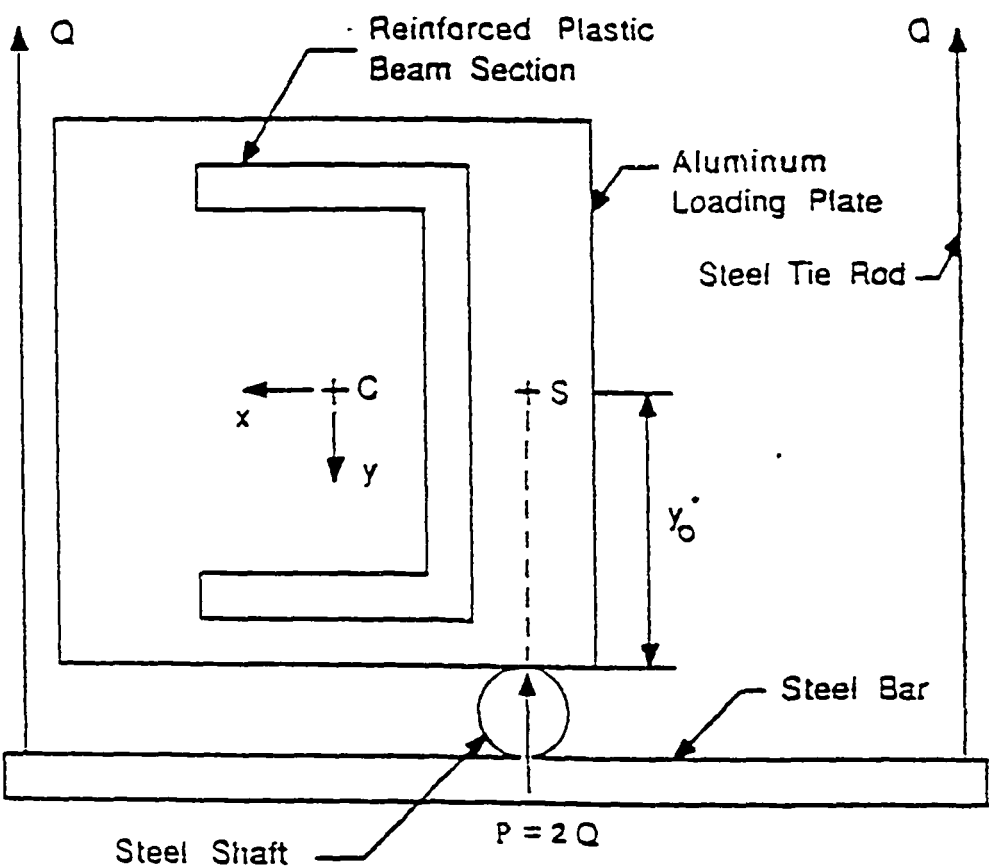


Figure 58 Cross-sectional schematic view at load application points (F and G) for channel section beam

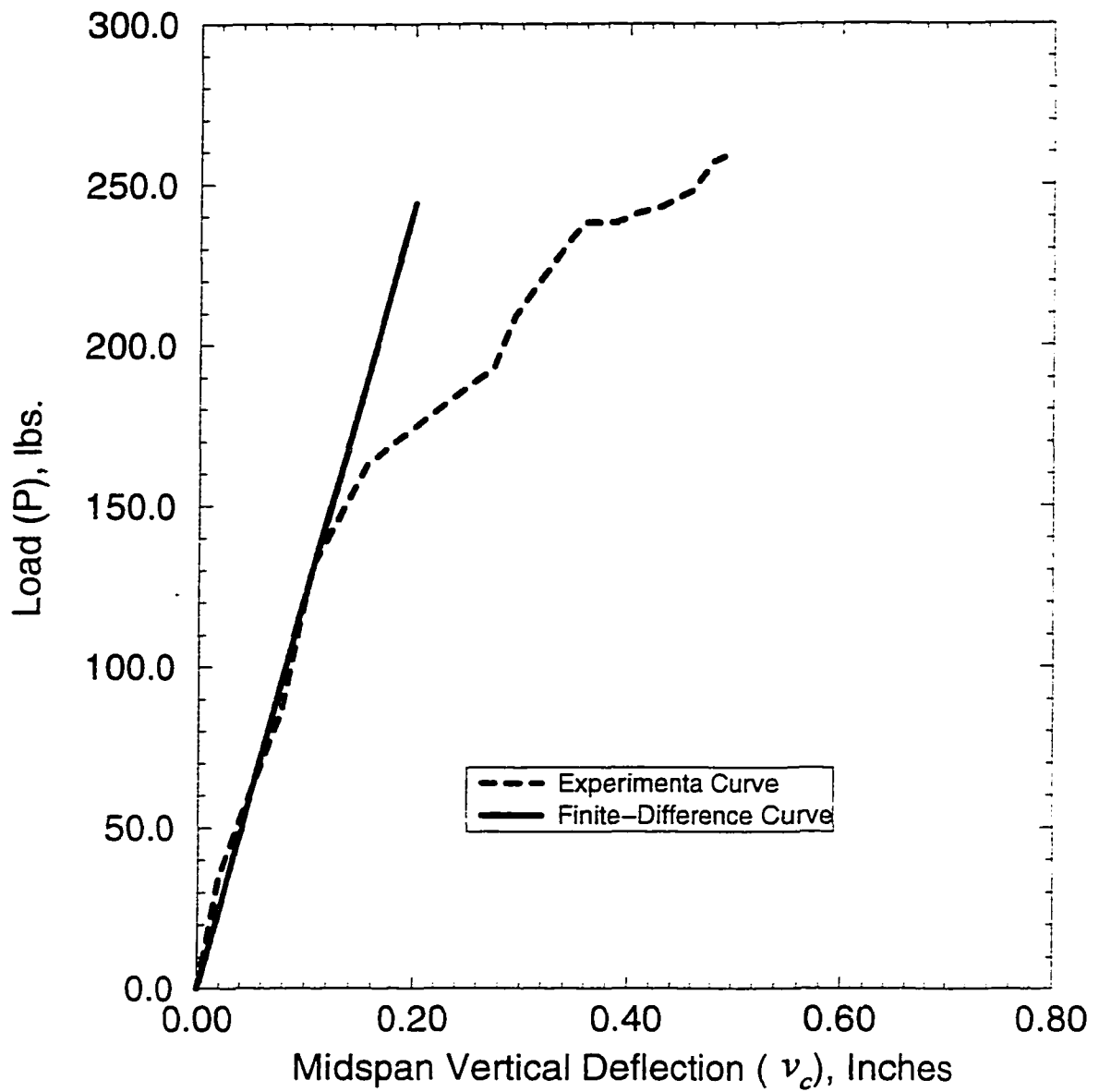


Figure 59. Load (P) versus midspan vertical deflection (v_c) for Test No. CFT3-1

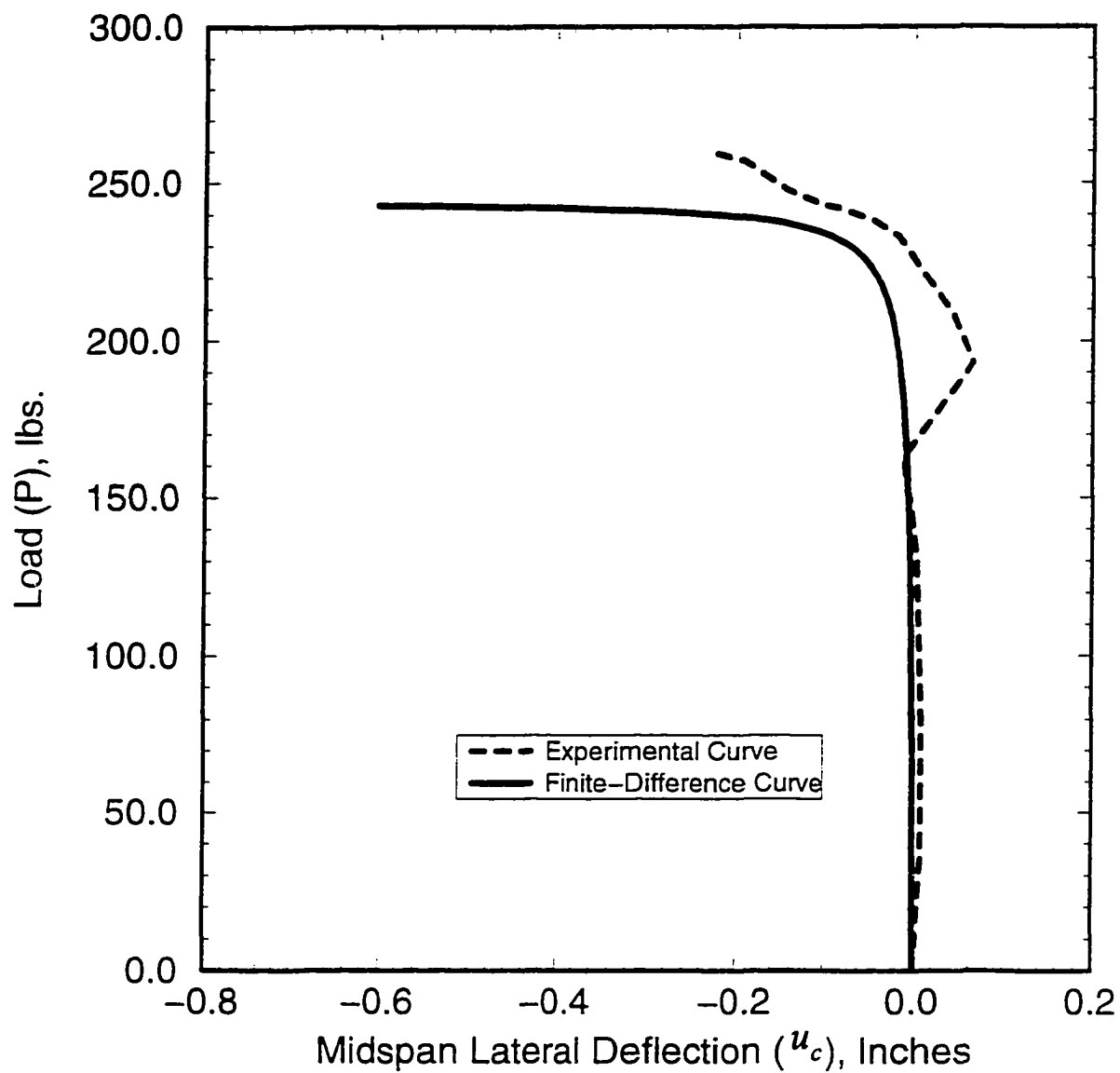


Figure 60. Load (P) versus midspan lateral deflection (u_c) for Test No. CFT3-1

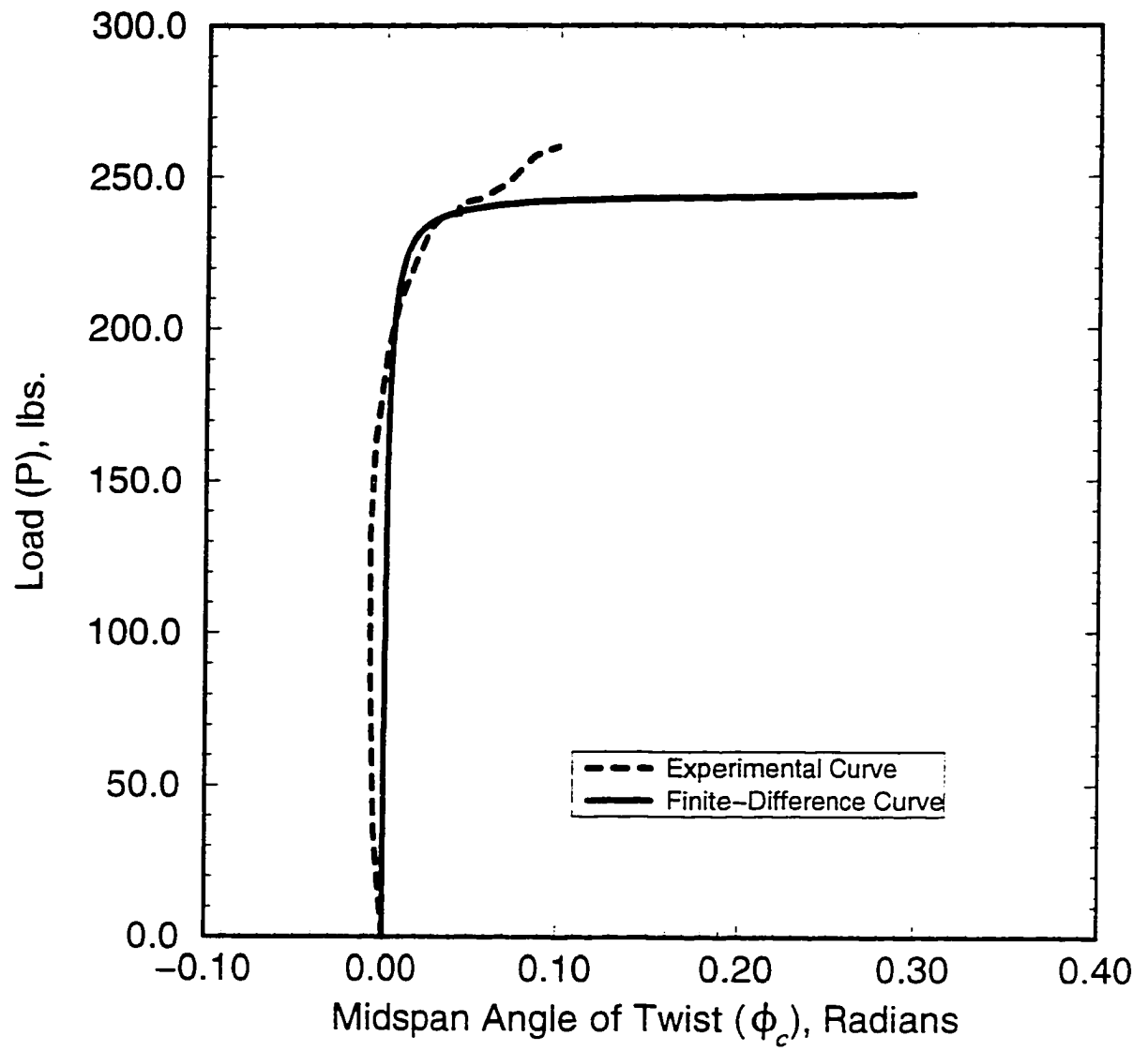


Figure 61. Load (P) versus midspan angle of twist (ϕ_c) for Test No. CFT3-1

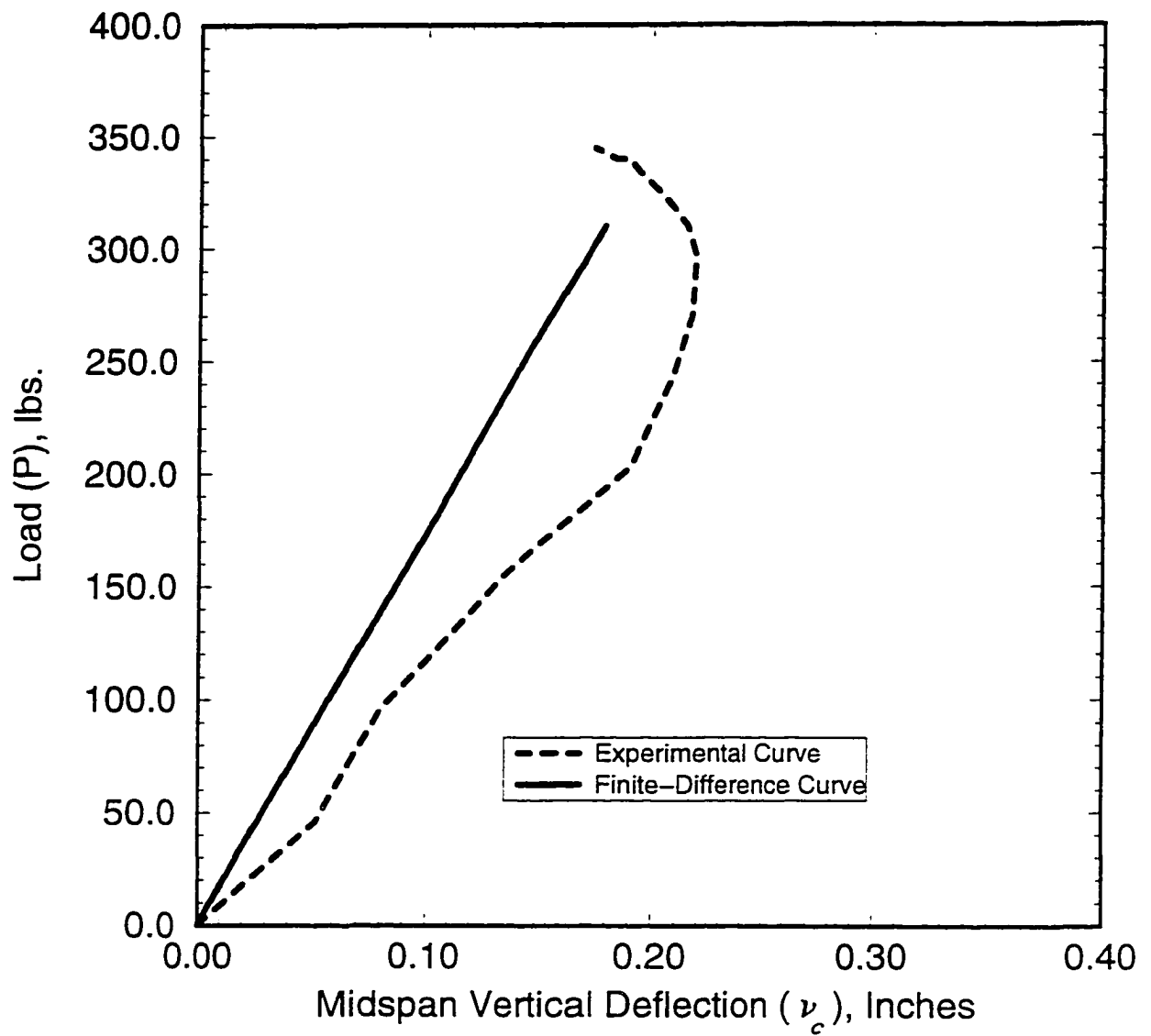


Figure 62. Load (P) versus midspan vertical deflection (v_c) for Test No. CFT3-2

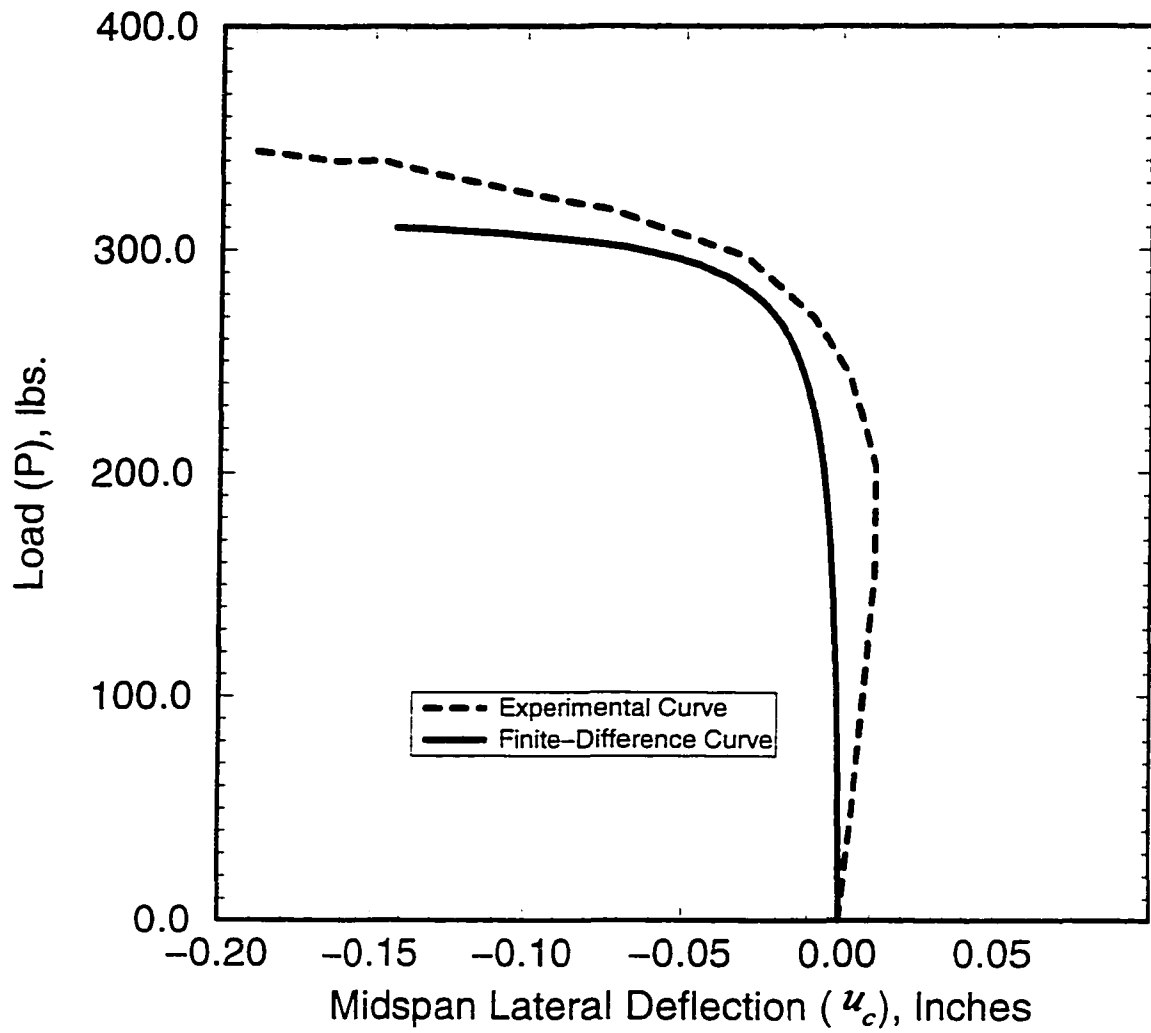


Figure 63. Load (P) versus midspan lateral deflection (u_c) for Test No. CFT3-2

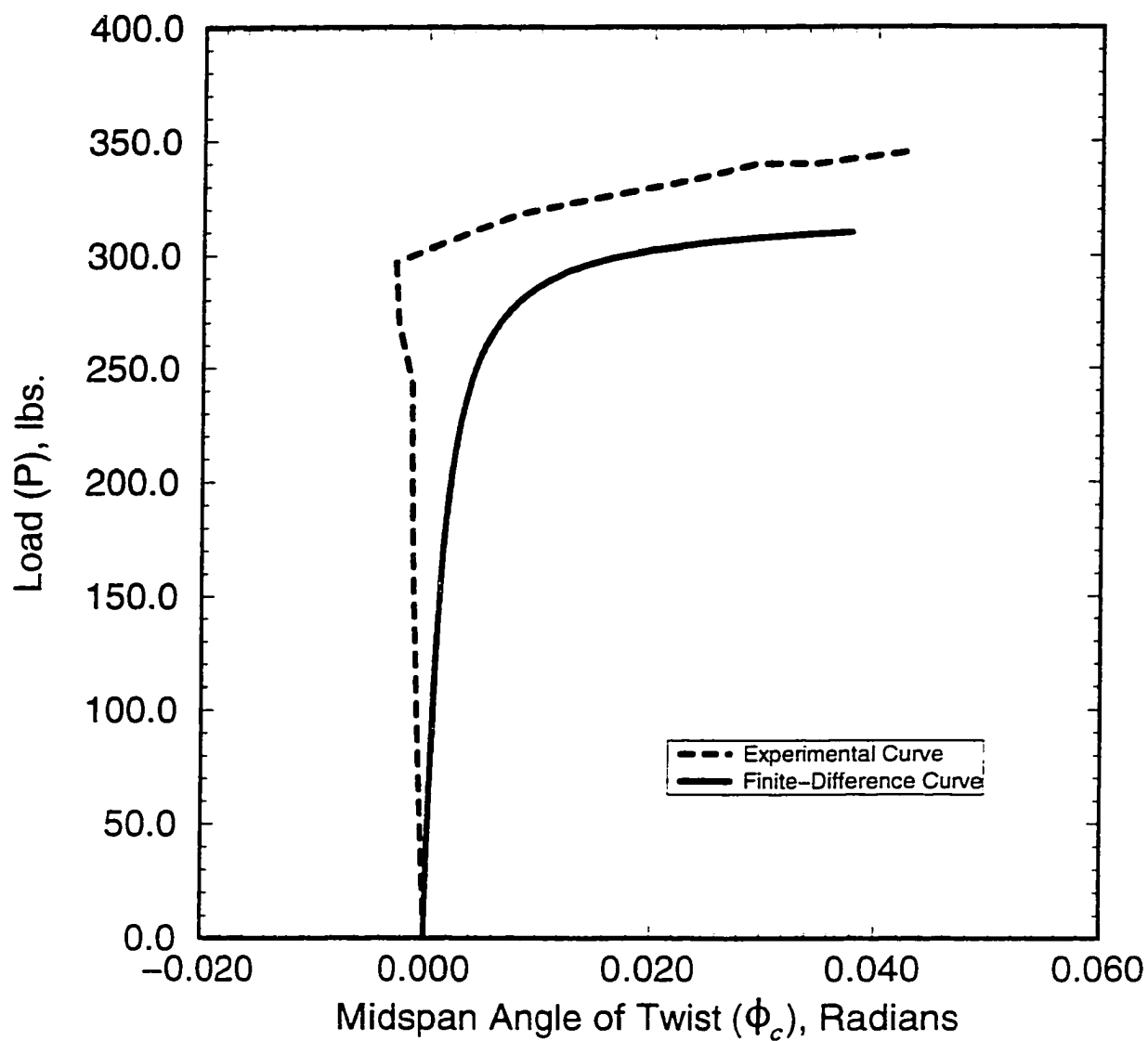


Figure 64. Load (P) versus midspan angle of twist (ϕ_c) for Test No. CFT3-2

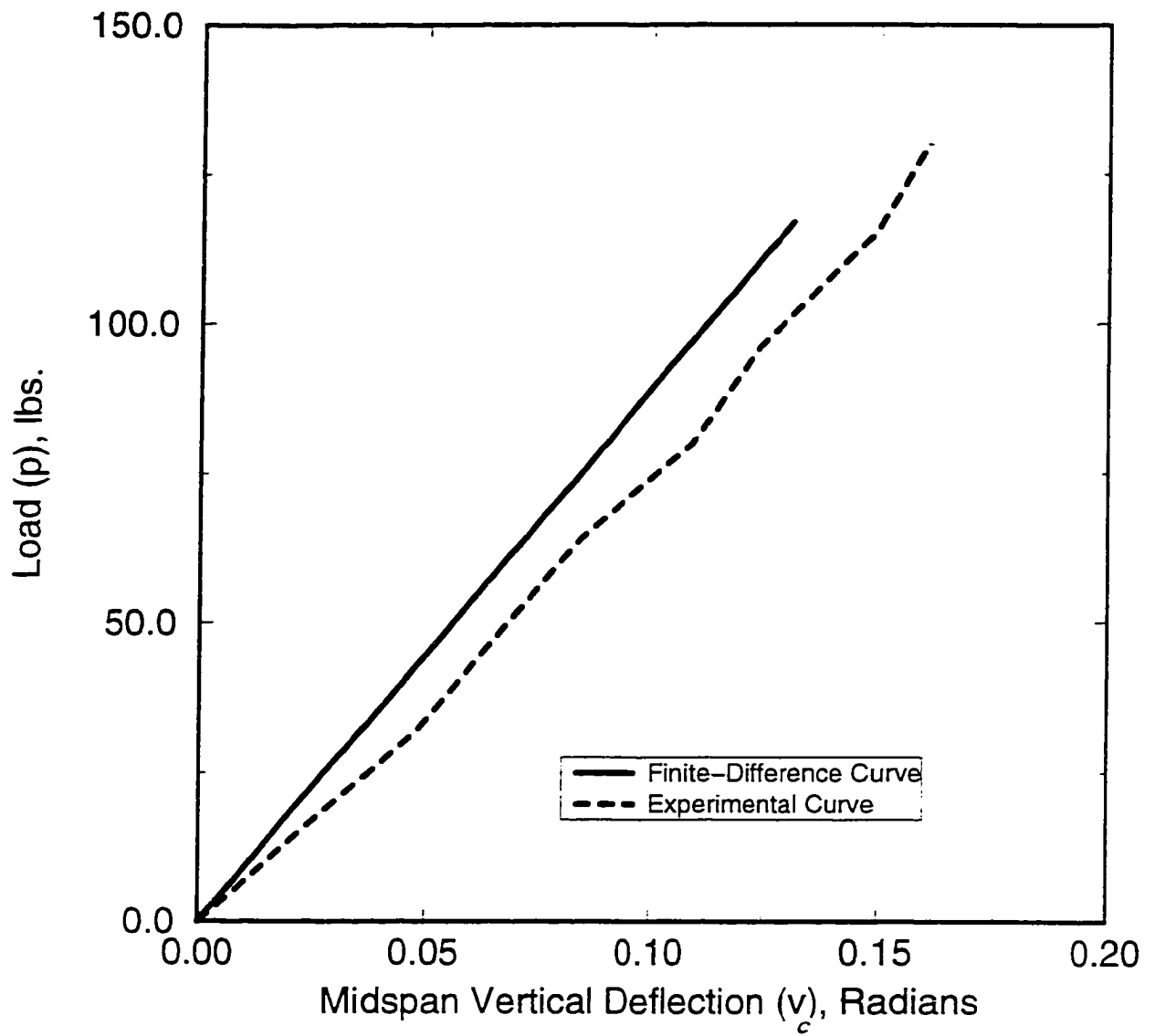


Figure 65. Load (P) versus midspan vertical deflection (v_c) for Test No. CFT4-1

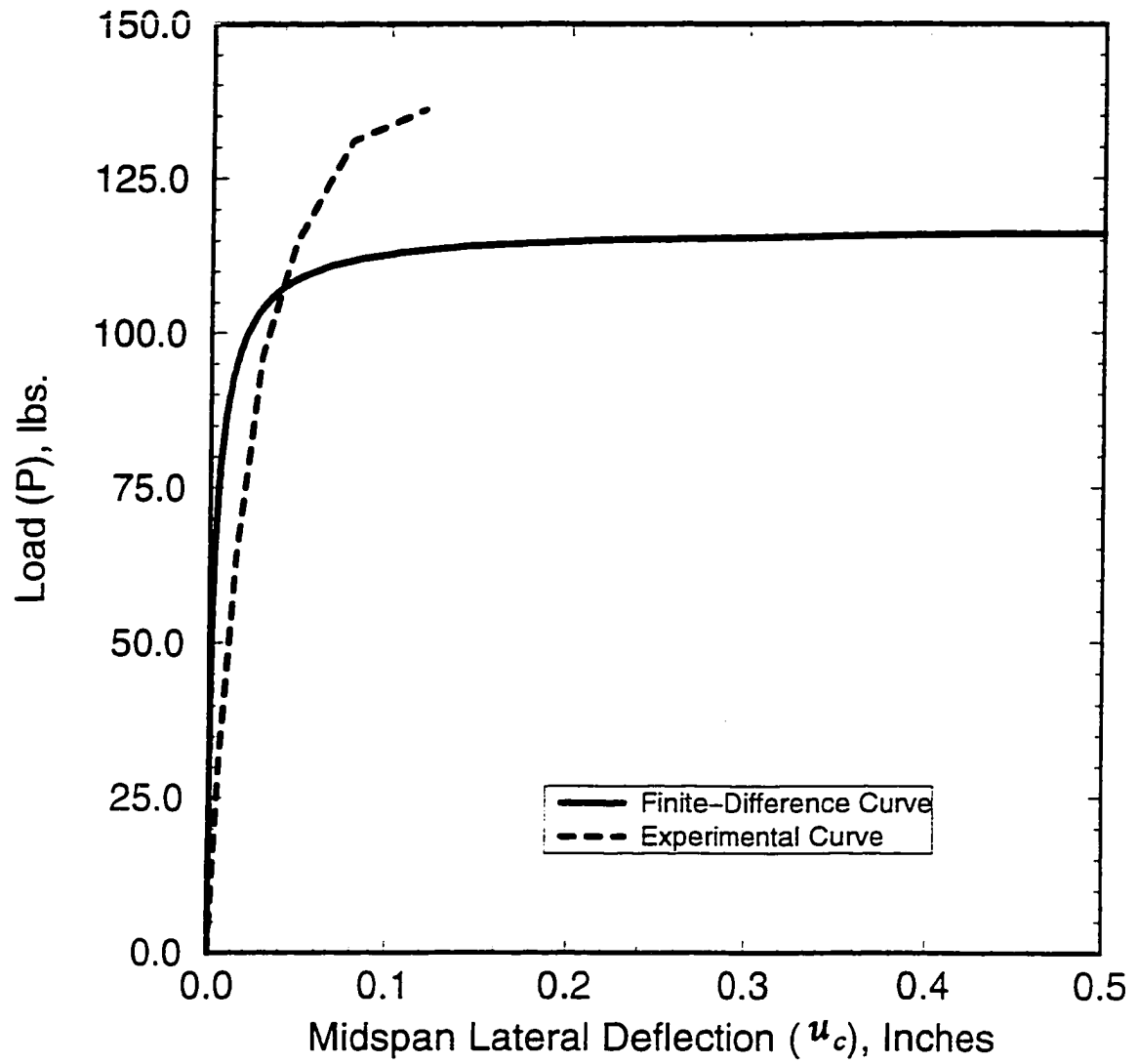


Figure 66. Load (P) versus midspan lateral deflection (u_c) for Test No. CFT4-1

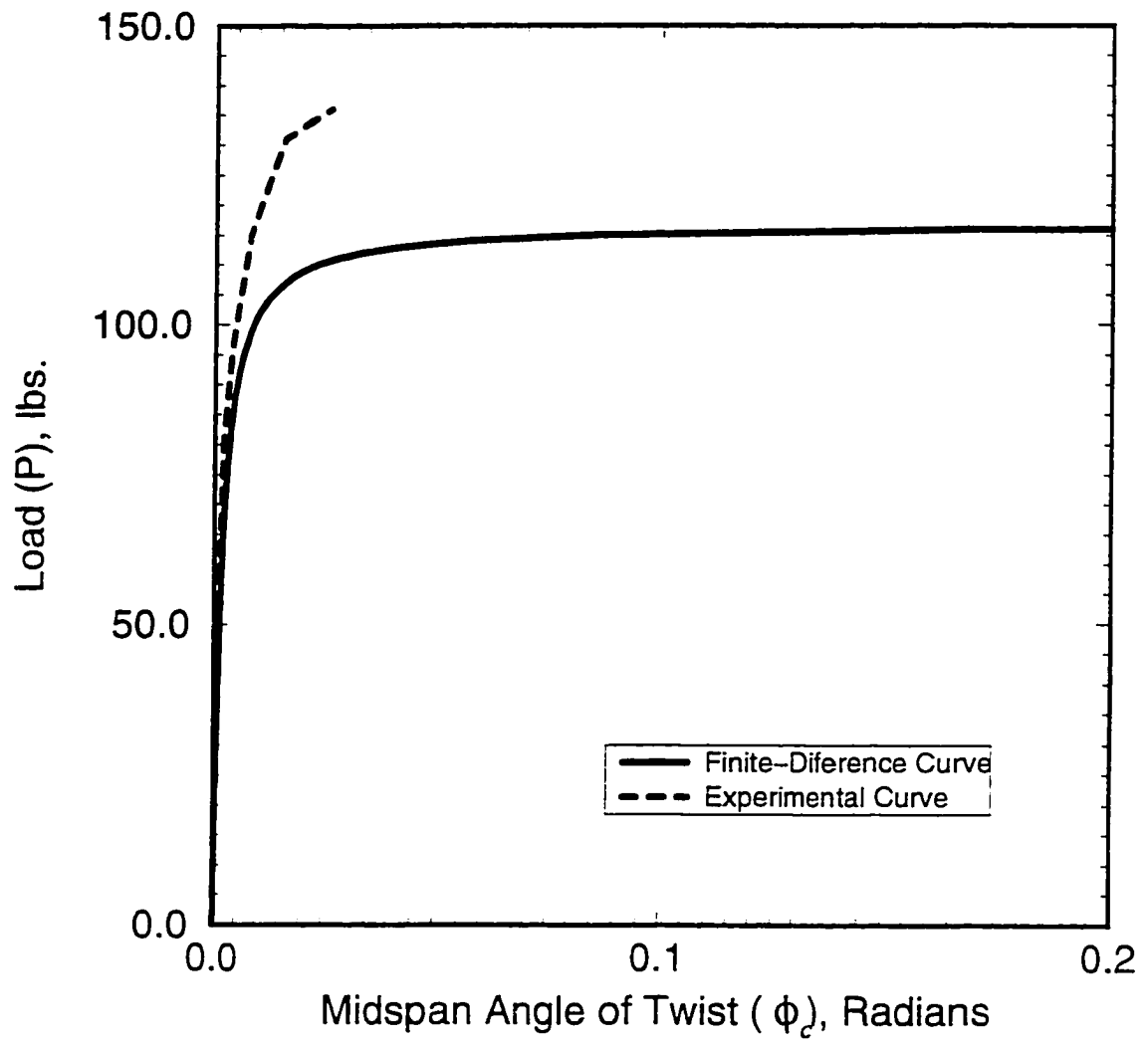


Figure 67. Load (P) versus midspan angle of twist (ϕ_c) for Test No. CFT4-1

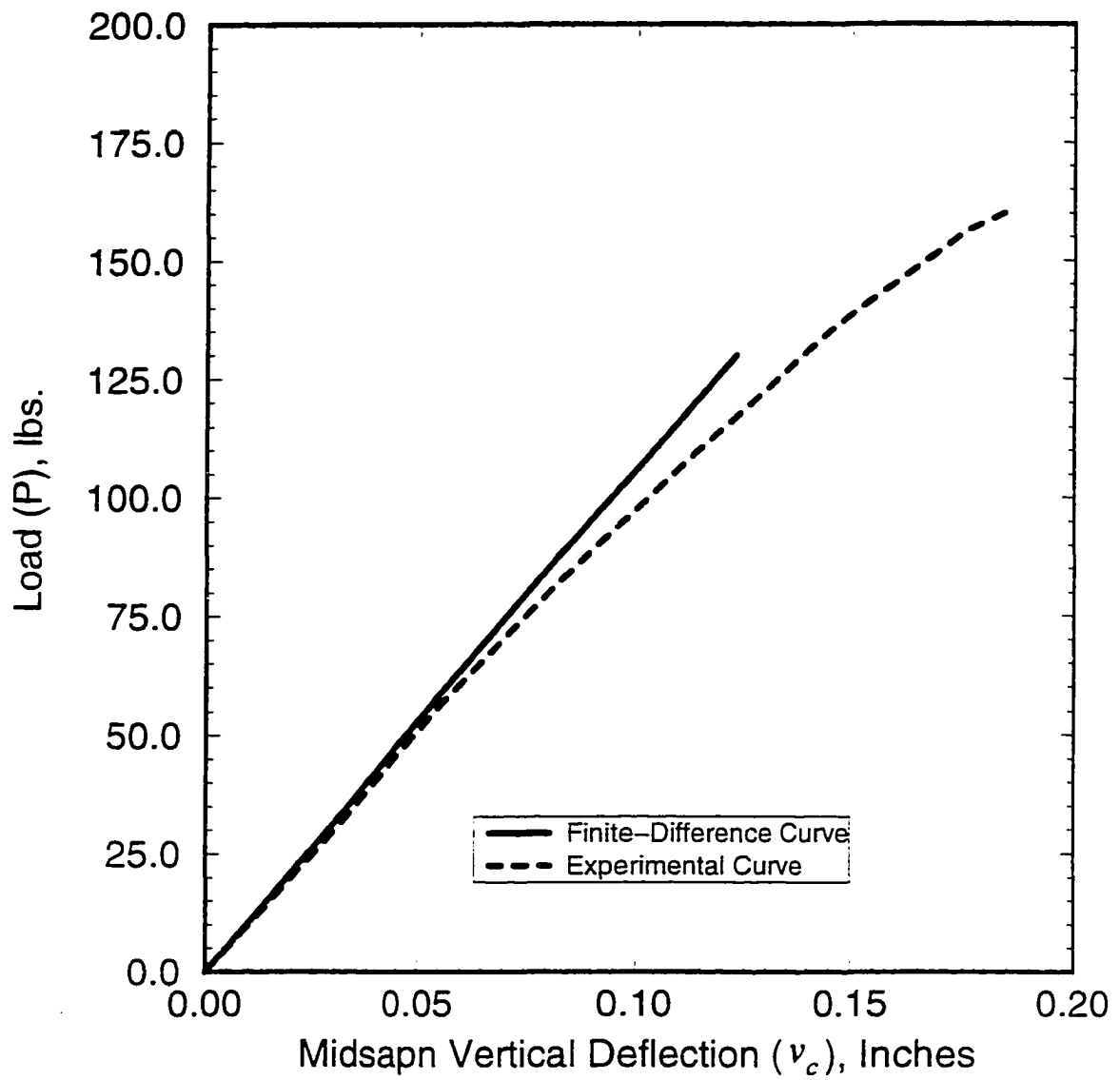


Figure 68. Load (P) versus midspan vertical deflection (v_c) for Test No. CFT4-2

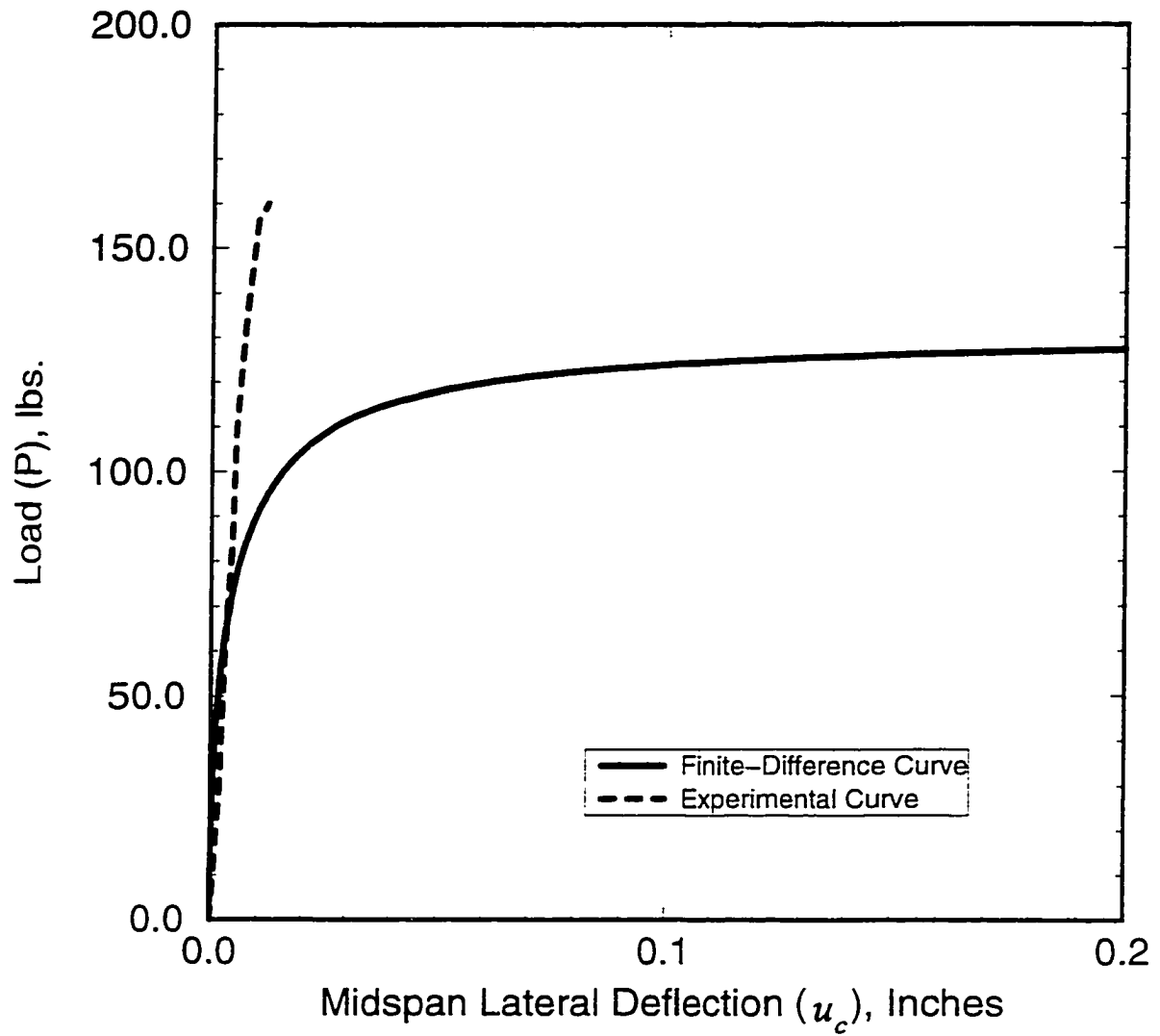


Figure 69. Load (P) versus midspan lateral deflection (u_c) for Test No. CFT4-2

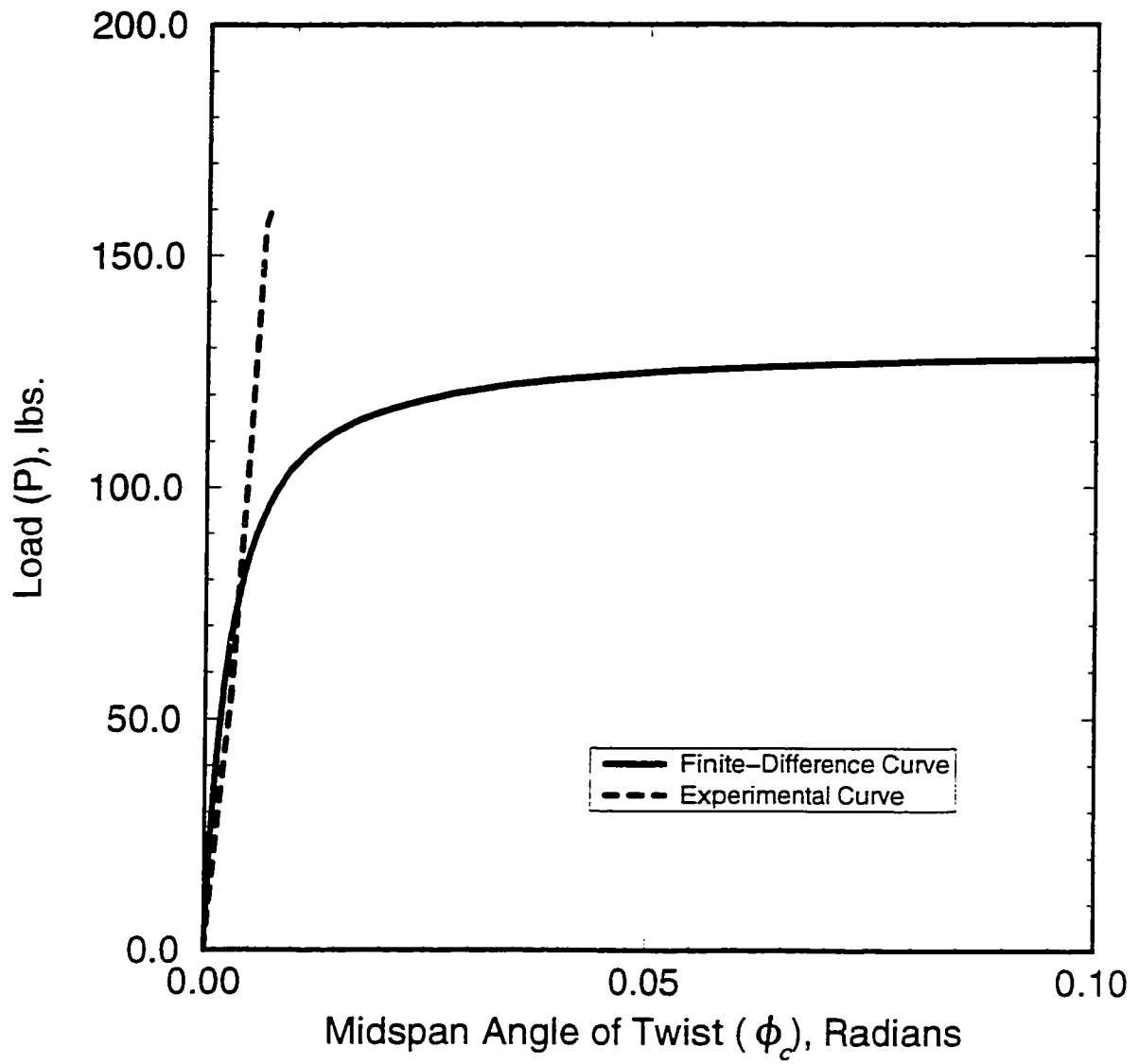


Figure 70. Load (P) versus midspan angle of twist (ϕ_c) for Test No. CFT4-2

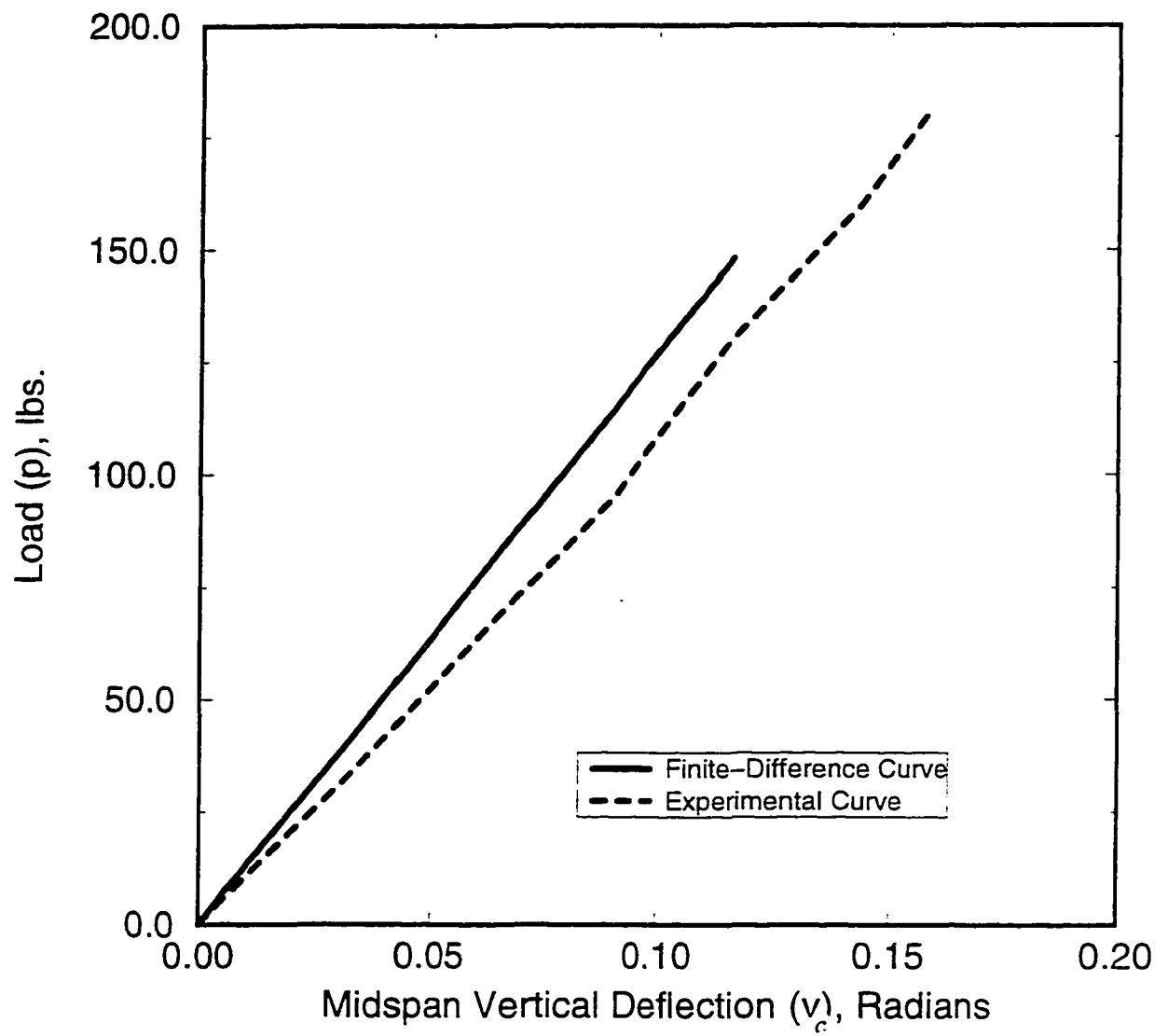


Figure 71. Load (P) versus midspan vertical deflection (v_c) for Test No. CFT4-3

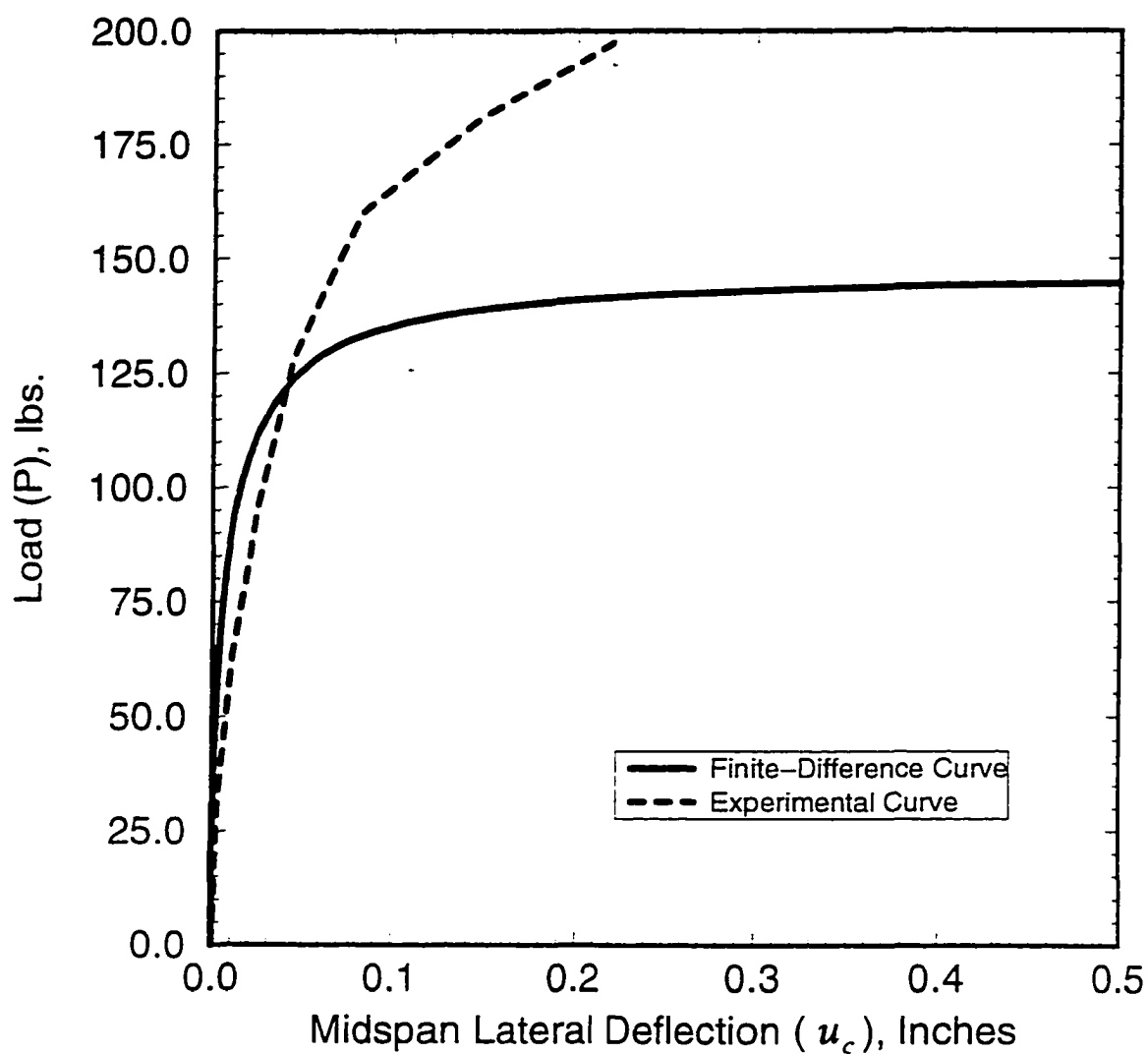


Figure 72. Load (P) versus midspan lateral deflection (u_c) for Test No. CFT4-3

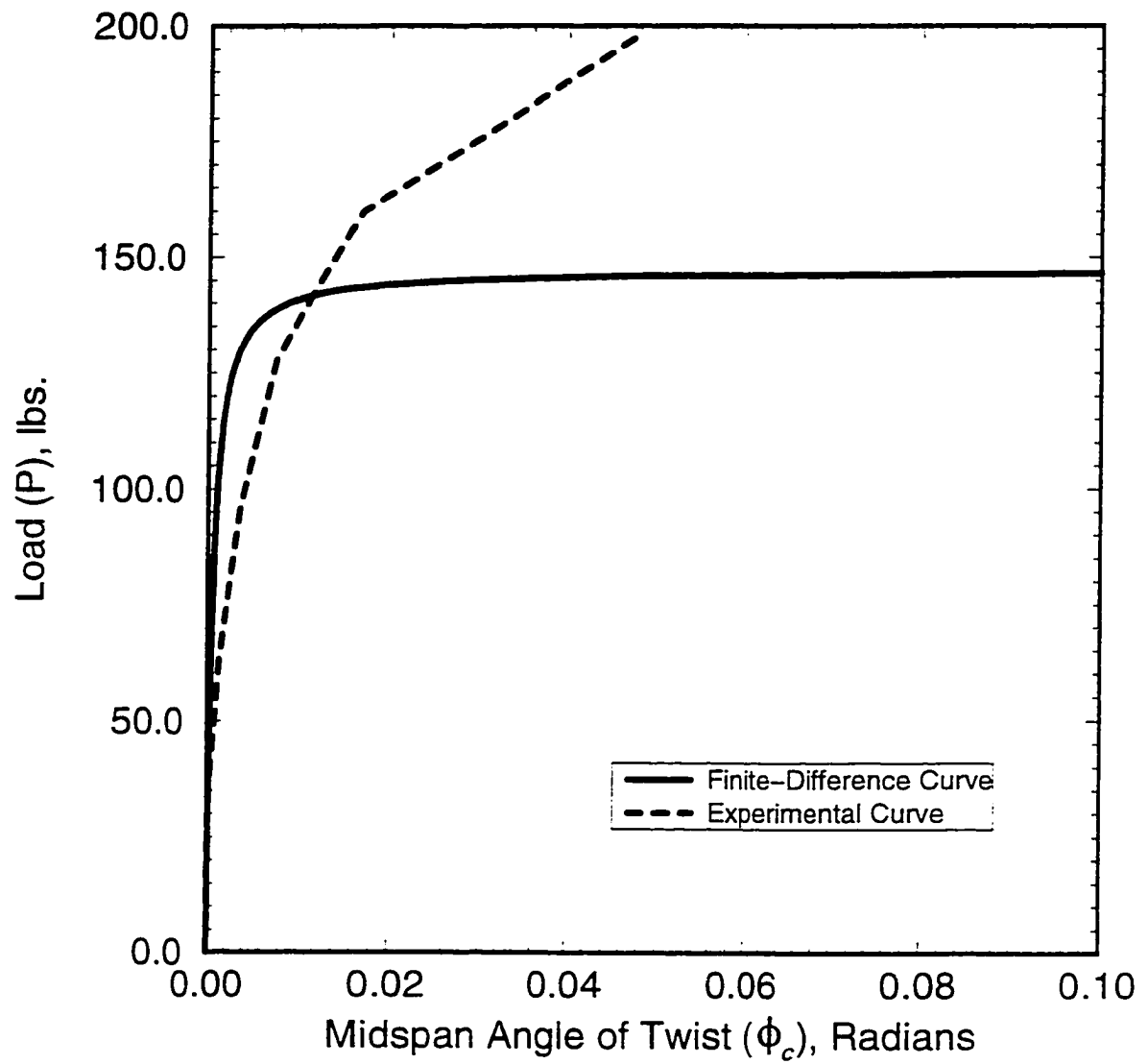


Figure 73. Load (P) versus midspan angle of twist (ϕ_c) for Test No. CFT4-3

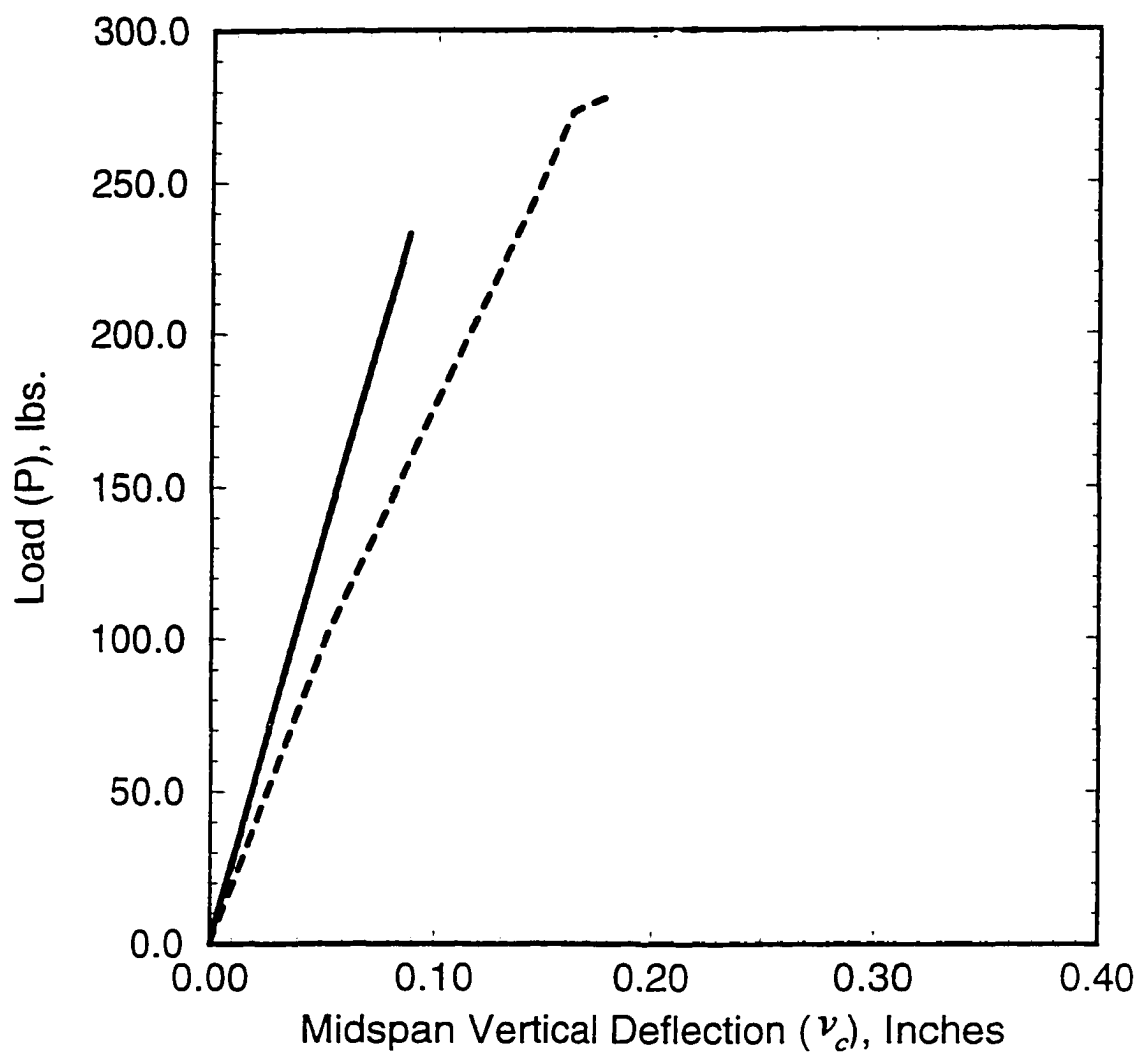


Figure 74. Load (P) versus midspan vertical deflection (v_c) for Test No. CFT4-4

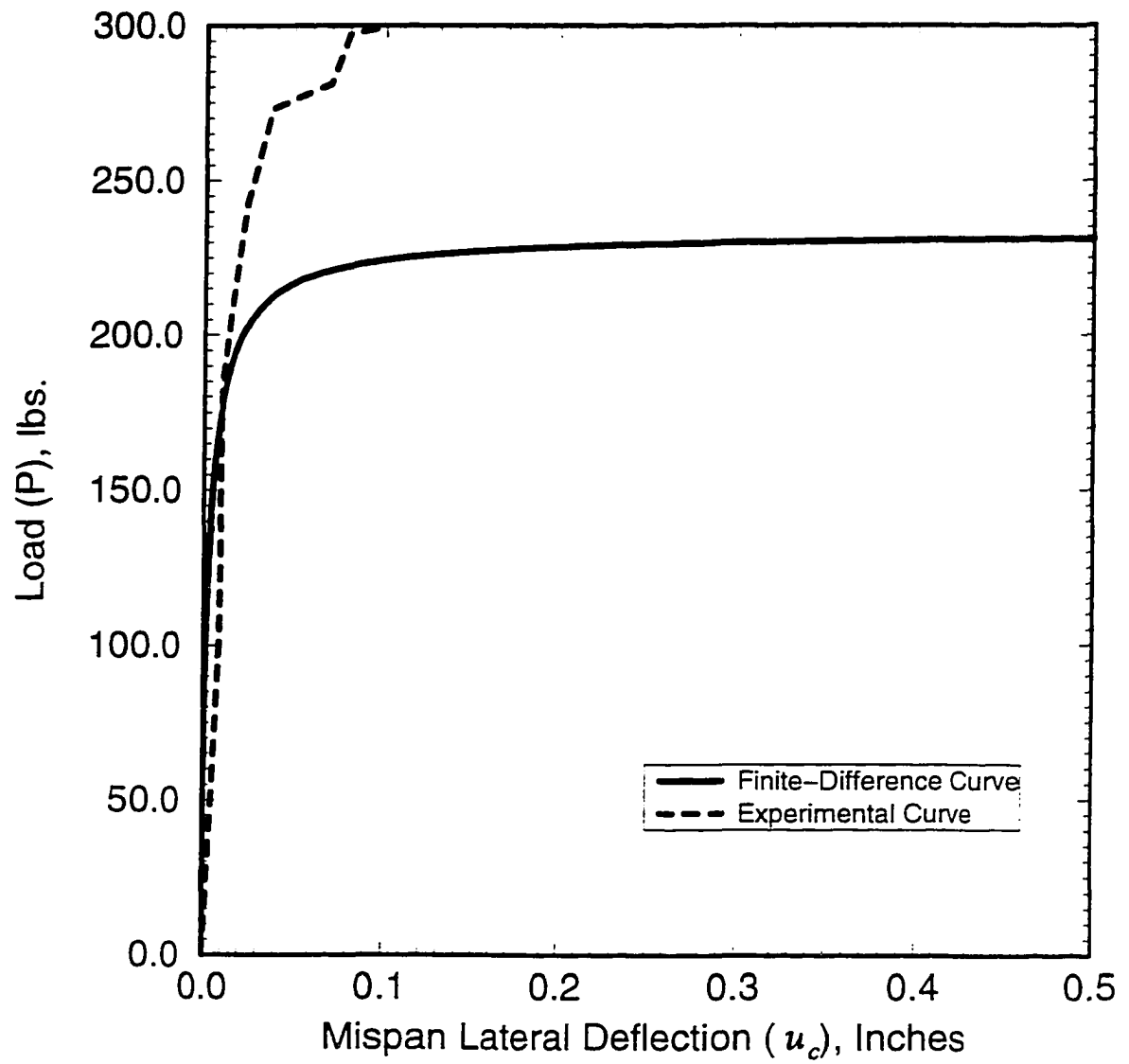


Figure 75. Load (P) versus midspan lateral deflection (u_c) for Test No. CFT4-4

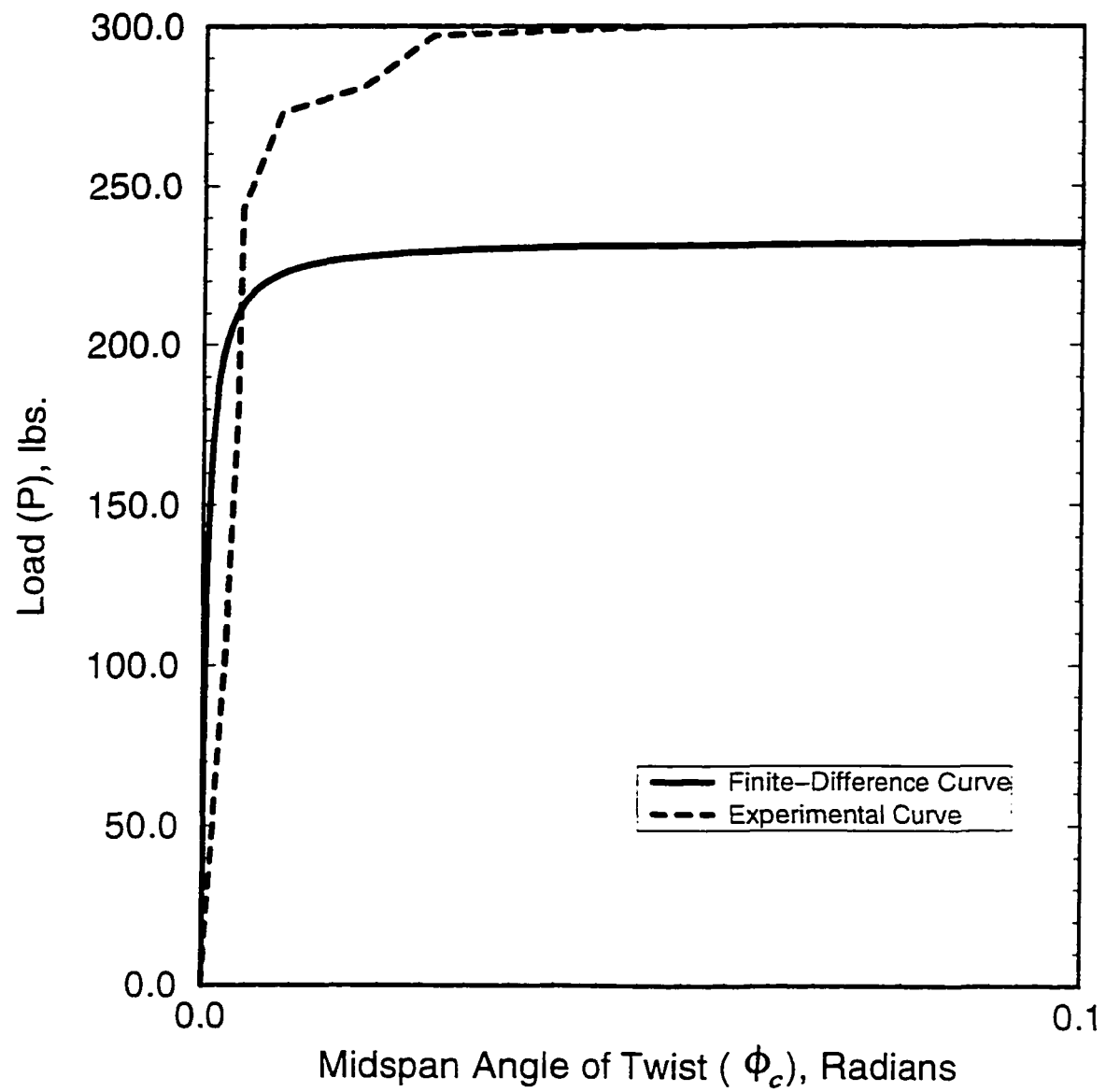


Figure 76. Load (P) versus midspan angle of twist (ϕ_c) for Test No. CFT4-4

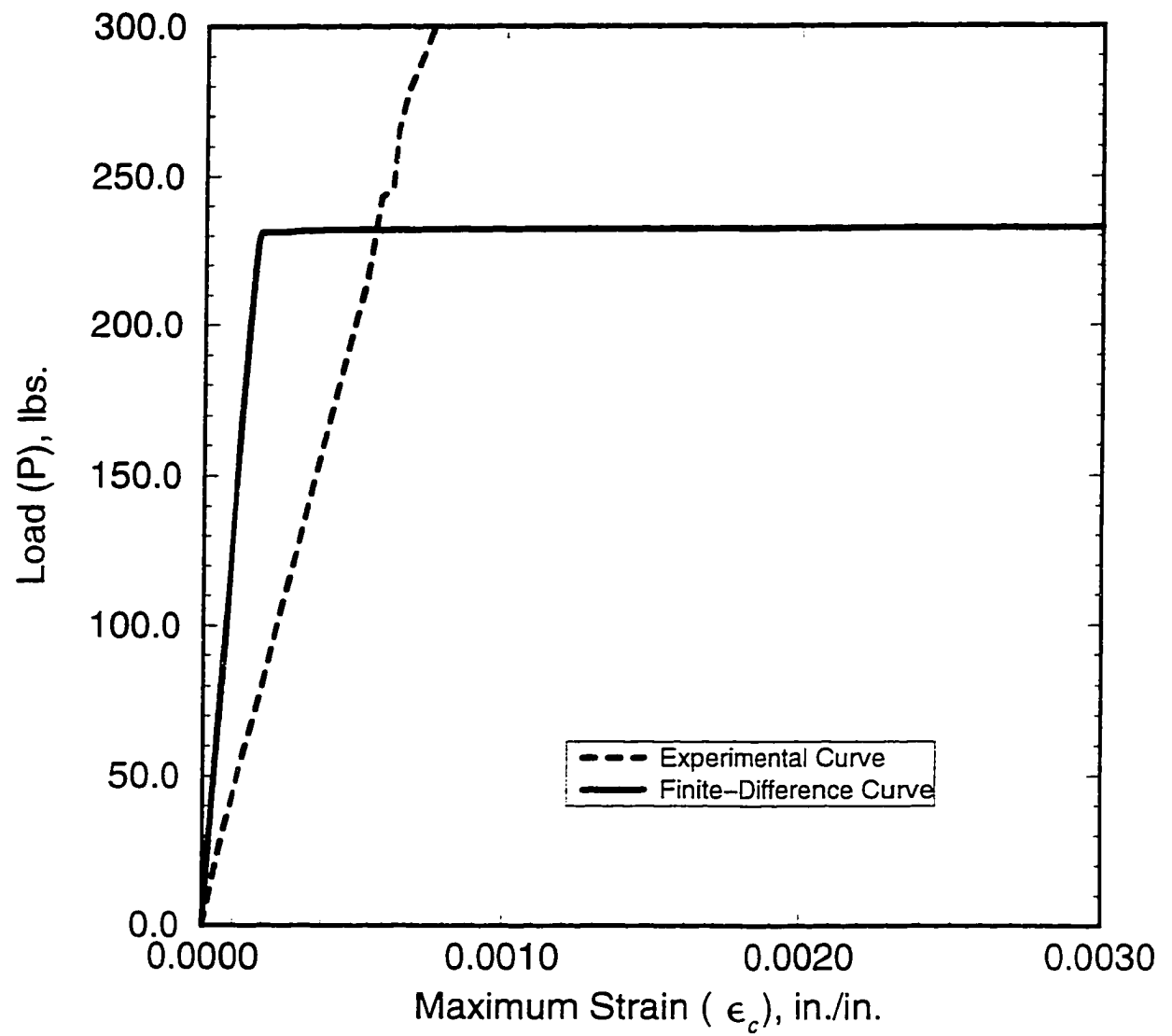


Figure 77. Load (P) versus maximum strain (ϵ_c) for Test No. CFT4-4

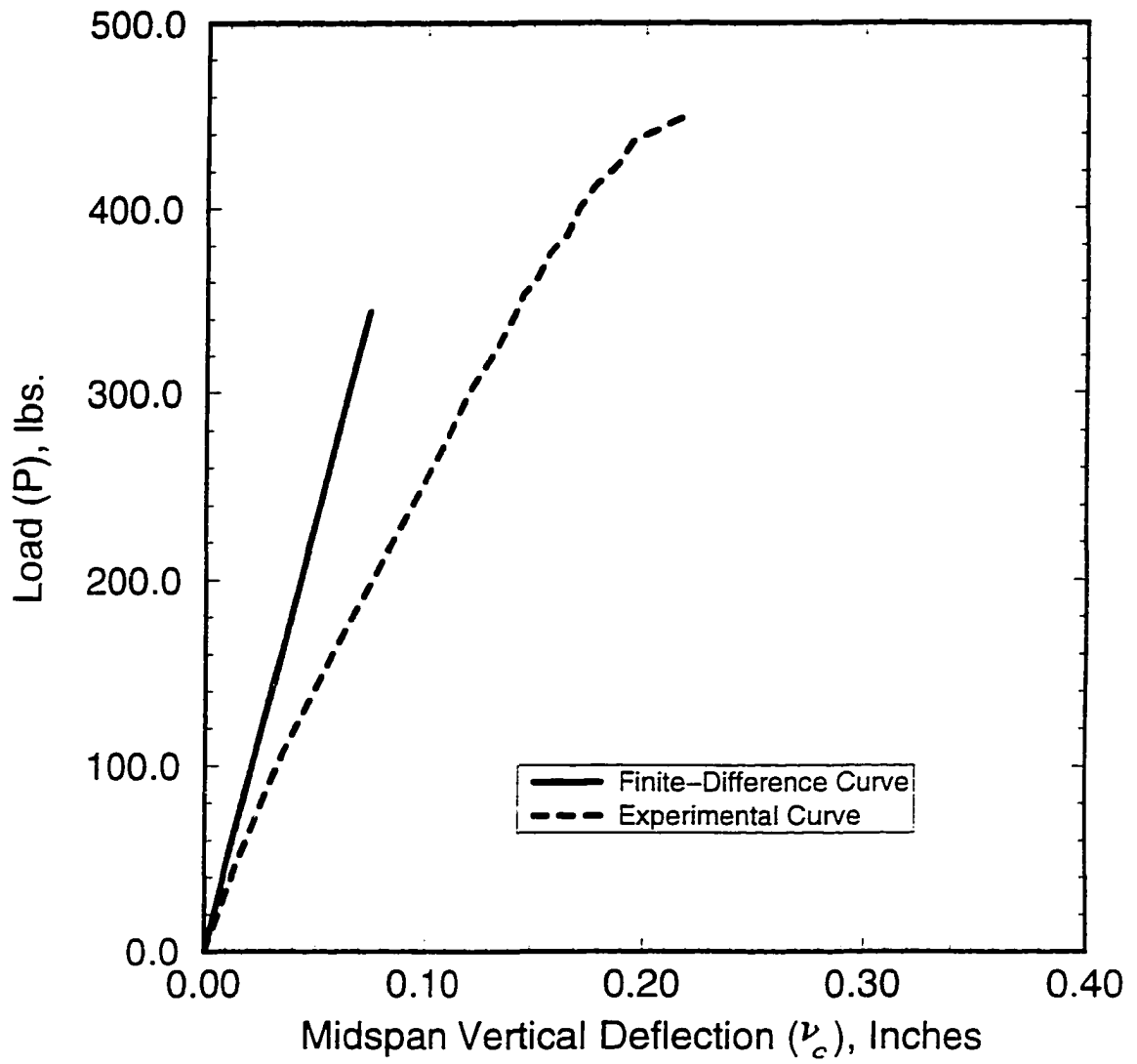


Figure 78. Load (P) versus midspan vertical deflection (v_c) for Test No. CFT4-5

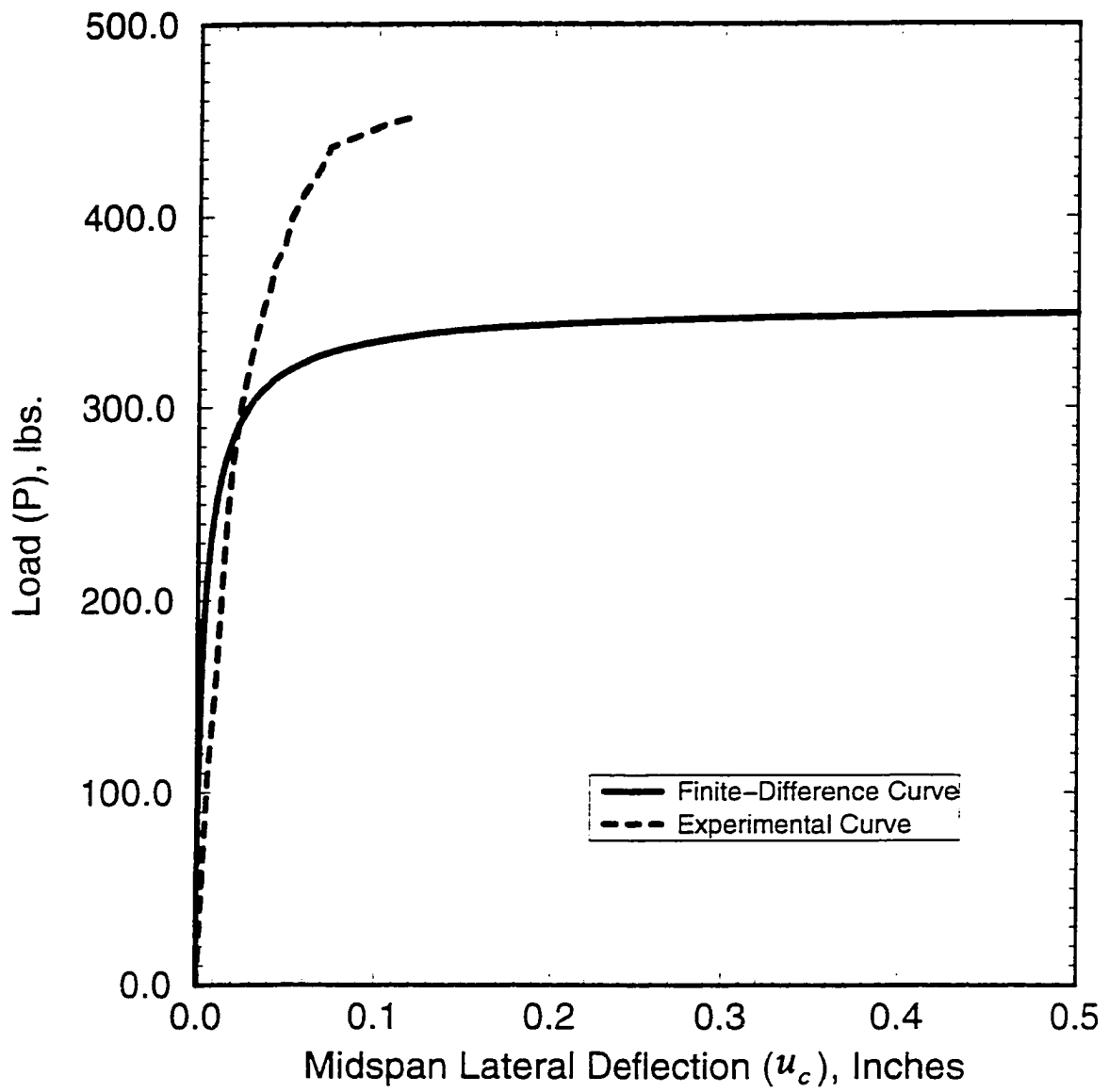


Figure 79. Load (P) versus midspan lateral deflection (u_c) for Test No. CFT4-5

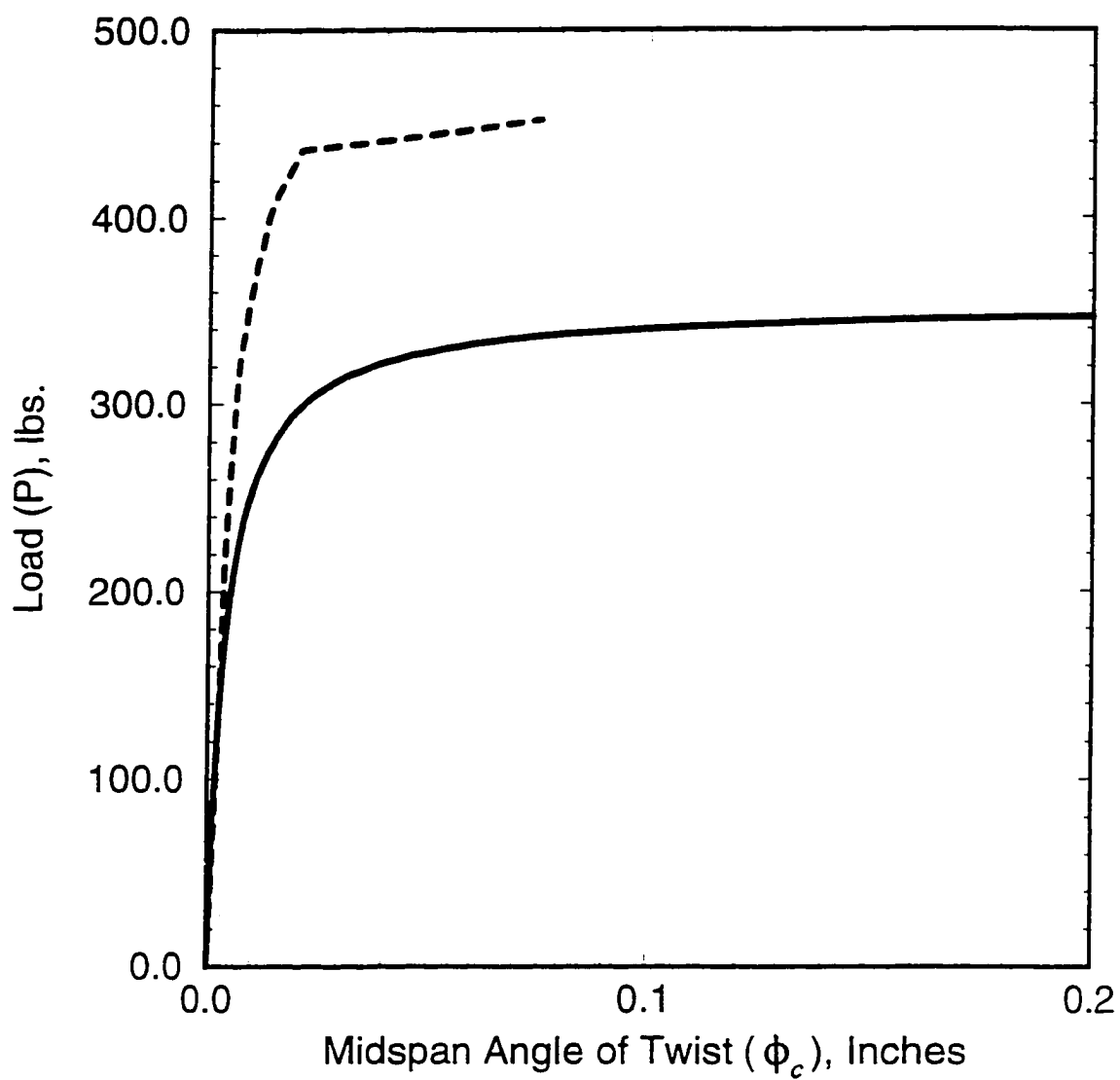


Figure 80. Load (P) versus midspan angle of twist (ϕ_c) for Test No. CFT4-5

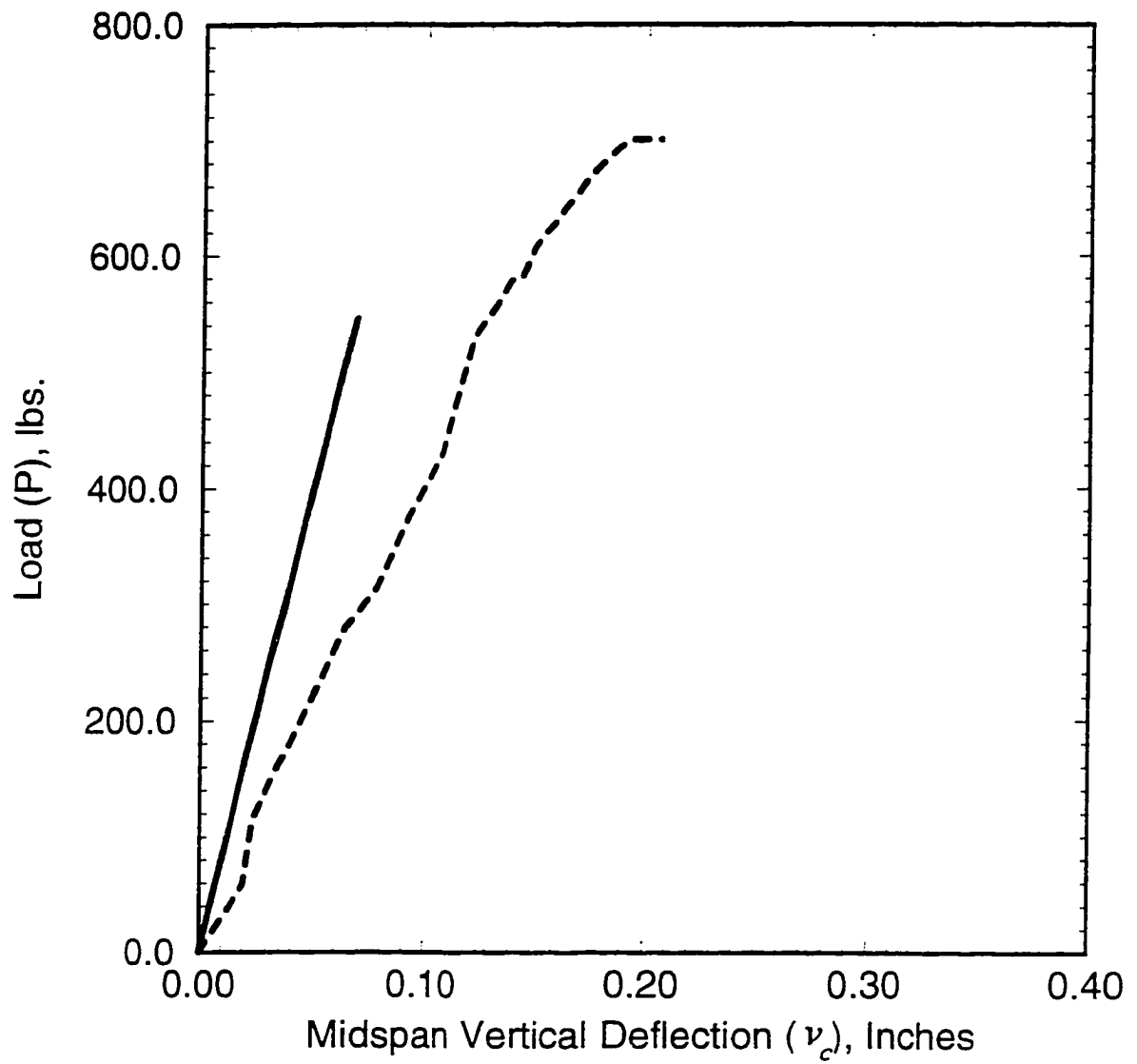


Figure 81. Load (P) versus midspan vertical deflection (v_c) for Test No. CFT4-6

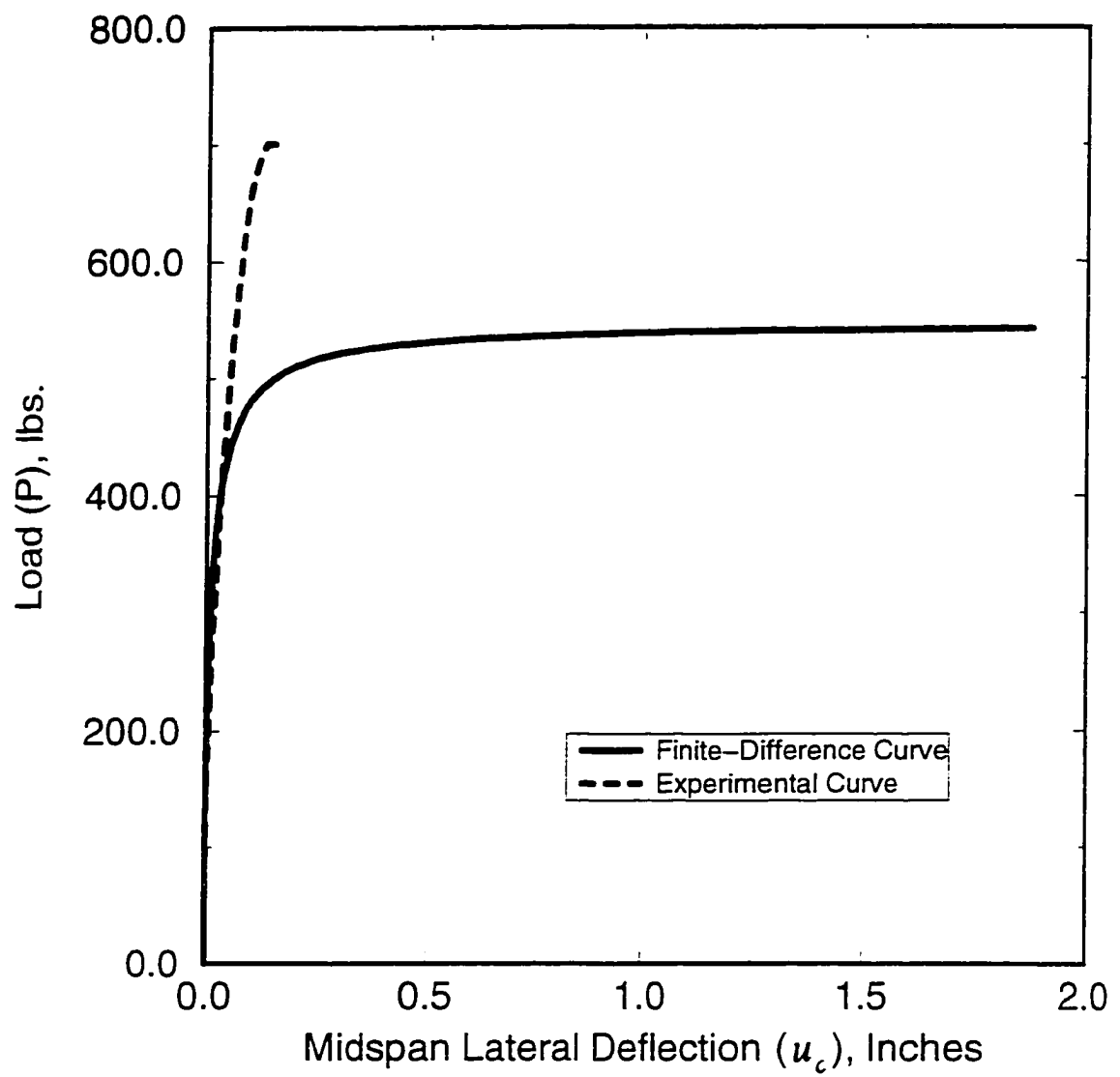


Figure 82. Load (P) versus midspan lateral deflection (u_c) for Test No. CFT4-6

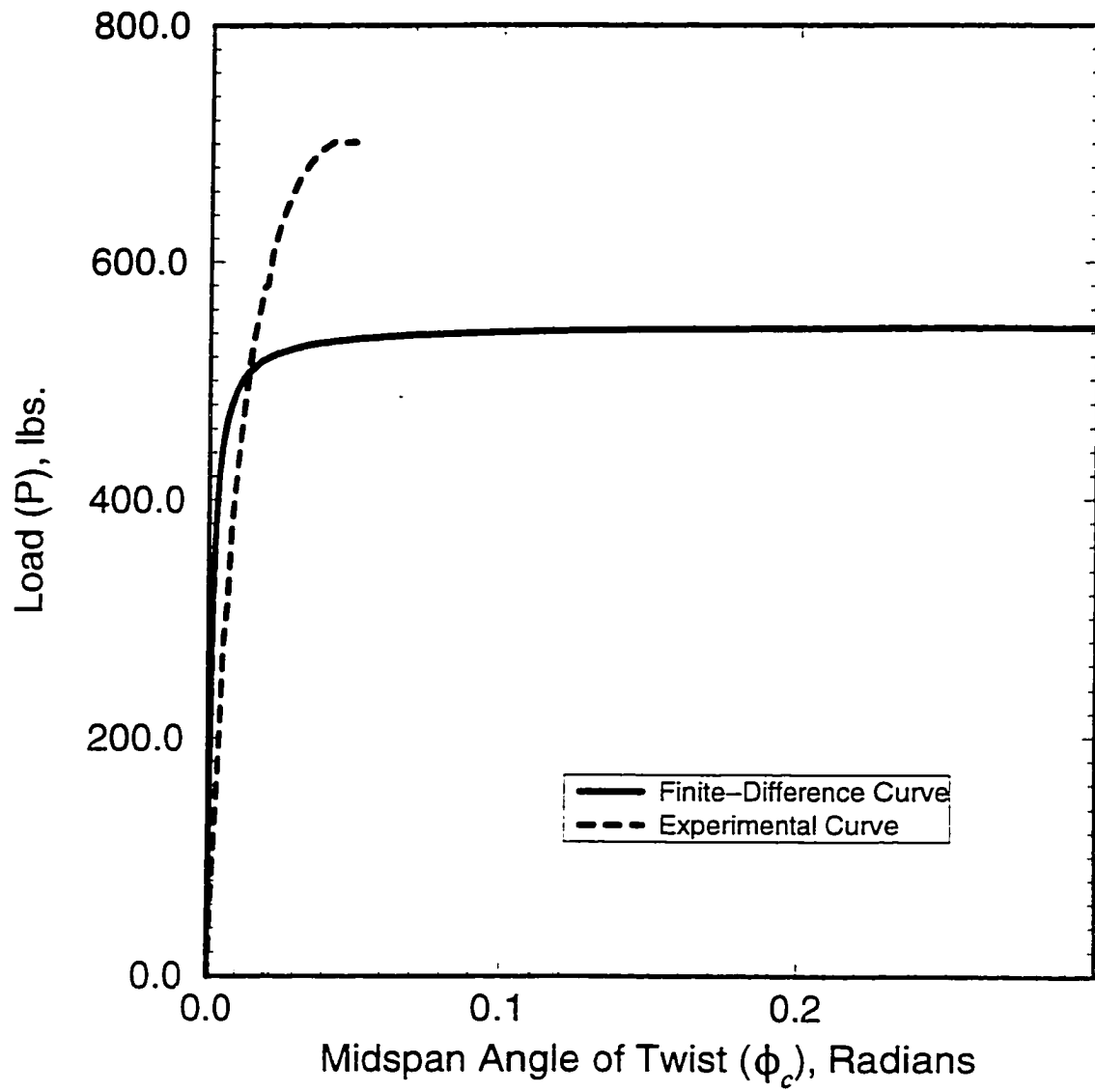


Figure 83. Load (P) versus midspan angle of twist (ϕ_c) for Test No. CFT4-6

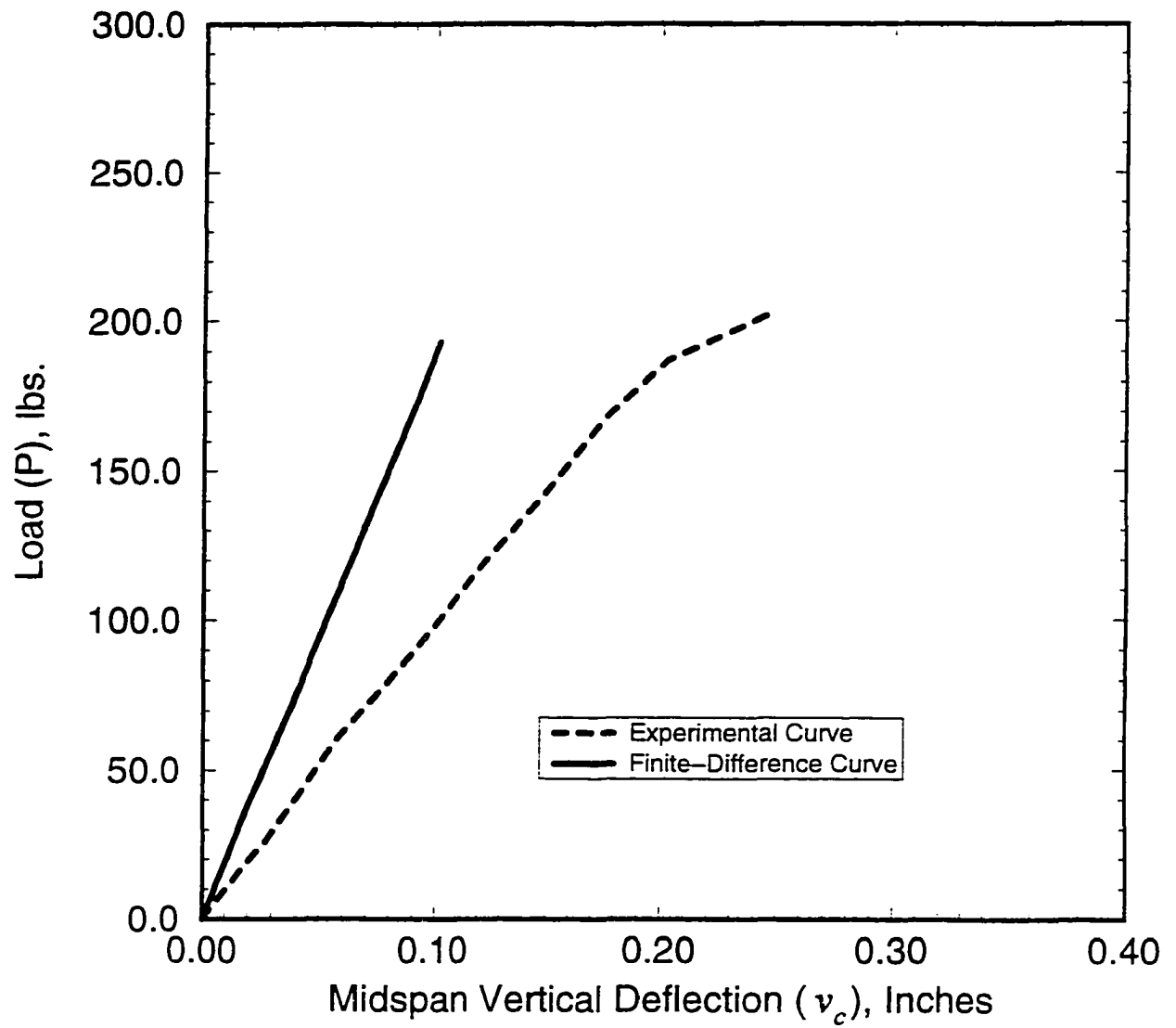


Figure 84. Load (P) versus midspan vertical deflection (v_c) for Test No. CFT4-7

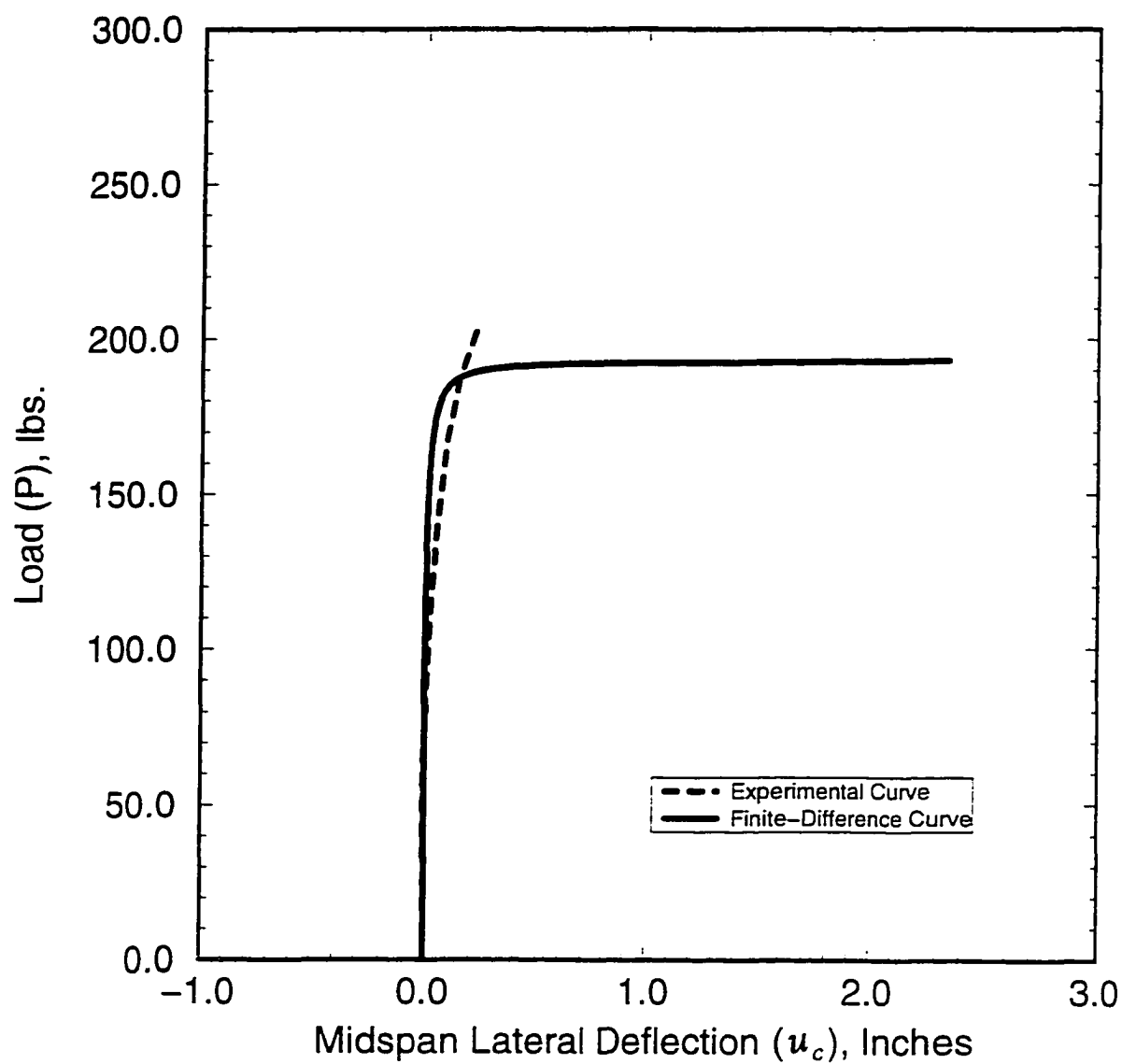


Figure 85. Load (P) versus midspan lateral deflection (u_c) for Test No. CFT4-7

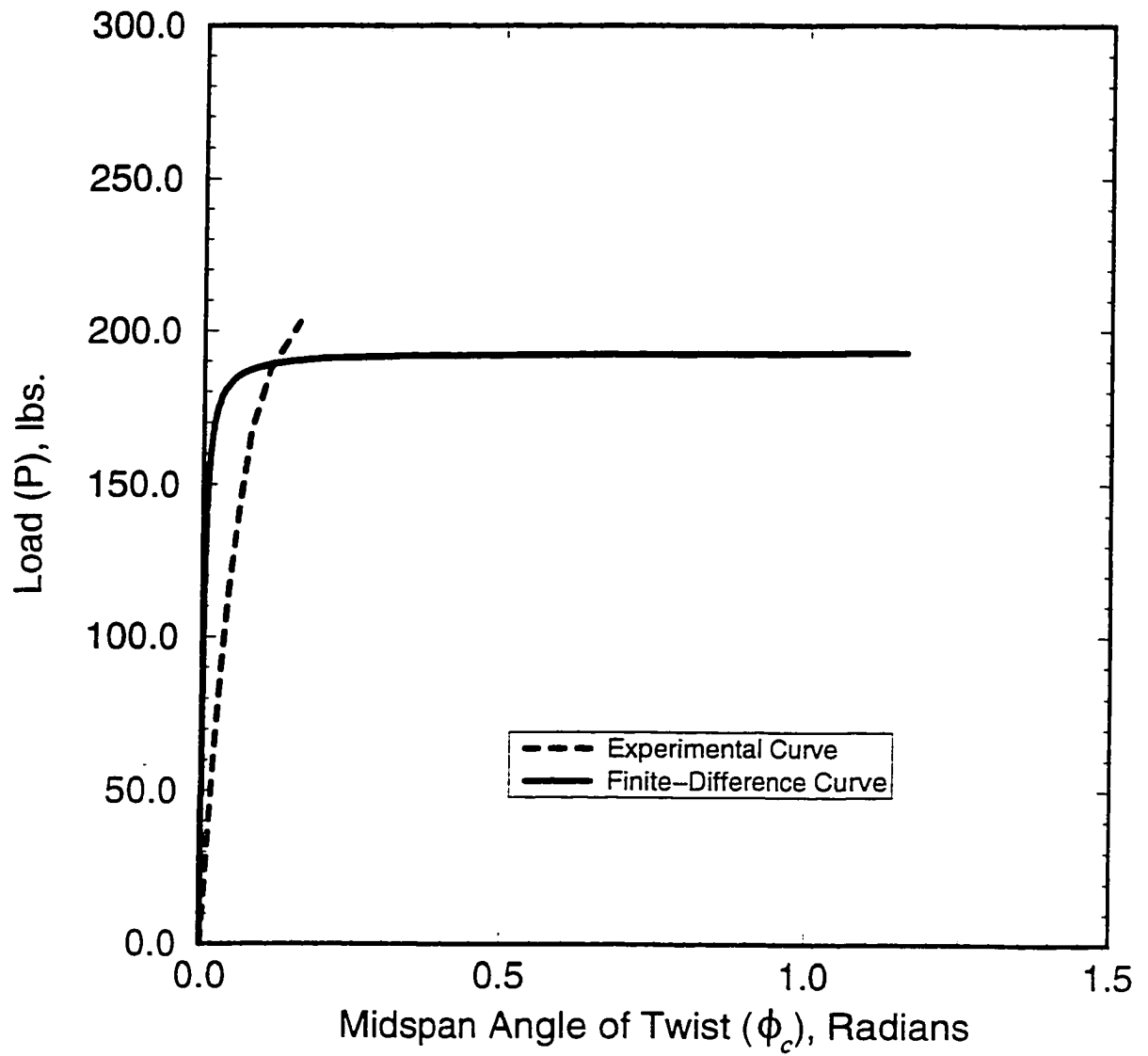


Figure 86. Load (P) versus midspan angle of twist (ϕ_c) for Test No. CFT4-7

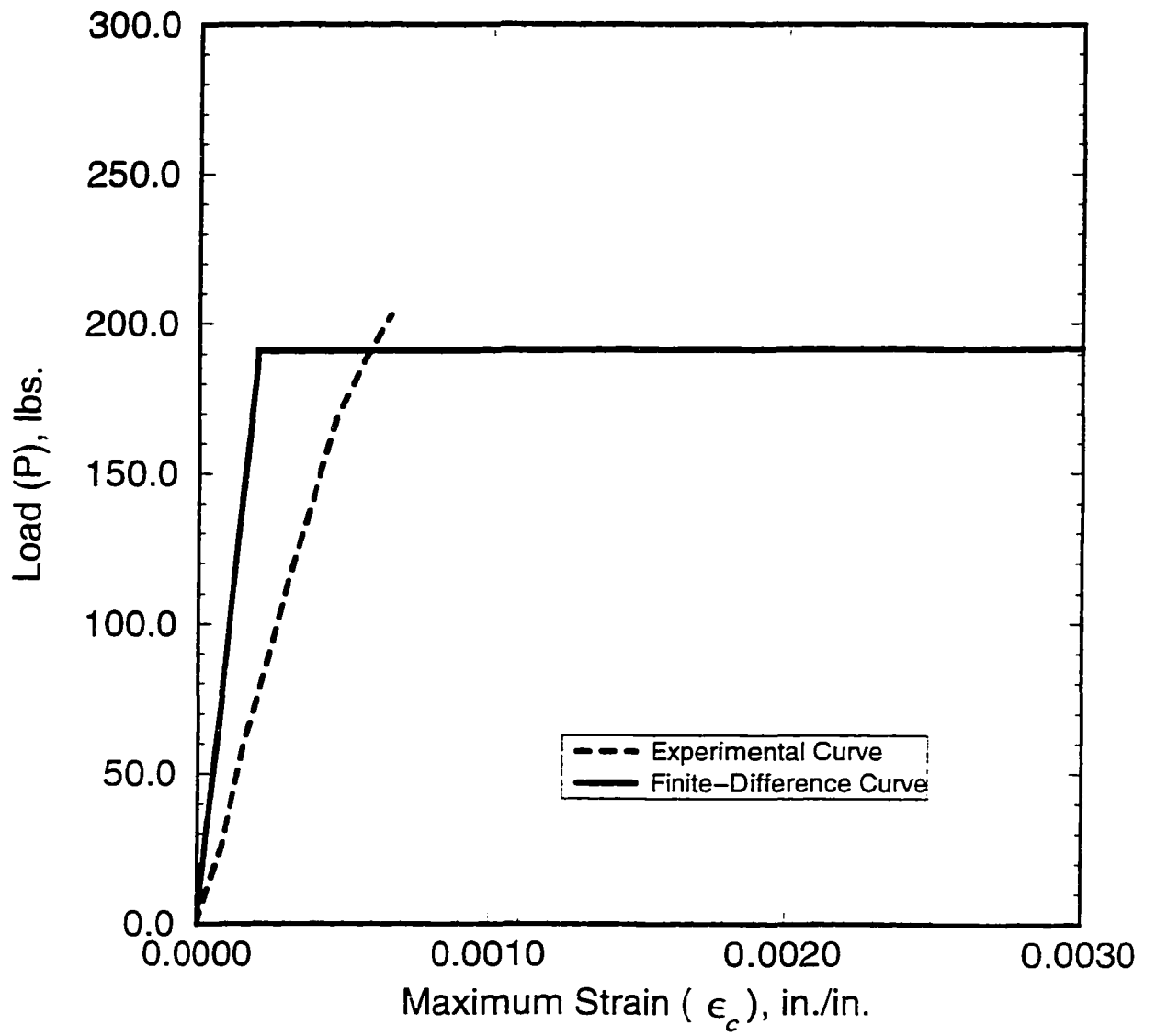


Figure 87. Load (P) versus maximum strain (ϵ_c) for Test No.CFT4-7

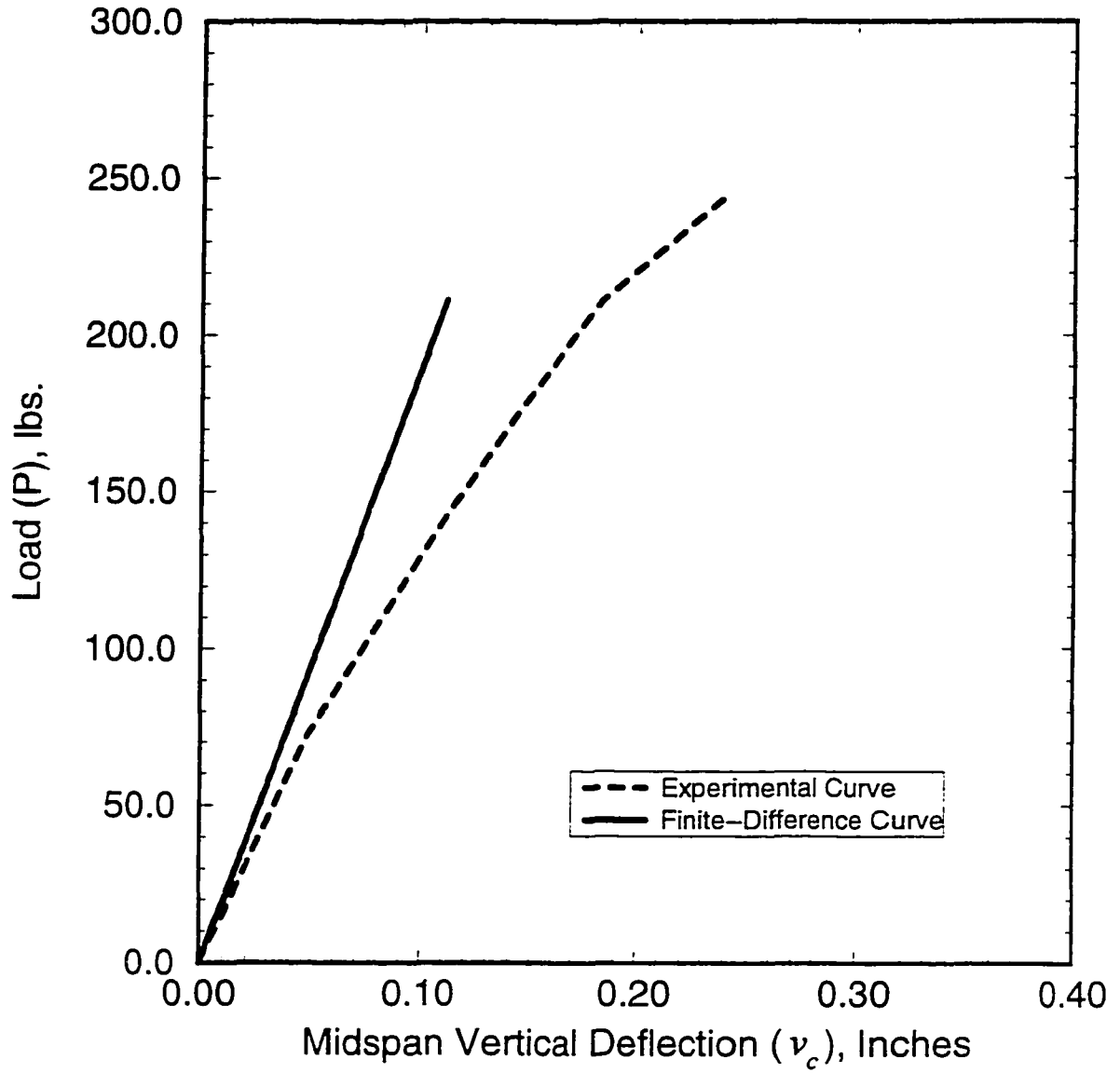


Figure 88. Load (P) versus midspan vertical deflection (v_c) for Test No.CFT4-8

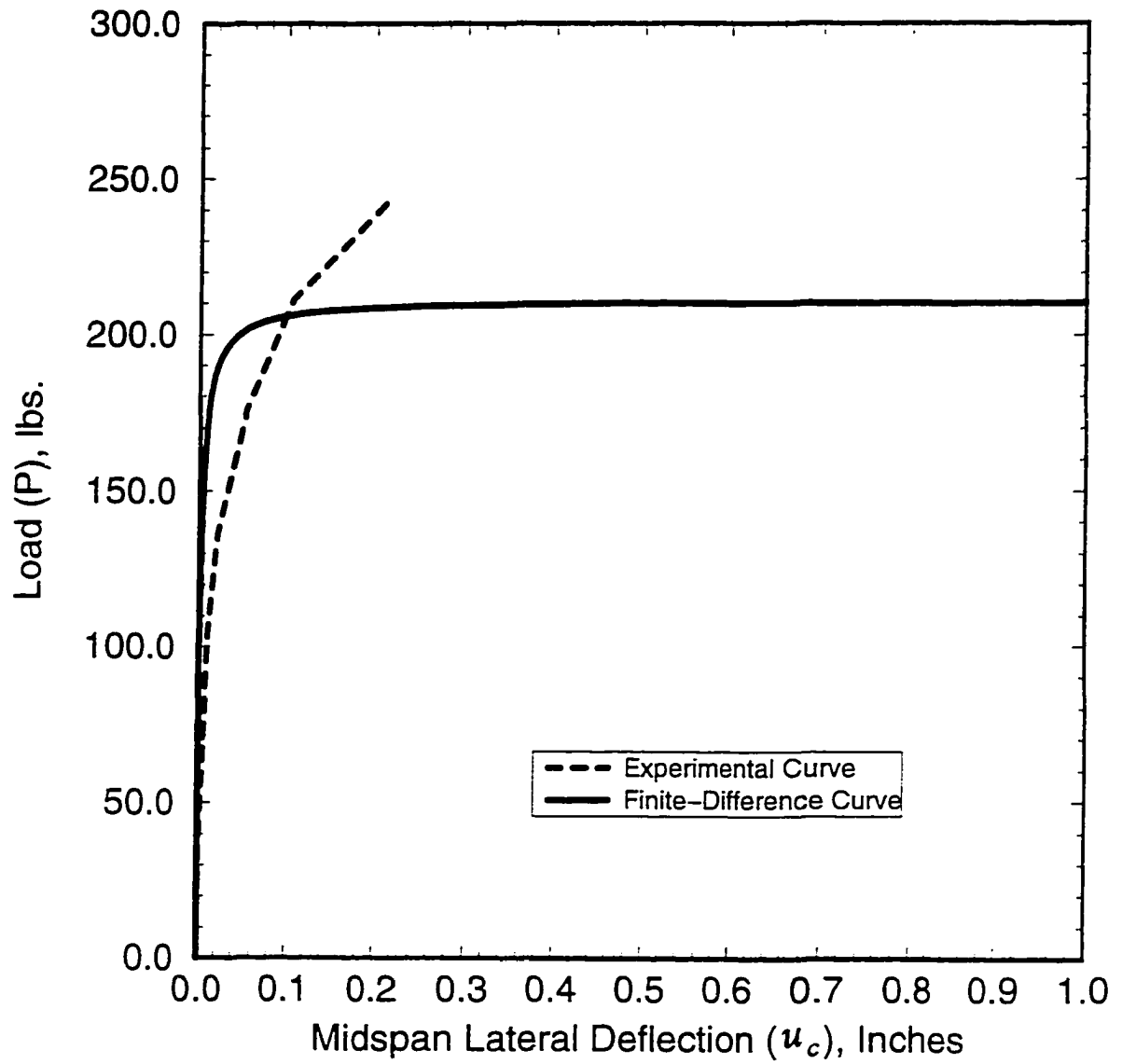


Figure 89. Load (P) versus midspan lateral deflection (u_c) for Test No. CFT4-8

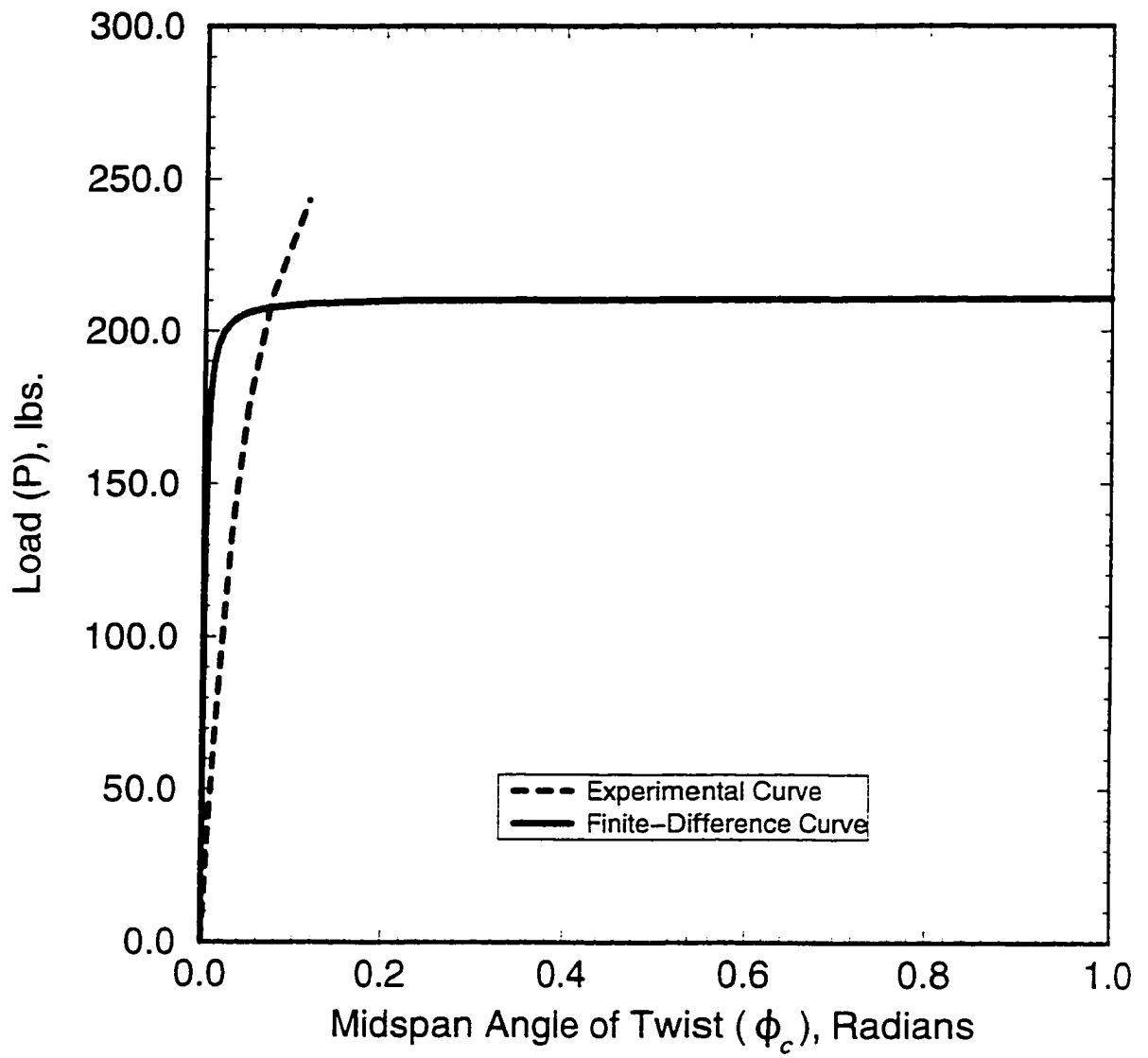


Figure 90. Load (P) versus midspan angle of twist (ϕ_c) for Test No. CFT4-8

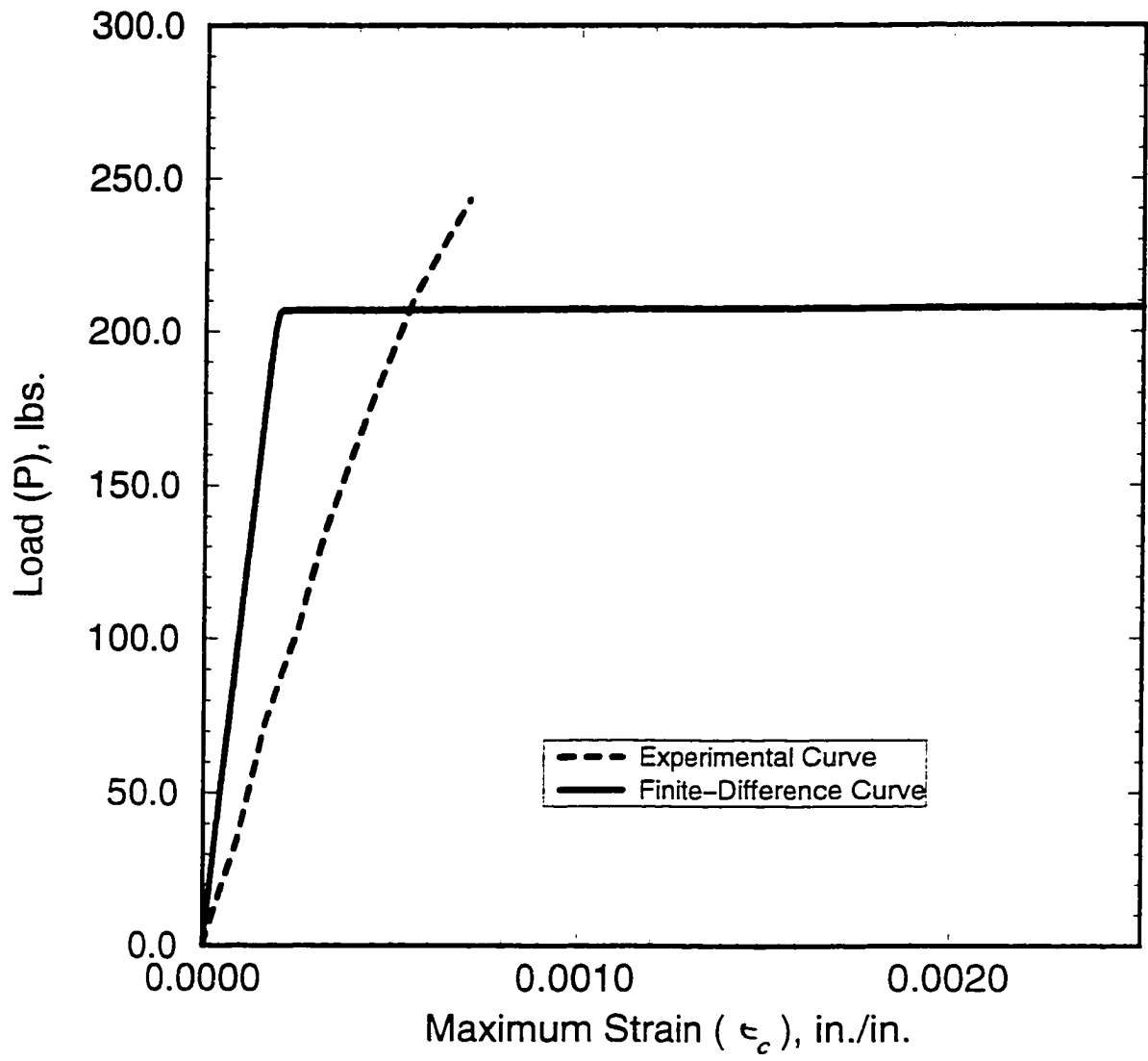


Figure 91. Load (P) versus maximum strain (ϵ_c) for Test No. CFT4-8

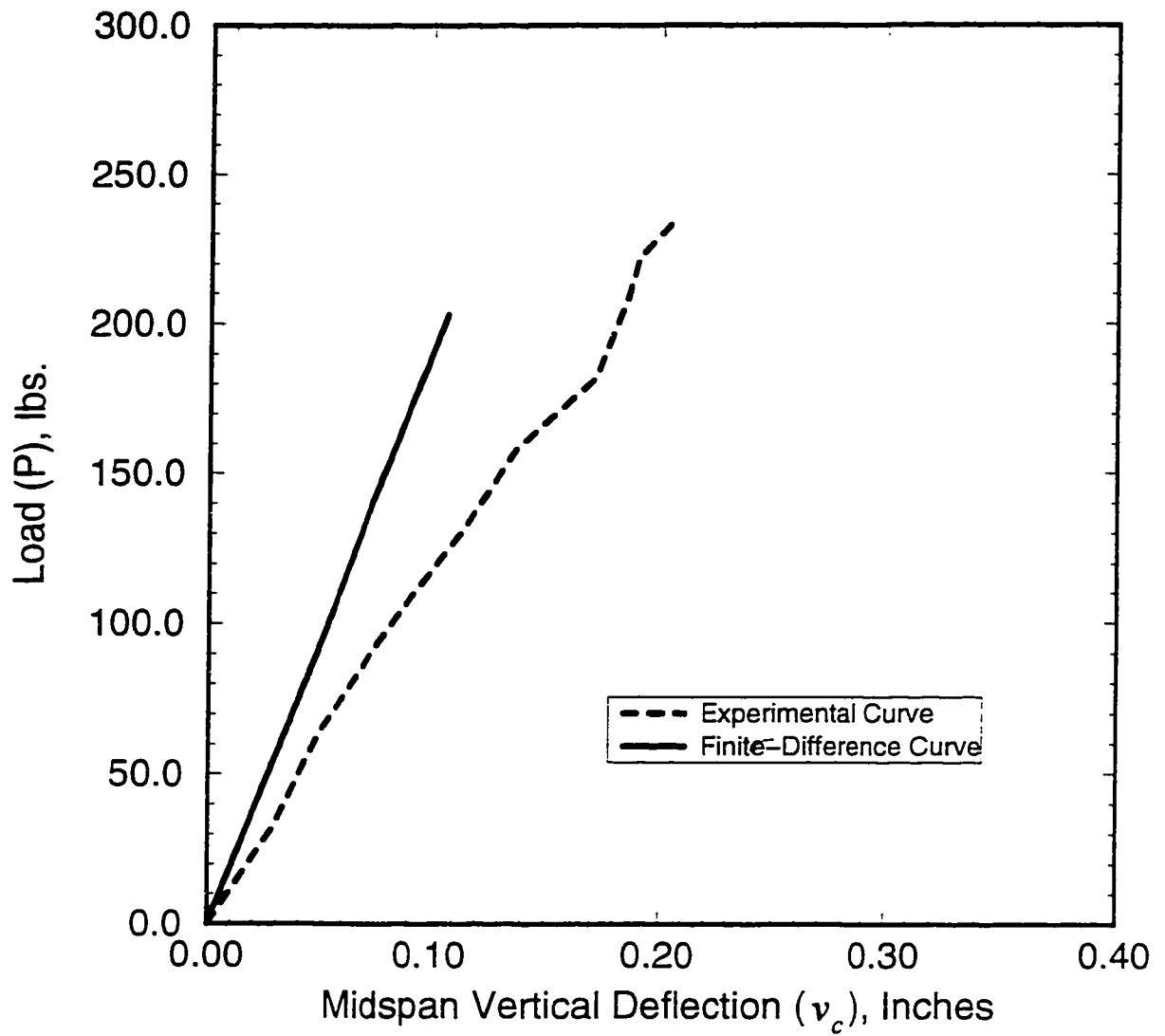


Figure 92. Load (P) versus midspan vertical deflection (v_c) for Test No. CFT4-9

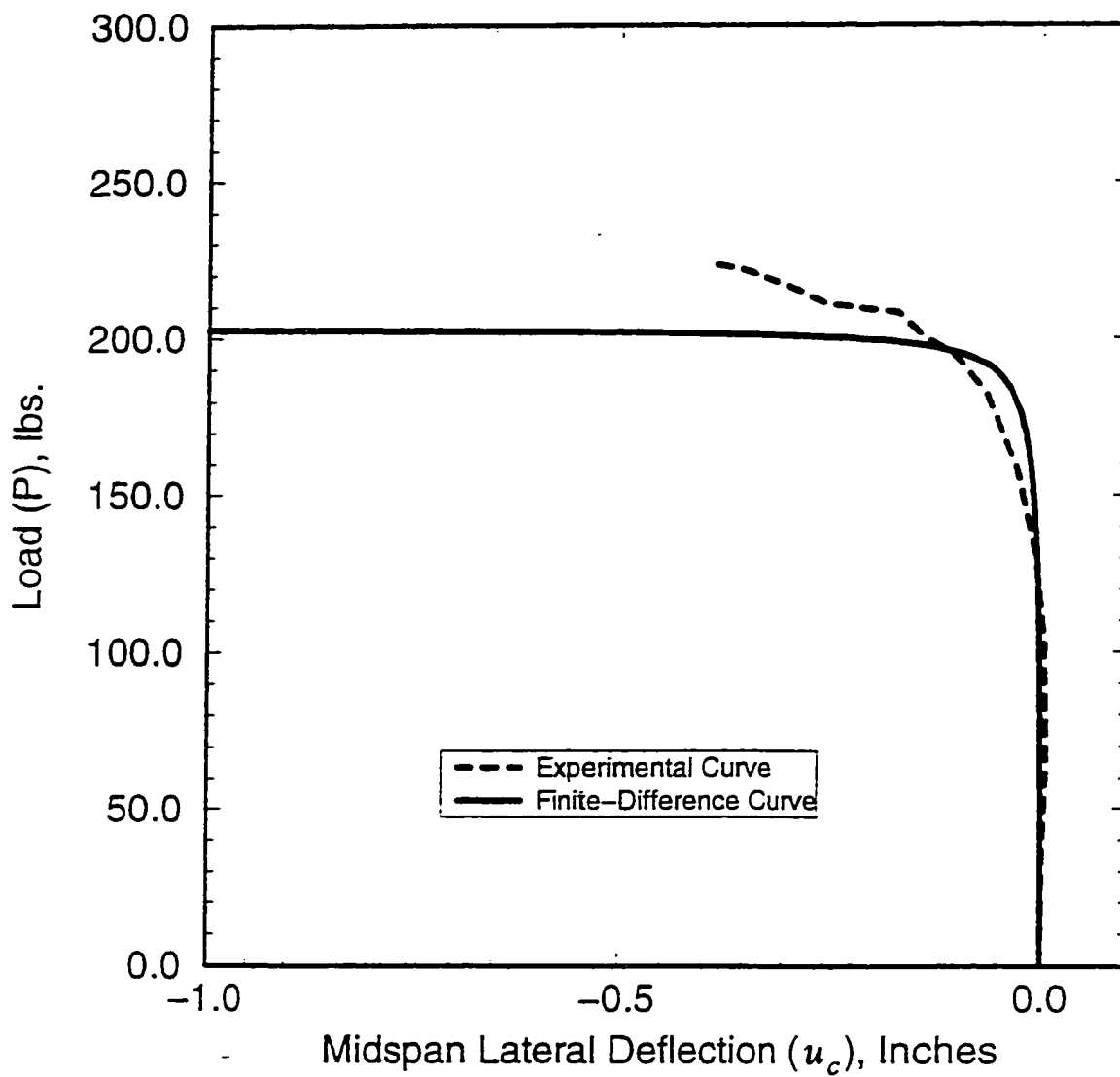


Figure 93. Load (P) versus midspan lateral deflection (u_c) for Test No. CFT4-9

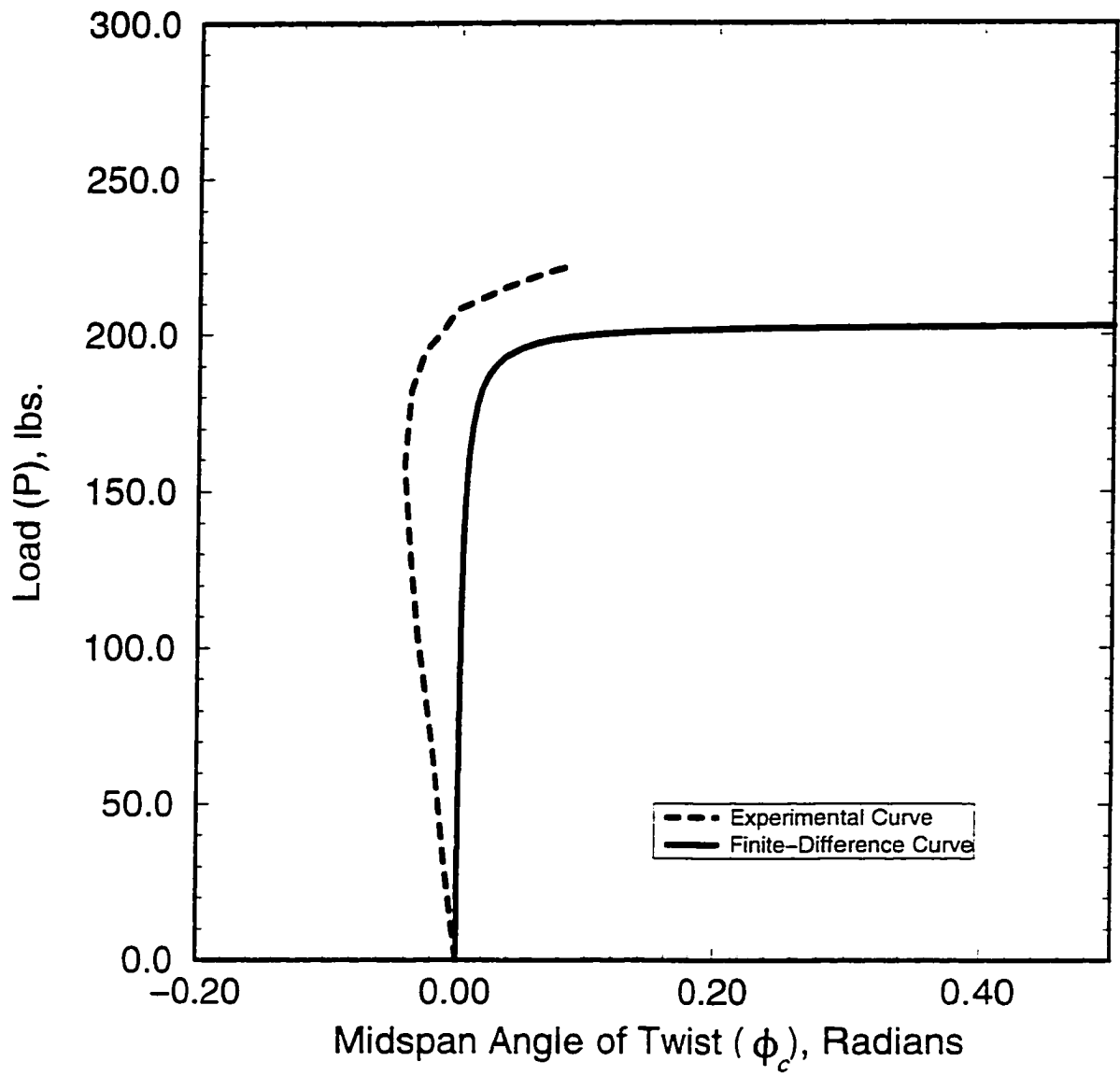


Figure 94. Load (P) versus midspan angle of twist (ϕ_c) for Test No. CFT4-9

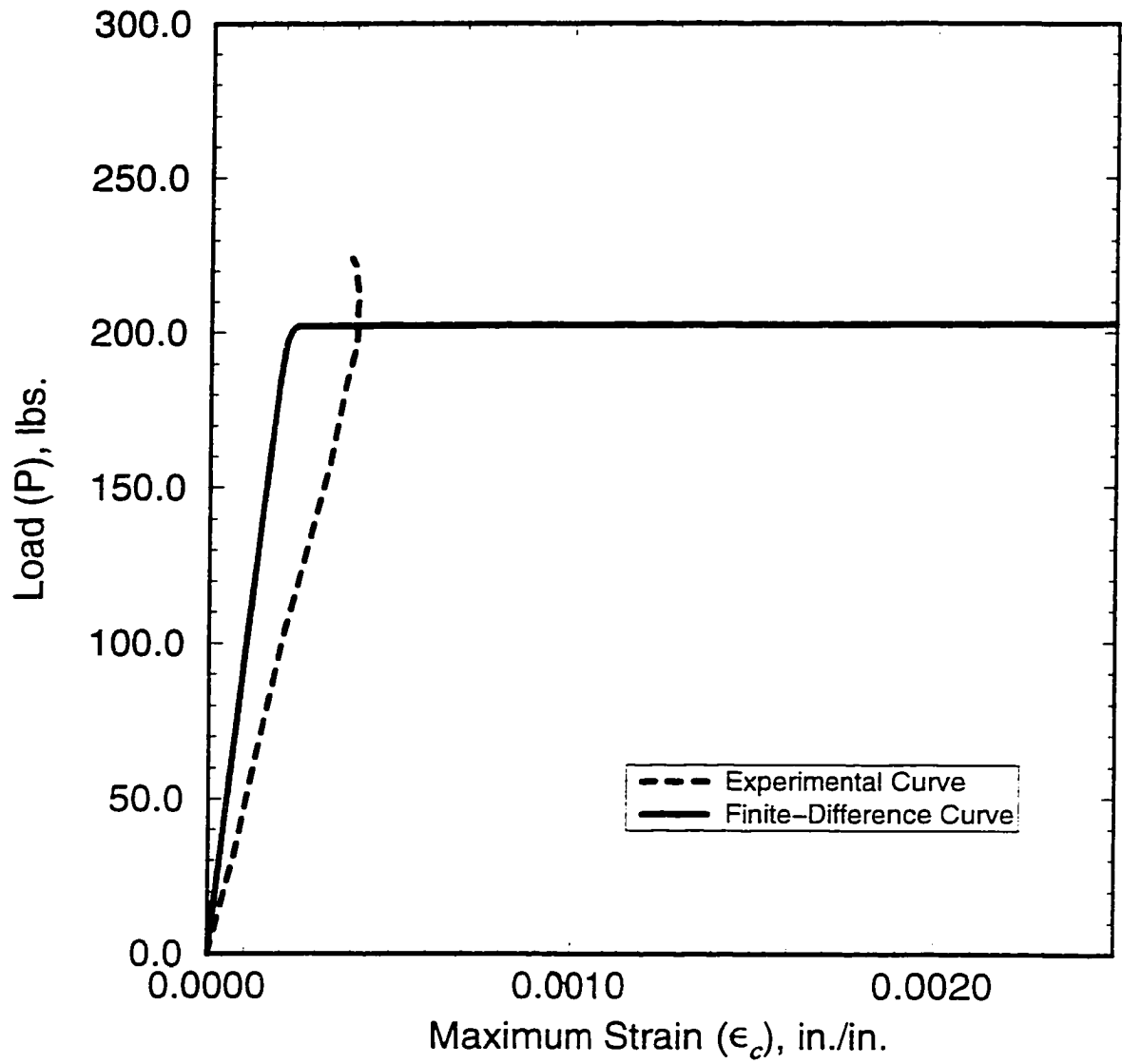


Figure 95. Load (P) versus maximum strain (ϵ_c) for Test No. CFT4-9

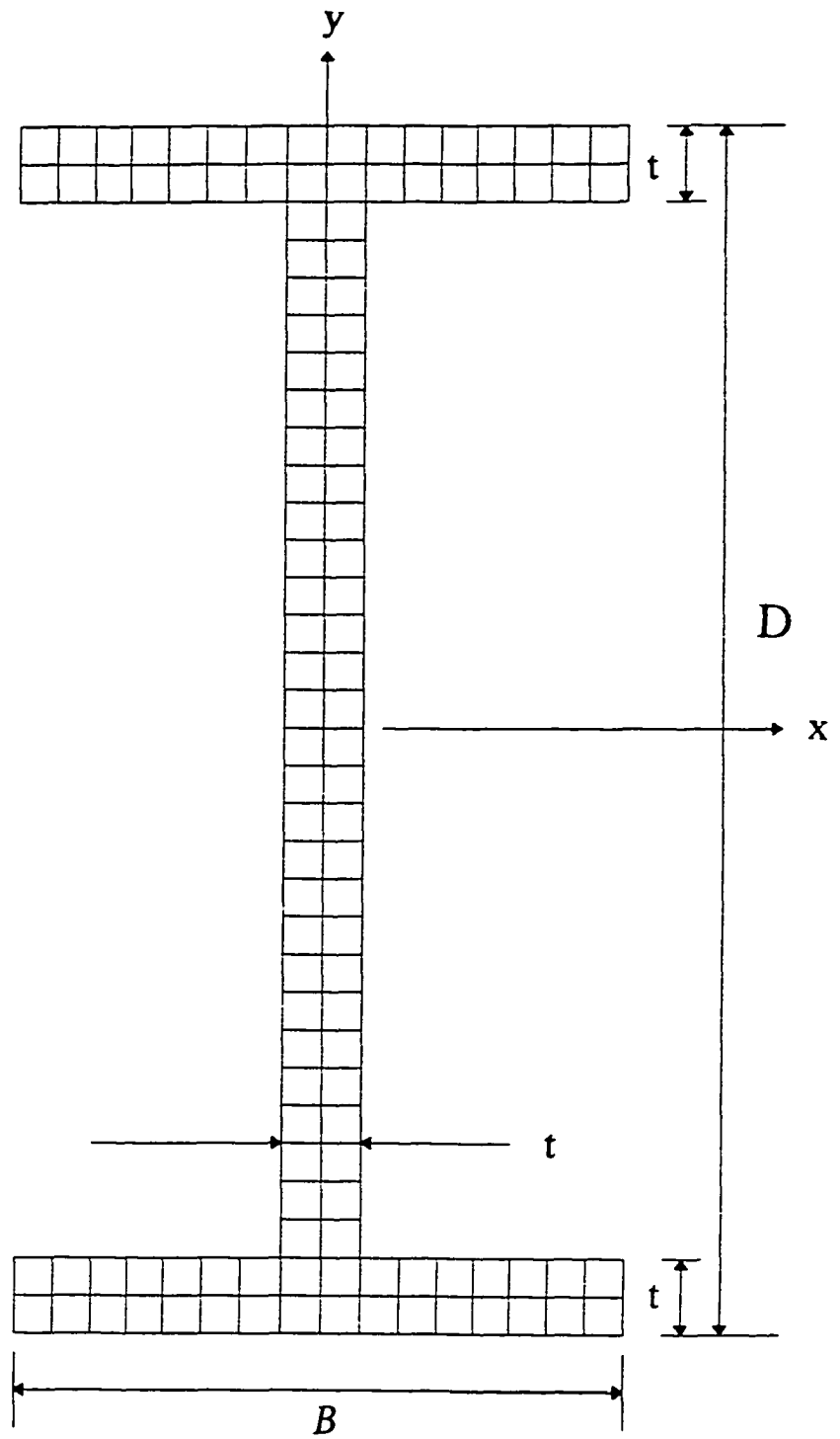


Figure 96. Discretized I-section

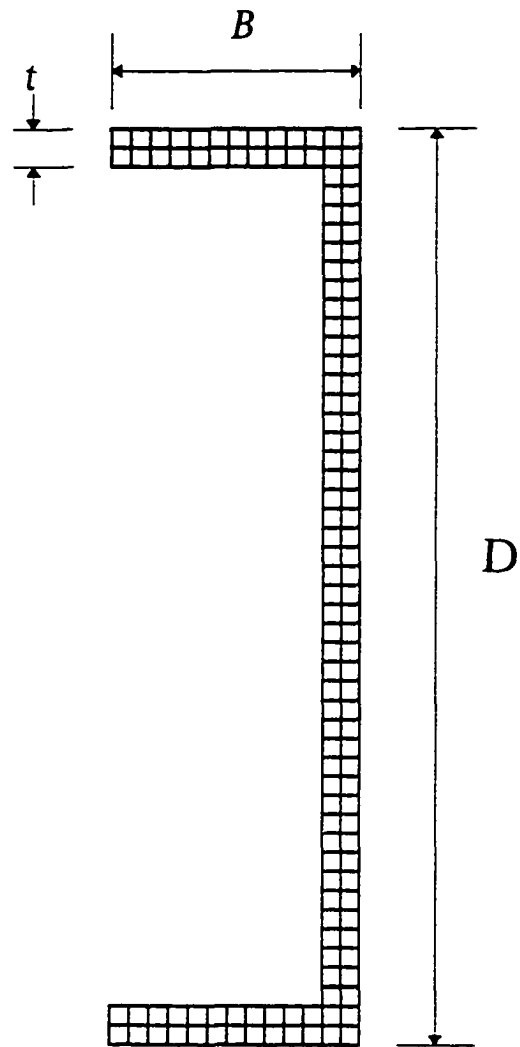


Figure 97. Discretized channel section

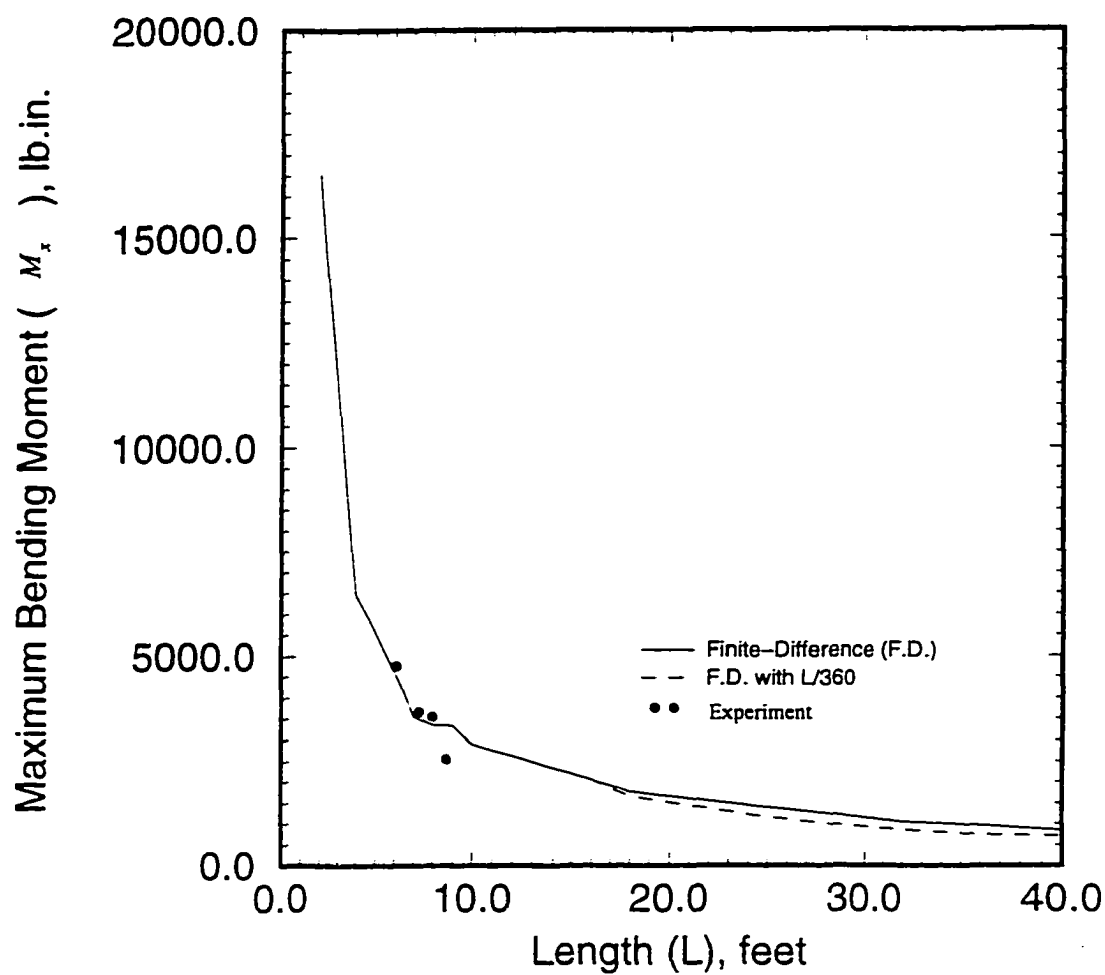


Figure 98. Maximum bending moment versus length curves for three-point loading of I-section FRP composite beams

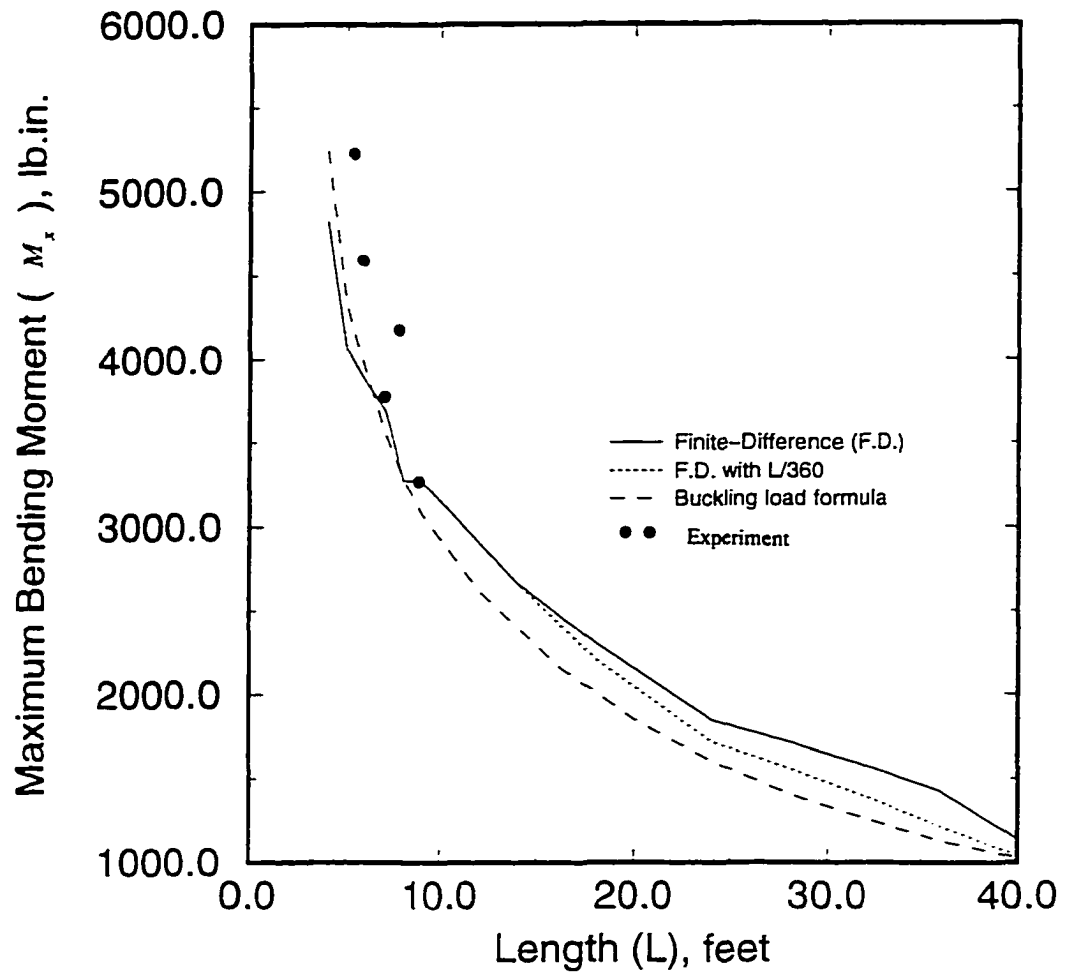


Figure 99. Maximum bending moment versus length curves for four-point loading of I-section FRP composite beams

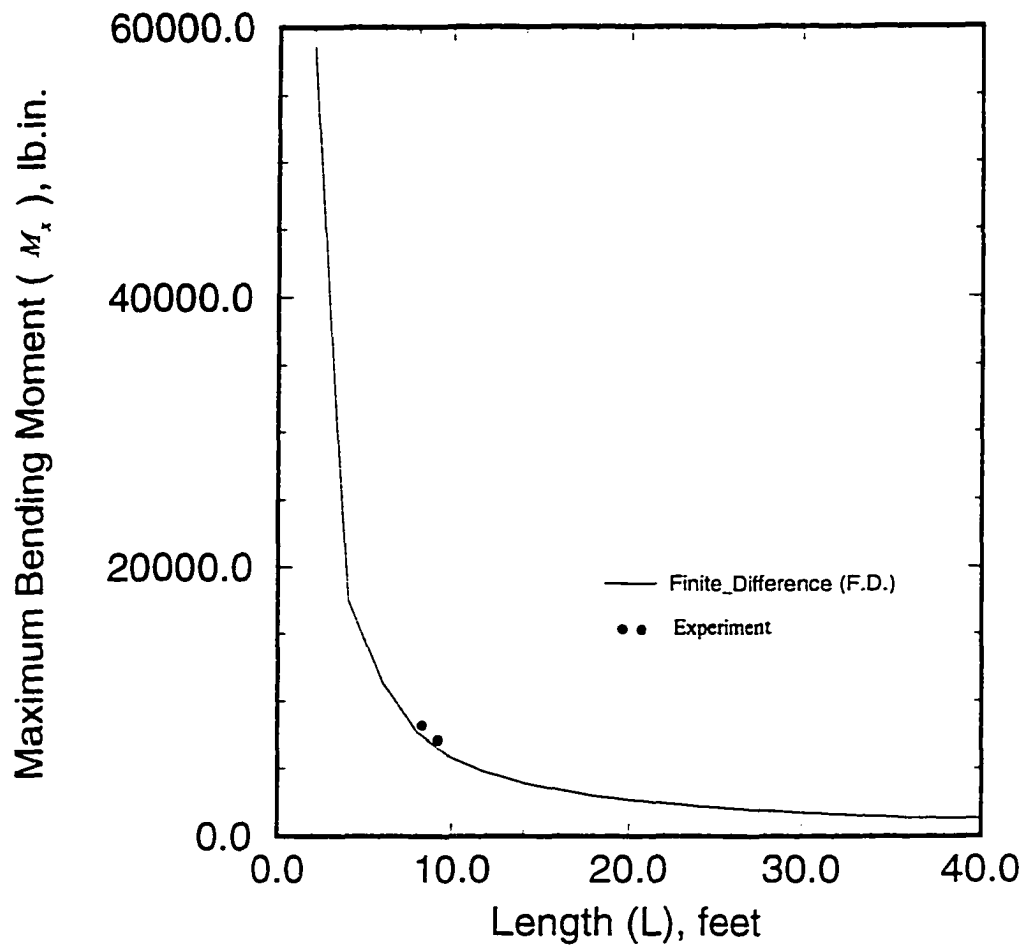


Figure 100. Maximum bending moment versus length curves for three-point loading of channel section FRP composite beams

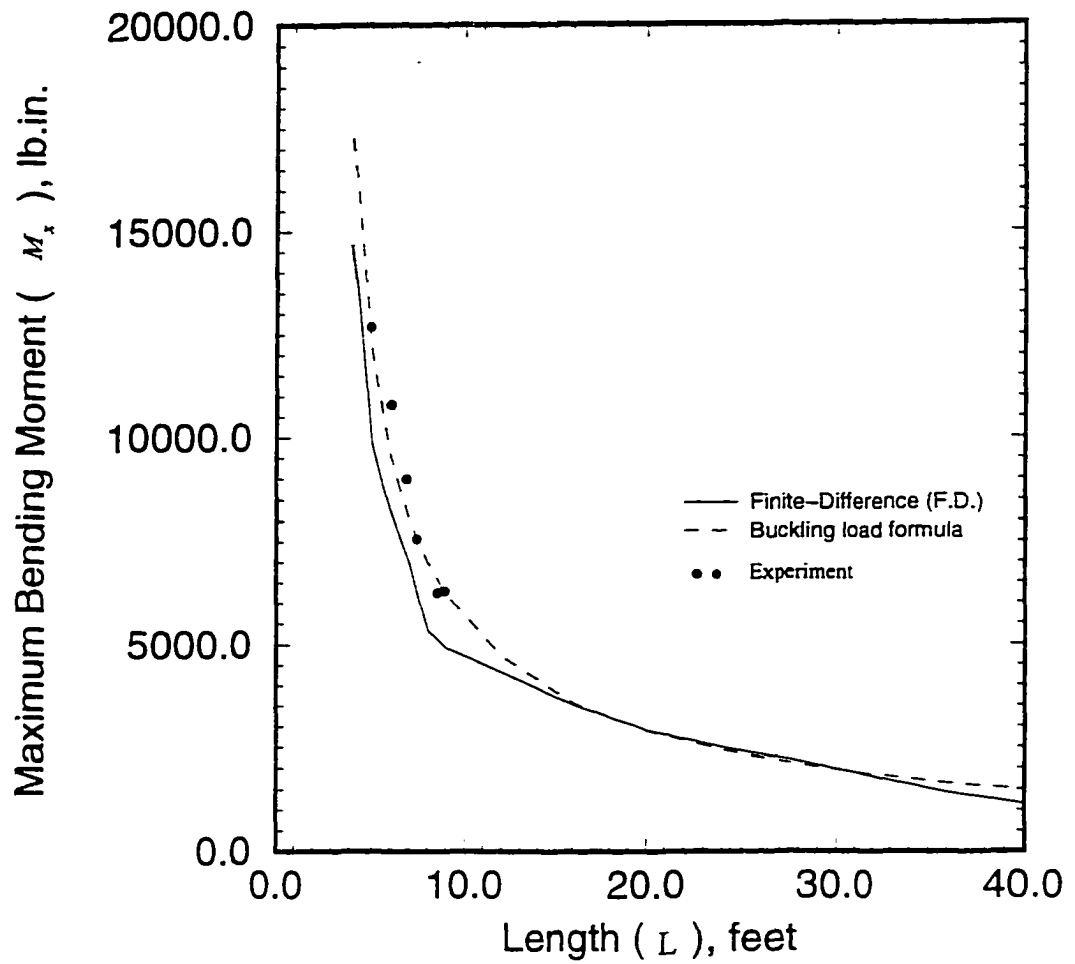


Figure 101. Maximum bending moment versus length curves for four-point loading of channel section FRP composite beams

APPENDIX

FINITE-DIFFERENCE PROGRAM FOR SOLVING SYSTEM OF FRP BEAM DIFFERENTIAL EQUATIONS

This appendix presents a sample listing of the computer program based on the finite-difference formulation given in Chapter III of this dissertation. This program is specially developed to solve the three-point loading problem. The input basically consists of beam geometry and material properties while the output is in the form of the applied load(s) versus deflections, angle of twist, strains, and stresses.

c

program mphi-I.f

```

implicit real*8(a-h,o-z)
real*8 xyarray(120,5),ixx,iyy,iw,pmax,mmax
*,pext,mext,pincr,mincr,m,pint,mint

integer totnumel,mfl,nfl,mweb,nweb

call input (flwidth,depth,flthick,webthick,mfl,nfl,mweb,
*          nweb,pmax,mmax,delta,pincr,mincr,pext,mext,
*          pint,mint,AvgAxialStrain,curvature)

call Isection
* (flwidth,mfl,flthick,nfl,flwidth,flthick,webthick,
*  depth,webthick,webeldepth,areaflel,areawebel,
*  mweb,nweb,xAbar,yAbar,elnum,totnumel,totelarea,xyarray)

call Translate (ixx,iyy,iw,xAbar,yAbar,totelarea,xyarray,x,y
*,totnumel,flwidth,depth,darea)

call deformation
* (pincr,mincr,AvgAxialStrain,
*  AvgAxialStraindel,curvature,curvaturesdel,xyarray,m)

stop
end

subroutine input (flwidth,depth,flthick,webthick,mfl,nfl,mweb,
*               nweb,pmax,mmax,delta,pincr,mincr,pext,mext,
*               pint,mint,AvgAxialStrain,curvature)

implicit real*8 (a-h,o-z)
real*8 mmax,AvgAxialStrain,curvature,pincr
*,mincr,pext,mext,pint,mint
integer mfl,mweb
flwidth=2.0
depth=4.
flthick=.25
webthick=.25
mfl=16
nfl=2
mweb=28
nweb=2
mmax=50
pmax=0.0
delta=1000
pincr=0.
mincr=0.
pext=0.0
mext=0.
pint=0.
mint=0.
AvgAxialStrain=0.0
curvature=0.0
end

```

c

subroutine cross-section

```

      subroutine Isection
*      (flwidth,mfl,flthick,nfl,flelwidth,flelthick,webthick,
*      depth,webelthick,webeldepth,areaflel,areawebel,
*      mweb,nweb,xAbar,yAbar,elnum,totnumel,totelarea,xyarray)

      implicit real*8(a-h,o-z)
      real*8 xyarray(120,5)
      integer elnum,mweb,nweb,mfl,nfl,i,j,totnumel

      totnumel=2*mfl*nfl+mweb*nweb
      flelwidth=flwidth/mfl
      flelthick=flthick/nfl
      areaflel=flelwidth*flelthick
      webelthick=webthick/nweb
      webeldepth=(depth-2*flthick)/mweb
      areawebel=webelthick*webeldepth
      totelarea=2*areaflel*mfl*nfl+areawebel*mweb*nweb
      xAbar=0.
      yAbar=0.
      elnum=1

c      using upper flange

      do 20 i=0,nfl-1
        do 10 j=0,mfl-1
          xyarray(elnum,1)=flelwidth*(j+.5)
          xAbar=xAbar+xyarray(elnum,1)*areaflel
          xyarray(elnum,2)=depth-flelthick*(i+.5)
          yAbar=yAbar+xyarray(elnum,2)*areaflel
          xyarray(elnum,3)=areaflel
          elnum=elnum+1
10        continue
20      continue

c      calculate the web

      do 40 i=0,mweb-1
        do 30 j=0,nweb-1

          xyarray(elnum,1)=(flwidth/2.-webthick/2.)+webelthick*(j+.5)
          xAbar=xAbar+xyarray(elnum,1)*areawebel
          xyarray(elnum,2)=(depth-flthick)-webeldepth*(i+.5)
          yAbar=yAbar+xyarray(elnum,2)*areawebel
          xyarray(elnum,3)=areawebel
          elnum=elnum+1
30        continue
40      continue

c      calculate the lower flange

      do 50 i=0,nfl-1
        do 60 j=0,mfl-1
          xyarray(elnum,1)=flelwidth*(j+.5)
          xAbar=xAbar+xyarray(elnum,1)*areaflel
          xyarray(elnum,2)=flthick-flelthick*(i+.5)
          yAbar=yAbar+xyarray(elnum,2)*areaflel
          xyarray(elnum,3)=areaflel
          elnum=elnum+1

```

```

60      continue
50  continue
    return
    end

    subroutine Translate (ixx,iyy,iw,xAbar,yAbar,totelarea,xyarray,x
*      ,totnumel,flwidth,depth,darea)
    implicit real*8 (a-h,o-z)
    real*8 xyarray(120,5),ixx,iyy,iw
    integer totnumel,i
    ixx=0.
    iyy=0.0
    iw =0.0
    x=xAbar/totelarea
    y=yAbar/totelarea

    do 70 i=1,totnumel
        xyarray(i,1)=xyarray(i,1)-x
        xyarray(i,2)=xyarray(i,2)-y
        ixx=ixx+xyarray(i,2)**2*xyarray(i,3)
        iyy=iiy+xyarray(i,1)**2*xyarray(i,3)

70      continue
    return
    end

c  *****
    subroutine deformation
*  (pincr,mincr,AvgAxialStrain,
*  AvgAxialStraindel,curvature,curvaturesdel,xyarray,m,flthick)

    implicit real*8 (a-h,o-z)
    real*8 xyarray(120,5)
*  ,AvgAxialStraindel,AvgAxialStrain,curvature,flthick
*  ,curvaturesdel,pincr,mincr,m,E,ixx,iyy,iw,s

    integer i

    E          =2.55*10**6
    pincr       =0.0
    moment      =0.0
    AvgAxialStrain=0.0
    xyarray(i,5) =0.0

    do ii=1,30

        if (ii.EQ.1) then
            mm=1
            nn=120
        endif

        if (ii.EQ.2) then
            ixx=0.0
            iyy=0.0
            iw =0.0
            mm=17
            nn=120-16

```

```

endif

if (ii.GE.3) then
  ix=0.0
  iy=0.0
  iw =0.0

  mm=32+(ii-3)*2+1
  nn=120-32-(ii-3)*2
endif

do i=mm,nn

  xyarray(i,5)=0.0
  xyarray(i,4)=0.0
  m=0.0
  curvature=0.0043715

  ix=ix+xyarray(i,2)**2*xyarray(i,3)
  iy=iy+xyarray(i,1)**2*xyarray(i,3)
  iw=iw+xyarray(i,1)**2*xyarray(i,2)**2*xyarray(i,3)

  xyarray(i,5)=curvature*xyarray(i,2)

  if (abs(xyarray(i,5)).GT.0.008743) then
    xyarray(i,5)=0.0
  endif

  xyarray(i,4)=E*xyarray(i,5)
  s=ix/xyarray(i,2)
  m=xyarray(i,4)*s

  curvature=0.008743/xyarray(i,2)
enddo
write(*,*) ,abs(curvature) ,abs(m)

enddo

return
end

```



```

      implicit real*8 (A-h,o-z)
      real*8 a(23,23), c(23), v(5), u(5), w(5), indx(23), Kt, L
*      , Ixe, Iye, Sxye, Isxsye

      integer p, num

      n = 23
      np= 23
      p      = 0
      num = 999999
      strainer=0.008743
c      strainer=0.011729

      do 99 p=0, num, 1
5      do i=1, n
6      do j=1, n
          a(i,j)=0.0
        end do
      end do

      y      = -3.5
      E      = 2.55*10**6
      q      = -0.002
      Ixe    = 4.4116210937500
      Iye    = 0.33544921875000
      Sxye   = 0.0
      Isxsye = 1.1720790863037
      G      = 420000.0
      Kt     = 0.0403
      h      = 13.5
      L      = 8.0*h
      delta  = L/10000
      theta  = 0.
      pi     = 3.1415927
      Bx=E*Ixe
      By=E*Iye
      Cw=E*Isxsye
      Ct=G*Kt
      Bxy=E*Sxye
      constN = Bx/h**2
      constA = By/h**2
      constNY = Bxy/h**2
      constC = Ct/(h*h)
      constD = Cw/h**4

      a(2,2) = constN
      a(2,3) = constNY
      a(2,5) = -2*constN
      a(2,6) = -2*constNY
      a(2,8) = constN
      a(2,9) = constNY
      a(11,5) = constN
      a(11,6) = constNY
      a(11,8) = -2*constN
      a(11,9) = -2*constNY
      a(11,11) = constN
      a(11,12) = constNY

```

```

a(8,8) = constN
a(8,9) = constNY
a(8,11) = -2*constN
a(8,12) = -2*constNY
a(8,14) = constN
a(8,15) = constNY
a(3,2) = constNY
a(3,3) = constA
a(3,5) = -2*constNY
a(3,6) = -2*constA
a(3,8) = constNY
a(3,9) = constA
a(12,5) = constNY
a(12,6) = constA
a(12,8) = -2*constNY
a(12,9) = -2*constA
a(12,11) = constNY
a(12,12) = constA
a(15,8) = constNY
a(15,9) = constA
a(15,11) = -2*constNY
a(15,12) = -2*constA
a(15,14) = constNY
a(15,15) = constA
a(1,1) = -constD
a(1,4) = constC+(4*constD)
a(1,7) = -2*constC-(6*constD)
a(1,10) = constC+(4*constD)
a(1,13) = -constD
a(16,4) = -constD
a(16,7) = constC+(4*constD)
a(16,10) = -2*constC-(6*constD)
a(16,13) = constC+(4*constD)
a(16,16) = -constD
a(9,7) = -constD
a(9,10) = constC+(4*constD)
a(9,13) = -2*constC-(6*constD)
a(9,16) = constC+(4*constD)
a(9,19) = -constD
a(17,11) = constN
a(17,12) = constNY
a(17,14) = -2*constN
a(17,15) = -2*constNY
a(17,17) = constN
a(17,18) = constNY
a(14,14) = constN
a(14,15) = constNY
a(14,17) = -2*constN
a(14,18) = -2*constNY
a(14,20) = constN
a(14,21) = constNY
a(18,11) = constNY
a(18,12) = constA
a(18,14) = -2*constNY
a(18,15) = -2*constA
a(18,17) = constNY
a(18,18) = constA
a(19,14) = constNY
a(19,15) = constA
a(19,17) = -2*constNY

```

```

a(19,18) = -2*constA
a(19,20) = constNY
a(19,21) = constA
a(10,10) = -constD
a(10,13) = constC+(4*constD)
a(10,16) = -2*constC-(6*constD)
a(10,19) = constC+(4*constD)
a(10,22) = -constD
a(13,13) = -constD
a(13,16) = constC+(4*constD)
a(13,19) = -2*constC-(6*constD)
a(13,22) = constC+(4*constD)
a(13,23) = -constD
a(20,14) = -1.0
a(20,20) = 1.0
a(21,15) = -1.0
a(21,21) = 1.0
a(22,16) = -1.0
a(22,22) = 1.0
a(4,4) = 1.0
a(4,7) = -2.0
a(4,10) = 1.0
a(5,5) = 1.0
a(6,6) = 1.0
a(7,7) = 1.0
a(23,13) = -1.0
a(23,16) = 2.0
a(23,22) = -2.0
a(23,23) = 1.0
a(12,10) = p*h
a(15,13) = 2*p*h
a(16,6) = -p/h
a(16,9) = 2*p/h
a(16,12) = -p/h
a(9,9) = -2*p/h
a(9,12) = +4*p/h
a(9,15) = -2*p/h
a(18,16) = 2*p*h
a(19,19) = 2*p*h
a(10,12) = -2*p/h
a(10,15) = 4*p/h
a(10,18) = -2*p/h
a(13,15) = -2*p/h
a(13,18) = 4*p/h
a(13,21) = -2*p/h
a(23,19) = (-2*(h**3)*p*y)/Cw

pi = 3.1415927
constNYC = 0.
constAC = 0.
constTC = 0.
constCC = 0.
constDC = 0.
constGC = 0.

c(2) = 0.0
c(11) = -constNYC*sin(pi/8.)-p*h
c(8) = -constNYC*sin(pi/4.)-2*p*h
c(3) = 0.0

```

```

      c(12)      = -constAC*sin(pi/8.)+
*              constTC*sin(pi/8.)
      c(15)      = -constAC*sin(pi/4.)+
*              2*constTC*sin(pi/4.)
      c(1)       = 0.0+p*q
      c(16)      = -constCC*sin(pi/8.)-constDC*sin(pi/8.)
*              +constGC*sin(pi/8.)+p*q
      c(9)       = -constCC*sin(pi/4.)-constDC*sin(pi/4.)
*              +2*constGC*sin(pi/4.)+p*q
      c(17)      = -constNYC*sin(3*pi/8.)-2*p*h
      c(14)      = -constNYC*sin(pi/2.)-2*p*h
      c(18)      = -constAC*sin(3*pi/8.)+
*              2*constTC*sin(3*pi/8.)
      c(19)      = -constAC*sin(pi/2.)+
*              2*constTC*sin(pi/2.)
      c(10)      = -constCC*sin(3*pi/8.)-constDC*sin(3*pi/8.)
*              +2*constGC*sin(3*pi/8.)+p*q
      c(13)      = -constCC*sin(pi/2.)-constDC*sin(pi/2.)
*              +2*constGC*sin(pi/2.)+p*q
      c(23)      = (-2*(h**3)*p*y*theta)/Cw
      c(5)       = 0.0
      c(6)       = 0.0
      c(7)       = 0.0
      c(4)       = 0.0
      c(20)      = 0.0
      c(21)      = 0.0
      c(22)      = 0.0

c      n = 23
      np= 23

      call ludcmp(a,n,np,indx,d)
      do 76 j=1,n
      d=d*a(j,j)
76      continue
      determ=d
      if (p.EQ.0.) then
      determZ=determ
      endif
      determbar=determ/determZ
      if (determbar.LE.-0.0001) go to 11
      call lubksb(a,n,np,indx,c)
      do i = 1,n
      enddo

      v(1)=c(5)
      v(2)=c(8)
      v(3)=c(11)
      v(4)=c(14)
      v(5)=c(17)

      u(1)=c(6)
      u(2)=c(9)
      u(3)=c(12)
      u(4)=c(15)
      u(5)=c(18)

      w(1)=c(7)
      w(2)=c(10)
      w(3)=c(13)

```

```

      w(4)=c(16)
      w(5)=c(19)

      do i=1,5
      enddo

      phix5   = c(14)-2*c(17)+c(20)
      phiy5   = c(15)-2*c(18)+c(21)
      phiw5   = c(16)-2*c(19)+c(22)

      straina = 2*phix5-1*phiy5+2*phiw5

      if (abs(straina).GE.straincr) go to 11

99      continue
11      continue
      stop
      end

c              LU DECOMPOSITION

      subroutine ludcmp(a,n,np,indx,d)
      implicit real*8 (a-h,o-z)
      parameter (nmax=100,tiny=1.0E-20)
      dimension a(np,np),indx(n),vv(nmax)
      d=1.
      do 12 i=1,n
      aamax=0.
      do 11 j=1,n
      if (abs(a(i,j)).GT.aamax) aamax=abs(a(i,j))
11      continue
      if (aamax.EQ.0.) PAUSE "Singular matrix."
      vv(i)=1./aamax
12      continue
      do 19 j=1,n
      do 14 i=1,j-1
      sum=a(i,j)
      do 13 k=1,i-1
      sum=sum-a(i,k)*a(k,j)
13      continue
      a(i,j)=sum
14      continue
      aamax=0.
      do 16 i=j,n
      sum=a(i,j)
      do 15 k=1,j-1
      sum=sum-a(i,k)*a(k,j)
15      continue
      a(i,j)=sum
      dum=vv(i)*abs(sum)
      if (dum.GE.aamax) then
      imax=i
      aamax=dum
      endif
16      continue
      if (j.NE.imax) then
      do 17 k=1,n
      dum=a(imax,k)
      a(imax,k)=a(j,k)
      a(j,k)=dum

```

```

17      continue
      d=-d
      vv(imax)=vv(j)
      endif
      indx(j)=imax
      if(a(j,j).EQ.0.)a(j,j)=tiny
      if(j.NE.n) then
      dum=1./a(j,j)
      do 18 i=j+1,n
          a(i,j)=a(i,j)*dum
18      continue
      endif
19      continue
      return
      end

c          SUBROUTINE LUBKSB

      subroutine lubksb (a,n,np,indx,c)
      implicit real*8 (a-h,o-z)
      dimension a(np,np),indx(n),c(n)
      ii=0
      do 12 i=1,n
          ll=indx(i)
          sum=c(ll)
          c(ll)=c(i)
          if (ii.NE.0) then
              do 11 j=ii,i-1
                  sum=sum-a(i,j)*c(j)
11          continue
              else if (sum.NE.0.) then
                  ii=i
              endif
          c(i)=sum
12      continue
      do 14 i=n,1,-1
          sum=c(i)
          do 13 j=i+1,n
              sum=sum-a(i,j)*c(j)
13          continue
          c(i)=sum/a(i,i)
14      continue
      return
      end

```

c program three-point loading for channel beam

```

implicit real*8(A-h,o-z)
real*8 a(23,23), c(23),v(5),u(5),w(5),indx(23),Kt,L
*   ,Ixe,Iye,Sxye,Isxsye

integer p,num

n = 23
np= 23
p    = 0
num = 999999
straincr=0.011729


do 99 p=0,num,1
5 do i=1,n
6   do j=1,n
      a(i,j)=0.0
   end do
end do


y      = -3.5
E      = 3.23*10**6
q      = -0.0003

Ixe    = 10.1833
Iye    = 0.4244
Sxye   = 8.326672684688D-17
Isxsye = 2.9639687861

G      = 420000.0
Kt     = 0.0455729
h      = 9.0
L      = 8.0*h
delta  = L/10000
theta  = 0.
pi     = 3.1415927


Bx=E*Ixe
By=E*Iye
Cw=E*Isxsye
Ct=G*Kt
Bxy=E*Sxye


constN = Bx/h**2
constA = By/h**2
constNY= Bxy/h**2
constC = Ct/(h*h)
constD = Cw/h**4


c

```

```

a(2,9)   =   constNY

a(11,5)  =   constN
a(11,6)  =   constNY
a(11,8)  =  -2*constN
a(11,9)  =  -2*constNY
a(11,11) =   constN
a(11,12) =   constNY

```

```

a(8,8)   =   constN
a(8,9)   =   constNY
a(8,11)  =  -2*constN
a(8,12)  =  -2*constNY
a(8,14)  =   constN
a(8,15)  =   constNY

```

```

a(17,11) =   constN
a(17,12) =   constNY
a(17,14) =  -2*constN
a(17,15) =  -2*constNY
a(17,17) =   constN
a(17,18) =   constNY

```

```

a(14,14) =   constN
a(14,15) =   constNY
a(14,17) =  -2*constN
a(14,18) =  -2*constNY
a(14,20) =   constN
a(14,21) =   constNY

```

C

B

```

a(3,2)   =   constNY
a(3,3)   =   constA
a(3,5)   =  -2*constNY
a(3,6)   =  -2*constA
a(3,8)   =   constNY
a(3,9)   =   constA

```

```

a(12,5)  =   constNY
a(12,6)  =   constA
a(12,8)  =  -2*constNY
a(12,9)  =  -2*constA
a(12,11) =   constNY
a(12,12) =   constA

```

```

a(15,8)  =   constNY
a(15,9)  =   constA
a(15,11) =  -2*constNY
a(15,12) =  -2*constA
a(15,14) =   constNY
a(15,15) =   constA

```

```

a(18,11) =   constNY
a(18,12) =   constA
a(18,14) =  -2*constNY
a(18,15) =  -2*constA
a(18,17) =   constNY
a(18,18) =   constA

```

```

a(19,14) =   constNY

```



```

a(19,15) = constA
a(19,17) = -2*constNY
a(19,18) = -2*constA
a(19,20) = constNY
a(19,21) = constA

```

c

C

```

a(1,1) = -constD
a(1,4) = constC+(4*constD)
a(1,7) = -2*constC-(6*constD)
a(1,10) = constC+(4*constD)
a(1,13) = -constD

a(16,4) = -constD
a(16,7) = constC+(4*constD)
a(16,10) = -2*constC-(6*constD)
a(16,13) = constC+(4*constD)
a(16,16) = -constD

a(9,7) = -constD
a(9,10) = constC+(4*constD)
a(9,13) = -2*constC-(6*constD)
a(9,16) = constC+(4*constD)
a(9,19) = -constD

a(10,10) = -constD
a(10,13) = constC+(4*constD)
a(10,16) = -2*constC-(6*constD)
a(10,19) = constC+(4*constD)
a(10,22) = -constD

a(13,13) = -constD
a(13,16) = constC+(4*constD)
a(13,19) = -2*constC-(6*constD)
a(13,22) = constC+(4*constD)
a(13,23) = -constD

```

c

B.C.

```

a(20,14) = -1.0
a(20,20) = 1.0

a(21,15) = -1.0
a(21,21) = 1.0

a(22,16) = -1.0
a(22,22) = 1.0

a(4,4) = 1.0
a(4,7) = -2.0
a(4,10) = 1.0

a(5,5) = 1.0

a(6,6) = 1.0

a(7,7) = 1.0

a(23,13) = -1.0
a(23,16) = 2.0
a(23,22) = -2.0

```

$$a(23,23) = 1.0$$

$$\begin{aligned} \text{c} \quad & \text{B} \\ & a(12,10) = 0.5*p*h \\ & a(15,13) = p*h \\ & a(18,16) = 1.5*p*h \\ & a(19,19) = 2*p*h \end{aligned}$$

$$\begin{aligned} \text{c} \quad & \text{C} \\ & a(16,6) = -0.5*p/h \\ & a(16,9) = p/h \\ & a(16,12) = -0.5*p/h \\ \\ & a(9,9) = -p/h \\ & a(9,12) = +2*p/h \\ & a(9,15) = -p/h \\ \\ & a(10,12) = -1.5*p/h \\ & a(10,15) = +3*p/h \\ & a(10,18) = -1.5*p/h \\ \\ & a(13,15) = -2*p/h \\ & a(13,18) = +4*p/h \\ & a(13,21) = -2*p/h \end{aligned}$$

$$\begin{aligned} \text{c} \quad & \text{B.C.} \\ & a(23,19) = -(h**3)*p*y/Cw \end{aligned}$$

$$\begin{aligned} \text{pi} &= 3.1415927 \\ \text{constNYC} &= 0. \\ \text{constAC} &= 0. \\ \text{constTC} &= 0. \\ \text{constCC} &= 0. \\ \text{constDC} &= 0. \\ \text{constGC} &= 0. \end{aligned}$$

$$\begin{aligned} \text{c} \quad & \text{A} \\ & c(2) = 0.0 \\ & c(11) = -\text{constNYC}*\sin(\text{pi}/8.) - 0.5*p*h \\ & c(8) = -\text{constNYC}*\sin(\text{pi}/4.) - p*h \\ & c(17) = -\text{constNYC}*\sin(3*\text{pi}/8.) - 1.5*p*h \\ & c(14) = -\text{constNYC}*\sin(4*\text{pi}/8.) - 2*p*h \end{aligned}$$

$$\begin{aligned} \text{c} \quad & \text{B} \\ & c(3) = 0.0 \\ & c(12) = -\text{constAC}*\sin(\text{pi}/8.) + \\ & * \quad \text{constTC}*\sin(\text{pi}/8.) \\ & c(15) = -\text{constAC}*\sin(\text{pi}/4.) + \\ & * \quad 2*\text{constTC}*\sin(\text{pi}/4.) \\ \\ & c(18) = -\text{constAC}*\sin(3*\text{pi}/8.) + \\ & * \quad 3*\text{constTC}*\sin(3*\text{pi}/4.) \\ \\ & c(19) = -\text{constAC}*\sin(4*\text{pi}/8.) + \\ & * \quad 4*\text{constTC}*\sin(4*\text{pi}/8.) \end{aligned}$$

```

c          C
      c(1)  = 0.0+0.5*p*q
      c(16) = -constCC*sin(pi/8.)-constDC*sin(pi/8.)
*          +constGC*sin(pi/8.)+0.5*p*q
      c(9)  = -constCC*sin(pi/4.)-constDC*sin(pi/4.)
*          +2*constGC*sin(pi/4.)+0.5*p*q

      c(10) = -constCC*sin(3*pi/8.)-constDC*sin(3*pi/8.)
*          +3*constGC*sin(3*pi/8.)+0.5*p*q

      c(13) = -constCC*sin(4*pi/8.)-constDC*sin(4*pi/8.)
*          +4*constGC*sin(4*pi/8.)+0.5*p*q

c          B.C.

      c(23) = (-2*(h**3)*0.5*p*y*theta)/Cw

      c(5) = 0.0
      c(6) = 0.0
      c(7) = 0.0
      c(4) = 0.0
      c(20) = 0.0
      c(21) = 0.0
      c(22) = 0.0

c
c      _____
      n = 23
      np= 23

      call ludcmp(a,n,np,indx,d)
      do 76 j=1,n
      d=d*a(j,j)
76      continue
      determ=d
      if (p.EQ.0.) then
      determZ=determ
c      write(*,*) "determ,p=",determ,p
      endif
      determbar=determ/determZ
      if (determbar.LE.-0.0001) go to 11
      call lubksb(a,n,np,indx,c)

c      _____
c      do i = 1,n
c      write(*,*) 'displacement, i,c(i) = ',i,c(i)
      enddo

      v(1)=c(5)
      v(2)=c(8)
      v(3)=c(11)
      v(4)=c(14)
      v(5)=c(17)

      u(1)=c(6)
      u(2)=c(9)
      u(3)=c(12)
      u(4)=c(15)
      u(5)=c(18)

      w(1)=c(7)
      w(2)=c(10)

```

```

w(3)=c(13)
w(4)=c(16)
w(5)=c(19)

write(*,*) ,p,w(5)
do i=1,5
c   write(*,*) ,i,v(i),u(i),w(i)
enddo

strainain = 2*v(5) -1*u(5)+2*w(5)

if (strainain.GE.straininc) go to 11

c   write(*,*) ,p,strainain
99  continue
11  continue
stop
end

c                                     LU DECOMPOSITION

subroutine ludcmp(a,n,np,indx,d)
implicit real*8 (a-h,o-z)
parameter (nmax=100,tiny=1.0E-20)
dimension a(np,np),indx(n),vv(nmax)
d=1.
do 12 i=1,n
aamax=0.
do 11 j=1,n
if (abs(a(i,j)).GT.aamax) aamax=abs(a(i,j))
11  continue
if (aamax.EQ.0.) PAUSE "Singular matrix."
vv(i)=1./aamax
12  continue
do 19 j=1,n
do 14 i=1,j-1
sum=a(i,j)
do 13 k=1,i-1
sum=sum-a(i,k)*a(k,j)
13  continue
a(i,j)=sum
14  continue
aamax=0.
do 16 i=j,n
sum=a(i,j)
do 15 k=1,j-1
sum=sum-a(i,k)*a(k,j)
15  continue
a(i,j)=sum
dum=vv(i)*abs(sum)
if (dum.GE.aamax) then
imax=i
aamax=dum
endif
16  continue
if (j.NE.imax) then
do 17 k=1,n
dum=a(imax,k)
a(imax,k)=a(j,k)
a(j,k)=dum

```

```

17      continue
      d=-d
      vv(imax)=vv(j)
      endif
      indx(j)=imax
      if(a(j,j).EQ.0.)a(j,j)=tiny
      if(j.NE.n) then
      dum=1./a(j,j)
      do 18 i=j+1,n
        a(i,j)=a(i,j)*dum
18      continue
      endif
19      continue
      return
      end

c                                SUBROUTINE LUBKSB

      subroutine lubksb (a,n,np,indx,c)
      implicit real*8 (a-h,o-z)
      dimension a(np,np),indx(n),c(n)
      ii=0
      do 12 i=1,n
        ll=indx(i)
        sum=c(ll)
        c(ll)=c(i)
        if (ii.NE.0) then
          do 11 j=ii,i-1
            sum=sum-a(i,j)*c(j)
11          continue
          else if (sum.NE.0.) then
            ii=i
          endif
          c(i)=sum
12        continue
        do 14 i=n,1,-1
          sum=c(i)
          do 13 j=i+1,n
            sum=sum-a(i,j)*c(j)
13          continue
          c(i)=sum/a(i,i)
14        continue
      return
      end

```

c program three-point loading for I-beam

```

implicit real*8(A-h,o-z)
real*8 a(23,23), c(23),v(5),u(5),w(5),indx(23),Kt,L
*   ,Ixe,Iye,Sxye,Isxsye

integer p,num

n = 23
np= 23
p   = 0
num = 999999
straincr=0.011729

do 99 p=0,num,1
5  do i=1,n
6    do j=1,n
      a(i,j)=0.0
    end do
  end do

y      = -3.5
E      = 2.55*10**6
q      = -0.002

Ixe    = 4.4116210937500
Iye    = 0.33544921875000
Sxye   = 0.0
Isxsye = 1.1720790863037

G      = 420000.0
Kt     = 0.0403
h      = 13.5
L      = 8.0*h
delta  = L/10000
theta  = 0.
pi     = 3.1415927

Bx=E*Ixe
By=E*Iye
Cw=E*Isxsye
Ct=G*Kt
Bxy=E*Sxye

constN = Bx/h**2
constA = By/h**2
constNY = Bxy/h**2
constC = Ct/(h*h)
constD = Cw/h**4

c      A
a(2,2) = constN
a(2,3) = constNY
a(2,5) = -2*constN
a(2,6) = -2*constNY
a(2,8) = constN

```

```

a(2,9)   =   constNY

a(11,5)  =   constN
a(11,6)  =   constNY
a(11,8)  =  -2*constN
a(11,9)  =  -2*constNY
a(11,11) =   constN
a(11,12) =   constNY

```

```

a(8,8)   =   constN
a(8,9)   =   constNY
a(8,11)  =  -2*constN
a(8,12)  =  -2*constNY
a(8,14)  =   constN
a(8,15)  =   constNY

```

```

a(17,11) =   constN
a(17,12) =   constNY
a(17,14) =  -2*constN
a(17,15) =  -2*constNY
a(17,17) =   constN
a(17,18) =   constNY

```

```

a(14,14) =   constN
a(14,15) =   constNY
a(14,17) =  -2*constN
a(14,18) =  -2*constNY
a(14,20) =   constN
a(14,21) =   constNY

```

c

B

```

a(3,2)   =   constNY
a(3,3)   =   constA
a(3,5)   =  -2*constNY
a(3,6)   =  -2*constA
a(3,8)   =   constNY
a(3,9)   =   constA

```

```

a(12,5)  =   constNY
a(12,6)  =   constA
a(12,8)  =  -2*constNY
a(12,9)  =  -2*constA
a(12,11) =   constNY
a(12,12) =   constA

```

```

a(15,8)  =   constNY
a(15,9)  =   constA
a(15,11) =  -2*constNY
a(15,12) =  -2*constA
a(15,14) =   constNY
a(15,15) =   constA

```

```

a(18,11) =   constNY
a(18,12) =   constA
a(18,14) =  -2*constNY
a(18,15) =  -2*constA
a(18,17) =   constNY
a(18,18) =   constA

```

```

a(19,14) =   constNY

```

```

a(19,15) = constA
a(19,17) = -2*constNY
a(19,18) = -2*constA
a(19,20) = constNY
a(19,21) = constA

```

c

C

```

a(1,1) = -constD
a(1,4) = constC+(4*constD)
a(1,7) = -2*constC-(6*constD)
a(1,10) = constC+(4*constD)
a(1,13) = -constD

a(16,4) = -constD
a(16,7) = constC+(4*constD)
a(16,10) = -2*constC-(6*constD)
a(16,13) = constC+(4*constD)
a(16,16) = -constD

a(9,7) = -constD
a(9,10) = constC+(4*constD)
a(9,13) = -2*constC-(6*constD)
a(9,16) = constC+(4*constD)
a(9,19) = -constD

a(10,10) = -constD
a(10,13) = constC+(4*constD)
a(10,16) = -2*constC-(6*constD)
a(10,19) = constC+(4*constD)
a(10,22) = -constD

a(13,13) = -constD
a(13,16) = constC+(4*constD)
a(13,19) = -2*constC-(6*constD)
a(13,22) = constC+(4*constD)
a(13,23) = -constD

```

c

B.C.

```

a(20,14) = -1.0
a(20,20) = 1.0

a(21,15) = -1.0
a(21,21) = 1.0

a(22,16) = -1.0
a(22,22) = 1.0

a(4,4) = 1.0
a(4,7) = -2.0
a(4,10) = 1.0

a(5,5) = 1.0

a(6,6) = 1.0

a(7,7) = 1.0

a(23,13) = -1.0
a(23,16) = 2.0
a(23,22) = -2.0

```


$$a(23,23) = 1.0$$

$$\begin{aligned} \text{c} \quad & \text{B} \\ & a(12,10) = 0.5*p*h \\ & a(15,13) = p*h \\ & a(18,16) = 1.5*p*h \\ & a(19,19) = 2*p*h \end{aligned}$$

$$\begin{aligned} \text{c} \quad & \text{C} \\ & a(16,6) = -0.5*p/h \\ & a(16,9) = p/h \\ & a(16,12) = -0.5*p/h \\ \\ & a(9,9) = -p/h \\ & a(9,12) = +2*p/h \\ & a(9,15) = -p/h \\ \\ & a(10,12) = -1.5*p/h \\ & a(10,15) = +3*p/h \\ & a(10,18) = -1.5*p/h \\ \\ & a(13,15) = -2*p/h \\ & a(13,18) = +4*p/h \\ & a(13,21) = -2*p/h \end{aligned}$$

$$\begin{aligned} \text{c} \quad & \text{B.C.} \\ & a(23,19) = -(h**3)*p*y/Cw \end{aligned}$$

$$\begin{aligned} \text{pi} &= 3.1415927 \\ \text{constNYC} &= 0. \\ \text{constAC} &= 0. \\ \text{constTC} &= 0. \\ \text{constCC} &= 0. \\ \text{constDC} &= 0. \\ \text{constGC} &= 0. \end{aligned}$$

$$\begin{aligned} \text{c} \quad & \text{A} \\ & c(2) = 0.0 \\ & c(11) = -\text{constNYC}*\sin(\text{pi}/8.) - 0.5*p*h \\ & c(8) = -\text{constNYC}*\sin(\text{pi}/4.) - p*h \\ & c(17) = -\text{constNYC}*\sin(3*\text{pi}/8.) - 1.5*p*h \\ & c(14) = -\text{constNYC}*\sin(4*\text{pi}/8.) - 2*p*h \end{aligned}$$

$$\begin{aligned} \text{c} \quad & \text{B} \\ & c(3) = 0.0 \\ & c(12) = -\text{constAC}*\sin(\text{pi}/8.) + \\ & * \quad \text{constTC}*\sin(\text{pi}/8.) \\ & c(15) = -\text{constAC}*\sin(\text{pi}/4.) + \\ & * \quad 2*\text{constTC}*\sin(\text{pi}/4.) \\ \\ & c(18) = -\text{constAC}*\sin(3*\text{pi}/8.) + \\ & * \quad 3*\text{constTC}*\sin(3*\text{pi}/4.) \\ \\ & c(19) = -\text{constAC}*\sin(4*\text{pi}/8.) + \\ & * \quad 4*\text{constTC}*\sin(4*\text{pi}/8.) \end{aligned}$$

```

c          C
      c(1)   = 0.0+0.5*p*q
      c(16)  = -constCC*sin(pi/8.)-constDC*sin(pi/8.)
*          +constGC*sin(pi/8.)+0.5*p*q
      c(9)   = -constCC*sin(pi/4.)-constDC*sin(pi/4.)
*          +2*constGC*sin(pi/4.)+0.5*p*q

      c(10)  = -constCC*sin(3*pi/8.)-constDC*sin(3*pi/8.)
*          +3*constGC*sin(3*pi/8.)+0.5*p*q

      c(13)  = -constCC*sin(4*pi/8.)-constDC*sin(4*pi/8.)
*          +4*constGC*sin(4*pi/8.)+0.5*p*q

c          B.C.

      c(23) = (-2*(h**3)*0.5*p*y*theta)/Cw

      c(5) = 0.0
      c(6) = 0.0
      c(7) = 0.0
      c(4) = 0.0
      c(20) = 0.0
      c(21) = 0.0
      c(22) = 0.0

c
c  _____
n = 23
np= 23

      call ludcmp(a,n,np,indx,d)
      do 76 j=1,n
      d=d*a(j,j)
76      continue
      determ=d
      if (p.EQ.0.) then
      determZ=determ
c      write(*,*)"determ,p=",determ,p
      endif
      determbar=determ/determZ
      if (determbar.LE.-0.0001) go to 11
      call lubksb(a,n,np,indx,c)

c  _____
do i = 1,n
c      write(*,*) 'displacement, i,c(i) = ',i,c(i)
      enddo

      v(1)=c(5)
      v(2)=c(8)
      v(3)=c(11)
      v(4)=c(14)
      v(5)=c(17)

      u(1)=c(6)
      u(2)=c(9)
      u(3)=c(12)
      u(4)=c(15)
      u(5)=c(18)

      w(1)=c(7)
      w(2)=c(10)

```

```

      w(3)=c(13)
      w(4)=c(16)
      w(5)=c(19)

      write(*,*) ,p,w(5)
      do i=1,5
c        write(*,*) ,i,v(i),u(i),w(i)
      enddo

      straina = 2*v(5)-1*u(5)+2*w(5)

      if (straina.GE.straincr) go to 11

c      write(*,*) ,p,straina
99      continue
11      continue
      stop
      end

c                                     LU DECOMPOSITION

      subroutine ludcmp(a,n,np,indx,d)
      implicit real*8 (a-h,o-z)
      parameter (nmax=100,tiny=1.0E-20)
      dimension a(np,np),indx(n),vv(nmax)
      d=1.
      do 12 i=1,n
      aamax=0.
      do 11 j=1,n
      if (abs(a(i,j)).GT.aamax) aamax=abs(a(i,j))
11      continue
      if (aamax.EQ.0.) PAUSE "Singular matrix."
      vv(i)=1./aamax
12      continue
      do 19 j=1,n
      do 14 i=1,j-1
      sum=a(i,j)
      do 13 k=1,i-1
      sum=sum-a(i,k)*a(k,j)
13      continue
      a(i,j)=sum
14      continue
      aamax=0.
      do 16 i=j,n
      sum=a(i,j)
      do 15 k=1,j-1
      sum=sum-a(i,k)*a(k,j)
15      continue
      a(i,j)=sum
      dum=vv(i)*abs(sum)
      if (dum.GE.aamax) then
      imax=i
      aamax=dum
      endif
16      continue
      if (j.NE.imax) then
      do 17 k=1,n
      dum=a(imax,k)
      a(imax,k)=a(j,k)
      a(j,k)=dum

```

```

17      continue
        d=-d
        vv(imax)=vv(j)
      endif
      indx(j)=imax
      if(a(j,j).EQ.0.) a(j,j)=tiny
      if(j.NE.n) then
        dum=1./a(j,j)
        do 18 i=j+1,n
          a(i,j)=a(i,j)*dum
18      continue
        endif
19      continue
      return
    end

c                                SUBROUTINE LUBKSB

      subroutine lubksb (a,n,np,indx,c)
      implicit real*8 (a-h,o-z)
      dimension a(np,np),indx(n),c(n)
      ii=0
      do 12 i=1,n
        ll=indx(i)
        sum=c(ll)
        c(ll)=c(i)
        if (ii.NE.0) then
          do 11 j=ii,i-1
            sum=sum-a(i,j)*c(j)
11          continue
          else if (sum.NE.0.) then
            ii=i
          endif
          c(i)=sum
12      continue
      do 14 i=n,1,-1
        sum=c(i)
        do 13 j=i+1,n
          sum=sum-a(i,j)*c(j)
13      continue
        c(i)=sum/a(i,i)
14      continue
      return
    end

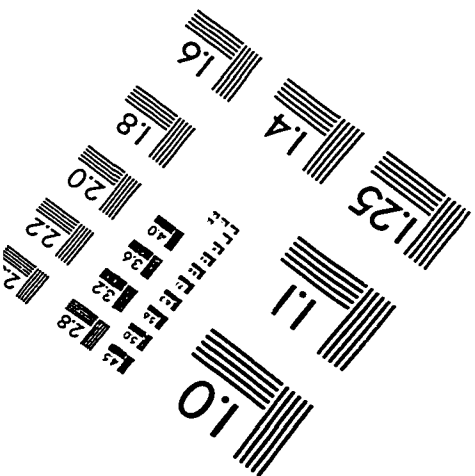
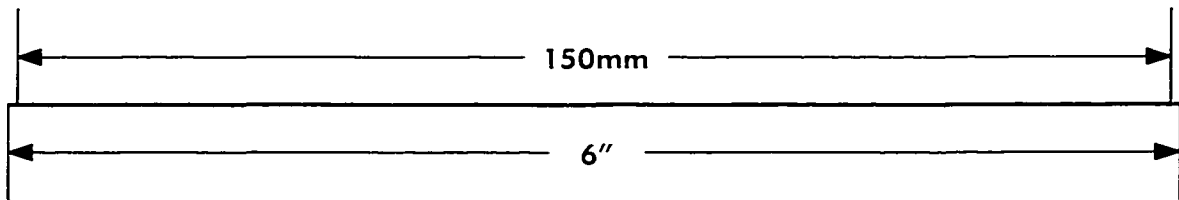
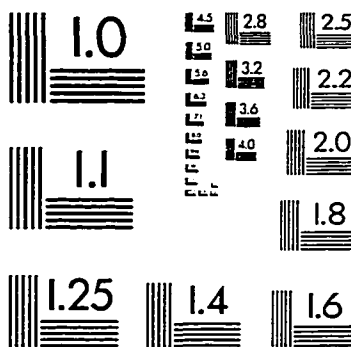
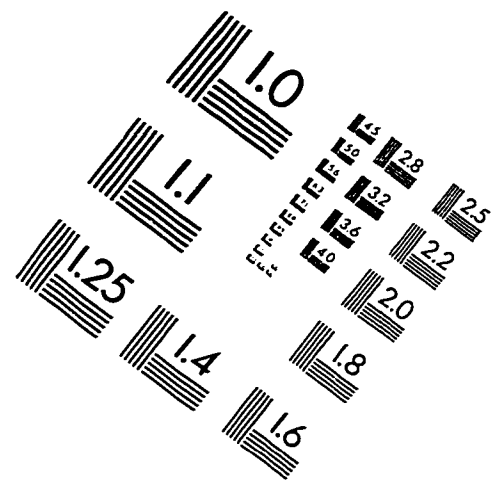
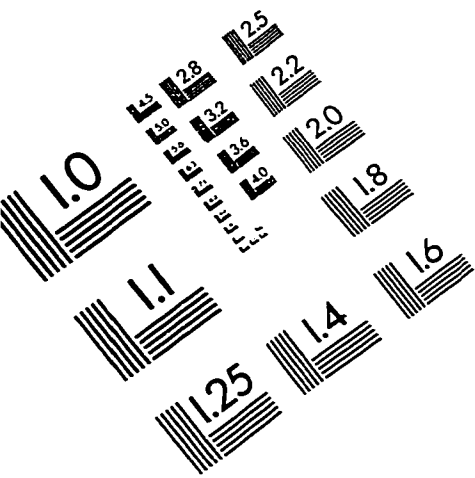
```

VITA

Name: Mojtaba B. Sirjani
Born: September 28, 1959
Place of Birth: Mashhad Iran
Permanent Address: Rehnamai-18 Palestine-15
House No. 31
Mashhad, IRAN

The author was born to Mohammed Sadgh and Nossrat Sirjani in the city of Mashhad, Iran. He completed his early education up to high school in Iran, and then briefly attended Tehran University in 1978. He received B.S. in Mechanical Engineering from Old Dominion University at Norfolk Virginia in May 1984. He finished M.S. in Manufacturing Engineering from North Carolina A&T State University in May 1989. He worked as a design engineer for W.F. Altenpohl, Inc. at High Point, North Carolina from 1987 through 1989. He taught as adjunct assistant professor for the department of technology at Old Dominion University from 1989 through 1992. The author has been teaching at Norfolk State University as assistant professor since 1989. In June, 1993, he entered Old Dominion University to pursue a Ph.D. degree program in Civil Engineering.

IMAGE EVALUATION TEST TARGET (QA-3)



APPLIED IMAGE . Inc
1653 East Main Street
Rochester, NY 14609 USA
Phone: 716/482-0300
Fax: 716/288-5989

© 1993, Applied Image, Inc., All Rights Reserved

